Additive Manufacturing of Aluminium-Metal Matrix Composite developed through Mechanical Alloying

OMOTOYOSI HELEN FAMODIMU (B.Eng., MSc.)

A thesis submitted in partial fulfilment of the requirements of the University of Wolverhampton for the degree of Doctor of Philosophy

September 2016

This work or any part thereof has not previously been presented in any form to the University or to any other body whether for the purposes of assessment, publication or for any other purpose (unless otherwise indicated). Save for any express acknowledgements, references and/or bibliographies cited in the work, I confirm that the intellectual content of the work is the result of my own efforts and of no other person.

Signature……

Date…….

Abstract

Laser melting of aluminium alloy - AlSi10Mg has increasingly been used to create specialised products in aerospace and automotive applications. However, research on utilising laser melting of Aluminium matrix composites in replacing specialised parts have been slow on the uptake. This has been attributed to the complexity of the laser melting process, metal/ceramic feedstock for the process and the reaction of the feedstock material to the laser. Thus an understanding of the process, material microstructure and mechanical properties is important for its adoption as a manufacturing route of Aluminium Metal Matrix Composites.

The effect of the processing parameters (time and speed) on embedding the Silicon Carbide onto the surface of the AlSi10Mg alloy was initially investigated in Phase 1 and 2 of the research. The particle shape and maximum particle size for each milling time and speed was analysed in determining a suitable starting powder for the Laser Melting phase. An ideal shape and size for the composite powder was obtained at 500 rev/min when milled for 20 mins.

The effects of several parameters of the Laser Melting process on the mechanical blended composite were investigated. Single track formations of the matrix alloy, 5% Aluminium Metal Matrix Composites and 10% Aluminium Metal Matrix Composites were studied for their reaction to the laser melting in Phase 3. Subsequently in Phase 4, density blocks were studied at different scan speeds and step-over for surface roughness, relative density and porosity. These were utilised in determining a process window to fabricate near fully dense components.

Phase 5 of the research focused on microstructural and mechanical properties of the laser melted matrix alloy using the normal parameters for the matrix alloy and the modified LM parameters for the composite powders. Test coupons were built in one orientation and some coupons were heat-treated to initiate precipitation-hardening intermetallics in the matrix and composite.

This study investigates the suitability of the mechanical alloying as a novel method of producing feedstock material for the LM process. This research further explores the interaction of the composite powders with the laser until suitable process parameters were obtained. Furthermore, the fractography, mechanical and microstructural evolution of the Al/SiC composite, with different percentage volume reinforcement manufactured by the LM and subsequently heat treated, was explored for the first time.

Table of Contents

Additive Manufacturing of Aluminium-Metal Matrix Composite developed through Mechanical Alloying 1

Abstract 2

Table of Contents 3

Acknowledgements 8

Conferences 9

List of Acronyms 10

List of Definitions 11

Chapter One 12

Introduction 12

1.1 Introduction 12

1.2 Research Justification 13

1.3 Aim and Objectives 13

1.4 Overview of the thesis 14

Chapter Two 15

Literature Review of Additive Manufacturing 15

2.1 Introduction 15

2.1.1 Additive Manufacturing for Metal Systems 15

2.1.2 Advantages of Additive Manufacturing for Metal Systems 16

2.1.3 Disadvantages of Additive Manufacturing 17

2.2 Laser Technology in Additive Manufacturing - Powder Bed Systems 18

2.2.1 Laser Melting (LM) of metal powders 19

2.2.2 Laser Melting Process in Powder Bed Systems 19

2.2.3 Laser Melting Parameters 21

2.3 Selective Laser Melting/Laser Melting for Metallic alloys and Metal Matrix Composites (MMCs) 25

2.3.1 Material /Powder properties for Metallic Alloys 26

2.3.2 Process optimisation and Track development 26

2.3.3 Selective Laser Sintering/Selective Laser Melting of Metal Matrix Composites .. 28
2.4 Summary and Critique of the Chapter 29
Chapter Three 31
Materials 31
3.1 Introduction to Materials utilised in research 31
3.2 Aluminium and its alloys 31
3.2.1 Properties and Metallurgy of AlSi10Mg 32
3.2.2 Effect of alloying elements 33
3.2.2.1 Major Alloying Elements 33
3.2.2.2 Minor Alloying Elements 34
3.2.2.3 Microstructure Modifiers – 34
3.2.2.4 Impurity Elements 34
3.2.2.5 Al-Si Phase Diagram 35
3.2.2.6 Addition of Magnesium to Aluminium-Silicon alloys 36
3.2.3 Powder Metallurgy of Aluminium Alloys 38
3.2.3.1 Gas Atomisation 38
3.2.3.2 Mechanical Alloying (MA) 39
3.2.3.3 Laser Melting for Aluminium alloys 44
3.3 Silicon Carbide (SiC) 45
3.4 Composites – Aluminium alloy/SiC Metal Matrix Composites (MMCs) 46
3.4.1 Particulate Reinforced Aluminium Metal Matrix Composites 48
3.4.2 Wettability and Chemistry of the Al-alloy and SiC interface 49
3.4.3 Components and Tailoring of Metal Matrix Composites 50
3.4.3.1 Matrix: 50
3.4.3.2 Reinforcement: 51
3.4.3.3 Interface 51
3.4.3.4 Volume and Shape of Reinforcement: 52
3.4.3.5 Location of the Reinforcement: - 52
3.4.4 Production of Aluminium Metal Matrix Composites 53
3.4.4.1 Liquid State Processing: 53
3.4.4.2 Solid State Processing: 53
3.4.4.3 Powder Metallurgy: 53
3.4.5 Strengthening Mechanisms in Particulate Reinforced Metal Matrix Composites 54
3.4.5.1 Solid Solution Strengthening: 54

3.4.5.2 Precipitate/Dispersion Strengthening: 55
3.4.5.3 Work Hardening: 55
3.4.6 Heat Treatment of Aluminium Metal Matrix Composites 55
3.5 Chapter Summary 58
Chapter Four 59
Experimentation and Methodology 59
4.1 Introduction 59
4.2 Introduction to Experimentation 59
4.2.1 Justification for Mechanical Alloying 60
4.3 Mechanical Alloying of the Composite Powder (Phase 1 and Phase 2) 63
4.3.1 Powder Preparation for Mechanical Alloying 63
4.3.2 The ZOZ Simoloyer CM01 Machine (ZOZ) 64
4.3.3 Powder Measurement for Reinforcement 64
4.3.4 Charging of the Ball Mill 65
4.4 Phase 1 - Experiment on Mechanical Alloying Parameters 68
4.5 Phase 2 - Experiment on Mechanical Alloying Parameters 70
4.6 Powder Characterisation 70
4.6.1 Characterisation by Scanning Electron Microscope (SEM) 71
4.6.2 Investigation of the Particle Size Distribution 71
4.6.3 Characterisation by X-Ray Diffraction (XRD) 72
4.6.4 Particle Shape Characterisation 75
4.7 Laser Melting of AlSi10Mg alloy and AlSi10Mg/SiC_p (Phase 3, 4 and 5) 76
4.7.1 Powder preparation for Laser Melting 77
4.7.2 Scanning Strategy for AlSi10Mg 79
4.8 Phase 3 – Parameters Investigation 79
4.8.1 Single Track Formation 80
4.9 Phase 4 – Laser Melting of Density Blocks 81
4.9.1 Characterization of the Samples 82
4.9.1.1 Surface Roughness 83
4.9.1.2 Determination of Relative Density 84
4.9.1.3 Determination of Porosity 85
4.10 Phase 5 - Mechanical and Destructive Testing 86

4.10.1 Heat Treatment 86
4.10.2 Transverse Rupture Stress (TRS) 88
4.10.3 Micro-Hardness Testing 90
4.10.4 Laser Melting Microstructural Observations. 91
4.10.4.1 Crystallographic Structure of Samples 91
4.10.4.2 Investigation of Fracture Surfaces 91
4.11 Chapter Summary 92
Chapter 5 94
Phase 1 and 2 94
Mechanical Alloying of Al-alloy and SiC powders. 94
5.1 Introduction 94
5.2 Alloying Parameters and Microstructural Evaluation – Phase 1 and Phase 2 94
5.2.1 Phase 1 – Mechanically Alloyed Blend 94
5.2.2 Phase 2 -Mechanically Alloyed Blend 97
5.2.3 Mixed Blend without Grinding Media 103
5.3 Particle Size Distribution 104
5.4 X-ray Diffraction Characterisation of Powder Samples. 107
5.5 Chapter Summary 110
Chapter 6 111
Phase 3 and 4 111
Laser Melting of the Composite Powder 111
6.1 Introduction 111
6.2 Phase 3 - Single Track Formation 112
6.2.1 Single Track Formation of the Matrix Alloy – AlSi10Mg 112
6.2.2 Single Track Formation of the Composite Powders - AlSi10Mg/SiC_p 113
6.3 Phase 4 - Sample Blocks using Varied Parameters 122
6.3.1 Visual Inspection of Aluminium Metal Matrix Composite Sample blocks 122
6.3.2 Effect of Scanning Speed on the Surface Roughness. 124
6.3.3 Effect of Energy Density on the Surface Roughness 131
6.3.4 Effect of Scanning Speed on Relative Density and Porosity 138
6.3.5 Effect of Energy Density on Relative Density and Porosity 140

6.3.6 Pore Classification on Variation of Scanning Speed and Energy Density 141
6.4 Chapter Summary 148
Chapter 7 150
Phase 5 150
Mechanical Testing and Microstructural Characterisation 150
7.1 Transverse Rupture Stress (TRS) and MicroHardness 150
7.2 Microstructural Characterisation 157
7.3 Fracture Surfaces 168
7.4 Evaluation of the Mechanical Properties 174
7.5 Evaluation of the Microstructural Development 176
Chapter 8 178
Conclusion and Future Work 178
8.1 Contribution to knowledge 178
8.2 Conclusions 178
8.3 Outlook and Future Work 180
References 182

Acknowledgements

I want to express my gratitude to my supervisors Prof. Mark Stanford, Prof. Chike Oduoza, Dr. Lijuan Zhang and Prof. Kevin Kibble for their patience, support and guidance throughout this study. My sincere thanks to the laboratory managers and technicians most especially, Iain Lyall, Daniel Wilmot, Colin Durnall, Dr. Keith Jones and David Townrow without whom I would never have completed this research. I'll forever admire your patience in answering my questions.

A special thanks goes to my parents, siblings and dearest friends, without your continuous support I would have never gotten to where I am today. You have always been there to listen, help me and pray when needed. I am blessed to have such a wonderful family. Thank you!

Finally, I wish to thank Joseph and Justus, for their love, patience and support during the duration of this research, without which I would never have achieved this much. You are my motivation and strength to achieve more than I can ever be.

This work is mainly dedicated to you and Justus, the strong men in my life.

Conferences

Olowofela O. H., Stanford, M., Zhang, L., Oduoza, C., Kibble, K. and Lyall, I. Mechanical Alloying for Additive Layer Manufacturing. Presented at ICCE-21 in Tenerife- Spain – July 21-27, 2013

Famodimu O. H., Stanford, M., Zhang, L. and Oduoza, C. (2014) Selective Laser Sintering of Aluminium Metal Matrix Composite. Presented at the 24th International Conference on Flexible Automation and Intelligent Manufacturing, May 20-23, San Antonio- Texas.

List of Acronyms

3D	Three Dimensions
AM	Additive Manufacturing
Al	Aluminium
Al-MMCs	Aluminium Metal Matrix Composites
Al/SiC_p	Silicon Carbide Particulate Reinforced Aluminium
AS	As-built
AST6	As-built and T6 heat treated
BPR	Ball to Powder Ratio
BSE	Back Scattered Electron Microscopy
CAD	Computer Aided Drawing
CNC	Computer Numeric Control
CO_2	Carbon Dioxide
DMLS	Direct Metal Laser Sintering
EBM	Electron Beam Melting
ED	Energy Density
EDS	Energy Dispersive X-Ray Spectroscopy
FCC	Face Centred Cubic
FDM	Fused Deposition Modelling
FS	Flexural Strength
HAZ	Heat Affected Zone
HCP	Hexagonal Close Pack
HIP	Hot Isostatic Pressure
IA	Image Analysis
LM	Laser Melting
MA	Mechanical Alloying
MMCs	Metal Matrix Composites
Nd: YAG	Neodymium-doped Yttrium Aluminium Garnet (Nd: $Y_3Al_5O_{12}$)
PM	Powder Metallurgy
Ra	Average Roughness
RD	Relative Density
SiC	Silicon Carbide
SEM	Scanning Electron Microscope
SLA	Stereolithography 3D printing
SLM	Selective Laser Melting
SLS	Selective Laser Sintering
SR	Stress Relieved
SRT6	Stress Relieved and T6 heat treated
STL	STereoLithography file
TRS	Transverse Rupture Stress
TS	Tensile Strength
XRD	X-Ray Diffraction
YS	Yield Strength

List of Definitions

Additive Manufacturing (AM) – A process of joining materials to make solid objects from three dimensional model data, usually layer upon layer.

Direct Metal Laser Sintering (DMLS) – A powder-bed fusion process used to make metallic parts without binders. This process achieves full melting of the metal powder by selectively melting a lower melting element in an alloy and thus, is usually used for multi-component metallic alloys. The terminology is mostly used by EOS GmbH.

Electron Beam Melting (EBM) – Metallic powders are spread in layers and fused together using electron beams unlike the laser systems.

Heat Affected Zone (HAZ) – The volume of material in the zone surrounding a laser melted area which the laser heat has conducted and altered due to the heat.

Laser Melting (LM) – Like the DMLS, LM can be used for multi-component alloy systems, however, unlike DMLS, LM in this research is used to fabricate metal matrix composites rather than metallic alloys.

Mechanical Alloying (MA) – Alloying of two or more powders utilising a milling machine Metal Matrix Composites (MMC).

Selective Laser Melting (SLM) – Metallic powder layers are spread and fully melted by the lasers, however this process is more suited to a mono-component system unlike DMLS. The terminology is mostly used for SLM Solutions processes.

Selective laser sintering (SLS) – A powder bed fusion process used to make parts without binders. This process does not achieve full melting of the metal powder from the laser but are sintered by making the powder fuse together at the molecular level and is usually used for non-metallic parts like ceramics and plastics.

Powder Metallurgy (PM) – The manufacturing of solid parts of desired geometry and material from metallic alloy powders.

Chapter One

Introduction

1.1 Introduction

The advent of Additive Manufacturing (AM) has led to the production of optimised parts, which are manufactured for design rather than designed for manufacture that traditionally was the customary manufacturing practice. As such reduction of lead times on new product development is becoming more and more common (Reeves, 2008). Its usage has been driven primarily by the needs of different industries like bioengineering to produce dental caps and knee braces, automotive and aerospace engineering to produce complex parts with intricate internal features. This has led to the rapid development of the technology from the initial stages of rapid prototyping to the predominant development of the polymer manufacturing and now investigations into different metallic systems. Additive Manufacturing (AM) also addresses major customer manufacturing concerns, through the rapid development of specialised components with integrated functionality, Keppler (2011).

The use of aluminium (Al) alloys in building high strength structural parts has increased over the years most especially in the automobile, mining, mineral, aerospace and defence industries (Davis, 1993). This has been driven mostly by a need to reduce energy consumption in social and industrial usage with their high strength and low weight characteristics. Aluminium reinforced structural parts have been utilised for an increasingly complex array of components in these industries (Ghosh and Saha, 2011). Metal Matrix Composites (MMCs) are one of such reinforced materials and are made from a mixture of reinforcements (carbides, oxides and nitrides of metallic or ceramic additions) in a tough metallic matrix. Different types of reinforcements; including continuous fibres (both monofilament and multifilament), short fibres, whiskers and particulates, from 10-60% by volume (Foltz and Blackmon, 1990) have been investigated. The percentage (%) reinforcement has a bearing on the properties together with the mode of manufacture which can vary with each type of reinforcement used. MMCs are emerging as important versatile materials due to the wide range of properties they provide. The advantage here is the ability to tailor properties to meet special requirements where conventional unreinforced materials are not suitable (Scudino *et al.,* 2009). Their usability however, highlighted by Rosso (2006) is limited due to poor toughness and expensive manufacturing techniques.

This thesis would thus explore the AM route to producing an MMC with a view to improving the mechanical properties of the matrix material while achieving the targets cited by Keppler (2011). This will be achieved by influencing the feed material through mechanical alloying to ensure a homogeneous output. This will also have an added benefit of reducing overhead production costs by fabricating the required component with a single manufacturing process. The use of additive manufacturing for the production of Al-MMCs is supported by (Looney *et al.*, 1992; Hao and Dadbakhsh, 2009) who have identified that due to the inclusion of ceramic reinforcement (especially carbides), conventional manufacturing techniques (machining and turning) are often more expensive due to the increase in tool wear during the direct manufacture of high performance materials. Moreover, aluminium powder metallurgy offers components with enhanced physical and mechanical properties and surface finish, which are achieved at a competitive cost to other metallic alloys and processing routes (Fogagnolo *et al.*, 2004).

1.2 Research Justification

This research investigates the processing of Al-MMCs with an aim to ensure homogeneity of the AM feed material and producing a near-full dense composite with improved properties comparable to Al-MMCs fabricated through traditional routes, while reducing manufacturing times through the use of Additive Manufacturing. The challenge for the Laser Melting (LM) process is to produce near-full dense homogenous particulate-reinforced parts from dissimilar materials such as metals and ceramics. In order to achieve this, the major problems of even distribution of the reinforcement particles in the Al-alloy powder and consistent powder morphology of the feed material (composite) for the LM process needs to be addressed. In addition, the difference in the particle size and individual properties of both reinforcement and matrix alloy create complications during the LM process that make this approach to manufacturing different from the conventional manufacturing methods, (Ghosh *et al*., 2010)

1.3 Aim and Objectives

This research aims to develop a laser melting process utilised in the fabrication of particulate reinforced aluminium alloy matrix composite with a view to understanding the material properties, process characteristics, metallurgy and chemistry needed to obtain optimal and reliable properties.

The key objectives include:

A. Producing a homogeneous feed material for the LM Process through Mechanical Alloying (MA).

1. Determine suitable mechanical alloying parameters for matrix and reinforcement.
2. Evaluate the effect of reinforcement particles on the growth size, shape and morphology of the matrix particle.
3. Limit the particle size distribution to regulate the packing density for the LM process.
4. Forestall any mechano-chemical reactions occurring during the MA process.
5. Prevent any contamination of the powder during the whole process either from the milling chamber or by oxidation.

B. Investigate the material/process interactions.

1. Explore the reaction of the composite powder to the laser, based on the matrix interactions.
2. Investigate the surface roughness, porosity and density to obtain suitable LM parameters.
3. Investigate and understand the mechanical, metallurgical evolution and chemical characteristics of the Al-MMC material manufactured by the LM process in comparison with Al/SiC_p composites fabricated through traditional methods.

1.4 Overview of the thesis

The thesis is organised into the chapters below

Chapter 1 is an introduction to the thesis.

Chapter 2 is the review and critically examination of relevant literature where LM was introduced and existing research reviewed.

Chapter 3 investigates the materials and material properties.

Chapter 4 is the experimentation and methodology adopted for the research.

Chapter 5 discusses the results of the mechanical alloying experimentation.

Chapter 6 discusses the results of the LM experimentation.

Chapter 7 discusses the mechanical tests and the microstructural changes observed.

Chapter 8 focuses on the conclusions and introduces areas for future research.

Chapter Two

Literature Review of Additive Manufacturing

2.1 Introduction

Additive Manufacturing (AM) involves an integration of materials science, mechanical engineering, and laser technology and is thus regarded as an important recent development in the manufacturing sector, (Lu *et al*., 2001). Additive Manufacturing (AM) is a process where three dimensional parts or components with complex geometry and thin structural walls are created directly from computer-aided-design models (Sachs *et al.*, 1993 and Bartkowiak *et al.*, 2011). It is different from other subtractive manufacturing processes as these processes create parts by removing unwanted material using cutting tools (Bineli *et al.*, 2011). AM initially started out from rapid prototyping of polymer-based powders from three dimensional (3D) printers into the production of complex shaped functional components, including metals, alloys and metal matrix composites (MMCs) that cannot be easily manufactured using conventional methods. AM has thus matured in order to meet the demanding requirements from aerospace, automotive and biomedical sectors by being able to produce optimised parts with improved strength to weight ratios (Manfredi *et al*., 2014).

AM methods vary depending on the modes of layering and material being used and are divided into seven major processes (Pinkerton, 2016) as defined in ASTM F2792 (2012) – Binder Jetting, Direct Energy Deposition, Material Extrusion, Material jetting, Powder Bed Fusion, Sheet Lamination and Vat Photopolymerization. These categories are further divided into many other processes such as Selective Laser Sintering (SLS), Fused Deposition Modelling (FDM), Stereolithography (SLA), Electron Beam Melting (EBM), Direct Metal Laser Sintering (DMLS) and Laser Melting (LM). AM has stimulated research for lighter-weight materials that offer environmental benefits through the reduction of waste material and emissions during manufacture and has been a catalyst for new research into alloying possibilities for enhanced composite development, (Schaffer, 2004).

2.1.1 Additive Manufacturing for Metal Systems

The commercial development of AM for metals systems started about 10 years ago when both lasers and electron beams were investigated as energy sources for melting the fine metallic particles in a powder bed. The process is similar to the SLS systems used in

producing polymer components as metallic powders are rolled on to the building platform and are either sintered or melted to form components. Each lowering of the platform in the Z-axis corresponds to the equivalent thickness of a single layer, which differs for each powder composition. The fine microstructure achievable in the process, which contributes to its mechanical properties, was attributed to the fast cooling of the molten alloy. Functional components created using the AM metal system have applications in biomedical [dentures and bone reconstruction; Herderick, (2011)] and automotive (brake discs) industries.

2.1.2 Advantages of Additive Manufacturing for Metal Systems

Buchbinder *et al.* (2011) highlight the benefits and potential of AM as being

a) **Resource Saving**: AM reduces the amount of raw materials processed as metal powder can be reused. In addition, there are savings generated through optimised designs due to the elimination of tooling time and reduction in waste generation during subtractive manufacturing processes used in fabricating metal parts. Waste is also reduced as the process eliminates the requirement for lubricants and coolants during manufacturing.
b) **Design Optimisation and Customization**: The optimised design for AM has benefitted the automobile and aerospace industry as increasingly complex structures are created and manufactured uniformly with reduced post processing. Therefore, it has enabled more parts to be designed for performance rather than manufacture which invariably saves money for manufacturing by reducing the manufacturing steps needed for niche products. In addition, the part complexity has little effect on manufacturing times or cost and the process has a wide range of materials like titanium, aluminium and stainless steel used in building components with full density achieved in the parts, Custom Part (2013).
c) **Production Efficiency**: Savings in production are achieved, as there are fewer processes to undergo during the manufacture of a component. Also, savings are achieved by the additive manufacturing of tooling thereby increasing production efficiency by reducing the downtime while also reducing assembly requirements as parts can be developed as a single component (Despeisse and Ford, 2015).

2.1.3 Disadvantages of Additive Manufacturing

The main constraints to the adoption of AM have been highlighted by Despeisse and Ford (2015) as follows.

a) **Mass Customisation:** The build rate of the process is usually too slow to be used in conventional manufacturing processes hence it is not wholly suited to high volume manufacturing. It increases the design to product realisation time especially for large volumes of components. Hence, it is usually used for specialized or one-off components except in some biomedical applications (like dental) which have been standardised, (Petrovic *et al.*, 2011).

b) **Lack of materials:** As the metal powders used in these processes have to be customised to suit the method of manufacture, it has restricted their growth and usage as a total replacement for conventional manufacturing processes (Despeisse and Ford, 2015). Currently stainless steel, titanium, cobalt chromium, nickel alloys, aluminium alloys and a few precious metals (Gold and Silver) have been characterised for use in most AM systems, however other metal powders like copper, silver and metal matrix composites need further research and development.

c) **Size Limitations:** Large sized objects are impractical to build, due to the protracted time necessary to manufacture the component thereby decreasing the productivity of the machines; furthermore, most machines have restricted build volumes for manufacturing (Poprawe *et al.*, 2015). Complex parts with protrusions also need to have in-built support structures, as internal designs and the weight of building powder may not be sufficient to sustain the component during building, (Stein, 2012).

d) **Expensive:** Although considerably cheaper than when it was first discovered, AM equipment is still too expensive for its occasional use in producing complex and delicate components as it is mostly still within the initial research phases and will thus increase the price of manufacturing (Daneshmand and Aghanajafi, 2012)**.** This is also hampered by the different metal systems from different companies thus leading to non-standardized specifications and parameters.

e) **Validation of properties:** Due to the layer building in AM systems, properties of the parts (anisotropy and surface finish) are better along the direction of the layer as compared to the direction of build thus requiring post-processing of parts (Petrovic *et al.*, 2011).

2.2 Laser Technology in Additive Manufacturing - Powder Bed Systems

There are two major energy systems utilised for generating the heat needed for melting the molten powder during the AM powder bed processes; electron beams and lasers. Electron Beam Melting (EBM) used by Arcam (Hiemenz, 2007), focuses electrons emitted from a tungsten filament to generate the heat used in melting the metallic powders while laser systems use different types of lasers to generate the required heat. Laser an acronym for light amplification by stimulated emission of radiation produces light waves in coherent phases that are amplified. AM systems use either Gas (for example carbon dioxide (CO_2)) or solid-state like Nd: YAG lasers as energy sources. Solid-state lasers use crystalline rods to set off chain reactions that produce an intense monochromatic light beam used in engineering applications. Kruth *et al.* (2003) noted that metallic systems and carbide ceramics absorb laser energy at lower wavelengths hence the shift from CO_2 lasers to ytterbium (Yb) and YAG lasers. Table 2.1 shows a summary of the metal systems with the energy source, process name, example materials and its operating company. This research focuses on laser systems that produce finer details and superior surface finish than the electron beam systems and they have greater flexibility in optimising new materials.

Table 2.1 Overview of current powder bed metal AM systems (Herderick, 2011)

Company	Process	Energy source	Material (Examples)	Machine
EOS	DMLS/LM	Ytterbium fibre (Yb-fibre) Laser	Maraging Steel, Cobalt Chrome, Ti6Al4V, AlSi10Mg, Bronze-based alloys, Nickel based alloys, Silver, Gold	M270 M280 M290
Concept Laser	Laser Cusing	Ytterbium fibre laser	Steel, Ti6Al4V, AlSi12, AlSi10Mg, Nickel based alloys	M1 M2 M3
Renishaw	SLM/LM	Ytterbium fibre laser	Maraging and Stainless Steel, Ti6Al4V, AlSi10Mg, Cobalt Chrome, Nickel based alloys,	AM250
Arcam	EBM	Electron Beams	Ti alloys, Cobalt Chrome	S12 A1, A2

2.2.1 Laser Melting (LM) of metal powders

Manufacturing companies have utilised LM of metals to propel global demand for increasingly complex designs and shorter product development times. LM was developed from the SLS/SLM processes in which an integral metallic powder is melted in layers without using a lower melting powder as a binder thus requiring a higher energy density; obtained from the laser beam, to accomplish full melting of the particles and achieve maximum part density. The chamber atmosphere is controllable allowing a range of materials to be manufactured, with components produced from highly reactive materials which are prone to oxidation thus an inert atmosphere filled with either nitrogen or argon is necessary (Petrovic *et al.*, 2011 and EOS Gmbh, 2007). LM parts are known to have a peculiar microstructure different from conventional manufacturing with small grain sizes and non-equilibrium phases (Thijs *et al.* (2010) and Kumar and Pityana (2011)). Grain sizes are much finer than cast or wrought alloys due to the rapid conduction of heat away from the molten pool and subsequent solidification of the area (Shellabear and Nyrhila, 2004).

2.2.2 Laser Melting Process in Powder Bed Systems

The part to be manufactured is designed using a 3D modeller which is converted into a model compatible with the LM machine; an Eosint M270 Xtended Platform; by slicing the 3D CAD model into 2D cross-sectional layers. The STL file triangulates the internal and external surfaces of the 3D model that is assessed for structural integrity, optimum build direction and supports. This is to ensure dimensional accuracy, optimum production time, accurate analysis of the layer thickness and the laser path (Campanelli *et al.*, 2010).

The sliced 2D file is uploaded to the Eosint M270 Xtended machine software for fabrication encompassing the information on the orientation and layer thickness. During the melting process shown in Fig. 2.1, the recoater blade distributes an even layer of powder; equal to the thickness from the sliced model, on the platform plate, which moves along the Z-axis. The layer of powder is then fully melted by the Yb-fibre laser (EOS, 2009) which generates sufficient energy to heat up and melt the powder particles forming a weld pool. When the 2D part shape on a layer has been fully melted, the recoater distributes another uniform layer and the process is repeated until the part is fully formed with each platform drop equal to the layer thickness (Campanelli *et al.*, 2010). The laser in a singular direction can scan the powder on each layer or as various researches have highlighted rotating, the scan pattern of each layer improves the densification of the part.

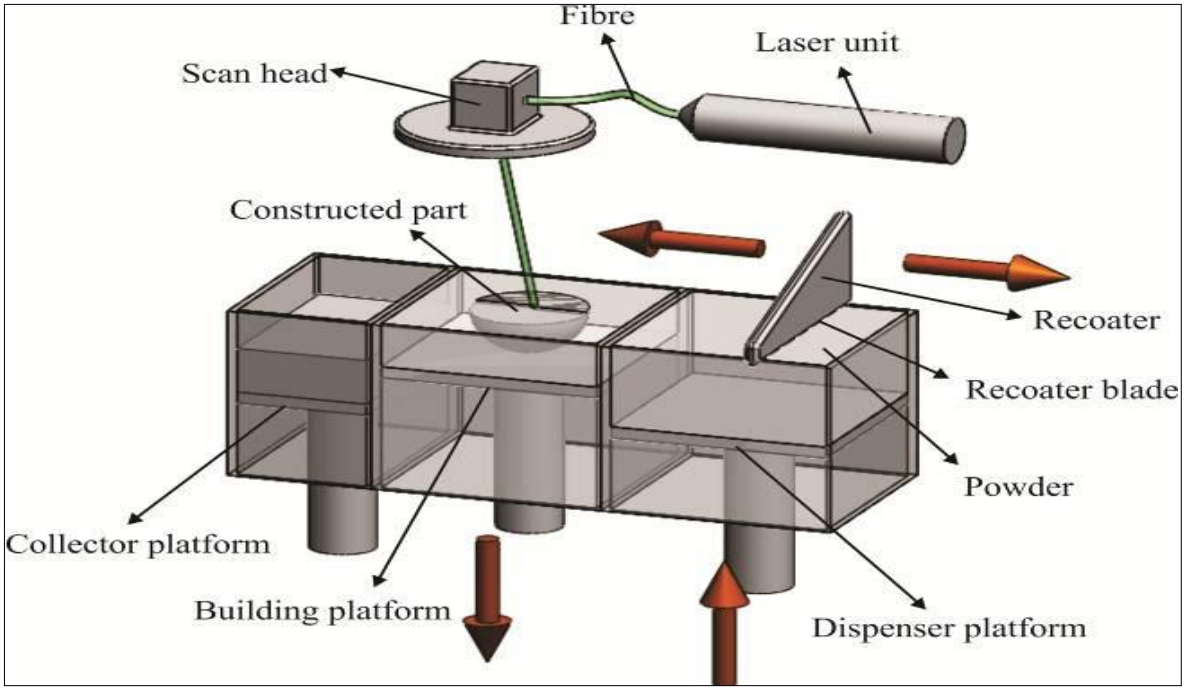

Figure 2.1 Schematic Diagram of the LM Recoating Process *(Bineli et al., 2011*)

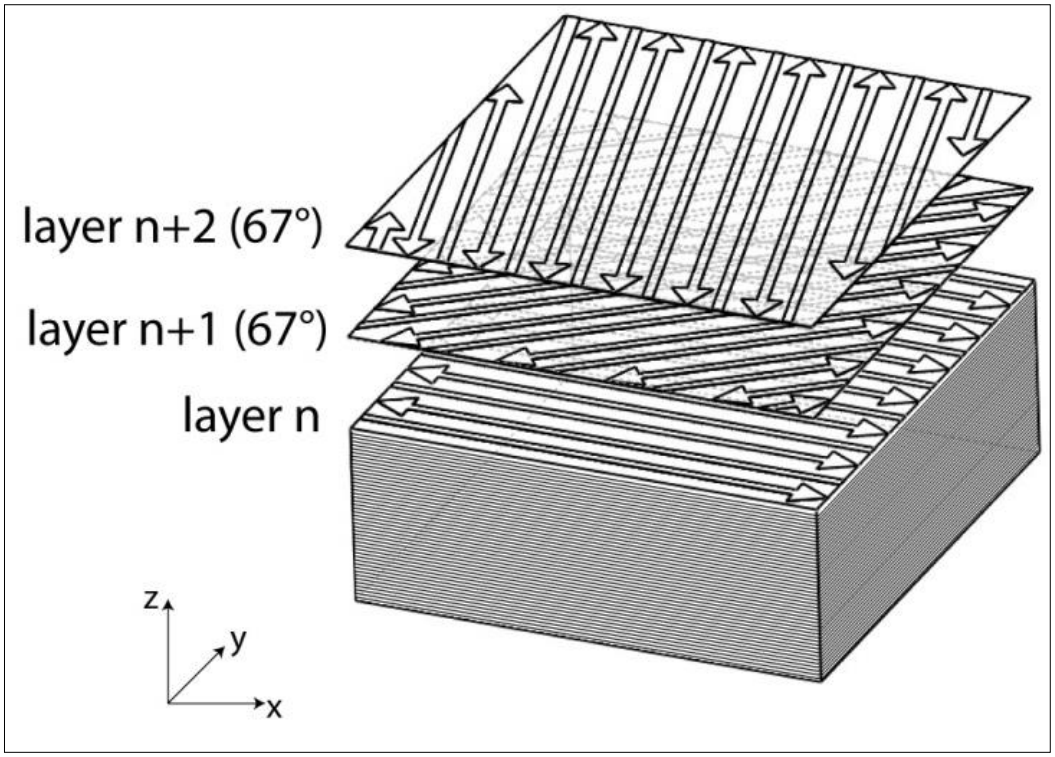

Figure 2.2 Raster scanning pattern for individual layers (Manfredi *et al.*, 2013)

The scanning pattern on the EOS mostly utilises the raster scan pattern in which the layers are each scanned at an angle of 67° to reduce porosity between layers and aid in heat dissipation, as observed in Fig. 2.2. The building platform is also preheated to an elevated temperature to minimize distortion and residual stresses arising from the sudden thermal shock the first layer

would experience otherwise. The temperature gradient develops when the laser heats the upper surface of the platform and as the heat is conducted slowly through the platform, a compressive strain in the direction of the colder sections results into stresses, Dadbakhsh (2012). The chamber is monitored closely to ensure that an inert atmosphere is maintained and there is minimal oxygen in the system that could lead to oxidation of the part and degradation of the powders.

2.2.3 Laser Melting Parameters

LM parameters are designated as the variables that control and influence the LM process from the 3D model through to the conclusion of fabrication and which can be modified to improve the properties of the part, (Williams and Deckard, 1998). Burakowski and Wierzchon (1998) also highlighted the importance of understanding the effect of process variables on material properties while Spears and Gold (2016) gives an overview of all parameters affecting the DMLS/SLM/LM processes**.**

These parameters are divided into 3 broad areas namely Pre-process Parameters, In-process Parameters and Post-process Parameters (Kumar, 2003).

I. Pre-process Parameters are considered before the commencement of the LM process and mostly involve the powder characteristics, which include particle size, particle size distribution, packing density and powder flowability. Gu and Shen (2007) state that the densification and the resultant microstructure of the DMLS component is due to the powder characteristics. The particle size distribution and packing density ensure that the correct thickness is deposited on each layer and the powder flowability ensures the layer is always uniform and even loading to full densification; this thus makes them important considerations for the LM process.

II. Post-Process parameters are considered after the LM process has concluded and are for enhancing the properties of the part. This includes removal from the substrate, heat treatment and improving the surface finish through shot peening if needed. The part removal process must not compromise either the part or its properties while the heat treatment is utilised in both reducing the residual stresses and improving the mechanical properties. Shellabear and Nyrhila (2004) observed that unlike conventionally manufactured 17-4 PH steel which can be precipitation hardened when heat treated resulting in increased strength and hardness, the laser sintered parts had reduced strength and hardness when heat treated. This was attributed to the

microstructural formation during the process, which forms a duplex structure of austenite and martensite. During the subsequent heat treatment, the duplex structure thus restricts the formation of more martensite hence the lower values.

III. In-Process parameters are controlled by the LM machine albeit with the user input, they are subsequently individually discussed below based on their effect in optimising new powders for the LM machine in order to achieve full densification. These parameters are discussed below with Fig. 2.3 and Fig. 2.4 showing the parameters and exposure patterns respectively used in the LM process.

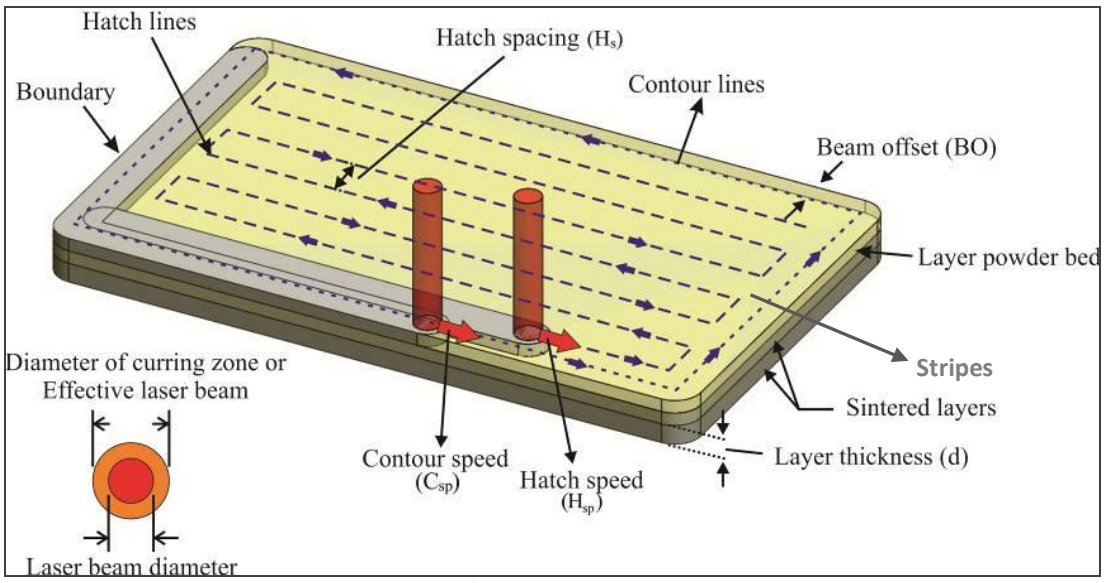

Figure 2.3 Schematic diagram of the LM Process Parameters (Bineli *et al.*, 2011)

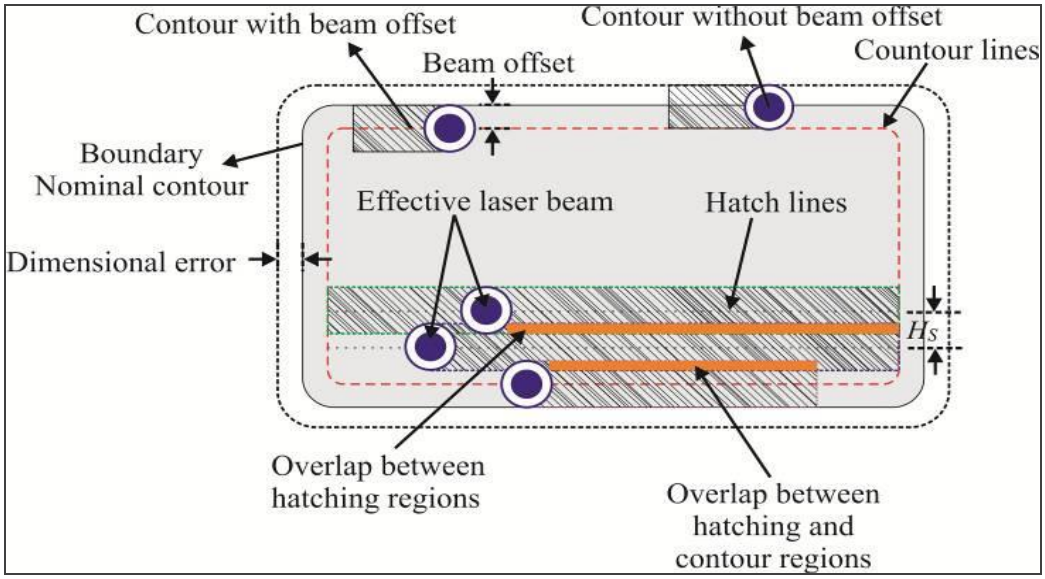

Figure 2.4 Schematic drawing of the LM Process Exposure Strategies (Bineli *et al.*, 2011)

a) **Laser Power:** Lasers generally produce heat on contact with materials with the laser in the EOS M270 Ext having a high beam quality that can be focused to a diameter of approximately 100 μm. The Yb-fibre laser is used rather than CO_2 fibres due to its shorter wavelength (1060-1100 nm) and generates up to 200 Watt power, which corresponds to an average power intensity of 25 KW/mm^2 for individual beam points (Shellabear and Nyrhila, 2004). The shorter wavelength leads to higher laser absorption and building speed for metals (Shellabear and Nyrhila, 2004) than the previously used CO_2 laser with a wavelength of 10.6 μm (Wang *et al.*, 2006).

b) **Scan speed:** Stwora and Skrabalak (2013) described it as the speed of the laser spot within an area and this affects the amount of heat available to generate the melt pool and thus a steady weld bead. It also has an important role in controlling the microstructure of the component by controlling the speed of liquidation and re-solidification of the metal. Excessive heating from slow scan speeds can lead to an increase in internal stresses caused by accelerated cooling and the thermal expansivity of the powder/molten metal system. Alternatively, at high scan speeds, increased porosity is observed as insufficient laser energy penetrates the powder layer aided by the highly reflective nature of Al alloys, (Pohl *et al.*, 2001). The heat absorbed from the low laser energy is unable to melt all the powder particles thus resulting in the increased porosity.

c) **Laser beam diameter:** The diameter of the laser beam is an important parameter as it determines the area of powder melted per second along with the scan speed. The focused laser beam melts a spot of powder and this creates a bigger weld pool than the beam spot as heat is conducted to the surrounding particles that consequently dissolve into the weld pool (Manfredi *et al.*, 2014). The heat is also conducted to the previous layers thereby creating a Heat Affected Zone (HAZ) in both the surrounding particles and previous layers. This area is influenced by the diameter of the laser beam because as the beam diameter increases, the HAZ also increases. The diameter of the melted area is therefore called the effective laser beam highlighted in Fig. 2.3, which includes the actual laser beam diameter and affected area melted by the residual heat around the diameter.

d) **Layer thickness/width:** The thickness of each powder layer spread during recoating corresponds to the distance travelled by the lowered platform after each laser scan, (Leu *et al.*, 2010). The layer thickness varies for each alloy depending on the metal/powder characteristics like melting point, thermal conductivity, and reflectivity.

When the layer thickness is too dense, the heat from the laser does not fully penetrate the layer resulting in incomplete melting of the powder particles and thus porosity. However, when the layer is shallow, the powder layer is rapidly degraded by the weld pool and melted particles are trapped between the layer and the recoater blade resulting in a poor structure (Buchbinder *et al.*, 2011 and Manfredi *et al.*, 2014).

e) **Hatch spacing:** Alternatively called the Step–Over is the distance between two laser tracks (hatches) during melting of the powder. Increasing or decreasing the specified value of the hatch spacing between the melted tracks can lead to particles of the irradiated region not being sintered or over sintered respectively, (Bineli *et al.*, 2011). The raster scanned areas, as per EOS standard scan parameter, are sintered in stripes that vary with each metallic alloy, across the platform and rotated at 67^{o} from layer to layer so that all the powder particles are fully sintered.

f) **Beam offset:** To compensate for the dimensional error caused by the effective laser beam, the actual laser beam is shifted by half the width from the contour to the core. It is always calculated from the boundary edge using a built calibration block in adjusting the offset. Incorrect calculations could lead to ineffective melting of the area and inaccurate dimensions from the original CAD data (Manfredi *et al.*, 2014).

g) **Overlap:** This is defined by Hanzl *et al.* (2015) as the area influenced by the repeated melting by the laser beam, that is when a track is melted, the heat generated in the molten weld pool re-melts a portion of another track which had previously been melted and solidified (Su and Yang, 2012). The re-melted portion is regarded as the overlap and is dependent on the size of the laser beam diameter and the weld pool. The beam diameter melts a portion of the powder and the flowing of the molten liquid results in a heat convection melting surrounding particles resulting in a bigger weld pool than the beam diameter. The molten metal then flows longer between scan tracks pushing out previously trapped air and encouraging inter-layer/inter-track binding while simultaneously reducing porosity. However, Guan *et al.* (2013) and Hanzl *et al.* (2015) both discovered that the overlap does not have a significant influence on the mechanical properties of SLM samples due to having sufficient energy to cause good melting conditions.

h) **Atmosphere:** The atmosphere during LM is important as the powder metals are prone to degradation and the molten metal prone to gaseous attack (oxygen and carbon dioxide) leading to porosity and inferior properties in the parts. Parts are therefore generally fabricated in an inert or vacuum environment (Campanelli *et al.*, 2010).

i) **Energy Density:** This is the ratio of the laser peak power to the frequency and width of the laser and is known as the Andrew Number, (Savalani *et al.*, 2011). It has an effect on the quality of parts, dimensional accuracy, density, and strength of the parts produced, (William and Deckard, 1998; Leong *et al.*, 2001). Low energy density results in insufficient melting of the powders and high energy density can cause vaporization of the powder (Savalani, *et al.*, 2011). Both of these conditions will lead to poor mechanical properties or dimensional inaccuracies resulting from distortions and layer delamination caused by layers not properly fused together or contraction of the molten metal, (Savalani, *et al.*, 2011; Matsumoto *et al.*, 2002). The formula of the energy density of the laser beam is given as:

$$E = \frac{P}{v * l * t}$$

Equation 2.1 (*Spierings and Levy, 2009*)

Where E is the Laser Energy Density (J/mm^2)

P is the Laser Power (W)

v is the Scan Velocity (mm/s)

l is the Step – over (mm)

t is the Layer thickness (mm)

2.3 Selective Laser Melting/Laser Melting for Metallic alloys and Metal Matrix Composites (MMCs)

Various studies in a review by Olakanmi *et al*. (2015) have investigated the material/powder characteristics and optimisation of the process parameters in SLM/LM systems, with the aim of achieving full densification of parts with mechanical properties similar to conventional manufacturing. An important condition highlighted for full densification of the part is the uniformity of each single track and good adhesion to the previously melted layer (Yadroitsev *et al.*, 2013). Therefore, a good understanding of the powder properties and process optimisation phenomena comprising phase transformations, laser absorption/reflection by powder particles, radiation, heat transfer, fluid viscosity, surface tension and chemical reactions that take place during the LM process is necessary to achieve full densification. Metal Matrix composites combine the ductility of metallic alloys with the high strength and elastic modulus of the ceramic reinforcement and are more complex to fabricate using additive manufacturing due to the differing physical properties (particle shape, laser absorption and thermal expansion/contraction) of the two components.

2.3.1 Material /Powder properties for Metallic Alloys

The properties of the alloy powder are important considerations for its utilisation in the LM system. Therefore, for each alloy system, the thermophysical properties of the alloy, granumorphometric characteristics (particle size, shape and particle size distribution) of the powder particles, melt/weld hydrodynamics of the molten alloy and powder flowability during recoating all have to be investigated in order to have a viable stable track formation and achieve full densification (Yadroitsev *et al*., 2010; Kumar, 2003).

Liu *et al.* (2011) have investigated the effect of particle size distribution on the properties of LM parts with the narrower range providing better powder flowability, which is calculated using Hausner's ratio (ASTM D7481). A ratio higher than 1.25 considered as an indication of poor flowability and subsequently better mechanical properties. Lee *et al.* (2009) investigated the influence of particle size and distribution during SLS and observed that a broader distribution size was better for increased packing density while Li *et al*. (2005) observed that the lower particle size distribution tends to decrease the sintering temperature of ceramics due to smaller grain boundaries and presence of cavities in the grains. Herzog *et al*. (2016) highlighted difficulties in the LM processing of Al alloys as their resistance to weldability, high reflectivity and low viscosity, which makes it difficult to tailor Al-alloys to the LM process.

2.3.2 Process optimisation and Track development

Shellabear and Nyrhila (2004) and Bineli *et al.* (2011) highlight the importance of tailoring and controlling the process parameters used in the LM process to obtain optimum properties for the parts generated from the laser melting mechanism. Lambrakos and Cooper (2011), using the inverse approach due to lack of thermo-physical data, have identified the important parameters to be investigated as laser power (power density, focus), scan speed and hatch spacing/ step-over increment. Beuth and Klingbeil (2001) have also developed a process map using finite element analysis, to aid in understanding the relationship that process variables including controlling the melt pool size and shape have on the properties of the powder and finished part.

Yadroitsev *et al.* (2013) stated that an essential requirement for obtaining a good quality 3D object is stability of the geometrical characteristics of each single track and a good adhesion to the previously remitted layer, which was achieved by varying the process parameters.

Yadroitsev *et al.* (2007) studied single line tracks of austenitic stainless steel and observed that of overall importance to the optimisation of the SLM/LM process is the laser power and scanning speed as these determine the temperature fields and thus the powder binding mechanisms during the process. Leu *et al.* (2010) listed powder bed temperature, energy density and layer thickness as the important parameters in their optimisation process for the SLS of zirconium diboride, which as a ceramic material will aid in optimising the process for an MMC. Buchbinder *et al.* (2011) investigated the high power SLM of Al alloys with the aim of achieving near a 100 % density. They demonstrated that changes in the scanning speed and laser power using a fibre coupled disk laser influences the energy density and that insufficient energy density leads to defects, which reduces the overall density of the part. Simchi and Pohl (2003) highlighted the most important parameters as laser power, scan rate, scanline spacing (offset), layer thickness, particle size and particle size distribution. Bourell *et al.* (1992) established that two major binding mechanisms influence the thermal activation of powder particles by the laser beam.

These are the melting of a low-melting-point phase in a mixed powder of differing chemistries and the viscous flow of the molten metal. These mechanisms are important factors for achieving full densification of MMCs in the LM process. This was corroborated by the research by Bunnell *et al.* (1995) who stated that for a binary system, the powder particles with the lower melting point - which form the liquid phase during SLM, should have a lower laser absorptance than the solid phase - the powder particles with the higher melting point. During SLM, the solid particles are therefore hotter than the liquid phase having absorbed the laser energy without melting, thus promoting capillary flow and wetting on interface between the 2 phases. However, in the study into the characterisation of Fe based laser sintered powder, Wang *et al.* (2006) stated that the presence of two or more different particles with different morphology and size distributions would influence the optimisation process as microstructural heterogeneity and porosity are prevalent in the mixed powder volumes.

From the various studies above, the mechanisms involved during LM therefore are considered to be the viscous-flow (flowability of the powder), curvature effect of the weld bead produced, particle wetting during laser beam irradiation and the melting of the alloy system. This is slightly different from SLM/SLS process which uses a lower melting powder for liquid phase sintering.

2.3.3 Selective Laser Sintering/Selective Laser Melting of Metal Matrix Composites

Few studies have been done on the LM of composites with much of the previous work focussed on the SLS/SLM of MMC systems rather than investigating the effect of process parameters on the properties during full melting. This signifies that the SLS of a composite powder system is based on the mechanism of liquid phase sintering involving the complete melting of a metallic alloy powder and the non-melting of the ceramic particles which was used to reinforce the composite, (Gu *et al.* 2006).

Simchi and Godlinski (2008) studied the effect of SiC addition to the densification of Al–7Si–0.3Mg alloy using SLS using a EOS M250Xtended. They established that the increase in the volume fraction of the reinforcement led to a corresponding increase in the melt stability giving a better surface morphology with smaller pores. However, this also led to lower sinterability of the composite due to the decrease in the packing density of the powder composite thus leading to a lower density except for the 5% reinforced alloy.

Ghosh *et al.* (2010) investigated the DMLS of Al–4.5Cu–3Mg and SiC_p using a modified CNC machine fitted with a pulsed Nd-YAG laser. They observed a gradual increase in the density of the composite with increasing volume fractions of the reinforcement up to 15 %, attributed to reinforcement clusters filling any created voids. Conversely, the density decreases with decreasing SiC_p particle sizes where they detected that at 1200 mesh size (approximately 12 µm), the SiC_p was at a risk of fully melting due to the temperatures reached within the chamber.

Ghosh and Saha (2011), in their research into the wear behaviour of Al-MMC, discovered the susceptibility to cracks from the residual thermal and contraction stresses. They also observed that above 15% reinforcement addition, the crack susceptibility increased significantly.

Miani (2012) states that the mechanical properties of the sintered component rely greatly on the internal porosity and the residual thermal stresses created during the process. All previous investigations have clarified that the LM is a complicated process with various parameters affecting the full densification and resultant microstructure of the material. The emphasis therefore is on process optimisation for full densification with minimal dimensional change for new alloy and MMC systems. To ensure suitable mechanical properties and homogeneity in the MMC and to prevent the appearance of cracks associated with stresses created from the differences in morphology, size and thermal expansions of the materials (Excell and Nathan,

2010), several process parameters are investigated and discussed in order to understand their influence on the material.

2.4 Summary and Critique of the Chapter

Additive Manufacturing was defined in this chapter as a recent development of creating functional parts directly from 3D CAD. Metal alloys and power-bed systems were focussed on with variations in the lasers, melting processes, process parameters and materials highlighted as the major differences in proprietary technologies. The key processes reviewed were the SLS/SLM/LM processes for metal systems with an aim to achieving near-full dense parts with properties comparable or better than conventional manufactured parts.

Material/Powder properties which detail the thermophysical and granumorphometric characteristics for each alloy system were reviewed as a pre-process characteristic of the LM process. Particle size distribution, morphology and flowabilty were discovered to be defining factors in achieving full densification. The material properties of Al alloys (high reflectivity and low weldability) were established to be particularly problematic for the laser systems as in-process characteristic. To overcome the material characteristics, alloying of the base material to improve weldability and flowabilty and therefore form a stable track weld were investigated resulting in Al-Si alloys which have a low melting/solidification range.

Alternatively, the laser systems are modified and tailored until repeatable process parameters are obtained. Controlling the melt pool size was deemed significant in monitoring the solidification of the molten metal and thus obtaining near-full density and suitable properties for the part. Different parameters were highlighted in controlling the melt pool, however, the energy density, laser power, scan speed, step-over and layer thickness were parameters most investigated for optimising the process. These were identified as having the most influence on the absorption, retention and conduction of heat from the molten pool which consequently determines the microstructure of the part.

Monitoring the SLS/SLM/LM process for metal matrix composites is even more important due to the differing mechanical and physical properties of the individual constituents. The emphasis of the process was based on utilizing the SLS systems in fabricating metal matrix composites with no attempt to modify the process parameters due to the change in the melt characteristics of the base powder on the introduction of reinforcement particles. Cracks were

observed at volume reinforcements above 15% and reduced density were also observed with decreasing reinforcement particle size.

Minimal attempts were also observed in modifying the delivery method for dispersing the reinforcement particles in the powder bed system except rudimentary mixing thereby giving a need for research into this area. Therefore, this research aims to explore both the delivery method for reinforcement and process optimization for MMCs in AM systems as novel concepts for analysis before industry-wide acceptance.

Chapter Three

Materials

3.1 Introduction to Materials utilised in research

One of the objectives of the research is understanding the microstructural evolution and mechanical properties of the LM Al/SiC_p composite in comparison with Al/SiC_p composites fabricated through conventional methods like casting. In order to fulfil these requirements, it is thus necessary to understand the chemistry, physical structure and properties of not only the matrix alloy and the particulate reinforcement but also the physical and chemical reactions of the Al/SiCp mixture/composites and its mechanical properties. This chapter reviews the metallurgy and chemistry of the materials (Al-alloys, AlSi10Mg, SiC_p and Al/SiC_p), the strengthening mechanisms and heat treatment of the elements and composites. Finally, an introduction to the experimentation stage and a justification for the research methodology is also discussed.

3.2 Aluminium and its alloys

The advent of the automobile and aircraft industry at the beginning of the 20th century saw an exponential increase in the usage of Aluminium (Murray, White and Weise, 2008) where it is desirable as a high strength structural metal due to its light weight (density - 2.7 g/cm3) but hampered by its low melting temperature (~660 ^{o}C). Other desirable characteristics include high strength-to-weight ratio, corrosion resistance and high flexural strength. Its excellent thermal conductivity, reflectivity, easy fabrication and recyclability has however extended its usefulness into modern technology, Aluminium Association (2001).

Aluminium is produced from the electrolytic reduction of Aluminium Oxide (Al_2O_3) and has a face centred cubic (FCC) structure. It is also considered very ductile due to its closed packed structure requiring lower forces to move its atoms. Pure aluminium is usually alloyed with other elements like Silicon, Magnesium, Zinc and Copper to either modify the microstructure or improve its intrinsic properties e.g. corrosion resistance. Higher strengths especially its specific strength (Strength-to-Density ratio) can also be achieved when heat treated making it comparable and sometimes superior to steel.

3.2.1 Properties and Metallurgy of AlSi10Mg

EOS GmbH provided the Al-alloy powder for LM and its composition is given in Table 3.1 with Fig. 3.1 showing the particles morphology obtainable from the gas atomisation process. The particles are spherical with a smooth surface except for the small particles, which are agglomerated to the larger particles (Fig 3.1 inset). AlSi10Mg is the ISO standard for the A.A. A360.2 alloy with a near-eutectic composition on the Al-Si diagram (Warmuzek, 2004) which makes it ideal as a weldable alloy with good resistance to chemical attacks that can be used under high dynamic loads, (Inno-shape GmbH, 2012). The addition of the Silicon and Magnesium as alloying elements to the aluminium improves the strength, heat treatment capabilities and makes it easier to cast and weld due to improved fluidity of the molten metal, (Bolton, 1989). Si also influences Al-alloys absorption of laser energy by altering the eutectic point through reducing the difference between the solidus and liquidus temperatures, (Wong, *et al.* 1997). The addition of Mg to Al-Si alloys enables the precipitation of Mg_2Si, which strengthens the matrix without compromising its inherent mechanical properties.

The AlSi10Mg alloy is considered a suitable matrix material; due to its improved fluidity and narrower solidification range, as a benchmark to which the Al alloy/SiC MMC will be compared during the rapid melting and solidification of LM process.

Table 3.1: Composition of AlSi10Mg (EOS, 2011)

Element	%Composition
Silicon (Si)	**9.0 – 11.0**
Magnesium (Mg)	**0.2 – 0.45**
Iron (Fe)	**Max. 0.55**
Manganese (Mn)	**Max. 0.45**
Titanium (Ti)	**Max. 0.15**
Zinc (Zn)	**Max. 0.10**
Lead (Pb)	**Max. 0.05**
Tin (Sn)	**Max. 0.05**
Copper (Cu)	**Max. 0.05**
Nickel (Ni)	**Max. 0.05**
Aluminium (Al)	**Rest**

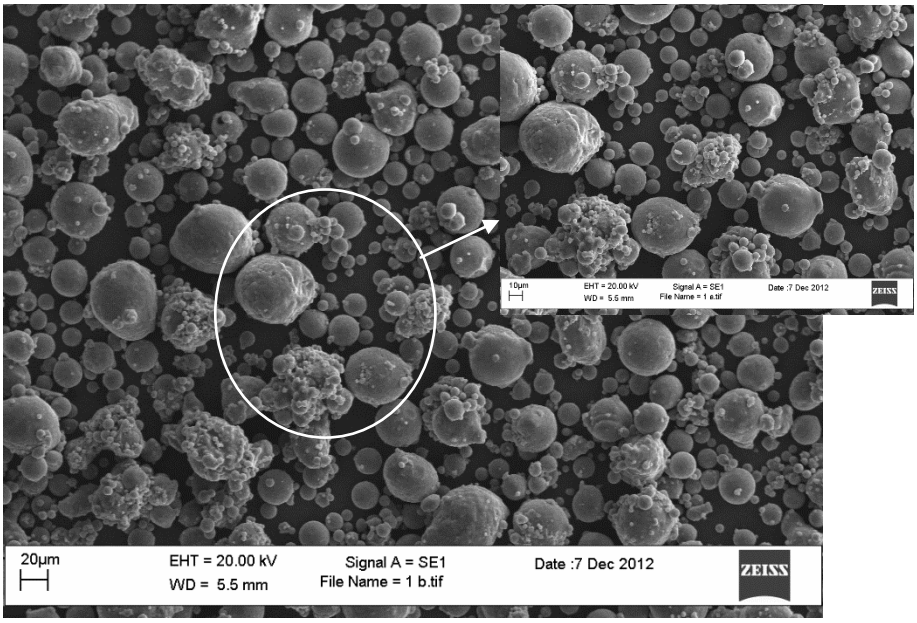

Figure 3.1 AlSi10Mg starting powder showing its spherical shape at 1000 X (inset – higher magnification 2000 X of highlighted area)

3.2.2 Effect of alloying elements

Other elements added to pure aluminium are designed to influence its mechanical properties through various different mechanisms. They are known to affect the formation of porosity, surface defects and thermo-mechanical processing during fabrication, thus alloying is important and carefully monitored especially for the LM process. Previous researches (ESAB, 2014; Kopeliovich, 2012; Rana, *et al.*, 2012a; Total Materia, 2002) have investigated the effects of the alloying elements in the AlSi10Mg alloy as discussed below

3.2.2.1 Major Alloying Elements

a) **Silicon (Si)** – improves castability of Al by improving fluidity, the alloy strength, its resistance to abrasive wear and reducing shrinkage of molten alloy. This is attributed to the low solubility of Si in molten Al resulting in essentially pure Si being precipitated out at eutectic conditions (<12% Si).
b) **Magnesium (Mg)** – improves weldability and solid-solution strengthening without a corresponding reduction in ductility and when alloyed with Si, Mg increases precipitation hardening mechanisms in the alloy with the Mg_2Si precipitate.
c) **Copper (Cu)** – increases tensile strength and hardness due to solid-solution strengthening while also aiding in precipitation hardening of the matrix. As it reduces the corrosion resistance of Al-alloys and increases its tendency to stress crack, it is alloyed as a trace amount in the AlSi10Mg alloy.

3.2.2.2 Minor Alloying Elements

d) Nickel (Ni) – increases the hot-hardness and strength of Al-Si alloys and also reduces the coefficient of thermal expansion; this property is advantageous during the LM process as the addition of SiC is expected to increase the thermal stress resulting from the different coefficients of thermal expansion. The presence of the Al_3Ni intermetallic in the Al-matrix detected by Hernández-Méndez et al. (2011) was established to increase the compressive strength and hardness of the Al-matrix.

e) Tin (Sn) – aids in reducing the high temperature friction and hot hardness during application.

3.2.2.3 Microstructure Modifiers –

These modify the microstructure of both Al and Al-Si alloys by either aiding the nucleation of primary aluminium or modifying the eutectic structure to improve its mechanical properties, however, they may be detrimental in the final microstructure as the mechanism for refinement can either be enhanced by heterogeneous nucleation or growth restriction, (Li *et al*. 2011)

f) Titanium (Ti) – aids in refining primary aluminium grains during solidification and also improves its corrosion resistance. Coarse grains are expected at additions around the peritectic point 0.15% (Jardeh and Carlberg, 2005) and embrittlement and microcracking have been detected by Saheb *et al*. (2001) with the formation of Al_3Ti at additions up to 4%. Despite this, the rapid solidification rate of the LM process and the low percentage of the Ti addition should prevent the coarse grains and Al_3Ti from developing.

g) Manganese (Mn) – encourages solid-solution and dispersion hardening mechanisms leading to an increase in the tensile strength of the Al-alloy.

3.2.2.4 Impurity Elements

Impurity elements are usually present in trace amounts in pure aluminium.

h) Iron (Fe) – usually regarded as an impurity element, Fe is added in small amounts to enhance the mechanical properties by forming complex intermetallic compounds. However, the addition is strictly monitored as the intermetallic compounds can also cause excessive shrinkage while also reducing ductility. Taylor (2012), highlighted

that for Al-Si alloys the critical Fe content by which ductility starts to decrease with the formation of a β-phase is given by

$$Fe_{crit} \approx 0.075 \cdot [wt\%\ Si] - 0.05$$ ***Equation 3.1 (Taylor, 2012)***

From the Equation 3.1, the range for the AlSi10Mg alloy approximates to 0.6 – 0.75% and at a maximum of 0.55 in the alloy composition, the β-phase should not be precipitated.

i) **Zinc (Zn) –** aids in precipitation hardening of the Al – matrix and aids the weldability of al-alloys.
j) **Lead (Pb) –** improves machinability

3.2.2.5 Al-Si Phase Diagram

Al has zero solid solubility in Si therefore, the beta phase is transformed wholly into pure silicon as seen in the Al-Si alloy phase diagram in Fig. 3.2. The eutectic point observed at 577 ^{o}C signifies a 12.6 mass %Si with its maximum solubility at 1.65% and the eutectic composition structure of FCC Alpha-Aluminium and diamond cubic Silicon, (Murray and McAllister, 1984). Equal volumes of both phases at eutectic results in a lamellar structure, however when one of the phases has a lower volume percentage, it results in a fibrous structure, (Makhlouf and Guthy, 2002). The difference in the microstructural orientation is attributed to the irregular crystalline solidification of the Si and low interfacial energy between the eutectic Si and Al, (Kurz and Fisher, 1998). Nikanorov *et al.* (2005) states that chemical composition, structure of the melt, rate of crystallization and temperature gradient at the liquid-solid interface are important factors which determine the structural and mechanical properties of Al-alloys.

The formation of coarse Si in the microstructure promotes brittleness, hence the addition of other alloying elements aid in tempering the brittleness. The alloy tempering is reinforced by Shankar *et al.* (2004) who established that trace amounts of Fe found in the in Al-Si alloys leads to the formation of β (Al, Si, Fe) intermetallic phases which encourages the Si nucleation prior to Al nucleation in unmodified hypoeutectic alloys during the solidification of the eutectic structure. The formation of each intermetallic phase is dependent on the

cooling rate and has a tendency to promote porosity by restricting pore nucleation and growth during solidification of the liquid alloy (Brodarac *et al.*, 2007), however, the phases do lead to improvements in the strength of the alloys (Kaufman and Rooy, 2004).

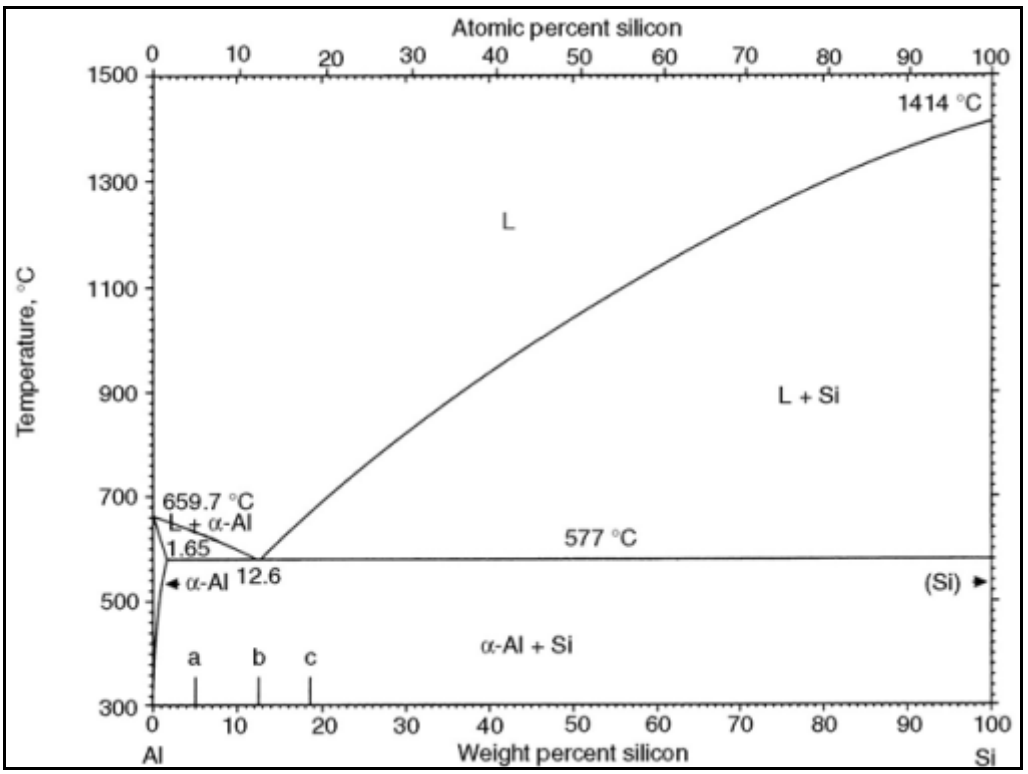

Figure 3.2: Al-Si phase diagram (*Warmuzek, 2004*)

3.2.2.6 Addition of Magnesium to Aluminium-Silicon alloys

The addition of Mg to Al-Si alloys promotes the susceptibility of the alloy towards heat treatment. These alloys are used for structural components due to their high strength and good corrosion resistance. The primary Al below the eutectic line has a Face Centred Cubic (FCC) structure, while the Si has a cubic diamond structure and the Mg a Hexagonal Close Pack (HCP) structure. The ternary phase diagram in Fig. 3.3 highlights these major phases and the subsequent combinations of the Al-Si-Mg mixture and Equation 3.2 (Voncina, *et al.*, 2005; Brodarac *et al.*, 2007) reflects the major elements and compounds/phases formed from the solidification of the Al-Si-Mg alloy from the liquid phase incorporating phases of the major alloying elements of the AlSi10Mg alloy. The compounds formed from the liquid phase are dependent on the cooling rate of the alloy especially when in contact with trace

elements. The addition of the 0.4-0.75 % Mg induces secondary hardening precipitates of Mg_2Si through age hardening especially in the presence of Fe containing a minimum of 4.5% Si.

Reaction		Temperature (°C)
e1	$L \rightarrow \alpha Al + Mg_2Si$	593
e2	$L \rightarrow Al_3Mg_2 + Mg_2Si$	
e3	$L \rightarrow Al_{12}Mg_{17} + Mg$	
E1	$L \rightarrow \alpha Al + Mg_2Si + \beta Si$	550
E2	$L \rightarrow \alpha Al + Al_3Mg_2 + Mg_2Si$	444
E3	$L \rightarrow Al_3Mg_2 + Al_{30}Mg_{23}(HT) + Mg_2Si$	445
E4	$L \rightarrow Al_{12}Mg_{17} + Mg + Mg_2Si$	434

$L \rightarrow$ development of dendrite network (αAl) + $Al_{15}(MnFe)_3Si_2$

$L \rightarrow \alpha_{Al} + \beta_{Si} + Al_5FeSi$

$L \rightarrow \alpha_{Al} + \beta_{Si} + Mg_2Si + Al_8Mg_3FeSi_6$

(Equation 3.2 - Voncina, et al., 2005; Brodarac et al., 2007)

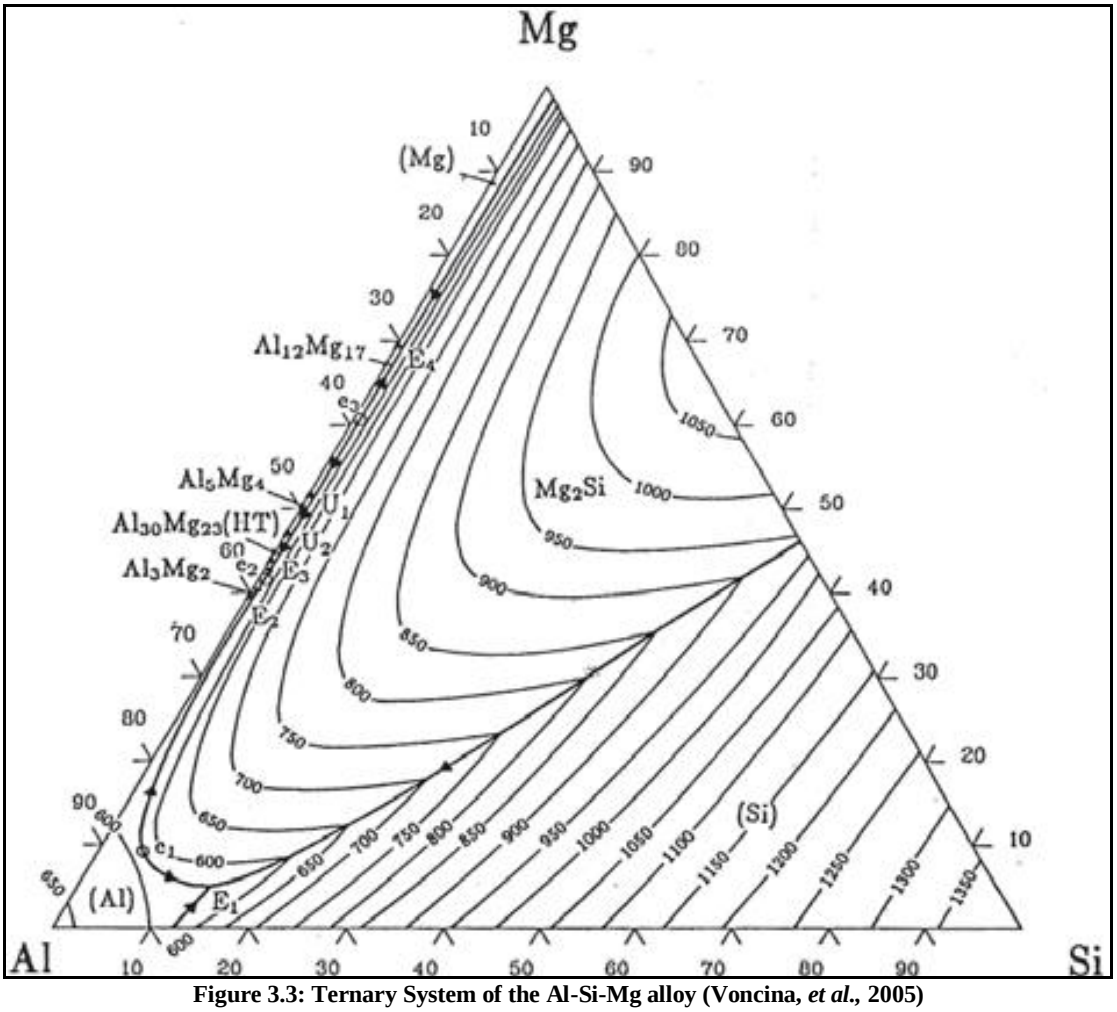

Figure 3.3: Ternary System of the Al-Si-Mg alloy (Voncina, *et al.*, 2005)

3.2.3 Powder Metallurgy of Aluminium Alloys

Powder Metallurgy (PM) which includes processes such as sintering, Hot Isostatic Pressing (HIP) and SLM, are processes where dense components with excellent mechanical properties are made by processing elemental, pre-alloyed powders or composites through compacting, blending, sintering or heating. Mechanical properties; including porosity, hardness, surface finish and wear resistance, increase due to the strengthening features (precipitates and dispersions which obstruct dislocations) from the powder surfaces and aided by the controlled atmosphere utilised in metallurgically bonding the particles together (Pickens, 1981). PM can produce complex geometry with good dimensional accuracy with minimum material loss and fewer manufacturing steps with a high production rate and low cost, (Bayraktar and Katundi, 2010).

Powder Metallurgy for aluminium has been used for a range of applications including the automotive/aerospace sector as it provides a wide range of benefits integrating weight savings, structural performance and design flexibility and replacing iron/steel based components with aluminium is justification for the on-going research into aluminium-PM, (Fogagnolo *et al.*, 2004). The design for aluminium-PM necessitates collaboration from part designer, manufacturer and end user from the initial conceptual stages of the component. This is to ensure that the design and manufacturing route undertaken will be fit for the purpose of the end user. PM of aluminium alloy is difficult, as care is needed to eliminate all porosity from the finished component and also to reduce the formation of Aluminium Oxide (Al_2O_3) on the surface of the powder during the sintering process, (Schaffer, 2004). The PM processes utilised for the AlSi10Mg powder and this research are discussed below.

3.2.3.1 Gas Atomisation

Atomisation, fast becoming one of the most popular methods of manufacturing Al-alloy powders are processed in a protective inert atmosphere which reduces the overall contamination of the powder particles. Gas atomisation is mostly preferred for Al-alloys used in the LM process due to the alloy homogeneity, spherical particle shape and minimal level of Al_2O_3 contamination from the process (Verlinden and Froyen, 1994). The process involves introducing molten metal through a small orifice in a protected inert gas atmosphere from a nozzle, the droplets of superheated liquid metal flowing from a vertical stream in a tundish,

causing rapid solidification into powder particles (Kalpakjian and Schmid, 2006; Thummler and Oberacker, 1993 and Groover, 1996). The resulting spherical powder particles have a smooth morphology with controlled particle sizes and particle size distribution determined by alloy composition, the flow rate of the pressurised gas and the molten liquid metal, atomising temperature, type of gas and nozzle design (Verlinden and Froyen, 1994). In his review on gas atomisation of Al-alloys, Jones (2004) highlighted the main benefits of gas atomisation of Al alloys as:

1. Reduction in the final grain size of the part due to the ability to control the particle size of the powder particles.
2. Increase in the alloying combination.
3. Utilising the unique chemistry of the alloying combinations to form novel Nano phase microstructures.
4. Increase in mechanical properties due to a reduction in gases/oxide contamination of the powder particles.
5. Overall, enhanced strength, strain rate and wear resistance have been observed as a combination of these factors.

The controlled grain size and alloying chemistry compliments the LM process as it aids in customizing alloys for the LM process.

3.2.3.2 Mechanical Alloying (MA)

Benjamin (1976) was one of the first adopters of Mechanical Alloying as a method of producing aluminium reinforced powders and this has since been utilised in various manufacturing processes including compression moulding, die casting, extrusion, re-melting and solidification. It involves solid state reactions through the repeated grinding of the mixed materials (the metal matrix and ceramic reinforcement). This causes severe plastic deformation (microstructural welding and forging) of the powder particles to form a variety of equilibrium, non-equilibrium phases and phase mixtures (Murty and Ranganathan, 1998), with the properties of the individual materials (Ohsaki *et al.*, 2007). The main difference between high energy milling, reactive milling and mechanical alloying is that high energy milling deals with a single component-system and reactive milling deals with multiple components-systems as does MA, it also indicates that a chemical reaction is present. However, chemical reactions are undesirable during MA rather; a solid state reaction is

preferred by the embedding of a small particulate reinforcement into the matrix (Pech-Cahul, 2011). The MA process has an ability to synthesise new materials by combining either elemental metals or their alloys with other materials like ceramics, otherwise not possible in conventional manufacturing due to their immiscibility, (Zoz *et al.*, 1999). The process does this with a high degree of success achieving a homogeneous structure and composition (Murty and Ranganathan, 1998).

According to Khakbiz and Akhlaghi (2009), the distribution of reinforcement particles is a function of the processing route and matrix-reinforcement particle size. MA produces fine grain structure solely in the solid state through the incorporation of particles to increase the solid solubility limits and achieve a different non-equilibrium amorphous state. The alloy powder characteristics and chemical constituents can be tailored which makes this pulverising route particularly suitable for LM used in the component manufacture as the high sintering temperature and the optimised characteristics lead to improved product properties, (Simchi, Petzoldt and Pohl, 2003).

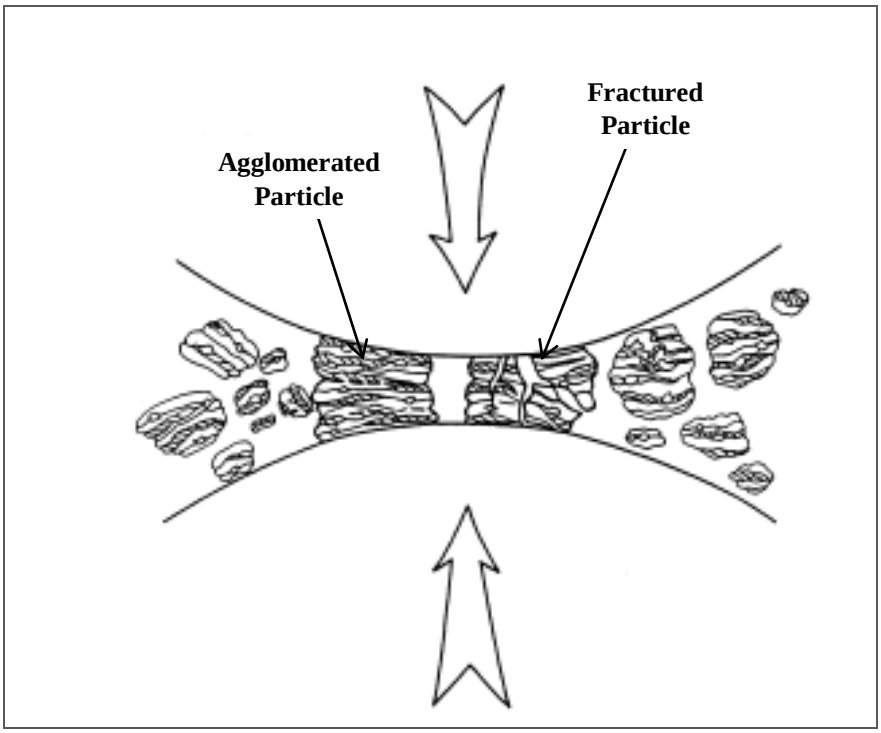

Figure 3.4 Ball-powder-ball collisions during MA (*Suryanarayana, 2001*)

Lu *et al.* (1998) highlight some of the parameters required to achieve good blending which include particle size, blending speed and duration that will lead to smaller particulate size which restricts the movement of dislocations thus increasing the strength of the material. The

percentage volume of the reinforcing material and mechanical alloying times are sometimes varied to determine the optimum volume of reinforcement and particle size for distribution during MA and also for subsequent AM. Fogagnolo *et al.* (2004), states that MA of the composite brings about an improvement in the composite structure and metallurgy leading to an increase in its mechanical properties when compared to standard Powder Metallurgy (PM) techniques. Fig. 3.4 features the collision between the powder particles and grinding balls resulting in agglomeration and fracturing which occurs during MA.

Garg *et al.* (2012) stresses that manufacturing of MMCs is still problematic, as finished components are difficult to machine and are prone to brittle failure. Benjamin and Volin (1974) have advocated that refinement and homogeneity of composite structures rely heavily on time, mechanical energy and the work hardening rate of the materials. Gu *et al.* (2010) however, identifies MA as a highly complex and difficult process with little manoeuvrability in getting the desirable phases or microstructures as the homogeneous incorporation of the reinforcement is difficult.

MA is also utilised to produce a homogeneous particulate distribution of ceramic carbide in the metal matrix to produce composite powder. The composite powder will then undergo LM to fabricate finished parts with the homogeneously incorporated SiC serving as a crack arrester and thereby inhibit crack propagation at the grain boundaries in Al-alloy composite systems. The alloying also reduces thermal stress cracks resulting from the different thermal expansion rates of the individual materials with the Coefficient of Thermal Expansion for the Al-alloy matrix being approximately 23.6 µm/m°C and 4.3 µm/m°C for the SiC particulate, Kalpakjian and Schmid (2006). The MA process parameters need to be controlled to offer suitable material for the LM and are highlighted as follows:

a) **Mill:** The different kinds of mills available for both industrial and laboratory use ensure there is a wide variety of milling times and speeds. These include vibration mills, jet mills, bead mills, planetary ball-mills and shaker mills to mention a few of them. However, the horizontal ball-mill seems to be the most suitable for dry processing at high velocities in either a vacuum or inert gas atmosphere. The ZOZ Simoloyer mill is aimed at providing a reactive/ high energy milling process for mechanical alloying. The operation leads to the intensive grinding of the materials, a shorter processing time; minutes as opposed to hours that are associated with other types of mills together with minimal contamination from the mill. The ZOZ mill functions by transferring kinetic

energy into the powders to be milled from the maximum relative velocity reached by the grinding media, (Zoz *et al.* 1999). Dead zones are eradicated by ensuring that the milling tool has access to all the powder in the grinding chamber to guarantee homogeneous alloying of the materials.

As Al is a highly reactive material, the presence of air-lock systems with gas/vacuum tight devices is an added benefit as it minimises the contamination of the composite by oxygen which can create deleterious oxides in the mix. De Castro and Mitchell (2002) advices that to minimise contamination of the composite, the grinding media should ideally be stronger than the powder being milled and preferably of the same material.

b) Particle Size: Particle size for mechanical alloying is important as this determines the amount of homogeneous alloying that will occur between the two materials. The reinforcing material should be small enough such that during MA, it will agglomerate with the matrix material in such a way as to enter its lattice and essentially restrict the movement of dislocations (Ashby, 1966). It will also impede the growth of cracks in the subsequent manufactured component arising from the differences in thermal expansions of the materials. Hong and Kao (1991) successfully embedded SiC into an Al matrix with an average particle size of 0.3 µm, however, the SIC was introduced into the ball mill at a size of 35 µm. The MA process served to reduce its particle size and also improve the agglomeration of the reinforcement particles. Repeated milling of the powder mixture in the ball mill effectively fractured the SiC particles to 3 µm.

c) Ball to Powder ratio: The ratio of balls to powder used in mechanical alloying the matrix and reinforcement; sometimes called the charge ratio, has to be carefully considered as there is a threshold where the balls can effectively hit the powder for maximum impact in initiating the alloying process. The ball to powder ratio used during this process is a function of the percentage weight of the powder with respect to the alloying chamber volume such that the powder and balls occupy half, (Suryanarayana, 2001) of the milling chamber volume and retain sufficient room for the charge to collide effectively during alloying.

d) Milling speed: The grinding works on the principle of critical milling speed of the balls; that is the speed at which the steel balls responsible for the grinding of particles

start rotating along the direction of the cylindrical device; thus causing no further grinding (Zoz *et al.*, 1999). Milling must thus be conducted below the critical speed in order to achieve effective milling of the powder. The LM powder comprising a soft ductile matrix and a hard brittle reinforcement is plastically deformed in the first stage of milling with the hard reinforcement covering the ductile matrix powder.

e) Milling Time: For the first period during milling, the particle size increases due to agglomeration and cold welding of the different materials to form an initial metastable composite (Suryanarayana, 2001). With increase in the milling time, the ceramic makes the Al more brittle and thus with continuous work hardening from the ball mills, the particles fracture leading to a cyclic cold welding and work hardening fracture phase until a steady state condition is obtained, Prabhu *et al.* (2006) estimated this time to be around 15 -20 hours and further milling will not have any effect unless nanoparticles are the aim in which case they will be milled for over 100 hours. However, the type of mill and its milling speed will also have a significant effect on the milling time. Particle size and distribution during the extended milling process is expected to be uniform and homogeneous throughout the composite and with an elimination of any possible defect in the microstructure (Ruiz-Navas *et al.*, 2006). This process improves distribution of the reinforcement by breaking up clusters. It also decreases the particle size and reduces cracks in the microstructure (Fogagnolo *et al.*, 2004).

Boey *et al.* (1998) suggests that MA of a specific particle size of an Al-Li alloy and SiC for 8 hours at 200 rev/min resulted in the best mechanical properties for the composite albeit with low elongation and ductile values. It is important to note that while the breakage/attrition process is dominant at the initial stages of the milling process, the agglomeration of the reinforcing particle into the metal matrix dominates the latter part of the process, (Khakbiz and Akhlaghi, 2009). Suryanarayana (2001) however, states that due to a potential increase in contamination and undesirable phases, milling should be restricted to the required duration for the powder mix.

f) Morphology of the Reinforcement: Reinforcement causes an increase in strength by reducing the mobility of dislocations and particles, however, this mobility increases with increase in temperature. It has been found that the mechanical properties of the a B_4C reinforced 6061 Al alloy is far superior to that of the SiC reinforced material due

to better interfacial products, higher particle strength and good wettability between the Al and B_4C ceramic, (Nayeb-Hashemi and Shan, 1999). However, SiC particles due to their density and crystals are better suited to reinforcing Al alloys as it encourages an increase in the Young's Modulus and tensile strength of the composite, Torralba, *et al*. (2003). SiC whiskers are generally not used as this causes large internal thermal stress due to the large difference in their thermal expansion and are not considered for this work as the shape of the whiskers will lead to a reduced wetting of the Al-alloy and other powder spreading issues during the LM stage.

g) **Effect of Milling Temperature**: Milling temperature as a parameter monitored during mechanical alloying affects the particulate growth and could trigger deleterious chemical/interfacial reactions in alloys, (Suryanarayana, 2001). Takacs (2009) also noticed an increase in the particulate grain growth after a highly exothermic powder mix induced a self-sustaining reaction leading to an increase in the temperature during MA. Degradation of the ceramic/Al-alloy interface at high milling temperature (535 ^{o}C), which also increases with milling time has been reported by Nayeb-Hashemi and Shan, (1999). The results of the temperature increase as observed from literature are however deleterious to the feedstock material for LM process as chemical reactions and interface degradation will limit the interlayer bonding and particulate growth size will reduce the packing density thus inducing porosity.

3.2.3.3 Laser Melting for Aluminium alloys

Aluminium is a highly reflective light metal with poor flowability (Buchbinder, 2011) thus requiring a high laser power; approximately 200 W, for complete melting of the aluminium particles (Thijs, 2013). Its high thermal conductivity approximately 113 W/mK (Kearney, 1990) and a low laser absorptivity (approximately 9%) leads to a high dissipation of heat from the scanning area. The high oxidation rate of al-alloys (Gu *et al.*, 2014) reduces particle wettability thereby causing pores in the sinter and thus hindering total melting and fusion of layers, (Louvis *et al.*, 2011). Process and laser parameters also influence the rate of solidification and hence the development of thermal stresses during LM of complex alloy systems having different thermal coefficients of expansion, (Jain *et al.*, 2006). The differential coefficients of thermal expansion and conductivity generate internal stresses due

to irregular melting and solidification rates of the constituent materials creating part distortion (Wollenberger, 2002). The introduction of Argon during processing has reduced the oxidation of the Al-alloys and this has allowed the LM of Al alloys with almost 100% density with mechanical properties comparable with conventionally manufactured alloys (Kempen *et al.*, 2012).

3.3 Silicon Carbide (SiC)

Silicon Carbide (SiC) is composed of Silicon and Carbon atoms in a strong covalent bonded hexagonal crystal lattice. The particles as seen in Fig. 3.5, are angular in shape and have a tendency to agglomerate into larger particles. It has good abrasive and mechanical properties such as a high tensile strength, hardness values with a low thermal expansion even at elevated temperatures. This ensures its constant usage in an increasingly wide range of high performance structural applications although parts are prone to brittle fracture. Its resistance to oxidation even at high temperatures also facilitates its usage in widely differing engineering applications, hence its addition to Al-alloys is expected to strengthen the matrix alloy despite the probable decrease in ductility, (Smith, 1986).

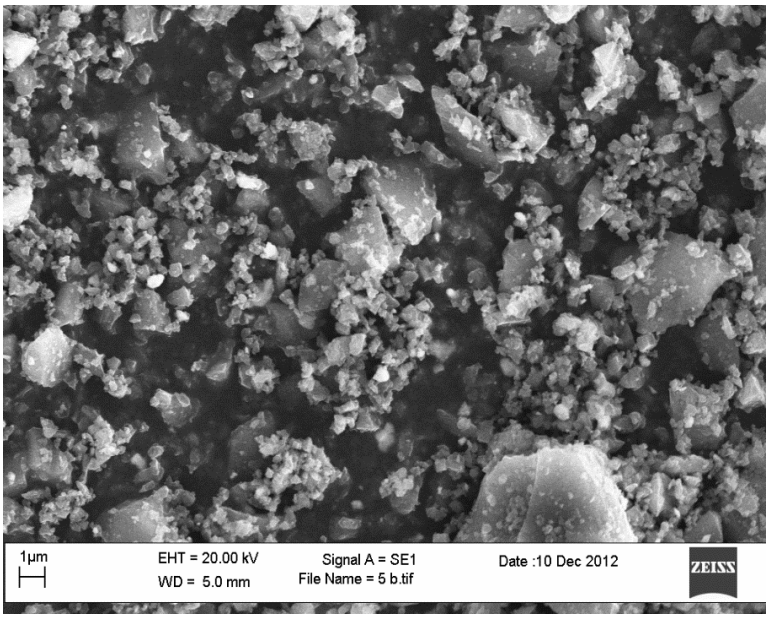

Figure 3.5 - SiC starting powder showing its angular shape.

Its density (3.21 g/cm^3) being only slightly higher than the Al-alloys, availability, low cost and different grades makes it well suited for reinforcing Al alloys, (Torralba *et al.*, 2003). SiC is used in the particulate form as other types of reinforcement (fibres and whiskers) will

impair the smooth flowing of particles in the powder bed thus leading to poor properties in the LM part.

The α-SiC (0.1 – 1 μm) is certified as 99% pure therefore exhibiting a greenish colour indicating that it is free from impurities especially Al (Lundqvist, 1949) and other elements in group 3 and 5 of the Periodic Table which are electronic donors and acceptors (Izhevskyi, 2000).

3.4 Composites – Aluminium alloy/SiC Metal Matrix Composites (MMCs)

Composites are defined as a mixture of two or more materials present in significant quantities imparting certain unique properties to the mixture, Murray *et al.* (2008). They derive their characteristics from the properties of its constituents, geometry and microstructure of the constituents and the interface properties generated between the constituents, (Surappa, 2003). They are usually classified by the chemical nature of the matrix phase, that is; polymer-matrix, metal-matrix or ceramic-matrix composites.

MMCs are usually reinforced with ceramic media with the view to strategically engineer and combine both matrix properties (ductility and toughness) and reinforcement properties (high strength and modulus) so that the composite has enhanced properties and improved service life, (Ibrahim *et al.*, 1991). MMCs are increasingly being used in the automobile and aerospace industries due to their improved mechanical properties including higher tensile strength, hardness and wear resistance together with weight savings capability (Kumar *et al.*, 2011). These materials also minimise the amount of unwanted reactions between matrix and reinforcement as the low manufacturing temperature prevents most of the undesirable interfacial reactions between them (Torralba *et al.*, 2003). The metallic matrixes are usually made from alloys which are in high demand like Al, Ti, Cu and Mg while the reinforcements may be fibres, whiskers or particulates. Zhang *et al.* (2006) suggest that the selection of reinforcement for an MMC depends mostly on its application and manufacturing method as these will determine the microstructure generated. Composite materials employing fibre and whisker reinforcements have a disadvantage of demonstrating anisotropic behaviour due to reinforcement being layered in a single direction thus the mechanical properties are strongest along that direction, whereas particulate reinforcements are homogeneously embedded into the softer metal matrix making it easier to process as the mechanical properties are homogeneously dispersed.

The development of Aluminium alloy MMCs has aided both the automotive and aerospace industries in the design of lightweight components (Wagener and Wolf, 1993). The use of Al-alloys has been impeded by their low melting point, low wear and abrasion resistance and limited strength, therefore, limiting their use for high temperature structural parts. The incorporation of ceramics or fibres into the matrix alloy to improve these properties has been widely investigated by different researchers over recent years. Aluminium matrix composites show excellent properties like high specific strength, high specific modulus, resistance to high temperature, resistance to radiation and good dimension stability, (Liu *et al.*, 2003).

Das *et al.* (2014a) gives a review of the various works conducted on the Al-alloy composites highlighting the various processes like casting, cold/hot isostatic pressing and powder metallurgy utilised in the fabrication of the MMCs. Different forms/allotropes of SiC were mostly reviewed and they observed that as the size of particulate reinforcement reduces, their distribution in the MMC became more uniform and Mg was frequently added to the melt to improve the wettability at the interface.

Fibre and whisker reinforced composites ideally obey the law of mixtures with regards to its constituent materials as shown in Equations 3.3 and 3.4 for both applied parallel and perpendicular stresses respectively, however, as the particulate reinforcements are usually dispersed in the matrix this rule is harder to apply. The direction and load bearing capabilities of particulate reinforcements in an MMC is difficult to assess due to being quite small and widely dispersed, hence when stress is applied, it is challenging to secure the direction of the applied stress either parallel or perpendicular to the particles.

$$E_c = (1-V_R)\,Em + V_R E_R$$ ***(Stress applied longitudinally)*** ***(Equation 3.3)***

$$E_c = V_R / E_R + (1-V_R)/ E_m$$ ***(Stress applied transversely)*** ***(Equation 3.4) (Ashby et al., 2007)***

Where E is the Elastic Modulus (N/m^2)
C is the Composite
V is the Volume Fraction (%)
R is the Reinforcement and
M is the Metal Matrix

3.4.1 Particulate Reinforced Aluminium Metal Matrix Composites

These are composites reinforced with particles usually (oxides, carbides or borides) with diameters between 3-200 µm that have an aspect ratio of less than 5, (Smith, 1986). The isotropic properties offered by these MMCs in conjunction with low production costs have made this method of MMC manufacture desirable for a range of applications Torralba *et al.* (2003). As composites are subjected to a variety of secondary forming operations, the particles are used to strengthen the matrix through dislocations originating from thermal contraction or plastic deformation during production and processing, Ibrahim *et al.* (1991). They are easier to produce through powder metallurgy than any other manufacturing route and this method has the benefit of ensuring homogeneity of the distributed particles, (Torralba *et al.*, 2003). Gur (2002), states that microstructural and mechanical properties of particulate reinforced MMCs are mainly influenced by the distribution and amount of reinforcing particles in the composite, with the uniform distribution depending on the particles size of both reinforcement and matrix. Uniform distribution of the particulate reinforcement is important as high cohesive energy in ultrafine particles results in a tendency of the particles to form clusters inducing brittle phases in the MMCs, (Tzamtzis *et al.*, 2009).

SiC, Al_2O_3 and B_4C are ceramic particulate materials used for the reinforcement of Al alloys and the resultant mechanical properties are related to the percentage volume used and the bond between matrix, reinforcement and the reinforcement particle size (Bermudez *et al.*, 2001). Silicon Carbide (SiC) though more expensive, is more suited and common in reinforcing Aluminium (Rosso, 2006), it offers more strength and stiffness than Al_2O_3 and B_4C and its density (3.2 g/cm^3) is also closer to that of the aluminium matrix (2.68 g/cm^3). Al_2O_3 also has increased angularity thereby increasing stress concentrations at the interface resulting in cavity erosion and subsequently composite failure, Wilson and Ball (1993).

Kumar *et al.* (2011) states that the properties, microstructure, homogeneity and isotropy of MMCs are determined by the volume of the added reinforcement, however, the composite properties are also influenced by the type of materials used (matrix and reinforcement) and their intrinsic properties. An increase in the strength of an Al-MMC is thus attributed to the strong interface bonds which allow the transference and distribution of loads between the homogeneous dispersion of the particulate reinforcements in the soft metallic matrix. Ma and Tjong (1997) also found the strength of a particle reinforced Al-MMC increased as the volume fraction of the reinforcement was increased. Strength increases were also associated

with smaller particle size and heat treatment which also decreased the propensity for crack generation. The change in properties observed is generally attributed to increased interfacial area between the matrix and the reinforcement. Zhang *et al.* (2005) however, reinforces this and cites large differences in the modulus and coefficient of thermal expansion, hence there will always be a non-uniform distribution of *in-situ* mechanical properties (ISMP) near the interface between the reinforcement and matrix.

3.4.2 Wettability and Chemistry of the Al-alloy and SiC interface

An assessment of the interphase is considered a prerequisite for the evaluation of the mechanical behaviour of a composite (Pech-Canul, 2011). The chemical reactions and bonding which occur at the interface plays a crucial role in the strength and performance of the composite. Insufficient wettability of the reinforcement by the matrix can lead to weak bonding at the composite interface, (Zhang *et al.*, 2004), resulting in interfacial failure originating from matrix-reinforcement debonding. This is aided largely by the lack of wettability of the SiC by the Al alloy thereby creating air inclusions in the microstructure leading to cracks/dislocations. Wettability of SiC by the Al-alloy system and the resulting chemistry is thus important to the LM processing route as this gives an indication of how good the interfacial bonds will be after the sintering.

According to Laurent *et al.* (1987), good atomic interaction at the Al/SiC interface is needed for strong thermodynamic adhesion which contributes to increasing the strength of the composite. Interfacial reactions increase at high temperatures as they are governed by the Arrhenius law; which expresses the temperature dependence of reaction rates, and has to be carefully monitored to obtain the desired microstructure while preventing undesirable reactions like the brittle intermediate phases Al_4C_3, (Rana *et al.*, 2012b). The interface between the Al-alloy and SiC is chemically stable below 650 ^{O}C but sufficient contact at temperatures exceeding 680 ^{O}C leads to interfacial reactions (Romero, Wang and Arsenault, 1996). Extended and excessive high temperature interaction causes detrimental chemical reactions at the Al-SiC interface forming Aluminium Carbide (Al_4C_3) which undermines ductility and strength of the composite (Noble *et al.*, 1997) as it is brittle and decomposes in water at room temperature to form methane, Equation 3.5, Pech-Cahul, (2011).

$$\mathbf{4Al_{(liquid)} + 3SiC_{(solid)} \leftrightarrow Al4C3_{(solid)} + 3Si_{(in\ liquid\ Al)}}$$

$$\mathbf{Al_4C_3 + 12H_2O \rightarrow 4Al(OH)_3 + 3CH_4} \qquad \textit{Equation 3.5 (Pech-Cahul, 2011)}$$

Lundqvist (1949) posited that as the crystal structure of Al_4C_3 is similar to that of the SiC, therefore the Al ionic atom is being substituted for the Si in the homopolar SiC during the chemical reaction of the Al-alloy and SiC. To stabilise the interface and reduce the formation of Al_4C_3 during the manufacturing process, the addition of Si 10% and above is recommended to increase the viscosity of the alloy and restrict the weld pool flow. The addition of Magnesium (Mg) into the alloy also aids as it lowers the surface tension of the Al-alloy thus enhancing its wettability for SiC and increasing the matrix hardness through the formation of Mg_2Si, Pech-Canul (2011). Slezenev *et al*. (1998) observed an increase in tensile strength and fracture toughness of composites when alloyed with 1.5% Mg with no appreciable increase noted from the addition of Si. Ozben *et al*. (2008) discovered that interface characteristics, reinforcement structure, size, morphology and distribution aid in determining the mechanical properties of the MMC as it decreases the fracture toughness, however good interfacial bond and high reinforcement rate was found to also improve the strength of the AlSi7-10 wt.% SiC MMC.

3.4.3 Components and Tailoring of Metal Matrix Composites

MMCs are comprised of three major constituents discussed in detail below due to their importance in obtaining correct balance for optimal mechanical properties. The alloy matrix, reinforcement, volume and shape of reinforcement, location of the reinforcement and fabrication method are important factors in tailoring a composite, (Singla *et al*, 2009).

3.4.3.1 Matrix:

The matrix in composites is usually a soft and ductile metal/material which serves as a base or host for the embedding of the reinforcement, (Newey and Weaver, 1990). The continuous matrix phase surrounds the reinforcement and supports the particles thus accepting any external load and transferring or distributing it with the reinforcement such that it can withstand more loading than an unreinforced alloy. According to Pech-Cahul (2011), several properties such as heat response, mechanical and corrosion behaviour are important in choosing a matrix and since Aluminium alloys exhibit these properties, their usage in the research for composites is becoming more commonplace. The matrix alloy has to be considered based on its subsequent usage. High temperature usage will require metallic alloys which retains its properties at high temperatures.

3.4.3.2 Reinforcement:

The reinforcement serves as the load bearer for fibre and whisker reinforced MMCs however the matrix is the load bearer in discontinuously reinforced alloys, (Surappa, 2003). Particulate reinforcement demonstrates anisotropic behaviour in the MMC properties when homogeneously reinforced unlike fibre and whisker reinforcements which exhibit isotropic behaviour. In addition, particulate reinforced metal alloys can be subjected to a variety of post-processing including extrusion, rolling and forging which makes it a desirable form of reinforcement especially for the LM process. The reinforcement strengthens the composite by restricting the movement of dislocations in the composite structure, however as this is size dependant, the smaller particles fit easier into the larger metal lattices.

The chosen reinforcement has to be considered for both interfacial reactions with the matrix alloy and the also the fabrication process. The reinforcement must be verified to have little damaging reactions with the matrix especially during fabrication. According to Ohring (1995) incoherent interfaces tend to develop between the reinforcement and matrix therefore submicron particles are better at impeding dislocation motion thus the smaller the particles, the greater their effectiveness. Pech-Cahul (2011) summarises that the volume fraction of the reinforcement needed is dependent on the choice of the composite processing route. Agglomeration is the main challenge to obtaining a homogeneous distribution of particulate reinforcement in the alloy matrix especially when present in higher volumes and smaller particle size (Lu *et al.*, 1998 and Prabhu *et al.*, 2006).

3.4.3.3 Interface

The interface between the matrix and the reinforcement is an important aspect of MMCs as it is a bridge between the matrix and reinforcement and ultimately determines the mechanical properties of the composite. The interface has a large surface area within composites and thus must not degrade during fabrication and withstand both corrosive and elevated-temperature environments. However, as the interface is not in thermodynamic equilibrium, the high chemical gradient of the matrix and reinforcement will lead to reactions, which are needed to obtain full bonding between the components in favourable environments. The interfacial structure between the reinforcement and the matrix alloy varies due to the different crystallographic structures, the chemical bonding between the two and the production method

thus making it difficult to have an easy characterization (Romero, Wang and Arsenault, 1996). The chemical reaction must be closely monitored to prevent the initiation of deleterious compounds such as Al_4C_3 when Al-alloys reacts with SiC. The addition of SiC particles also leads to an increase in the flow stress of the composite compared with the unreinforced Aluminium metal, (Liu *et al*, 2003). Thus an understanding of the thermodynamics and kinetic reactions of each matrix-reinforcement mixture is needed to facilitate load transfer from matrix to the reinforcement such that optimum properties can be obtained, (Kirk-Othmer, 2001). The particle/matrix interface adhesion is a function of the wetting angle interface. Small wetting angles offer high adhesive strength at the interface and any failure at the interface will be by shearing of the particle from the matrix. Alternatively, high wetting angles tend to decrease the adhesive strength and failure occurs in this instance by tensional fracture of the particle. Therefore, the particle/matrix bonding must be balanced by a corresponding chemical reaction at the interface which will aid in strengthening the composite, (Kainer, 2006).

3.4.3.4 Volume and Shape of Reinforcement:

The ratio of reinforcement to the matrix used in a composite is carefully considered based on the load bearing capacity of the part. High strength structural parts will require higher amounts of reinforcement than low strength parts for less demanding environments. The shape of reinforcement is also important especially when considering fabrication processes as angular reinforcements are stress concentrators, reduce ductility and could restricted packing geometry in powder manufacturing processes, (McGeough, 2014).

3.4.3.5 Location of the Reinforcement: -

The location of the reinforcement in the manufactured part can be tailored to provide maximum strengthening to the matrix. The type of reinforcement and its crystal structure can be chosen to reinforce the matrix either by substitution or interstitial replacement of the matrix atoms.

3.4.4 Production of Aluminium Metal Matrix Composites

There are three major methods of producing aluminium MMCs

3.4.4.1 Liquid State Processing:

The alloying of the composite is done with the matrix in the liquid state and either the reinforcement is introduced into the molten metal or the molten metal is poured into the preformed reinforcement. This includes processes like Stir-casting, Pressurised Infiltration, Reactive Infiltration and In-situ Deposition with the fundamental factor being to achieve sufficient wetting between the reinforcement and alloy melt. Liquid state processing must sufficiently wet the surface of the reinforcement to avoid weak interface or undesired interfacial reactions from occurring. These difficulties are largely resolved by coating the reinforcement thus preventing the formation of oxides or other interfacial reactions (Libo e*t al*., 2004).

3.4.4.2 Solid State Processing:

The ability to control the orientation and volume fraction of added reinforcement has made this technique quite common in the manufacture of Al-MMCs. The atoms of the matrix and reinforcement diffuse into each other at high temperatures therefore leading to a good bonding at the interface. These include processes like the Hot Isostatic Pressing (HIP), Spray Deposition and Deformation Processing (Montanari, 2009).

3.4.4.3 Powder Metallurgy:

This technique is used to fabricate discontinuously reinforced MMCs and usually involves cold/hot pressing and sintering after the powders of the matrix and reinforcement have been blended together. Processes like degassing and extrusion which are included in the procedure, reduce the inherent defects in the composites by removing any moisture and encouraging recrystallization at the interface respectively (Pech-Cahul, 2011). Increase in mechanical properties of MMCs fabricated by this method has been attributed to metallurgical effects like the Hall-Petch and Orowan mechanisms, (Wagener and Wolf, 1993).

Hall-Petch mechanism increases strength and toughness by decreasing grain size and has increasingly been be used in casting Al-alloys to refine the grain size and improve the strength of Al-alloys. Orowan mechanism encourages dislocations to loop around precipitates in order to circumvent them rather than cutting through the precipitates when loaded. With increases in the number of dislocation loops, the distance between 2 particles along a slip plane decreases therefore the stress required to form a new dislocation loop increases. This is especially useful in Al-Si-Mg alloys with the precipitation of Mg_2Si used for inducing higher strength.

3.4.5 Strengthening Mechanisms in Particulate Reinforced Metal Matrix Composites

Developing a suitable model for strengthening in MMCs is complicated due to a number of factors including varying matrix composition and strength, particle size and shape, particle-matrix bonding and heat treatment (Sarkar, 1995). Strengthening in particulate MMCs is divided into two major categories direct and indirect strengthening (Chawla, 2012). According to Chawla and Shen, (2001), in direct strengthening, also called load transfer strengthening, an external load is transferred from the weaker alloy matrix through the interface to the stronger reinforcement, with the reinforcement carrying the majority of the load applied. However, due to thermal mismatch between the coefficient of expansion between the matrix and reinforcement, dislocations are created at the interface which then serve to impede movement invariably strengthening the crystal structure, this is known as indirect strengthening also known as matrix strengthening, (Sarkar, 1995). Strengthening mechanisms for the reinforcement are discussed below:

3.4.5.1 Solid Solution Strengthening:

This is the deliberate addition of reinforcement solute atoms to the aluminium alloy matrix in the solid state to form solid solutions thereby creating stress fields around each solute atom which then impede the movements of dislocations (Ashby *et al.*, 2007). The reinforcing particles occupy different lattice positions at random thereby introducing large elastic strains around dislocations, (Fischer, 2009). Smith (1986) states that differences in atomic size between the matrix and reinforcement and clustering of similar atoms in random mixtures are the two major conditions which affect the solid solution strengthening of solids through the distortion of the crystal lattice.

3.4.5.2 Precipitate/Dispersion Strengthening:

Small reinforcement particles having a high melting point and different composition, structure and bonding type, (Fischer, 2009) from the alloy matrix are dispersed into the molten matrix to obstruct dislocation movement, in this instance the particles need to be homogeneously distributed and within close proximity in the matrix to be an effective strengthening mechanism, (Newey and Weaver, 1990). The difference between precipitation hardening and dispersion hardening is that for precipitation hardening, the reinforcing particles are precipitated out of a supersaturated solid solution while for dispersion hardening, the reinforcing particles are mixed or blended with the matrix (Wu and Ferguson, 2011).

3.4.5.3 Work Hardening:

This is also known as strain hardening and is strengthening by plastic deformation through the accumulation of several dislocations within the matrix's crystal structure caused by an externally applied force. The work hardening of MMCs based on the work of Ashby (1966), showed that as long as the reinforcing particles do not deform plastically, the interface between matrix and reinforcement remains intact, thus secondary slip occurs around each particle during the externally applied load, causing secondary dislocations which then impede the movements of the matrix crystals' regular movements.

Dispersion of the SiC particles into the Al alloy matrix will be the major strengthening mechanism for the composite, however the rapid solidification of the melt during the LM process is expected to generate precipitates of primary silicon phase and Mg_2Si in the eutectic thus leading to a fine microstructure which contributes more grain boundaries to impede distortion, crack movement and avoid embrittlement.

3.4.6 Heat Treatment of Aluminium Metal Matrix Composites

Heat treatment of metallic parts has been conducted in order to improve the properties of the parts either by manipulating the grain structure or relieving the internal stress in the samples. Annealing is recommended for parts made from metallic powders to reduce the stress concentrations and induce precipitation of the supersaturated phases which would otherwise lead to work hardening and strain of the lattice (Thummler and Oberacker, 1993) which cause brittle failure in the parts. Fink *et al.* (1940) explained that during the initial stages of age-hardening of aluminium alloys the lattice parameter of the aluminium matrix remains the same because of the heterogeneous nature of the precipitation; however different phases were

seen to precipitate at low and high temperatures thereby straining the lattice. The introduction of ceramic reinforcements into the lattice will also introduce strain into the lattice and along with the alloy solid solution precipitates create severe stresses in the lattice hence the need for heat treatment.

The heat treatment of Al-MMCs studied by various researchers and reviewed by Das, *et al.* (2014a) was consistently a T6 heat treatment for Al-alloy/SiC MMCs. The T6 heat treatment cycle is an Artificial Aging cycle for Al-alloys. Samples were solution treated at high temperatures generally above 500 C for a minimum of 2 hours to ensure phase homogeneity and all elements are dissolved thereby producing a solid-solution. Samples were then quenched in water either at room or elevated temperatures to obtain a supersaturated solid solution (SSSS) and finally samples were subsequently artificially aged at around 175 °C and allowed to cool to room temperature leading to the decomposition of the SSSS and the formation of strengthening precipitates. The heat treatment regime was found to improve the mechanical properties and facilitated the closure of some pores in the fabricated parts. Some of the research reviewed also suggested that preheating the reinforcement particles before its addition to the Al-alloy will remove moisture leading to oxidization of the surface and leads to improvements in wettability. The addition of Mg also reduced surface tension and improved the particulate dispersion in the matrix thereby improving the overall mechanical properties during the heat treatment of the samples. Yuan and An (2012) observed the dissolution of the soluble $\eta(MgZn_2)2^{nd}$ phase into the α-Al matrix and a precipitation of fine intergranular / intragranular AlZnMgCu phase after a solution heat treatment and aging of extruded 7090/SiCp composite which led to improvements in the tensile strength and fracture toughness of the composite.

In their research on the heat treatment of 6061 Al-alloy, Rajasekaran *et al.* (2012) plotted the aging sequence described below for the formation of stable phases and their correlation to the hardness of the alloy. It was reported that the samples of 6061 Al/SiC composite exhibit better strength and higher hardness values when solution heat-treated at 558°C rather than 530°C. The variation of the hardness can be correlated to the phase transformations taking place during the aging treatment. This is due to the melting of the ternary eutectic Mg_2Si-(Al) -(Mg) phase at 558°C according to the A1-Mg-Si phase diagram. The formation of hardening precipitates in Al-alloys can thereby be explained by thermodynamics as the decomposition of a single phase into a different phase/phases going through stages of nucleation, nuclei

growth, coarsening of nuclei and stabilization. Polmear (1995) suggested the precipitation behaviour for Al-Si-Mg alloys as below:

- **Al-Si-Mg Supersaturated solid solution** results into clusters of solute (Mg-Si) atoms and vacancies which are otherwise **Primitive Guinier-Preston (GP) zones**. These GP zones occur at higher temperatures than the ageing temperature due to the higher solvus temperature.
- The primitive GP zones decompose into a **β" monoclinic needle-shaped GP zone.** These lie along $<100>_{\alpha}$ direction, {a = 1.534 nm, b = 0.405 nm, c = 0.683 nm, β = 106°}.
- The Needle-shaped β" GP zone then decomposes into a **Rod-shaped, metastable, hexagonal, semi-coherent Mg_2Si β' phase** which lie along the $<100>_{\alpha}(001)_{\beta'}//(100)_{\alpha};[100]_{\beta'}//[011]$ direction and the β" phase can also be formed {a = 1.04 nm, c = 0.405nm}.
- Some of the Rod-shaped, Metastable, hexagonal, Mg_2Si β' phase transforms to form another **metastable phase of semi-coherent laths** which lie along the $<100>_{\alpha}(0001)_{\beta'}//(001)_{\alpha};[10\bar{1}0]_{\beta'}//[510]$ direction and forms alongside the metastable hexagonal β' phase as this is favoured by the high ratios of Si:Mg in the melt, {a =1.04 nm, c = 0.405).
- **The Metastable Rod and Lath β′ phases** finally transforms to form a Stable, incoherent, face-centred cubic $M_{g2}Si$ β phase with some of the platelets on $\{100\}_{\alpha}$ transforming directly from β' $[100]_{\beta'}//(100)_{\alpha}$; $[110]_{\beta}//[100]_{\alpha}$, {a = 0.639}.

The precipitation hardening behaviour of Al-Si-Mg alloys is thus summarised from the above description in Equation 3.6

$$\alpha(sss) \rightarrow GP\ zones \rightarrow \beta'' \rightarrow \beta' \rightarrow \beta \qquad \text{Equation 3.6}$$

The introduction of the reinforcement into the Al-Si-Mg alloys causes a mismatch due to the differences in the coefficient of thermal expansion (Δα) of both the reinforcement and matrix. Any small change in the temperature gradient caused either through solution treatment and rapid precipitation will generate thermal stresses in the matrix which then undergoes plastic yielding. These thermal stresses also induce high dislocation densities near the matrix-reinforcement interface which serves as sites for the nucleation of strengthening precipitates.

Therefore, these nucleation sites act as an avenue for accelerated aging with Dutta *et al.* (1988) finding that accelerated aging increases with a corresponding increase in the volume fraction of reinforcements. The volume fraction of the reinforcement causes the matrix to over-age earlier than the matrix when it undergoes the same heat treatment regime, which leads to coarse silicon embrittlement and thus a reduction in the ductility and strength of the composite.

3.5 Chapter Summary

This chapter introduced AlSi10Mg as a casting alloy suitable for the LM process with a high specific strength and ductility. The main alloying elements (Si and Mg) were shown to improve its castability and high temperature capabilities thus making it a feasible replacement for steel in high temperature structural applications. Si also reduced the solidification range, thus making it a viable alloy for the LM process. The properties of SiC (density, thermal expansion and tensile strength) which makes it a suitable reinforcement for Al-alloy during the LM process were also discussed.

Matrix-Reinforcement homogeneity was discovered to be an important factor in achieving anisotropic properties during powder metallurgy fabrication of particulate reinforced Al-MMCs. The interface was also considered essential in achieving the desired mechanical properties due to their load carrying capabilities.

Strengthening mechanisms and heat treatments were identified as methods of further improving the mechanical properties of both the matrix and composite. The phase transformations of Al-alloys especially during heat treatment was mapped and their reaction to the introduction of reinforcement was also discussed with a view towards mapping the heat treatment reactions of the MMC fabricated through LM.

Chapter Four

Experimentation and Methodology

4.1 Introduction

This chapter explores the justification for the methodology, experiments and results carried out to determine parameters for MA of the individual powders, the LM of the composite powder and the characterization of the microstructural and mechanical properties. MA parameters (rotation speed and time) were investigated to obtain suitable composite powder morphology and particle size distribution which can be used in the LM system. Single line track and density blocks were fabricated from the base alloy matrix alloy and composite powder for investigations into the effect of laser melting on the composite powder. Subsequently, the microstructures of test samples manufactured with a range of scan speeds and step-overs were evaluated. An appropriate scan strategy was obtained for the composite to fabricate mechanical samples. The general aim of the investigation is therefore to study the influence SiC has on the AlSi10Mg alloy during laser melting while avoiding large temperature gradients and internal stresses during the part build as they instigate crack initiation, propagation and brittle failure of the part. This is achieved by pre-process evaluation of the powder and environment, in-process evaluation of some process parameters and post-processing using heat treatments.

4.2 Introduction to Experimentation

SiC particulate reinforced Al-alloys have been used in an increasing number of automotive and aerospace applications. Surappa, (2003) sums up the driving force for the utilisation of aluminium alloy MMCs as its performance, economic and environmental benefits to these industries. This has led to the Al-MMC replacing existing materials or even facilitating major changes to previous product designs.

From the literature review in both chapters 2 and 3, the economic considerations and process parameters for developing a MMC though the LM process have been discussed, however, little research has been conducted into the production of an Aluminium/SiC MMC by the LM route, in addition little or no research was found that utilised mechanical alloying as a delivery agent. Manfredi *et al.* (2013) blended their powder in a ball mill but no grinding media was used. This research proposed obtaining a near-dense part with comparable

properties to conventionally manufactured MMCs, therefore the upskin and downskin values for surface finishing were ignored and work was concentrated on varying process parameters to determine their effect on properties. The research focused on the LM powder production and powder particles characteristics, along with LM process optimization and chemical/microstructural interaction of the powder particles with the laser.

4.2.1 Justification for Mechanical Alloying

This research work aims to decrease the post-processing stage in the fabrication of a MMC part after LM in comparison to the conventional manufacturing route in Fig. 4.1. Thus, the requirements for composite powder from a typical mechanical alloying route are different from that required for the LM production process. For composite materials which have been mixed to obtain a blended composite powder, there is a danger of separation/ segregation during recoating process as ceramic particulate reinforcements are usually less dense and have smaller particle sizes than the matrix. The metal alloy needs to act as a mechanism for carrying the reinforcement particles thus ensuring the recoating process spreads the composite powder homogeneously. The metal matrix which melts at a lower melting temperature is therefore used to transport and exert a capillary pull on the reinforcing particle such that it induces particle rearrangement and facilitates densification (Erasenthiran and Beal, 2006). Fig. 4.1 also displays the route and phases undertaken during the course of the research.

During the research in MMC fabrication through LM, MA is utilised in processing the AlSi10Mg/SiC_p composite powder where the AlSi10Mg matrix is used as a delivery medium for the smaller SiC reinforcement particles onto the powder bed for LM process. The LM process requires powder particulates that are homogeneous, spherical and of a required particle size distribution to facilitate the spreading of the powder and ensure good packing details (Herzog, *et al*., 2016). Consequently, the MA process must not overly refine the morphology of the matrix particle but must incorporate the SiC particles homogeneously into it without overly increasing the particle size or altering its shape and morphology. In this instance, the time for MA has to be considerably shortened so that a specific particle size range is generated whilst maintaining homogeneity. This is in contrast to extended MA times that generate nano-particulate associated with conventional MA.

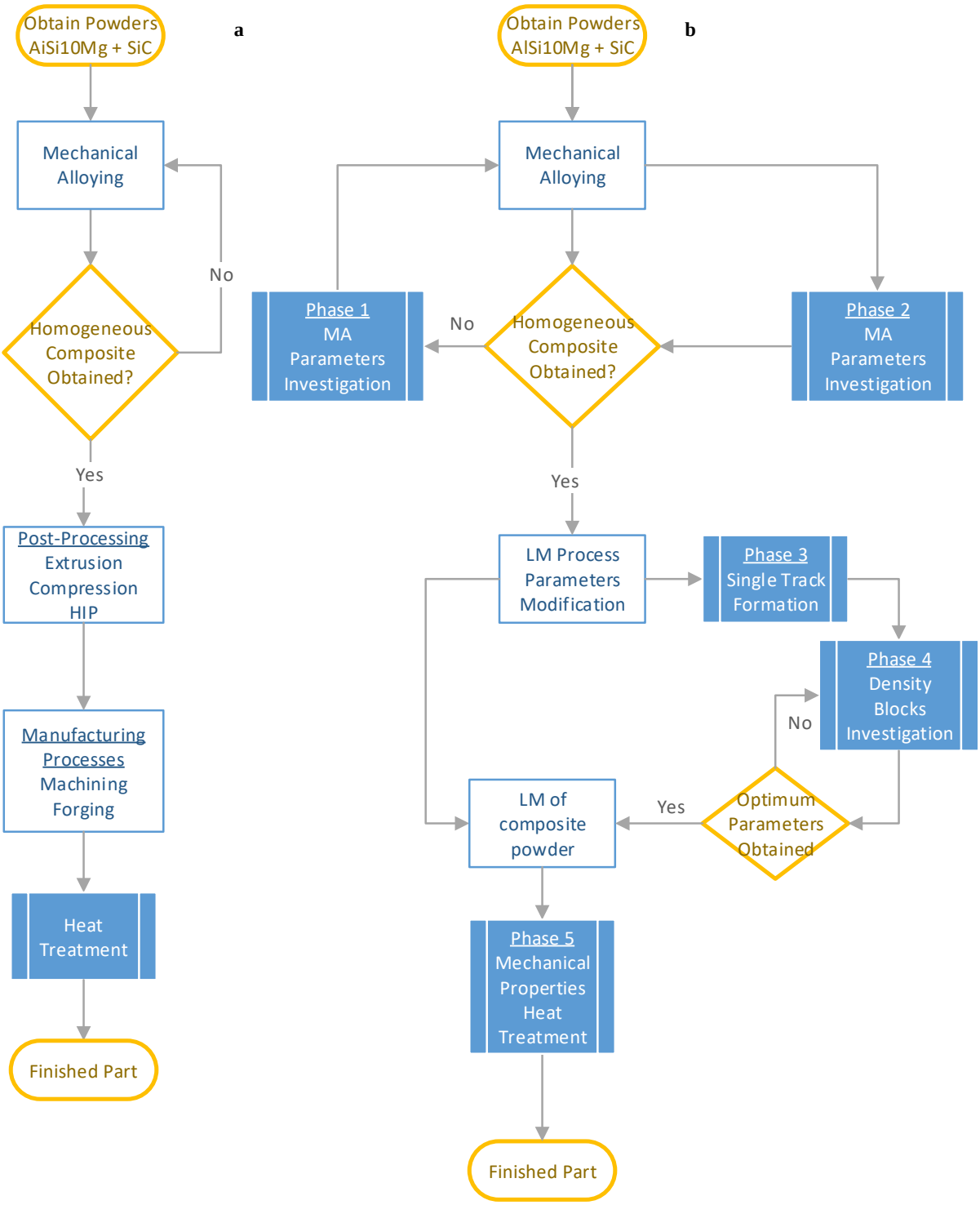

Figure 4.1: Methodology for MMC production: a) Conventional Route; b) Proposed LM Route

MA is generally carried out using a high attrition mill where high rotational speeds during milling and prolonged impact during alloying leads to strain hardening of the powder particles thereby deforming the grain structure, (Bao *et al.*, 1991). The MA process of the alloy and reinforcement can be defined under the terms of Mechano-chemistry, in which intramolecular bonds are mechanically broken by the repeated cold welding, fracturing, and

re-welding of powder particles in order to achieve new compounds. However, from reported work undertaken, the total transformation of the powder into a new compound is deemed unnecessary as the LM process only requires minor atomic displacements which should not affect the crystallographic phase or bonds in the powder particles and this process is instead termed as Mechano-physics (Kaupp, 2009).

In choosing a reinforcement material, angular SiC particles will provide a more powerful barrier at the grain boundaries than Al_2O_3 due to their affinity for Al-alloys (Kumar *et al.*, 2011) thus enhancing the interfacial bonds between reinforcement and matrix. In this instance the strength of the composite has been found to increase with the increase in the volume percentage of the reinforcement. Surappa (2003) observed that the particulate reinforcement volume fraction used for structural and wear resistance applications is usually less than 30%. In addition, a decrease in the particle size of the reinforcement leads to better distribution in the matrix with 15% being stated as the optimised volume for reinforcing an Al-alloy. Ghosh and Saha (2011) and Miracle and Donaldson (2001) advocated that a substantial amount of reinforcement, approximately 10% or more, is needed for any useful increase in the properties of the composite. Slipenyuk *et al.* (2004) also stated that although larger particles improve homogeneity of the reinforcement distribution, however larger particles also decrease mechanical properties as it reduces the work hardening rate and densification rate (Simchi and Godlinski, 2011).

Therefore, a spatial distribution of matrix to reinforcement particle size ratio was suggested. However, as the research into Al-MMC is relatively new for the LM process, both 5% and 10% reinforcement volume fraction was deemed appropriate as a commencement point for the recoating process for this research. The effect of reinforcement particle size (10 µm and ≤1 µm particles) on the particle size distribution was also investigated. The wettability of the reinforcement has also been shown to increase the interfacial bonds thus simultaneously increasing the strength of the composite.

The MA process was chosen for the LM feed powder production in order to achieve a homogeneous feed material for the LM process. Simchi *et al.* (2003) indicate that a high packing density, a high flow rate and low oxygen content are preferred for the DMLS process. The LM process is influenced by the shape, size, and distribution of the particles, together with the chemical constituents of the powder system. Yadroitsev *et al.* (2012)

emphasize that the quality of each deposited layer of powder is of prime importance and each layer must be deposited with a constant thickness, homogeneity, with the highest packing density possible. Kempen *et al.* (2011) corroborate this by stating the requirements for a successful LM processes are:

- Powder production and characteristics
- Effect of particle size
- Processing Parameter optimization
- Chemical interaction of the elements
- Economic consideration.

Other considerations that need to be accommodated as stated by Gu (2015) include the laser absorptance, laser weldability and the Marangoni effects that take place within the molten liquid when there is a shear stress leading to convective movement. Material mismatch will cause a balling effect to reduce the surface tension. This condition can be reduced by adjusting the laser melting parameters and powder characteristics. The packing density and the addition of alloying elements thus become critical and highlights the importance of studying the pre-process powder characteristics as well as the in-process LM characteristics.

4.3 Mechanical Alloying of the Composite Powder (Phase 1 and Phase 2)

In order to achieve a suitable powder for the LM process, the MA of the individual powders were considered in the processes below.

4.3.1 Powder Preparation for Mechanical Alloying

The AlSi10Mg matrix powder was dried in a Nabertherm laboratory batch furnace at 80 ^{O}C for 2 hours to remove any residual moisture content in the powder. Aluminium alloys are highly reactive and has a tendency to form a passivation layer of aluminium oxide on the surface of the alloy after contact with the moisture in air. The rate of reaction is more pronounced in aluminium powders due to the higher surface area exposed by each powder particle. Moisture rich powder has a detrimental effect during the MA and LM processes. The passivation layer Al_2O_3 makes processing problematic as it introduces a higher percentage of ceramic reinforcement into the powders than required and the liberation of oxygen during the laser melting of the composite powder reduces the flowability of the molten layer and its adherence to the previous layer, Liu *et al*, (2011).

4.3.2 The ZOZ Simoloyer CM01 Machine (ZOZ)

The ZOZ is a high energy attrition ball mill used for milling of powder in processes like, reactive milling, wet and dry fine grinding and MA. The technical data of the equipment is shown in Table 4.1 and the operational data and processing is controlled by the Maltoz 3.2 software which also acts as storage for the data files created for the milling jobs (Zoz, 2002). The ZOZ boasts an airtight airlock system with dead-zone free drain chamber and drain gratings for taking powder samples and also features an efficient temperature control system which aids in reducing chemical reactions during milling.

Power is supplied to the horizontal rotating motor which efficiently transfers high kinetic energy to the grinding balls which collide with each other and the powder particles at a relative velocity of up to 14 m/s, (Zoz and Ren, 2000)

Table 4.1 Technical Data of the ZOZ Simoloyer CM01

Dimensions (mm)	750 * 400 * 500
Power (KW)	1.35
Rotation Speed (RPM)	200 – 1800
Nominal Volume (litres)	2
Atmosphere	Vacuum, Inert Gas, Air
Cooling System	Water
Electronic Control	Maltoz 3.2 Software

4.3.3 Powder Measurement for Reinforcement

From previous studies on Selective Laser Sintering (SLS) of reinforced metals, 15% volume fraction has been observed to be the maximum percentage reinforcement achievable, prior to a notably increase in crack density of SLS composites (Ghosh and Saha, 2011) while the minimum for appreciable increase in strength for the matrix alloy is 5% volume fraction. Therefore 5% $_{(vol)}$ and 10% $_{(vol)}$ SiC powder was reinforced into the Al-matrix respectively to determine the differences in the microstructural and mechanical properties in each composite material. The SiC powder was measured in weight and the Al-alloy was made up as a balance to obtain the effective powder charge for the ZOZ mill. Calculations were based on the ball to powder ratio as seen below.

Ball to powder ratio is given as 10:1

Weight of total powder in milling chamber = Weight of balls

10

If the weight of balls was measured to be 2850g, then the weight of total powder to be used in the chamber is 285g. The density of a material is given as the mass per unit volume and expressed in Equation 4.1 as

$$\sigma_p = \frac{M_p}{V_p}$$ ***Equation 4.1 (Kalpakjian and Schmid, 2006)***

Where M_p = Mass of Powder (g)

V_p = Volume of Powder (cm^3)

σ_p = Density of Powder (g/cm^3)

Assuming 100% volume = 285g, then calculations for 5% and 10 % volume reinforcements based on the density of SiC (3.21 g/cm^3) is given in Table 4.2.

Table 4.2 Weight to Volume Calculation

SiC		AlSi10Mg		Total Powder	
(g)	(% cm^3)	(g)	(% cm^3)	(g)	(% cm^3)
16.05	5	268.95	95	285	100
32.10	10	252.90	90	285	100

4.3.4 Charging of the Ball Mill

To have an effective charge in the ball mill, it has been noted from previous studies that the milling chamber must be filled to approximately 50% of its volume and 70 - 80% for attrition mills (Suryanarayana, 2001; Balaz, 2008) with the remaining space used to allow the charge to mix and the room to generate the velocity needed once milling has commenced. The effective charge includes both the grinding balls and the powder to be milled. Bond (1958) emphasises the importance of using correctly sized grinding balls which are big enough to crush the biggest feed stock in this case the 63 µm AlSi10Mg alloy. This is especially important as incorrectly sized balls will adversely influence the grinding efficiency and particle size distribution generated. As the particle size distribution is important for the LM phase of the research, this has to be carefully monitored through regular observations during milling. However, as the aim of the research is not to mill the powder into nanoparticles and to retain the original particle size and particle size distribution, the size of the milling balls used in crushing the particles was deemed negligible. Therefore, the balls were to be utilised in driving the SiC reinforcement particles onto the surface of the Al-matrix rather than actual mechanical alloying.

Stainless steel grinding balls (5 mm in diameter) were loaded into the stainless steel grinding chamber of the ZOZ in Fig. 4.2 with a Ball to Powder Ratio (BPR) of 10:1. This was followed by the AlSi10Mg matrix alloy (grey coloured) shown in Fig. 4.3, and the SiC reinforcement powder (green coloured) in Fig. 4.4. After charging the chamber, the ZOZ is sealed and fully assembled for taking samples as shown in Fig. 4.5.

The BPR is an important aspect of controlling the velocity and rate of milling the powder. The higher the BPR, the more efficient the milling is, however with lower BPR, the velocity of the balls are increased. Research (Suryanarayana, 2004; Lu and Lai, 2013; Othman and Zakaria, 2011) has shown that a BPR between 10:1 and 20:1 had been used to achieve effective milling in horizontal mills, however 10:1 was mostly used for mechanical alloying in ZOZ experiments, Zoz *et al*. (1998).

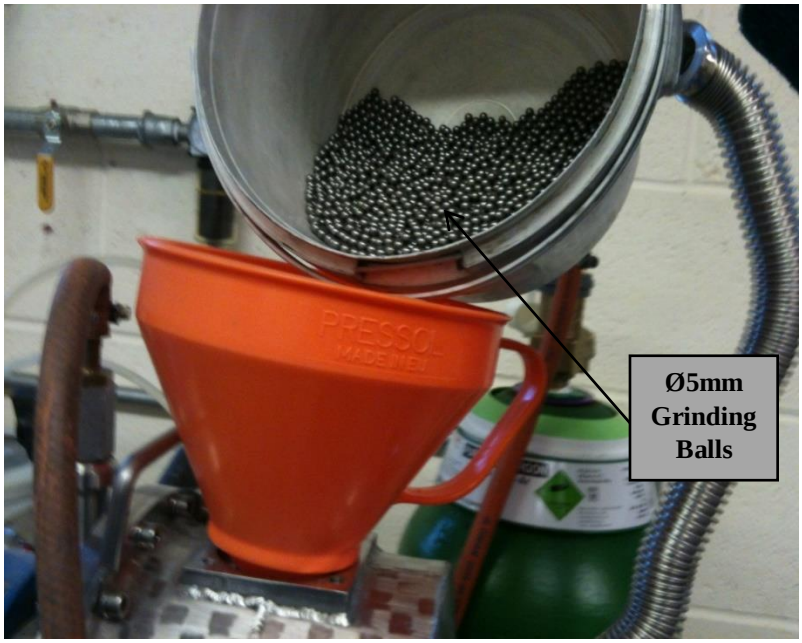

Figure 4.2 Loading of the stainless steel grinding balls

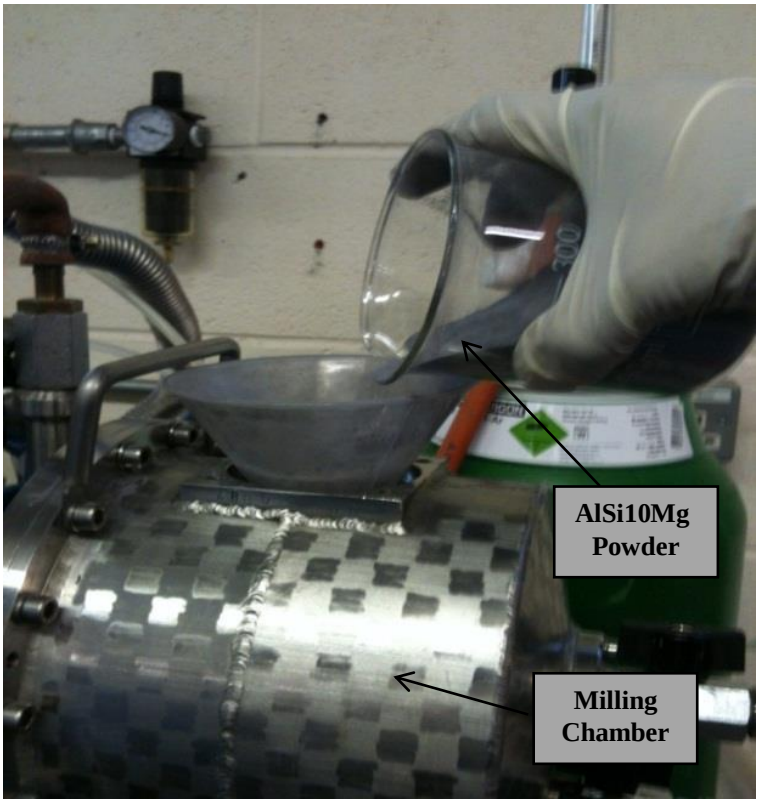

Figure 4.3 Loading of the AlSi10Mg matrix

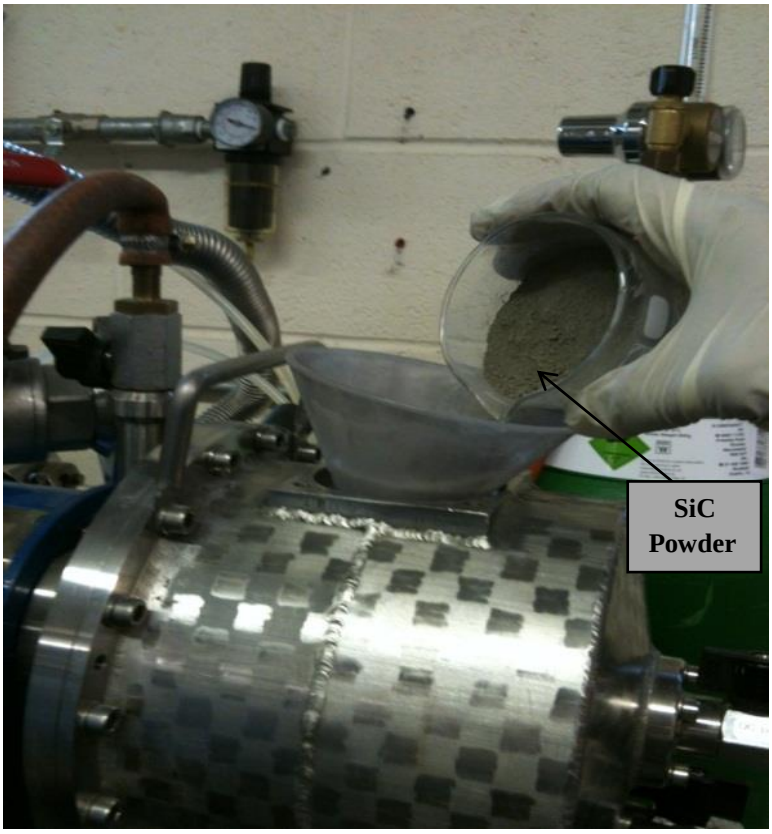

Figure 4.4 Loading of the SiC powder

4.4 Phase 1 - Experiment on Mechanical Alloying Parameters

The chamber was sealed with screws, vacuum pumped to 10^{-3} mbar with the Edwards Inlet dust filter pump and monitored using the Edwards AGD Pirani gauge attached to the front of the milling chamber throughout the duration of the process. The chamber was then pressurised with argon (Ar) gas to prevent re-oxidation and to regulate the atmosphere within the chamber. During the air/O_2 vacuum pumping and Ar flushing, the discharge valves opened to ensure no air was trapped in the enclosed discharge tubes. They are subsequently shut at the onset of milling to prevent powder loss by convection flow of the light powder particles resulting from the high velocity, during the milling process.

The Maltoz 3.2 software was used to program the machine and set the milling parameters. It was initiated by selecting the type of grinding equipment and milling chamber, further to this, selections are made with regards to the process control time, cooling down time and maximum temperature for the MA process. The Maltoz 3.2 software also recorded the rotational speed, torque and total energy consumption during the process. To determine the operational parameters for the embedding of the SiC onto the surface of the Al-alloy in the composite powder production, the milling speed and time were varied as shown in Table 4.3.

These were initial values selected based on the review into high energy milling. Initial values were set at 1200 rev/min (Zoz *et al.*, 1998). Similarly, the MA of Ti-Mg alloy and WC-Ni composites at 800 rev/min by Chikwanda and Maweja, (2008) and Torres and Schaeffer (2010) respectively. The research perimeters of the MA stage were constrained within the objectives of obtaining a composite powder blend for LM by varying the time and speed of rotation, both of which have the most impact on the shape and size of particles. This is to prevent the particles from segregation and clustering arising from the differences in component density, shape and size, Liu *et al.* (1994). In order to prevent contamination (oxide, temperature and environmental) and to improve homogeneity, specific parameters stated below, were maintained throughout the alloying process.

- Ambient temperature (20 ^{o}C) maintained within the chamber throughout milling.
- Argon Environment
- Initial mixing stage at 200 rev/min for 20 mins to ensure both powders were thoroughly mixed before the onset of the MA process.
- Water circulation through the vessel and rotor to monitor process temperature via a thermocouple attached to the wall of the vessel.
- Final discharge step at 200 rev/min for 10 minutes.

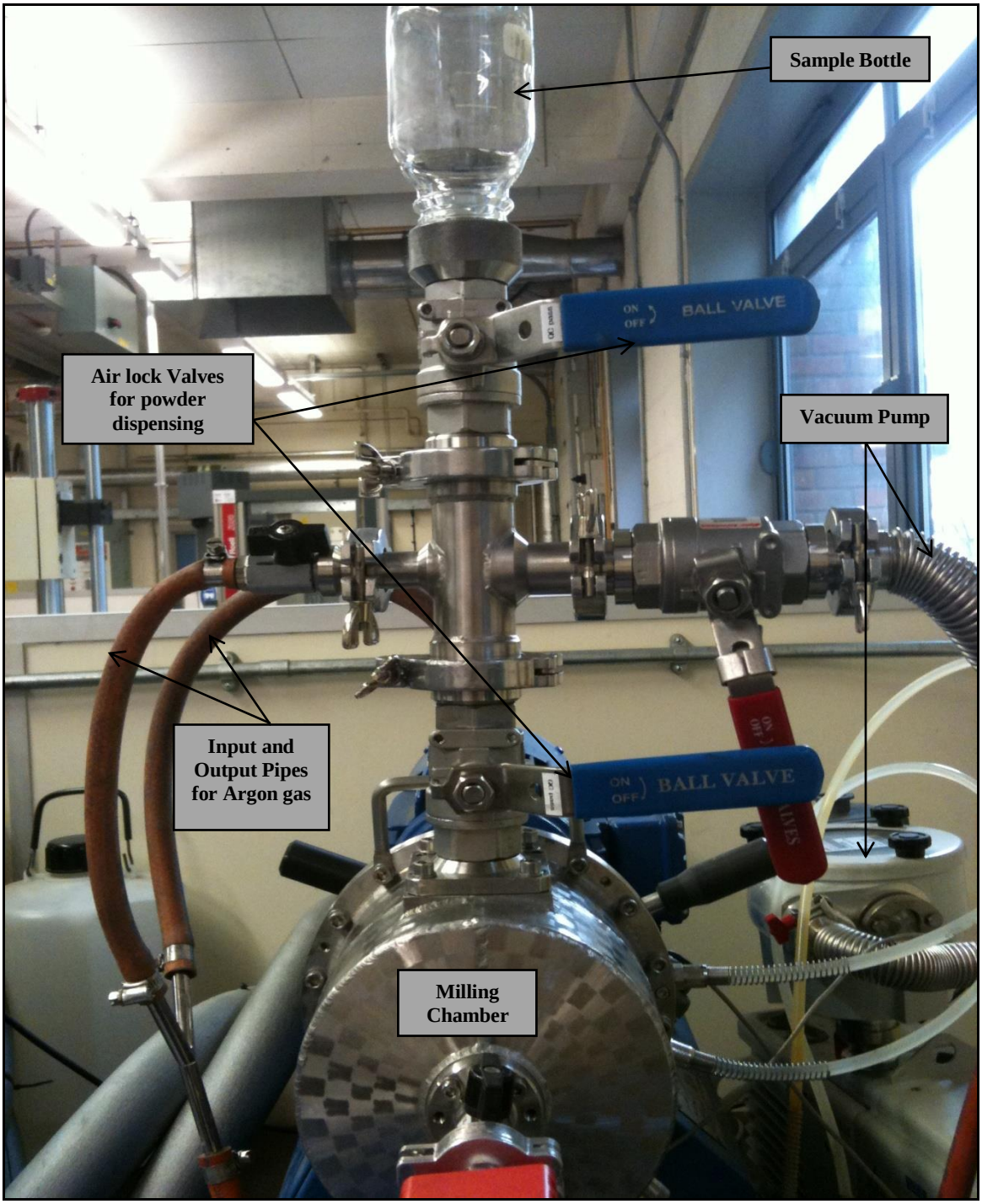

Figure 4.5 ZOZ Simoloyer CM01 utilised for Mechanical Alloying

Table 4.3 Mechanical Alloying parameters – Phase 1

Alloying Parameters	Speed (rev/min)	Time (minutes)
A1	1200	5
A2	800	10

4.5 Phase 2 - Experiment on Mechanical Alloying Parameters

Based on the phase 1 results where high particle deformation and change in morphology were observed, the speed and time of the MA process was further investigated with the parameters in Table 4.4, starting at a much slower speed to monitor the rate of deformation and degradation. No appreciable results were found at speeds lower than 300 rev/min therefore subsequent investigation were started at 350 rev/min.

After results of the phase 2 experiments were verified, another batch of the AlSi10Mg and SiC powders were poured into the ZOZ attrition ball mill and blended together for 20 mins at 500 rev/min using the high energy of the equipment to mix the two powders thoroughly. No milling balls were added to the powder-mix for this stage as the purpose was not alloying but rather achieving a homogeneous composite blend for the LM process. These tests allowed observations to be made regarding the severity of the process and the capability of using the MA process to reduce composite powder development time.

Table 4.4 Mechanical Alloying parameters – Phase 2

Alloying Parameters	Speed (rev/min)	Time (minutes)
B1	350	15
B2	350	20
B3	400	15
B4	400	20
B5	450	15
B6	450	20
B7	500	15
B8	500	20
B9	550	15

4.6 Powder Characterisation

Simchi *et al.* (2003) state that powder characteristics including a high packing density, high flow rate and low oxygen content are preferred for the LM process which is in turn influenced by the chemical constituents, shape, size, and distribution of the particles. The LM

process utilises spherical particles with a distinctive particle size distribution to ensure powder flowability and accurate finishing quality (Liu *et al.*, 2011). A viable range of particle size distribution for LM is aimed to improve the powder stability during the LM process with layer uniformity and packing density ensuring that the same amount of laser energy is absorbed by each layer guaranteeing that each layer is bonded to the next (Sames *et al.*, 2016). This is achieved through ensuring that:

i. There is an overlay between the matrix particles and reinforcement particles which is solved by the MA process.
ii. There is a standard distribution of particle sizes which in turn encourages a homogeneous and uniform layer during recoating.
iii. A precise packing density is ensured through the distribution of both small and large particles.

4.6.1 Characterisation by Scanning Electron Microscope (SEM)

The powders from each parameter were examined with a (SEM) for homogeneity, shape and morphology. A thin layer of powder particles from each sample were mounted on plastic carbon-based self-adhesive stub and loaded on a rotary sample loader in the SEM chamber. The chamber was vacuum pumped and the beam switched on with operational conditions set at the following for samples to be analysed: Accelerating voltage – 20 KV, Beam current – 100 mA, Secondary electrons detector and Working distance – 10 mm. The Energy Dispersive-X-Ray Spectroscopy (EDS) analysis of each sample was also conducted utilising the Oxford INCA AZTEC EDS system which is capable of collecting data from multiple points/areas of interests. Data was conducted at a working distance of 8.5 mm and magnification of 2000 X. Particles were characterised for their spherical shape, morphology, clustering and the amount of SiC reinforcement embedded onto the AlSi10Mg matrix alloy.

4.6.2 Investigation of the Particle Size Distribution

The composite powders obtained from the MA process were measured for particle size and their distribution utilising the Malvern Mastersizer 3000E which utilises laser light diffraction method; as known as Low Angle Laser Light Scattering (LALLS), to separate the particles in a medium. The Mastersizer utilises the Mie theory of scattering to analyse the light scattering passing through the dispersed homogeneous particulate samples for both large and small particles with the angle of diffraction inversely proportional to each particle size thereby predicting the results of the particle size from each angle, Malvern (2015).

It is assumed that all sample particles including the matrix alloy and reinforced composites are spherical and fully conforms to Mie's theory, however this method is somewhat constrained by the fact that particles like SiC tend to agglomerate into a clump thereby giving false readings. The introduction of an ultrasonic boom into the dispersant (water) by the Mastersizer 3000E has resolved this issue as the ultrasonic boom is used to separate the agglomerated clumps, Malvern (2015).

The powder samples are extracted with a scoop and inserted into the powder tank of the equipment. Scattered light is focused onto the obscuration detector and the sample either absorbs, reflects, diffracts or scatters the light. For good results, obscuration is recommended between 10 % – 20 % as this ensures sufficient noise signal for measurements while eliminating the possibility of multiple scattering. The reflective index of the particles given as 1 and that of the water dispersant (1.33) are entered into the Mastersizer software which are then utilised to calculate the diffraction/reflective angles and a volume distribution and concentration is then generated for analysis.

Results from the Mastersizer for the analysis of the initial feed samples are given in Chapter 5. These illustrate the difference between the unalloyed matrix, alloyed composite and mixed composite. Particles are measured in percentiles representative of volume measurements for each percentile

Where P_{10} - Average diameter of particles under 10%

P_{50} - Average diameter of particles under 50%

P_{90} - Average diameter of particles under 90%

4.6.3 Characterisation by X-Ray Diffraction (XRD)

Light (including X-rays and Laser rays) can be refracted, reflected, absorbed or transmitted when it impinges on the surface of a material. When light rays are impinged on a material which is not absorptive or reflective, the light waves can be diffracted around the material by bending around its edges. When X-ray radiation is directed on a sample powder, diffraction occurs through the production of a coherent array of radiation from individual electrons at specific angles "θ" as observed in Fig. 4.6. The coherent array of radiation must produce a constructive interference in order to produce an amplified wave which can be measured by the diffractometer. Metallic materials due to their high crystallinity resulting from the consistent arrangement of their atomic structures produce particular constructive scattering

intensity from the diffracted angles, (Das *et al.*, 2014b). The scattering intensity follows Bragg's Law in Equation 4.2.

$$n\lambda = 2d\sin\theta$$ *Equation 4.2 (Das et al., 2014b)*

where n = integer defining the order of diffracted beams

λ = X-ray wavelength (nm)

d = Distance between crystal lattice planes (nm)

θ = Diffraction angle (°)

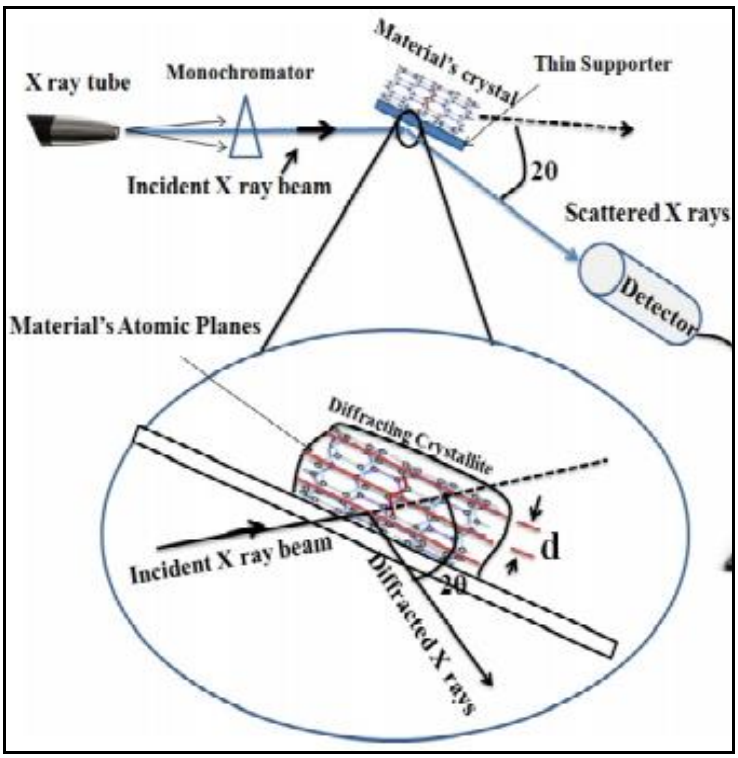

Figure 4.6 Schematic diagram of XRD basic principle (*Das et al., 2014b*)

For each lattice spacing d, Bragg's law predicts a maximum characteristic diffraction angle θ and for parallel atom planes (h, k, l) in a material separated by the lattice distance d_{hkl}, the constructive scattering intensity can only be measured when Bragg's law is satisfied (Das *et al.*, 2014b). To satisfy Bragg's Law θ must therefore change as "d" changes due to the different spacing between each plane, Birkholz, (2006).

For XRD measurements, the incident beam of the X-rays interferes with one another as they leave the crystal that are detected and recorded by the equipment. When the intensity of the detected X-rays is plotted as a function of angle θ, a diffraction pattern is obtained which is characteristic for each specific material, Birkholz (2006). For cubic crystals like Aluminium

the length of each side (a, b, and c) and their corresponding angles are equal to each other in Equation 4.3 and can be determined by XRD.

$$\mathbf{a = b = c = a_0 \text{ and } \alpha = \beta = \gamma = 90°} \qquad \textit{Equation 4.3}$$

where

$$a_0 = d_{hkl}\sqrt{(h^2 + k^2 + l^2)} \qquad \textit{Equation 4.4 (Kamwaya, 2002)}$$

When strain is introduced into a lattice for example through mechanical alloying, it exhibits a change in the diffraction pattern depending on the type of strain introduced as observed in Fig. 4.7, (Garg and Gurao, 2013). When a uniform strain is introduced, the diffraction peak moves but does not change shape thereby lowering the diffraction angle however, when the strain is non-uniform, the peak broadens and the lattice spacing gradually changes from top to bottom of the peak due to change in the interatomic distances (Graat, 2004).

The Empyrean PANalytical X-Ray Diffractometer utilised for the research was a Philips Model PW1770 based at the University of Wolverhampton. It operates with a copper anode which has an average wavelength of 1.542 Â and the x-ray scans were conducted on the powders samples of the matrix alloy, 5% and 10% reinforced composites between the 2θ values of 5° and 80° with a step size of 0.0130 and a temperature of 25° C.

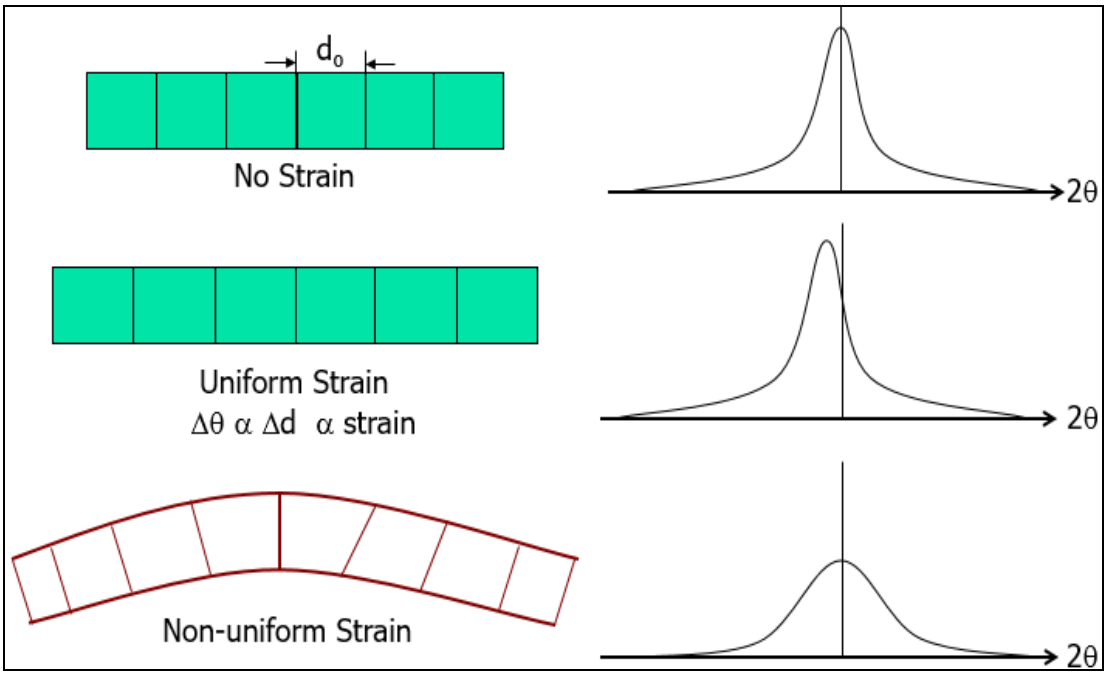

Figure 4.7 Distortion of XRD Peaks under strain, (*Garg and Gurao, 2013*)

4.6.4 Particle Shape Characterisation

Geometric shape factors are used to characterise the shape of particles utilising the BS EN ISO 3252 standard glossary for the description of the powder grains as classified below (Fig. 4.8). Shapes were categorised by viewing them under the SEM and matching their descriptions to the standard.

- Acicular – Needle shaped – Fig. 4.8a
- Angular – Sharp edge, roughly polyhedral – Fig. 4.8b
- Dendritic – A branched crystalline shape – Fig. 4.8c
- Fibrous – Regularly or irregularly threadlike – Fig. 4.8d
- Flaky – flaked, platelike – Fig. 4.8e
- Granular – Approximately equidimensional but irregular shape – Fig. 4.8f
- Irregular – Lacking any symmetry – Fig. 4.8g
- Nodular – Rounded, irregular shaped – Fig. 4.8h
- Spherical – Globular shaped – Fig. 4.8i

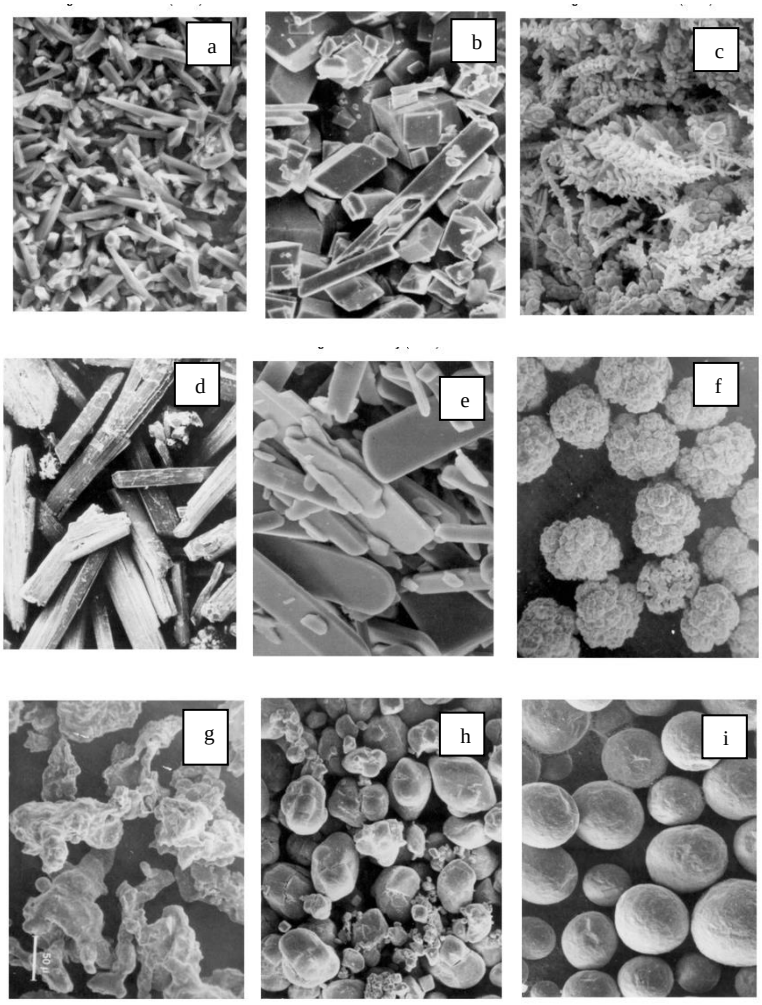

Figure 4.8 Particle shape characterisation – a) Acicular, b) Angular, c) Dendritic, d) Fibrous, e) Flaky, f) Granular, g) Irregular, h) Nodular, i) Spherical (*BS EN ISO 3252, 2000*)

4.7 Laser Melting of AlSi10Mg alloy and AlSi10Mg/SiC_p (Phase 3, 4 and 5)

The research work has been carried out on the EOSINT M270 Ext (M270-X) laser melting system with its full characteristics described as follows:

- The M270-X system uses a continuous ytterbium (Yb) fibre laser with a wavelength of 1070 nm which achieves a maximum nominal output power of 200 W with the maximum power of 195W achievable in the building area, due to energy losses in the optical focussing. It utilises F-theta optical lenses with a focal length of 410 mm to focus the high speed scanner which attains a speed of 7000 mm/s, thereby giving the laser system a highly focused and stable beam. The diameter of the laser beam can be varied between 100 -500 µm through focus adjustment depending on the material being used.
- The M270 X utilises a high speed stainless steel blade recoater arm for aluminium alloys which moves in a horizontal direction from right to left in a single motion of powder recoating (Fig. 4.9).
- The build platform is heated to between 40 – 80 ^{O}C with an aim to reduce internal stresses while reducing any moisture in the powder thereby ensuring a good bonding of the first few layers. The layer building occurs in a protective inert atmosphere either argon or nitrogen depending on the material being processed to minimise oxidation and contamination.
- The dimensions for the M270-X building envelope are 250 mm x 250 mm x 200 mm (L x W x H), however this was modified prior to the start of the research into a smaller building platform (Fig. 4.10) with dimensions 120 mm x 120 mm x 90 mm (L x W x H), suitable for smaller parts and research samples by reducing the amount of powder consumption needed for processing and samples built on a smaller substrate.
- Data files were prepared using CAD and converted to a Stereolithography (STL) format using EOS RP tools software. Parts were then placed and oriented on the virtual platform utilising Materialise Magics RP 3.1 software which was also used to generate supports for overhangs where needed. Magics was also used to fix any errors within the STL files such as bad edges, contours, hole filling, overlaps and intersecting triangles. The STL files were then saved as job files and further converted into the EOS format (SLI) and loaded onto the machine through the EOS PSW 3.4 software. Processing parameters were also modified using this software to include laser power, scanning speed, beam offset, hatch spacing, hatch pattern and scanning strategy.

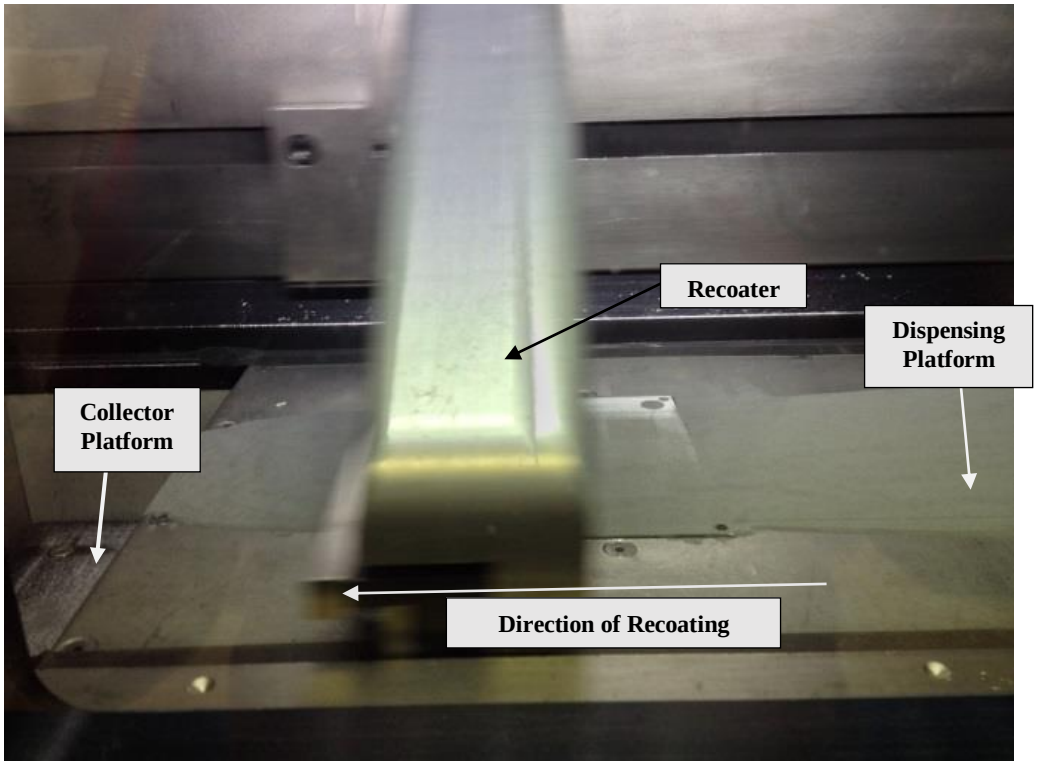

Figure 4.9 Powder Recoating during LM

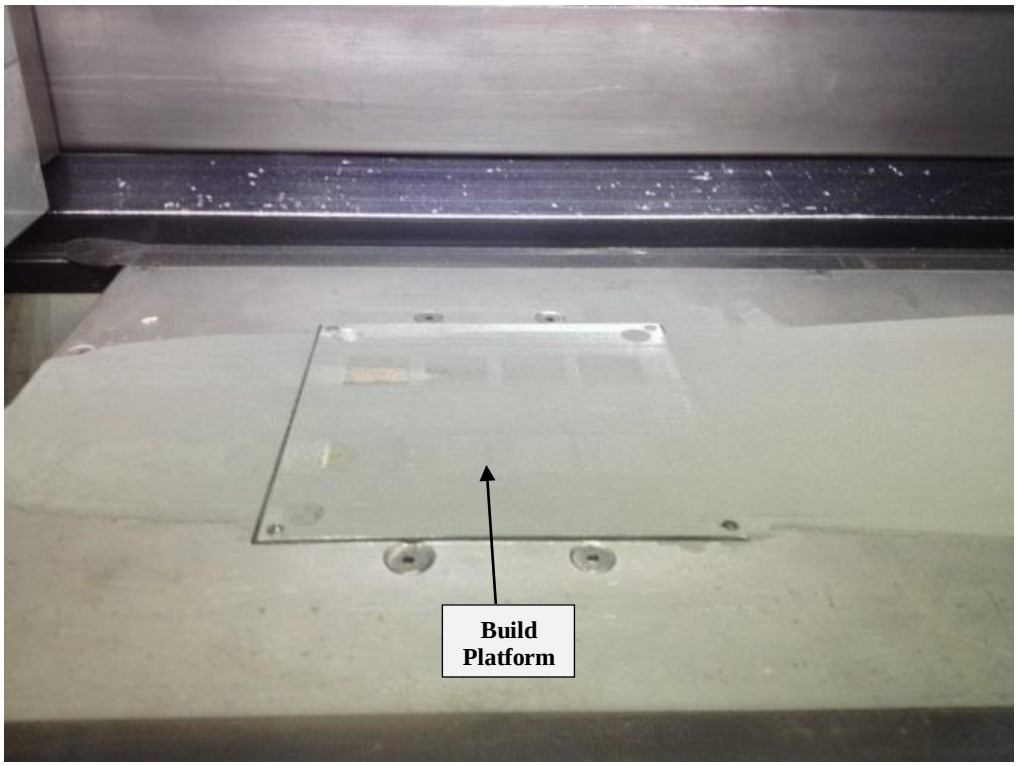

Figure 4.10 Mini-platform for Research Samples

4.7.1 Powder preparation for Laser Melting

The AlSi10Mg matrix powder and the composite powder AlSi10Mg/SiCp were dried in the batch furnace at 80 OC for 2 hours to remove any residual moisture content in the powder which may have been absorbed during the MA process. The dried powders were sieved in a

Fritsch Analysette 3 Pro mechanical shaker (Fig. 4.11) placed in a glove compartment box to prevent re-oxidation and environmental contamination of the powder. The powder was sieved through woven 125 µm, 75 µm and 63 µm meshes which conform to the ASTM E11 (2015) standards for 20 mins at a pulse frequency of 1.5 Hz. Powder particles from the 63 µm mesh as recommended by the EOS parameters for LM, were transferred into the M270-X. Spierings *et al*., (2011a) have shown that smaller particles improve the surface quality of metal fabricated by LM.

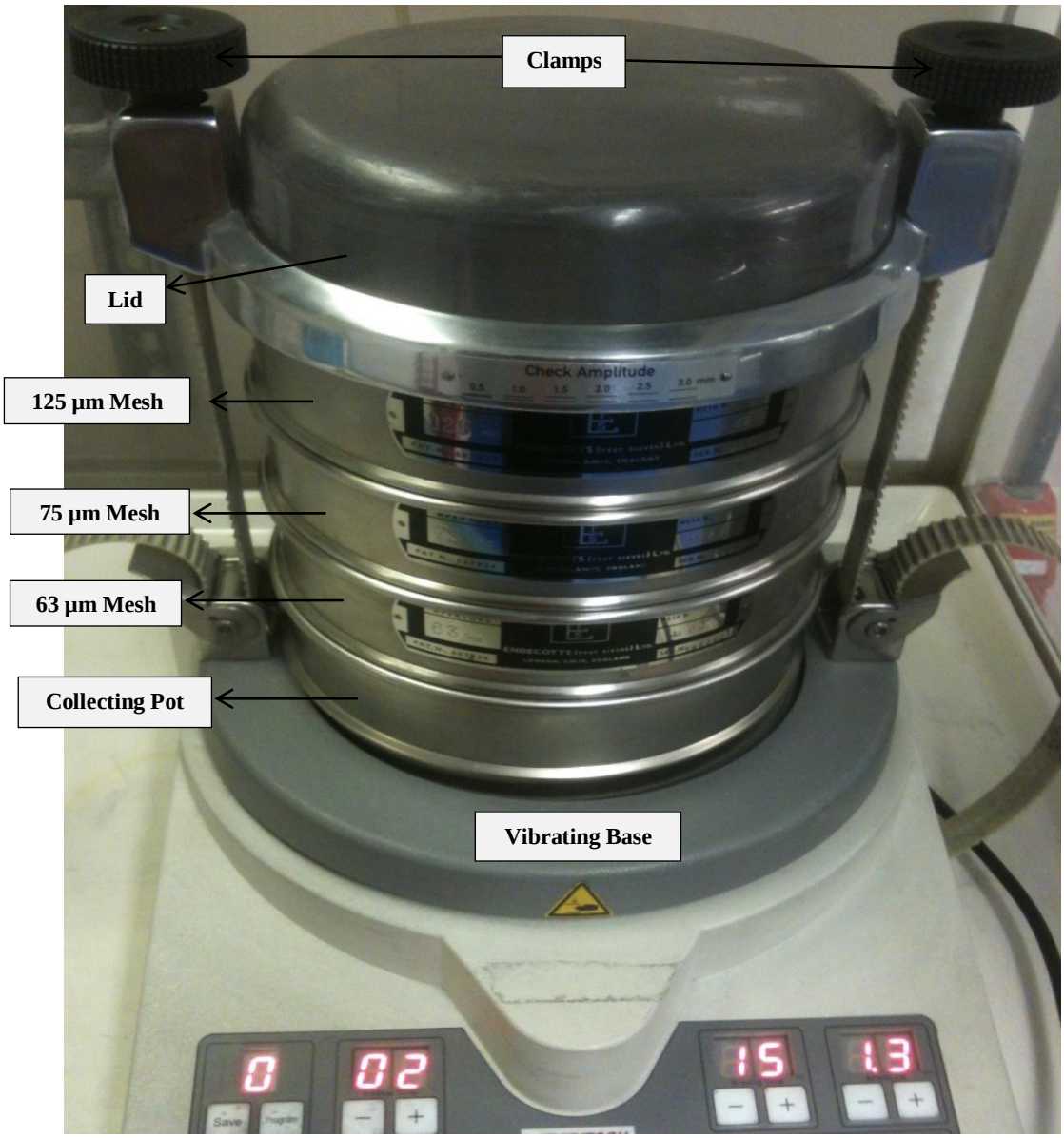

Figure 4.11 Sieving the Composite powder

4.7.2 Scanning Strategy for AlSi10Mg

The laser power used for the fabrication of all sample pieces was set at the maximum value of 200 W due to the highly reflective nature of Al-alloys with the working energy density on test samples noted to be 195 W from the energy losses in the optical path of the laser. Based on EOS recommendations for AlSi10Mg and the particle size distribution in section 4.5, the layer thickness and stripe width used in the fabrication of all samples was 30 µm and 5 mm respectively, with the samples built on a 120 mm by 120 mm aluminium alloy substrate plate set on the build platform with a maximum temperature of 35 °C. The values for the layer thickness and laser power were adopted as a compromise to achieve high build rates, part resolution and final density of the parts. The AlSi10Mg alloy was scanned with the DirectMetal strategy which ensures that unlike the previous versions of the machines does not require separate infill parameters for the skin and core regions of the part. Utilising a single infill parameter (Table 4.5) for the whole part ensures anisotropic properties in the part.

Table 4.5 Scanning Parameters for AlSi10Mg EOSINT M270-X

Parameters	Value
Laser Power (W)	195
Scan Speed (mm/s)	800
Step-over (mm)	0.17
Stripe Width (mm)	5.00
Stripe-Overlap (mm)	0.50
Laser Spot Size (mm)	0.10
Atmosphere	Argon
Oxygen Concentration	<0.1%

4.8 Phase 3 – Parameters Investigation

This section describes the methodology and research work that was carried out to study the effect of the laser parameters on the density of the composite samples with an aim to obtain near fully dense parts. The results are reported and discussed in Chapter 6.

4.8.1 Single Track Formation

In order to study the effect of SiC on the melting characteristics of the Al alloy matrix, single line tracks were sintered for the matrix alloy and composite powders using different sets of process parameters. The build platform was initially shot blasted to provide a rough surface which assists in trapping the powder particles when the initial layer was spread thereby ensuring good adhesion of the powder to platform on the application of the laser heat. It was secured to the build platform using 4 screws and lowered for levelling. The build platform was levelled and aligned with the recoater blade to ensure that the build plate is parallel with the underside of the recoater and the same amount of powder is deposited each pass. A single track of the AlSi10Mg matrix alloy was sintered with a laser power of 195 W (standard EOS scan parameter for Al-alloys). The composite material with 5 % and 10 % SiC were scanned as per parameters in Table 4.5 (Fig. 4.12). The macrostructure of the sintered tracks was evaluated using the SEM for evidence of pits in the welded track, degradation of the effective laser beam area, appropriate height and width for the weld bead and the amount of powder melted.

Other standard parameters of the Eosint M270 for LM of aluminium alloys remain fixed as in Table 4.5 with the exception of the step-over which has been widened and fixed at 0.50 mm to ensure the single tracks can be studied between each adjacent weld bead. The scan pattern rotation was also fixed so that tracks could be laid in a straight line with the black line in Fig. 4.12 showing the direction of powder recoating.

Single line tracks were also melted for the mixed powders to verify the effect MA has on the scanning parameters. The single line tracks examined were made of three layers to reduce interference from the residual particles of the shot blast on the build plate. In addition, as the build plate acts as a heat sink, multiple layers are required for accurate characterisation of the weld bead as the previous layers will act as the heat sink rather than the build plate. The information is important as the heat dissipates through previous layers during part build.

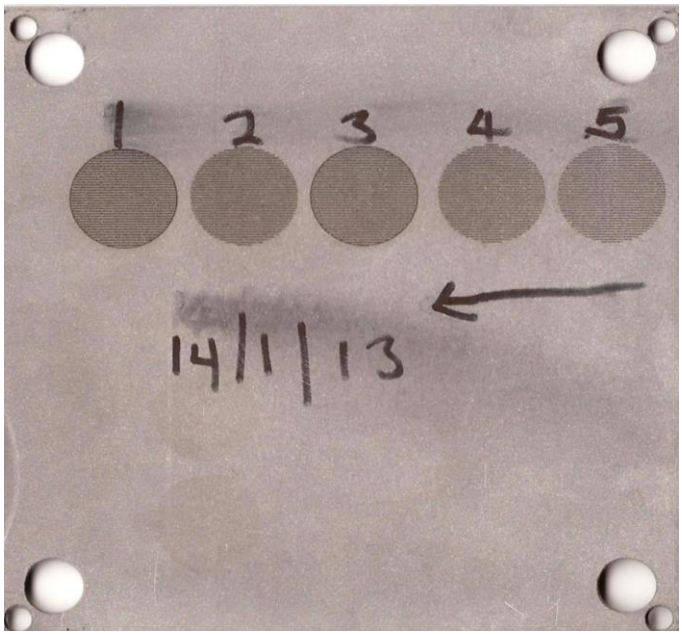

Figure 4.12 Overview of single line tracks with variable scan speeds

4.9 Phase 4 – Laser Melting of Density Blocks

20 mm by 20 mm by 5 mm blocks were fabricated from all the powder samples using the parameters in Table 4.6 for both the alloy matrix powder and the composite powders. Using the infill scan strategy with the various scanning speed between 640 mm/s and 1120 mm/s, density blocks were fabricated (see Fig. 4.13). Another set of sample blocks were also fabricated using the parameters in Table 4.7 where both the laser scanning parameters and the step-over values were simultaneously changed to investigate the influence of the energy density on the factors discussed. Energy density which is the amount of energy absorbed by a specific volume of powder is influenced by process parameters, Ciurana *et al*. (2013). As previously established in section 2.2.3, energy density influences the dimensional accuracy and density of parts therefore making it an essential parameter to investigate. All infill parameters as no UpSkin/DownSkin or contour parameters were utilised in the experiments, as the result is to achieve full density. From Equation 2.1 energy density depends on the laser power, scan speed, layer thickness and step-over, however, the laser power and the layer thickness were kept constant due to the high reflectivity of Al-alloys and machine parameters for Al respectively. The scan speed and step were therefore varied to determine their effect on the energy density.

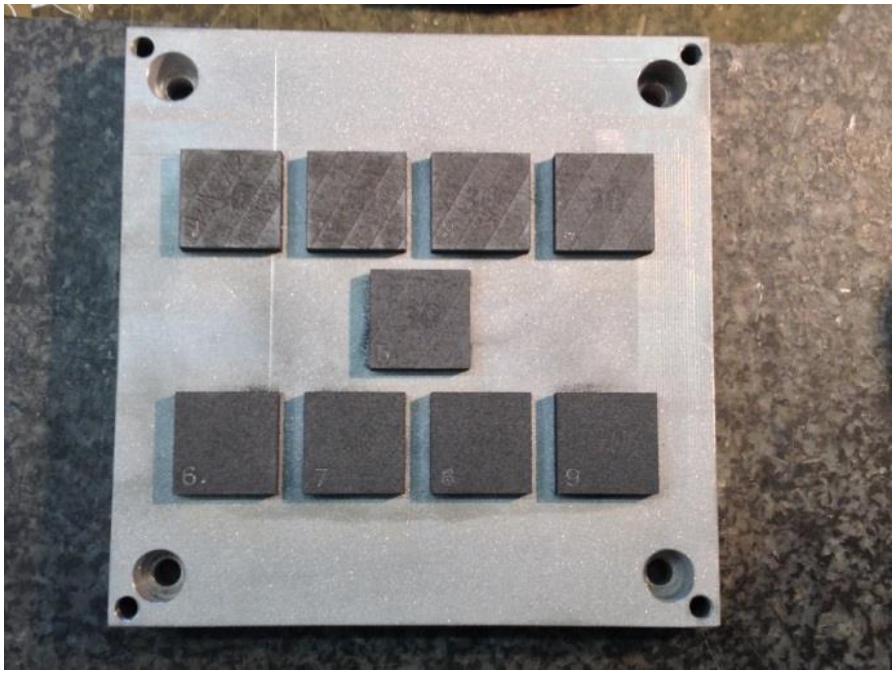

Figure 4.13 LM blocks with different parameters

Table 4.6 Density blocks with variable scan speed

Variation (%)	-20	-10	Nom	+10
Block No	1	2	3	4
Scan Speed (mm/s)	640	720	800	880
Step-Over (mm)	0.17	0.17	0.17	0.17

Table 4.7 Density cubes with variable step over and scan speed

Variation (%)	-4	-2	Nom	+2
Block No	1	2	3	4
Scan Speed (mm/s)	640	720	800	880
Step-Over (mm)	0.13	0.15	0.17	0.19

4.9.1 Characterization of the Samples

The as-fabricated blocks were cross-sectioned with a hacksaw mounted in a thermosetting phenol formaldehyde resin using an automatic Buehler Metaserv mounting press and polished to carry out microstructural and crystallographic analysis with reference to metallographic preparation of aluminium alloys by Davis (1993) and the SiC reinforcement. The mounted samples blocks were initially ground on a Metaserv grinding wheel fitted with resin bonded diamond MD Piano discs after which they were polished to a mirror surface on

a Kruger polisher using DP-Paste containing polycrystalline diamonds of 6 µm and 1 µm respectively according to parameters in Table 4.8. Samples were washed and cleaned with both water and ethanol between each step to prevent transference of abrasive from previous grades to progressive grades.

Samples were then etched for 10 – 30 seconds using the Keller's reagent containing - 1 % Hydrofluoric acid (HF – 2ml), 1.5 % Hydrochloric acid (HCl – 3ml), 2.5 % Nitric acid (HNO_3 – 5ml) and 95% Distilled Water (H_2O – 190 ml) to stain and differentiate the grain boundaries.

Table 4.8 Grinding and Polishing regime for samples

Step	Mesh	Speed (rev/min)	Time (mins)	Lubricant
Rough grinding	220	300	5	Water
Plane grinding	500	150	10	Water
Fine grinding	1200	150	10	Water
Rough polishing	6 µm	150	10	Water
Fine polishing	1 µm	150	15	Water

4.9.1.1 Surface Roughness

The effects of the changing parameters in Tables 4.6 and 4.7 on the surface roughness of the samples was investigated due to its influence on the powder coating and density of the part. In order to study the effect of changing parameters, the surfaces of the unpolished sample blocks were scanned and measured using the confocal Olympus Lext OLS3000 Microscope which was calibrated to obtain results consistent with a stylus instrument with the advantage of non-contact measurements. To minimise errors caused by vibrations to the scanning table, it is mounted on a Table Stable TS – 150 LP vibration isolation stabilising system.

To measure the surface roughness of the samples, the top and side surfaces were examined to obtain the average roughness (Ra) readings from 3 different areas of interest. Ra is defined as the arithmetic mean of the deviation from the centerline profile along the specified sampling length (Manas *et al.,* 2008). An average of seven readings across each area of interest is obtained to determine the depth and waviness of the surface using an objective lens of 20x. To obtain accurate readings 3D scanning was employed with excessive noise removed from each profile before any measurements were taken using the Intelligent Noise Removal Algorithm in the Lext OLS software (Olympus, 2010). The recorded values of each sample

were then measured against the Ra values of the matrix alloy with the deviation reported in Chapter 6.

4.9.1.2 Determination of Relative Density

The Archimedes method (ASTM B962-15) was used to determine the density of each sample. Masses of each block were measured in both air and 100 ml of deionised water three different times using a SciChem precision electronic balance in Fig. 4.14 with ±1 mg accuracy obtainable. The average mass from the readings obtained at ambient temperature, were calculated and utilised in calculating the relative density given by Equation 4.6.

$$RD = \frac{\rho_{air}}{\rho_{deionised\ water}} = \frac{W_{air}}{W_{air} - W_{water}}$$ ***Equation 4.6 (ASTM B962-13)***

Where RD = Relative Density

ρ = Density (g/cm^3)

W = Mass (g)

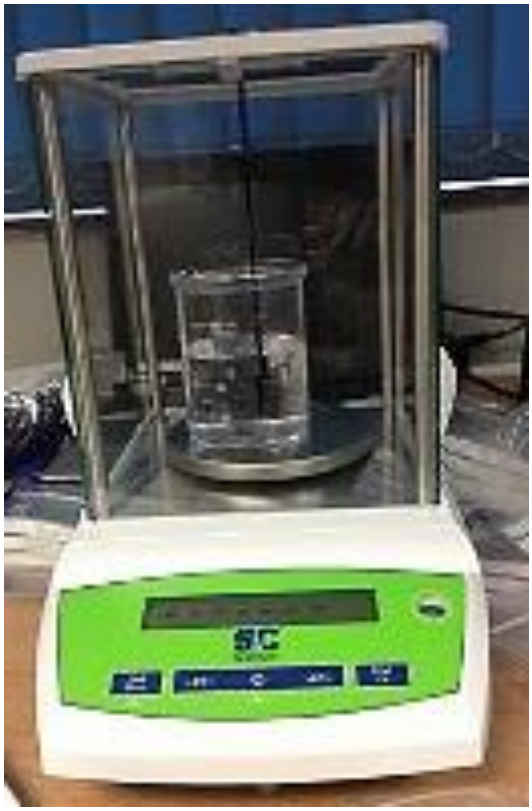

Figure 4.14 SciChem Precision Balance showing Archimedes Principle

The values of the relative density were then represented as a percentage of the relative density of the matrix alloy assuming the matrix is 100% dense in section 6.3.4.
The results from the surface roughness, porosity and relative density measurements along with the initial investigations on the scan lines were therefore used to determine the best set of parameters utilised in fabricating samples for further experimentation including heat treatment, hardness and flexure tests.

4.9.1.3 Determination of Porosity

Prior to etching, samples were characterised under the optical light microscope to analyse the percentage porosity. To obtain a quantitative evaluation of the porosity values, each sample block was sectioned as observed in Fig. 4.15, mounted in Bakelite and polished. The cross-sectional images of each sample in both the direction of the recoater blade (parallel cross-section) and core positions (vertical cross-section) were examined utilising the LEXT 3000 OLS Olympus optical microscope and the Stream Essentials Image Analysis (SEIA) software developed by Olympus. Although this analysis does not represent the real 3D analysis of the pores as analysis is only conducted on the polished section, it indicates the density and quality of the parts.

The images obtained from the optical microscope were transferred to the SEIA software where they are calibrated into readable pixels using the measurement bar on the pictures. Calibration is done by converting the measurement bar into millimetres which are further converted into pixels using the calibration tool in SEIA. The calibration converts the J.peg images into black and white pixels, which can be interpreted by the software. To ensure traceability and repeatability, calibration at a magnification of 5X was carried out at the same values for each sample. Samples were calibrated for pore calculation by focussing on the pores in each image while increasing and decreasing the threshold values until a suitable percentage was obtained at 75% representative of the pores. This aided the software in calculating the ratio of the black pixels to the white pixels with the black pixels translated as the pores while allowing a variation for multi-phased alloys. 2 sets of pictures were taken from different locations of every sample to obtain an average value given as the percentage porosity.

Porosity in LM can be established as either continuous or totally enclosed. Continuous porosity would extend through the layers of the LM part especially when viewed in the perpendicular direction to build/recoater direction. These would mostly be from unmelted powder particles or from splatter entrapped on the previous layer. Totally enclosed porosity is characterised by gas pores and thus associated only to single layers. The porosity of LM parts is determined by the material and process parameters especially the step-over Spierings *et al*. (2011b).

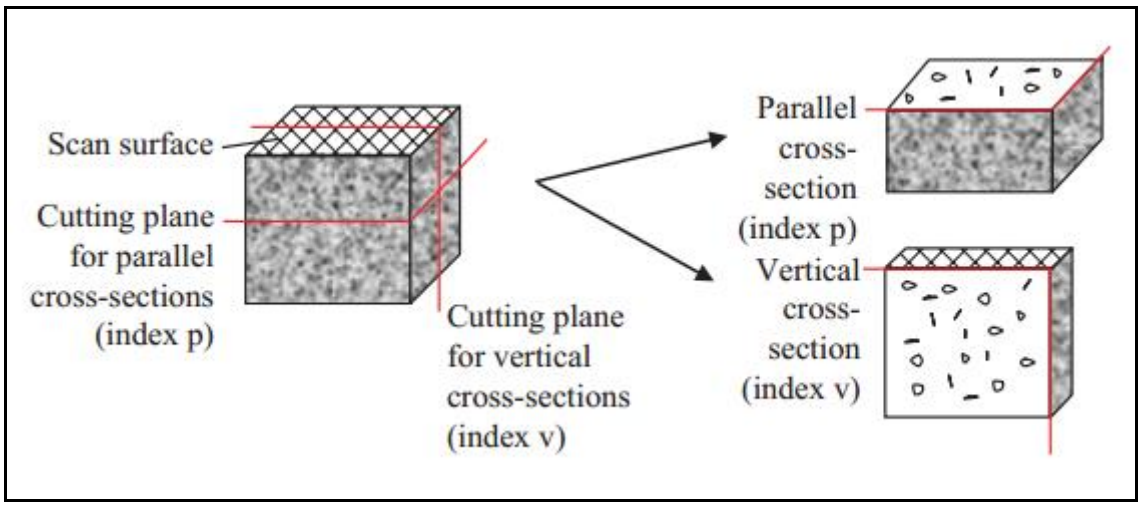

Figure 4.15 Cross-section for Microstructural Image Analysis (Spierings *et al.*, 2011b)

4.10 Phase 5 - Mechanical and Destructive Testing

After the determination and validation of the appropriate scanning parameters for obtaining a near dense specimen, transverse rupture test specimens were made for mechanical testing of the MMC and validated with the data obtained for the matrix alloy. Samples were LM at a Scanning Speed of 880 mm/s and Step-over 0.17 mm as determined from the results of Phase 3 of the research.

4.10.1 Heat Treatment

Precipitation hardening of the composites was conducted to determine the effect of heat treatment on the material properties. The as-built samples were immediately removed from the build plate and half of the samples were heat treated to the T6 regime. In the meantime, 10 samples of each material (matrix alloy, 5 % reinforced composite and 10 % reinforced composite) were stress relieved in the Nabertherm laboratory batch furnace on the build plate in accordance with EOS recommendations for AlSi10Mg alloy (EOS, 2011) to reduce both

thermal and mechanical stresses prevalent with LM before being removed from the substrate. Specimens were removed from the build plate using an Ona-Prima E-250 Wire Electro-Discharge Machine (EDM) using a 0.25 mm diameter brass wire and a 0.05 mm spark gap in a deionised water bath at a distance of 0.2 mm from the base plate. The total 0.5 mm distance was calculated as a support structure into the original LM design in the Magics software which was uploaded to the EOSINT M270X.

For stress relieving, samples were heated up to 300 ^{o}C, soaked at the temperature for 2 hours and slow cooled in the furnace based on the EOS recommendation (EOS, 2011) to reduce thermal stresses incurred during the LM process. However, for the T6 heat treatment in Fig. 4.16, 5 samples of both the as-built and the stress relieved test specimens were subjected to a solution treatment at 530 ^{o}C for 3 hours 30 minutes, then quenched in water to room temperature at 20 ^{o}C. The samples were loaded back into the furnace and allowed to age artificially at 160 ^{o}C for 6 hrs after which they were subsequently allowed to cool to room temperature in the furnace, (Manfredi *et al.*, 2014). The time for aging was reduced due to the size of samples and to prevent over-aging.

Figure 4.16 Furnace Loading heat treatment

The regime of heat treatment, based on the literature review (Das *et al*., 2014a; Rajasekeran *et al*., 2012), was designed with investigations on 4 different parameters namely:

- As-built (AS) – Test specimens cut and taken directly from the build plate before testing.
- As-built and T6 heat treated (AST6) – Test specimens cut and taken directly from the build plate and subjected to the T6 heat treatment before testing.
- Stress relieved (SR) – Test specimens stress relieved on the build plate before cutting for testing.
- Stress relieved and T6 heat treated (SRT6) – Test specimens stress relieved on the build plate before cutting and subjected to the T6 heat treatment before testing.

4.10.2 Transverse Rupture Stress (TRS)

Testing was done according to the BS ISO 14610 (2012) as there is no standard for the transverse rupture of metals or metal matrix composites and the standard for hardmetals was not deemed applicable to the soft and ductile AlSi10Mg matrix despite the introduction of the SiC ceramic reinforcement. Unlike MMCs, hardmetals would be classified as ceramic matrix composites (CMC) and are usually carbides of tantalum, titanium, tungsten, and/or vanadium alloyed with metallic alloys, hence the unsuitability of the standard for this study.

The rectangular samples measuring 70 mm length by 8 mm width by 6 mm height were designed using SolidWorks in Fig. 4.17 ensuring that the long edges of the samples were chamfered at an angle of 45º and 0.1 mm diameter in Fig. 4.18 according to BS ISO 14610 (2012) in order to reduce premature failures arising from the crack initiations caused by stress concentrations along the rectangular edges which are initiation sites for cracks. The final file was translated as an STL file and transferred to the Materialise Magics software where it is loaded on the platform for LM.

The 4-point flexure test jig was assembled on a calibrated Zwick/Roell Universal Testing Machine with the loading roller centrally positioned between the support rollers. Before the commencement of testing, each test sample was measured using Vernier callipers and dimensions recorded. Test samples were then placed on the supporting fixtures with an outer span of 60 mm, the crosshead lowered and situated on the test samples with an inner span of 30 mm. Tests were conducted using a crosshead speed of 0.5 mm/min with an incremental

load of 0.25 KN/s with tests conducted until failure occurs or the loading fixture stops or the exerted force reaches 20 KN to prevent any damage to the equipment.

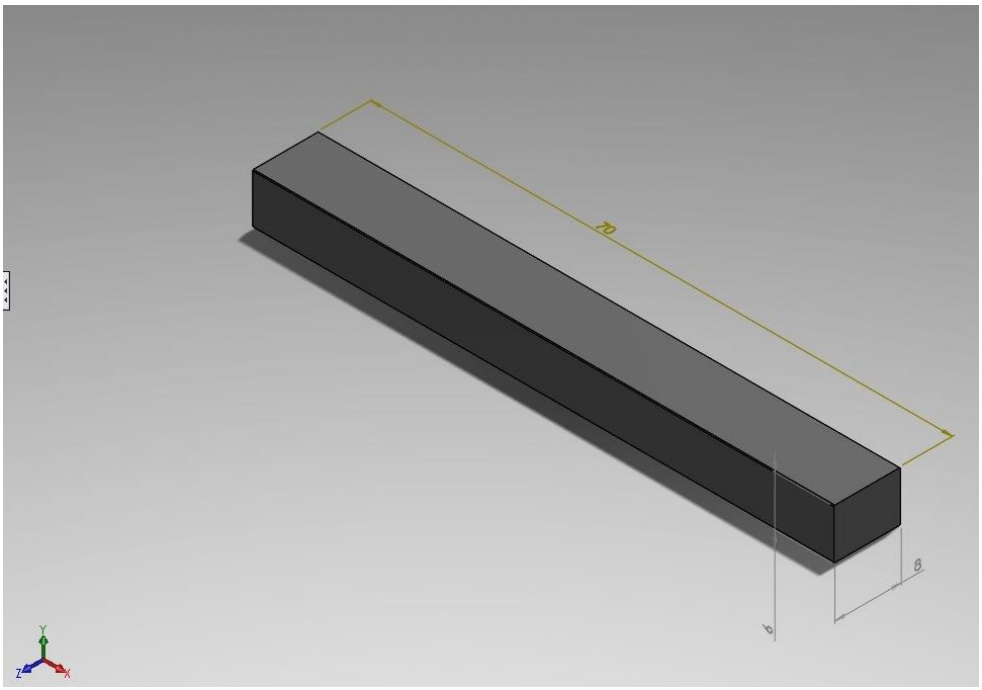

Figure 4.17 SolidWorks design of TRS Samples

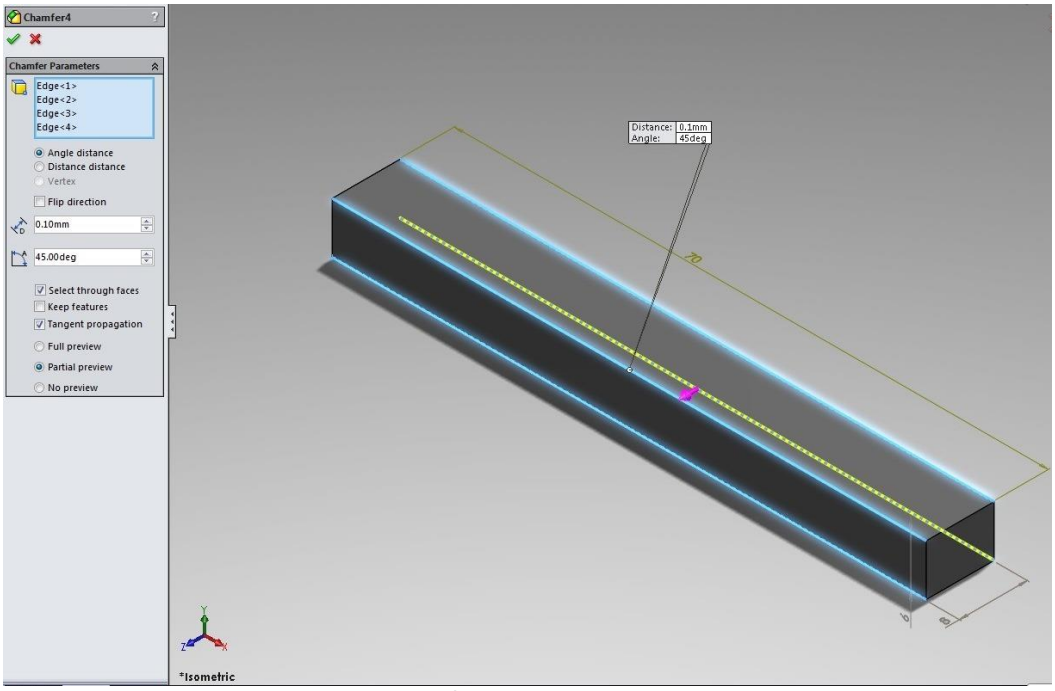

Figure 4.18 Edges chamfered according to BS ISO 14610 (2012)

The flexural strength is then calculated using Equation 4.7, and the results of five sample tests were recorded along with the mean value and the standard deviation for the five tests.

$$\sigma_f = \frac{3\,P\,(L-l)}{2bd^2}$$

Equation 4.7 **(BS ISO 14610, 2012)**

Where σ_f is the four-point flexural strength (MPa)

P is the maximum load up to rupture of the test (N)

l is the distance between internal support points (mm)

L is the distance between external support points (mm)

b is the width of the test piece (mm)

d is the thickness of the test piece (mm)

4.10.3 Micro-Hardness Testing

After the transverse rupture testing investigations had been completed, samples from each specimen were polished following the metallographic preparation in section 4.8.1 to ensure a completely flat surface. Micro-hardness is measured using the Zwick-Roell ZHVμ Micro Vickers Testing Equipment with a 0.01 kg load ($HV_{0.01}$). The samples were tested according to ISO 6507-1 (2005) with a minimum of ten hardness indentations (Fig. 4.19) and an average value of both diagonals of the pyramids taken. The mean values of the readings were recorded as the hardness value for each sample.

Research has shown that for metallic alloys the yield and tensile strength of the samples can be predicted using the Equation 4.5 (Tiryakioglu *et al.,* 2015). This method was however not utilised as the flexural strength was utilised in predicting the tensile behaviour of the composite.

Vickers Hardness (HV) ~ 0.3 × Ultimate Tensile Stress (in MPa) Equation 4.5

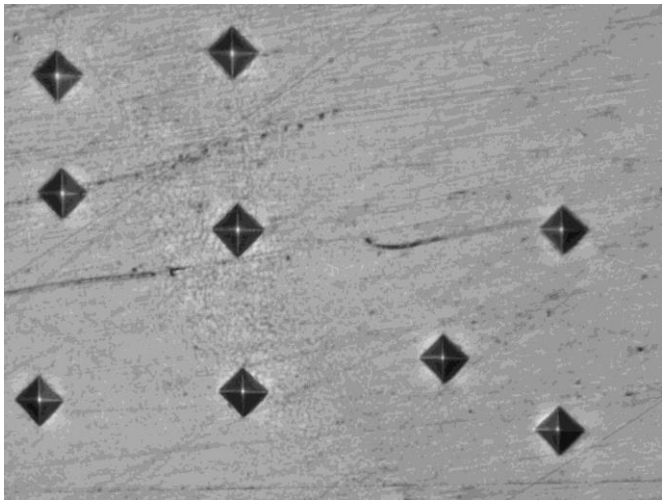

Figure 4.19 Micro-hardness measurement on samples.

4.10.4 Laser Melting Microstructural Observations.

Optical microscopy was used for the metallographic study of the samples and cross-sections of the samples after the TRS testing. Samples for each heat treatment regime utilised for microstructural analysis were polished as per the polishing regime in section 4.8.1 and subsequently etched in Keller's reagent. The grain structures of each specimen regime was observed and analysed to determine the effect of the heat treatment regimen using an optical and scanning electron microscope (SEM).

The fracture surfaces of the samples from the TRS testing were carefully preserved to prevent damage to the surfaces for observation in the SEM.

4.10.4.1 Crystallographic Structure of Samples

Microstructural analysis including grain morphology and size were determined using the laser imaging on the optical microscope. Particles were measured using the SEM in different positions to ensure a wide range of sampling. The SEM analysis utilising both the secondary emissions and back-scattered electron (BSE) imagery on the Carl Zeiss Evo 50 were conducted at different magnifications of 5000, 10000 and 20000. Finally, the chemical composition of each sample was determined using energy dispersive x-ray spectroscopy (EDS) and XRD to investigate the effect of the volume reinforcement and heat treatment on material microstructure. The existence of secondary phases like Mg_2Si which is triggered by the recrystallization of Al-Si-Mg alloys (Taylor, 2012), was also investigated using the XRD technique and the crystallographic structure and orientation of each phase was determined.

4.10.4.2 Investigation of Fracture Surfaces

Fractures are defined as a failure mode in which a material ruptures due to the propagation of a crack when stress is applied to the material at temperatures below the melting point. Fractures are classified into either ductile or brittle fractures with ductile fracture characterised by plastic deformation and necking where the crack will not propagate further unless the applied stress in increased. Brittle fracture however propagates rapidly without any increase in stress or plastic deformation, Kalpakjian and Schmid (2006).

The SEM was used to examine the fracture surfaces of the TRS samples to investigate the formation of voids, metallurgical inclusions, cleavage cracks which aid in crack propagation. The effect of microstructure and crystallography from the heat treatment procedure on the formation, size and morphology of the cracks were also investigated to offer an insight into the ductility and yield properties of the samples.

Fracture samples from each lot (matrix alloy, 5% and 10% reinforced composite) and heat treatment regime were sectioned to about 2 cm high from the TRS samples using a hacksaw, taking care to preserve the fracture surfaces from contamination. Samples were affixed unto sticky carbon pads to prevent movement which causes error during the electron transmission and measurements in the SEM. Samples were loaded into the SEM with the edge where the tensional forces were applied aligned upwards as the fractural cracks were initiated along this edge and the edge with compressional forces aligned downwards. Samples were viewed at different magnifications – 100 X, 500 X, 5000 X (5 KX) and 20000 X (20 KX) to map the fracture surfaces where fracture dimples were observed and measured at 20 KX. The size of the dimples was used to analyse and estimate the ductility or brittleness of the samples**.**

4.11 Chapter Summary

This chapter showed the research divided into five phases as detailed in Fig. 4.1 and also explores the methodology and equipment utilised during the course of the research. This includes the composite powder preparation, development and characterisation in Phases 1 and 2, through the use of the ZOZ Simoloyer for mechanical alloying of individual powders, the SEM and Mastersizer for monitoring the homogeneity, morphology and powder size distribution respectively of the composite powder. XRD was also used to characterise the composite powder obtained to verify no chemical reactions occurred during the MA process. The aim was to obtain a suitable feedstock composite material; with a homogeneously reinforced Al matrix while retaining its spherical and smooth morphology, for the LM process.

LM parameters based on the Eosint M270 Extended were initially investigated through the observation of the single line tracks in the SEM in Phase 3 with an aim to determine the laser interaction of the composite powder at differing scan speeds. Furthermore, density blocks were fabricated in Phase 4 to investigate the surface roughness using the confocal microscope, relative density using the precision balance and internal porosity of the

composite blocks using the SEM. This was done with a view to obtaining a set of parameters more suitable to achieve near full densities in the Al-MMC blocks.

Lastly, in Phase 5, the heat treatment regime using a laboratory furnace and subsequent mechanical testing of the transverse rupture strength on the universal testing machine and micro-hardness on a Zwick-Roell micro-hardness machine were investigated. The SEM was also utilised in investigating the microstructure and fracture surfaces of the samples while the XRD was utilised in detecting the phases changes during the heat treatment regimes.

Chapter 5

Phase 1 and 2

Mechanical Alloying of Al-alloy and SiC powders.

5.1 Introduction

This chapter details the results from the microstructural evaluation of the powder blends obtained from the mechanical alloying activities. This is discussed below with regards to Phase 1 and Phase 2 of the research.

5.2 Alloying Parameters and Microstructural Evaluation – Phase 1 and Phase 2

5.2.1 Phase 1 – Mechanically Alloyed Blend

The results from the mechanical alloying parameters in Table 4.2 are discussed with relation to Figs. 5.1 and 5.3 which show the sample morphology. In Fig. 3.1, the Al-alloy matrix particles are observed to be dark grey, smooth and spherical which is regarded as the suitable morphology for the LM process, Sustarsic *et al.* (2014).

Milling the powder sample A1 at 1200 rev/min for 5 minutes in Fig. 5.1a displays a dramatic increase in particulate growth with significant SiC embedded in the Al-matrix. As Al-alloys are soft and ductile, agglomeration is aggressive and extensive when the material is in its powder form, thus at high speeds the tendency to agglomerate increases due to the rapid cold-working of the powder particles resulting from the continuous collisions with both the milling balls and other particles within the milling chamber.

With further milling, the agglomerated composite powder embedded with SiC will disintegrate into smaller particles (El-Eskandarany, 1998) however, as the LM process requires a spheroidal morphology, the fracturing and re-agglomeration stages were prevented by reducing the milling time. Thus, the MA process time was monitored and concluded before the fracturing stage of the process after the initial agglomeration. Observations in Fig. 5.1 show that despite the shortened milling time, the composite particles at this point in the MA process lost most of their spherical shape. They had a rough surface finish and were irregular and nodular in morphology and appearance. The white particles were identified through EDS as Tungsten Carbide contamination. This contamination was from the attrition

milling in the Fritsch Pulverisette 5 and abrasion of the tungsten carbide vessels and grinding balls during the milling go the SiC reinforcement. This operation was needed to break down the SiC from 30 µm to 10 µm prior to alloying. The EDS trace is shown in Fig. 5.2 confirming the tungsten contamination.

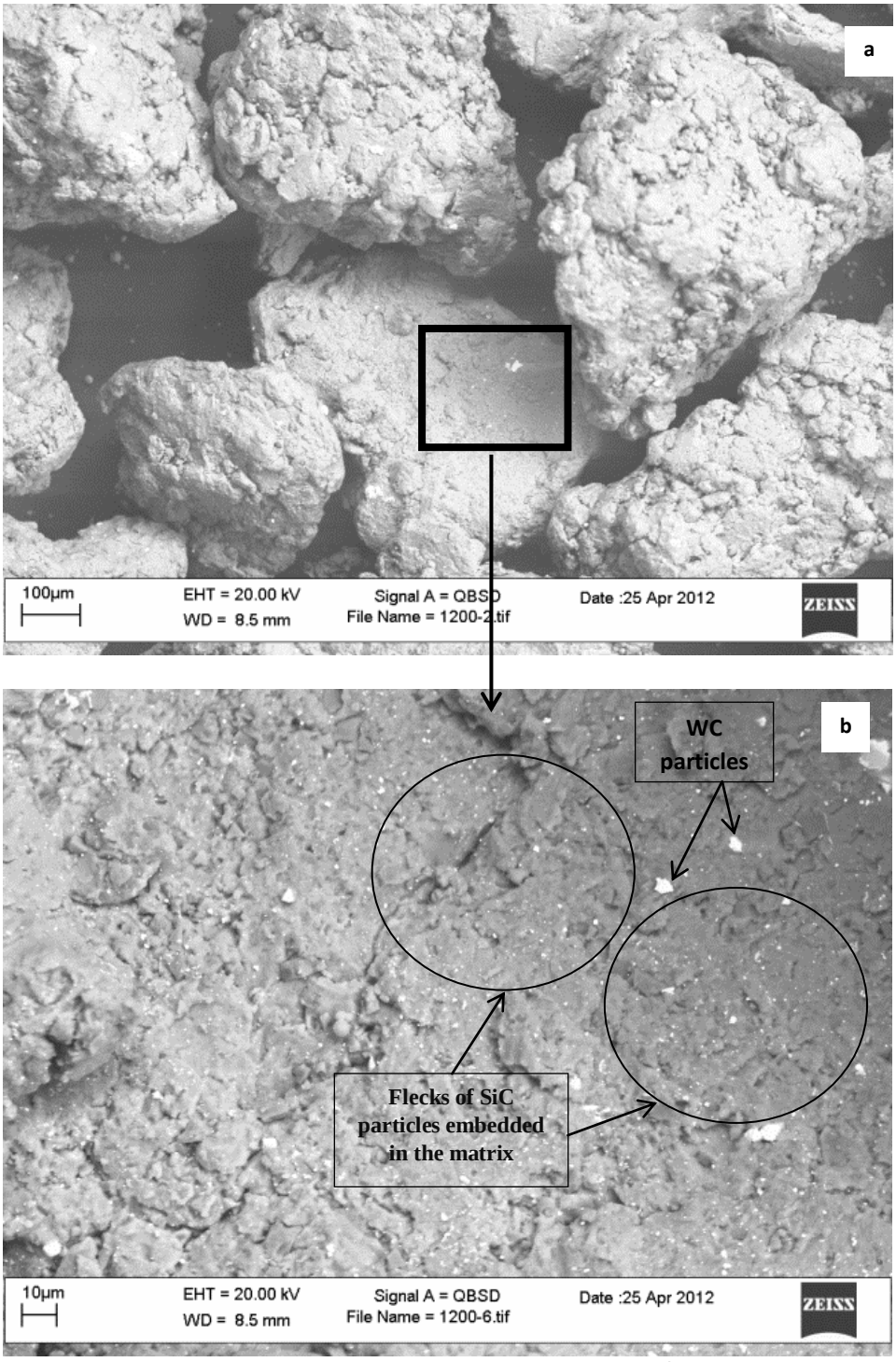

Fig. 5.1 Sample A1 - Alloyed AlSi10Mg with SiC (a) At 1200 rev/min for 5 mins - mag 1000 X (b) At 1200 rev/min for 5 mins - Sample A1 mag 5000 X

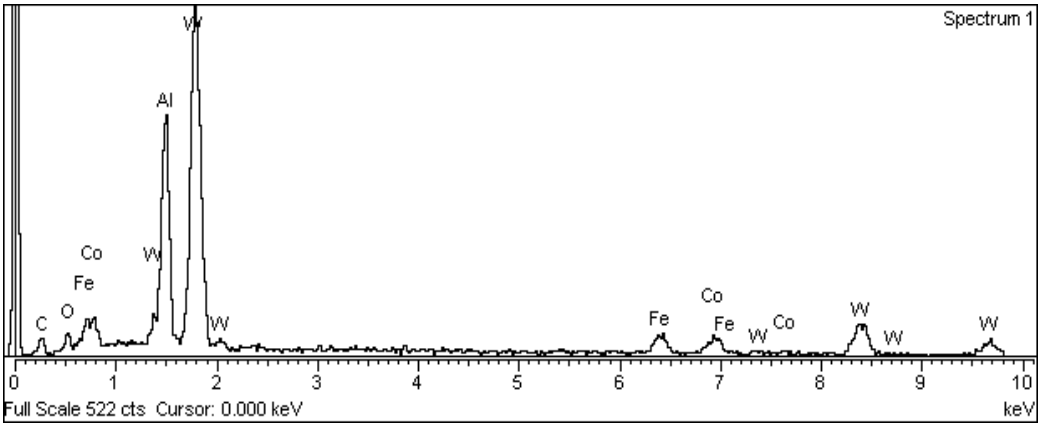

Figure 5.2 EDS results of the white particle embedded in the composite powder

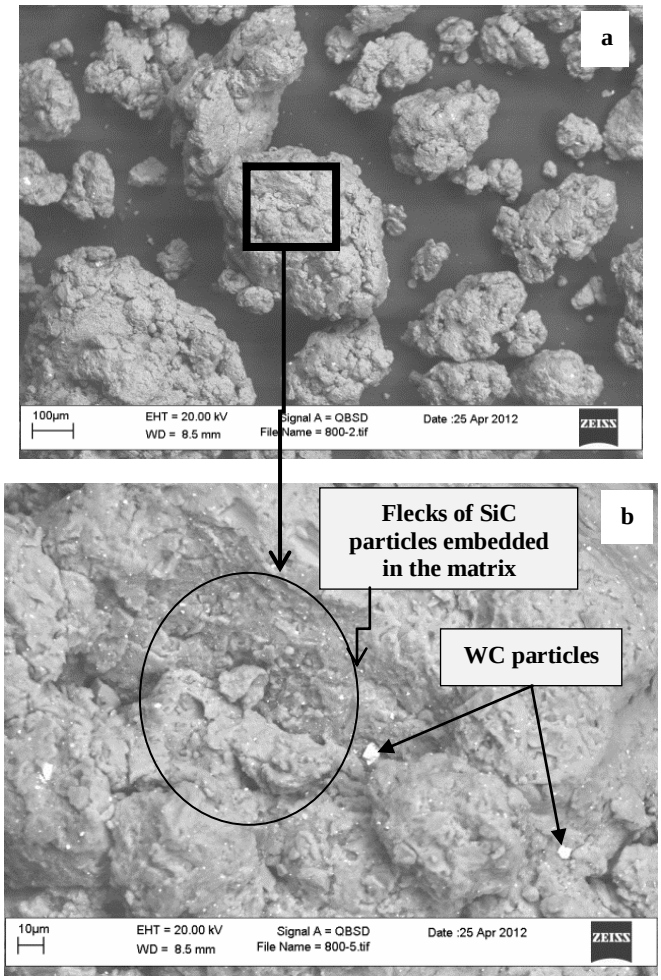

Figure 5.3 Alloyed AlSi10Mg with SiC (a) 800 rev/min for 10 mins -Sample A2 mag 1000 X (b) 800 rev/min for 10 mins - Sample A2 mag 5000 X

Due to the change in morphology of milled sample A1 from that of the base alloy, another set of parameters were investigated for Sample A2; milled at a slower speed of 800 rev/min for 10 minutes. Fig. 5.3 shows that despite the change in parameters there was still an increase in particulate size observed in Fig. 5.3a albeit the particulate size was smaller than in sample

A1. Figs. 5.1b and 5.3b confirmed that the MA process was embedding the reinforcement in the alloy matrix and more aggressive alloying parameter emphasised this. Hence there is more alloying in sample in 5.1b than in 5.3b images. The morphology of the composite particles was significantly altered after alloying for both samples A1 and A2, deviating from the Al matrix's smooth surface and spherical shape prior to mechanical alloying. The increase in particulate size is a disadvantage as the larger particles would be removed during the 63 µm sieving operation prior to use in the EOSINT M-270 LM machine. Other than losing a large amount of the composite powder there is the added disadvantage of poor recoating during the LM process. WC from the milled SiC samples was discovered as a contaminant in both composites albeit in small quantities and as a precaution against further WC contamination, a new batch of SiC particles (approximately 1 µm or below in size) was purchased analysed and used for the rest of the research.

5.2.2 Phase 2 -Mechanically Alloyed Blend

Due to the results from phase 1 of the research, further investigations at much slower speeds and shorter time intervals were considered. Tests were undertaken with speeds at 350 rev/min to 550 rev/min in 5 min to 20 min duration. Particle morphology were viewed with the SEM and no evidence of embedding or agglomeration was observed between 5 min and 10 min therefore only the results from the 15 – 20 min tests are reported.

In figure 5.4 Sample B1 ($AlSi10Mg/SiC_p$) was alloyed at 350 rev/min for 15 mins but little change in morphology of the Al-alloy was observed (Fig. 5.4 inset) except for a few agglomerated particles with the SiC broken down without being reinforced into the alloy. This can be attributed to there being insufficient energy from the colliding balls to effect any change in the morphology and size of the particles. To minimise the amount of powder to be sieved out at 63 µm for the LM phase, the large particles were measured as an indication of particle growth to be monitored. The average particle size for this speed was 56.43 µm.

In Fig. 5.5, Sample B2 shows signs of alloying at the same speed, as the morphology has changed with particles being slightly deformed into oval shapes rather than the original spherical shape. A few SiC particles were visibly embedded in the Al particles (observed in the inset) which suggests inhomogeneity of the reinforcement. The change in morphology suggests that with increased time (20 mins) milling at this speed has initiated reinforcement

but an increase in the chance of contamination is higher due to the prolonged time for homogeneity to be achieved.

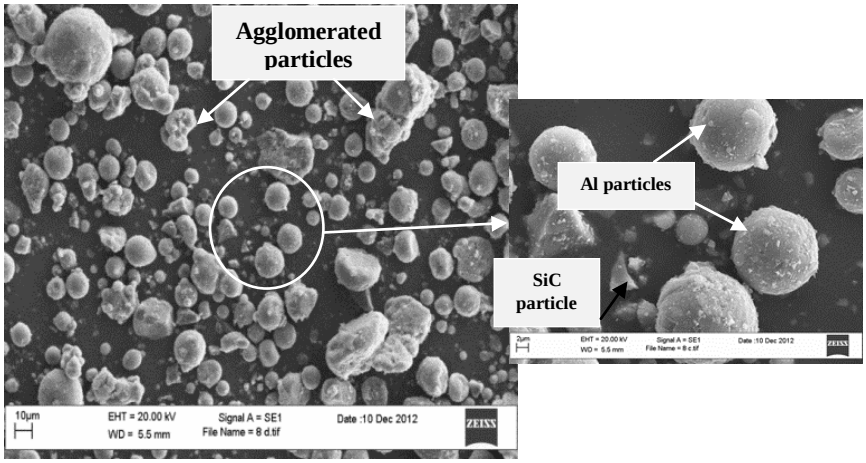

Figure 5.4 Sample B1 milled at 350 rev/min for 15mins at 1000 X (Inset – 2000 X)

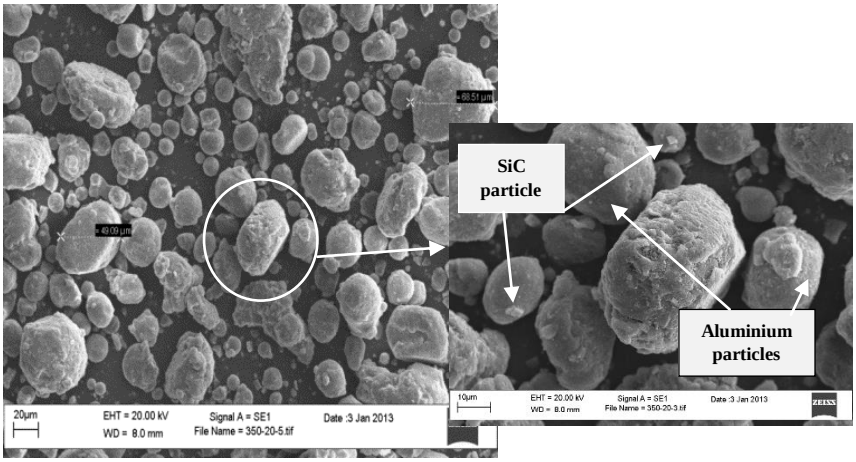

Figure 5.5 Sample B2 milled at 350 rev/min for 20mins at 1000 X (Inset – 2000 X)

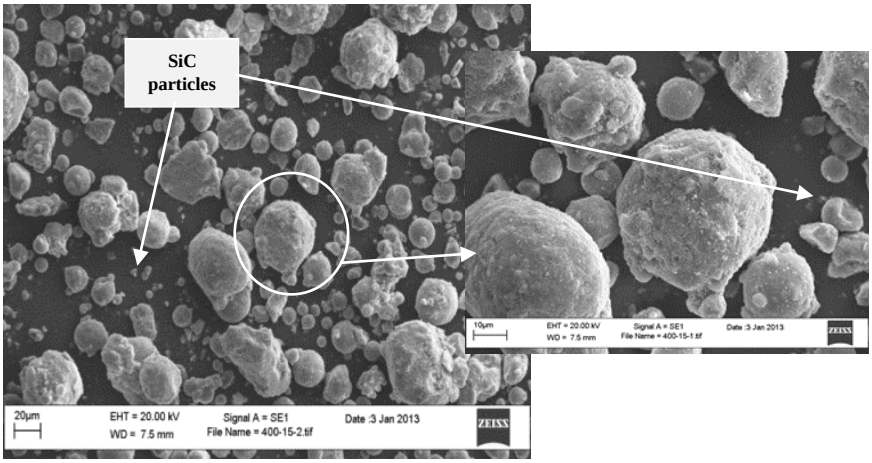

Figure 5.6 Sample B3 milled at 400 rev/min for 15mins at 1000 X (Inset – 2000 X)

Sample B3 in Fig. 5.6 alloyed at 400 rev/min for 15 mins, showed a progression in alloying as more particles show signs of deformation and had more SiC embedded. Alloying of the reinforcement was not homogeneous although more particles are embedded on the surface of the Al particles (Fig. 5.6 inset). Small localised Sic particles can be observed in the background of the Fig. 5.6. Alloying at this speed for 20 min in Fig. 5.7 showed the onset of an agglomeration phase (Fig. 5.7 inset) for the particles unlike normal MA practices. Previous research by Suryanarayana (2001) and Lu and Lai (2013) describes the initial phase in the MA process as a micro-forging process where the particles get flattened. However, in Fig 5.7, the smaller particles are observed to be agglomerated to the large particles suggesting a ductile-ductile system. Particles of sample B4 were still mostly spherical but only a fraction of the SiC particles were embedded in the Al-alloy matrix. The number of fine particles also appear reduced thereby confirming the initiation of the agglomeration phase.

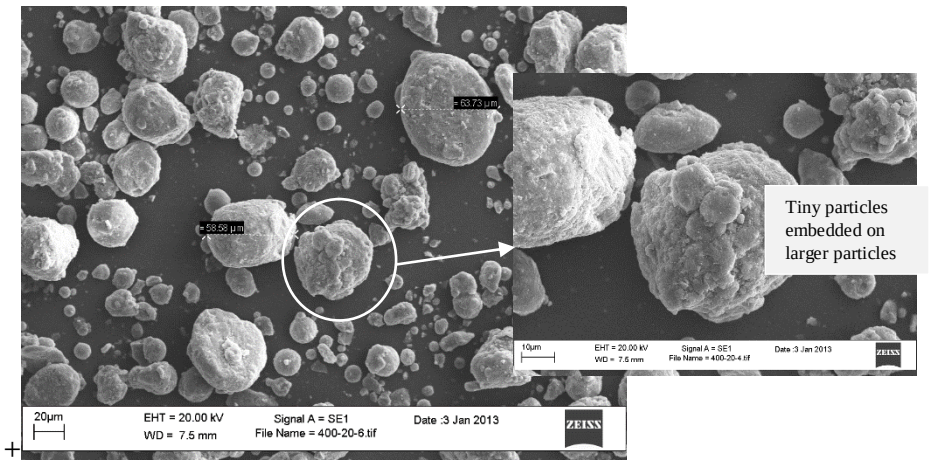

Figure 5.7 Sample B4 milled at 400 rev/min for 20mins at 1000 X (Inset – 2000 X)

In Fig. 5.8 sample B5, which was alloyed at 450 rev/min for 15 mins showed the commencement of the initial stage for the MA process. Deformation of some particles into nodular particles can be observed. SiC particles (white flecks) were seen to be embedded into the Al matrix (grey particles) albeit not homogeneously in the backscattered image (Fig. 5.8 inset). The initial MA stage progresses in Fig. 5.9 where sample B6 was alloyed at 450 rev/min for 20 mins. Additional particles were observed to be nodular and irregular rather than the original spherical shape although the average particle size for the large particles was still within the range for the LM process at 57.91 µm. This was attributed to the micro-forging dominating this stage of the process. Due to the changed morphology of the particles and the residual unalloyed SiC, further alloying was done to obtain optimum feed material for the LM process.

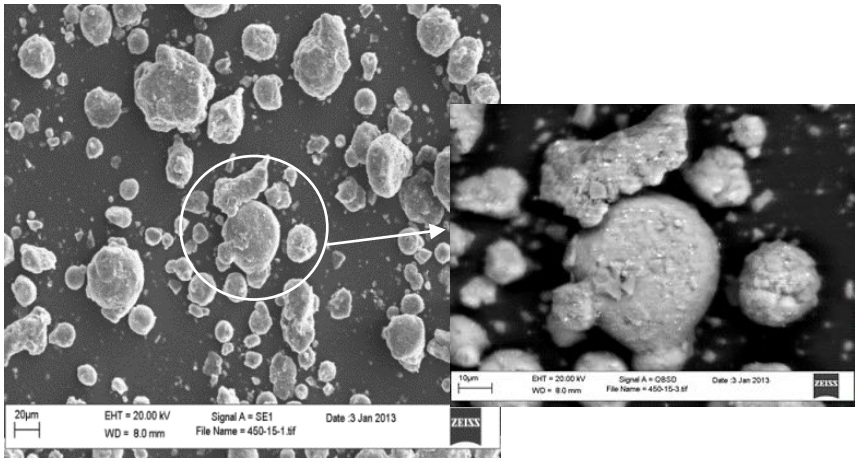

Figure 5.8 Sample B5 milled at 450 rev/min for 15mins at 1000 X (Inset – Backscattered Image at 2000 X)

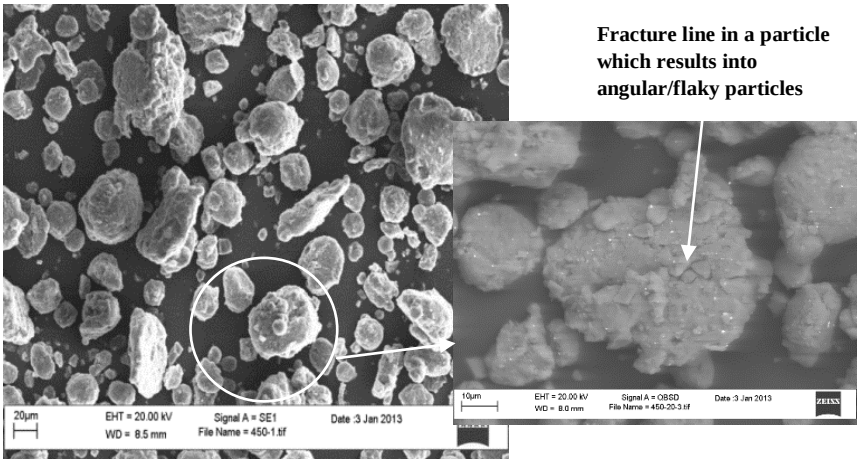

Figure 5.9 Sample B6 milled at 450 rev/min for 20mins at 1000 X Inset – Backscattered Image at 2000 X)

In Fig. 5.10, sample B7 alloyed at 500 rev/min for 15 mins, showed a further stage in the MA process. Re-agglomeration after the initial fracturing has resulted in globular powder morphology albeit with some irregular particles visible. Fracturing must have occurred earlier due to the higher milling speed as this directly affects the speed of the grinding balls. Unfortunately, the particles are too angular for smooth and uniform distribution in the LM machine. The SiC was observed to be homogeneously embedded into the matrix with minimal residual SiC particles not reinforced into the matrix, here the average maximum particle size was 41.8 µm. Sample B8 in Fig. 5.11 which had been alloyed for 500 rev/min for 20 mins, shows the fully homogeneously reinforced composite with the morphology sufficiently spherical and globular for a smooth and uniform spread during the LM recoating process. The image in Fig. 5.11 suggests that agglomeration of the fractured particles had taken place thereby changing the morphology of the particles again. An increase in particle

size was minimised at 55.9 µm when compared to earlier alloying at 800 rev/min and 1200 rev/min, which saw a rapid increase in the particle size at short alloying times.

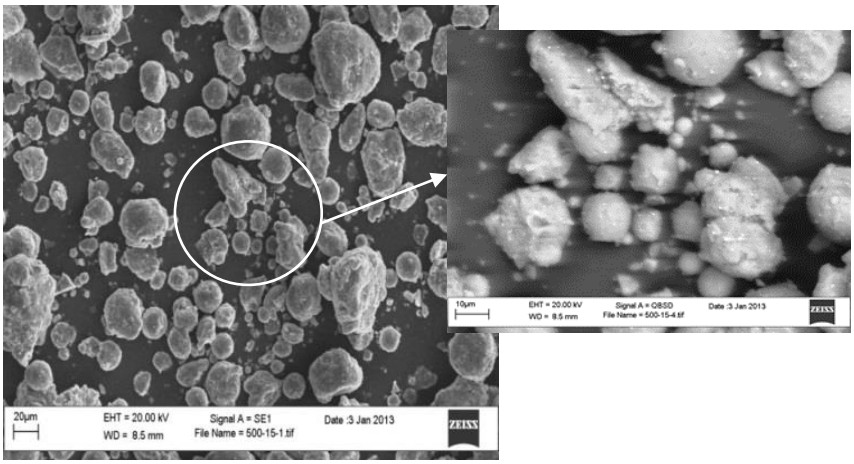

Figure 5.10 Sample B7 milled at 500 rev/min for 15mins at 1000 X (Inset – 2000 X)

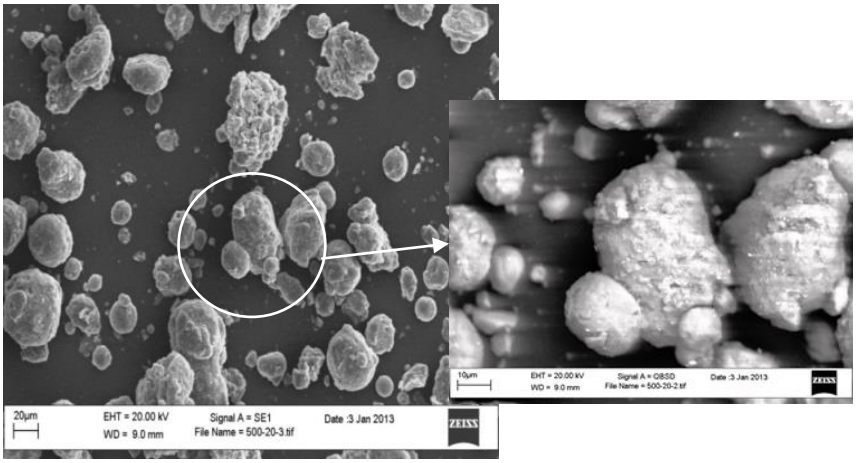

Figure 5.11 Sample B8 milled at 500 rev/min for 20mins at 1000 X (Inset – 2000 X)

To verify the accuracy of the alloying at 500 rev/ min at 20 mins as an optimum, Sample B9 was alloyed at 550 rev/min for 15 mins and is shown in Fig. 5.12, the particles were observed to be flaky and angular with a rapid increase in particle size (73.65) µm, due to the initiation of another round of cold welding and agglomeration together with evidence of homogeneous reinforcement. The increase in size and severe change in shape, renders Sample B9 unsuitable for the LM process, as a significant portion of the powder would be sieved out and the angular particles would prevent a uniform spread of the powder layer during recoating. Due to the rate of deformation observed at 15 mins at the 550 rev/min speed, further continuance until 20 mins was deemed unnecessary.

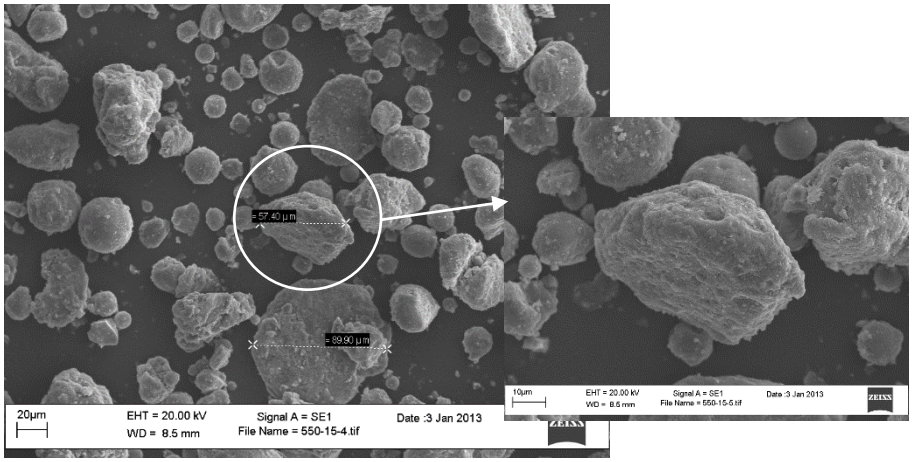

Figure 5.12 Sample B9 milled at 550 rev/min for 15mins at 1000 X (Inset – 2000 X)

Fig. 5.13 both shows the maximum particle size achieved when the speed and time of milling was varied. Initial fracturing of the particles and a subsequent agglomeration was observed as particles were observed to be lower in particle size after 15 mins than after 20 mins. Table 5.1 describes an overview of the MA process, results of the particle morphology, rate of reinforcement homogeneity and average particle sizes.

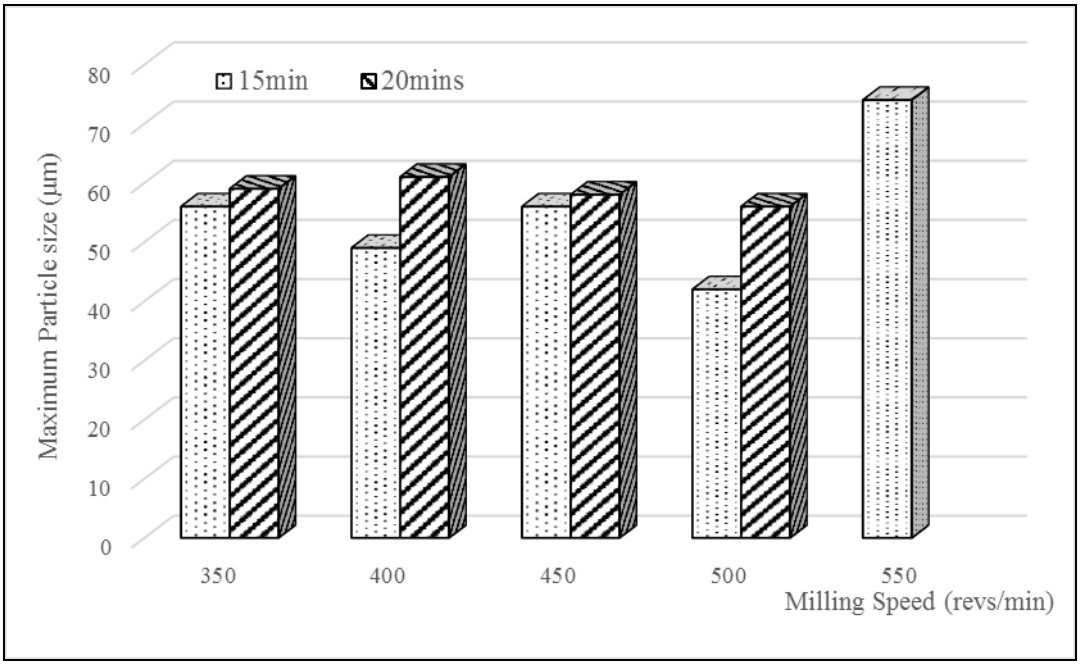

Figure 5.13 Maximum particle size achieved with milling speed during MA

Table 5.1 Summary of MA observations

Speed-Time (revs-min)	Morphology	Homogeneously reinforced/blended	Maximum Particle Size (µm)
350-15	No Change Observed	SiC seen mixed with the Al-matrix	56.43
350-20	No change observed	SiC seen mixed with the Al-matrix	58.80
400-15	Commencement of agglomeration	commencement of SiC embedding	48.71
400-20	Mostly spherical, however agglomeration phase prominent	Partial embedding of SiC	61.16
450-15	Distribution of angular, nodular and spherical shaped particles	Partial embedding of SiC	55.83
450-20	Particles shape is mostly nodular and irregular	Moderate embedding of SiC	57.91
500-15	Particles are angular as a result of cold welding brittleness	SiC homogeneously embedded	41.80
500-20	Spherical shape and globular particles observed	SiC homogeneously embedded	55.90
550-15	Most particles are flaky with negligible spherical particles in the blend	SiC homogeneously embedded	73.65

5.2.3 Mixed Blend without Grinding Media

In Fig. 5.14, the powder sample was mixed in the ZOZ-Simoloyer CM01 without any grinding media and was assessed for SiC homogeneity and morphology. It shows an overview of the powder samples with the particles retaining their spherical shape and smooth morphology while the inset shows the 2000x magnification of a single particle with negligible SiC particles visible on the surface of the matrix. Energy Dispersive X-Ray Spectroscopy (EDS) analysis of the sample also confirmed that the SiC particles are not homogeneously dispersed in the feed material. A few particles of SiC seem alloyed into the Al alloy; however most seem clustered together.

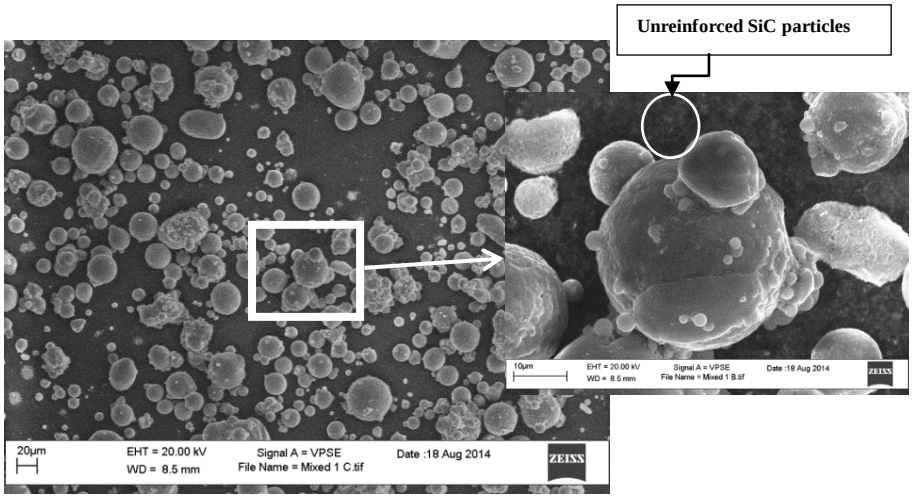

Figure 5.14 Mixed Blend Composite Broad overview of the material at 1000x (Inset at 2000 X Mag)

By comparing the results from Fig. 5.11 - sample 8 and Fig. 5.11 - mixed sample, a significant difference is observed in the reinforcement homogeneity, shape, morphology and size of the composite particles. The SiC particles in Fig. 5.12 show a tendency to embed into the surface of the Al particles when compared to the sample that was only mixed, albeit with more agglomerated and flaky particles than with the mixed spherical particles. This change in morphology was attributed to the mechano-physical action caused by the addition of the grinding balls into the attrition chamber of the ZOZ-Simoloyer CM01 otherwise absent in the mixed blend. The inhomogeneity of the mixed blend therefore eliminates it as a source of feed stock for the LM phase of the project.

5.3 Particle Size Distribution

The particle size distribution defines the relative amount of particles present and their proportions in a sample up to 100 % generally measured in volume in a cumulative distribution. To accurately determine if the particle sizes of the composite particles have not deviated from that of the matrix alloy, powder samples were subjected to a further particle size distribution analysis using the laser diffraction method explained in section 4.5.2. The results given in Table 5.2 will also aid in determining the presence of clusters (agglomerated particles) by showing a large increase in the amount of large particles while reducing the amount of fine particles. Previous researches (Liu, *et al.*, 1994; Liu, *et al.*, 2011; Lu and Lai, 1998) reported that the distribution of the reinforcement particles influences the porosity and mechanical properties of the final component therefore emphasizing the importance of having a suitable particle size distribution (20 -45 µm) in the LM chamber. Due to the layering process, a distribution of fine particles (Fig.5.15b) is required to fill the gaps between the large particles (Fig.5.15a) which ensures that porosity from those gaps are avoided.

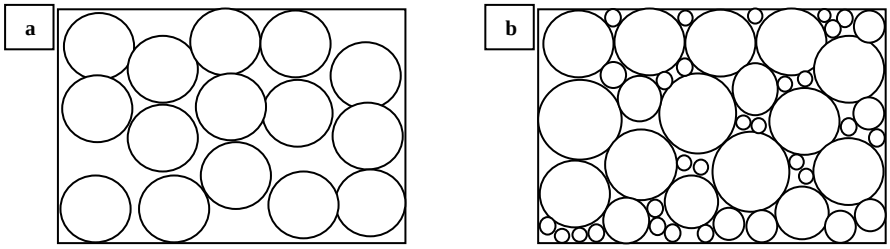

Figure 5.15 Importance of particle size distribution in layering a) Distribution with only large particles b) Distribution with both large and fine particles

Fig. 5.16 shows Gaussian profiles obtained for the sample while Fig. 5.17 displays the histogram of the results, which shows the wide particle distribution apparent through the 3 percentiles at P_{10}, P_{50} and P_{90}. The particle distribution variation for the mixed sample was less than 10% each for all percentiles and this supports the conclusion from section 5.2.3 that the SiC has not been fully homogenised. An increase in the amount of large particles is observed for the alloyed composites with the initial 1-10 µm particulate size having a higher size distribution. An increase in the fine particles (below 1 µm) was also observed for the 10 µm reinforced MMC also supporting the decision to source for a cleaner and smaller particulate size of reinforcement. The amount of fine particles available for the composite powder should be sufficient to obtain a close packing density, which will also aid the flowability of the powder during layering for the LM process.

The standard variation values of the alloyed 1 µm reinforced composite in Table 5.2 demonstrates that despite the larger particle sizes and lower fines, it is still within a standard deviation of the mean particle distribution of the matrix. This indicates that during the LM process, the same layer thickness can be utilised for both the matrix and the 1 µm composite blend taking into consideration that the particle shape and morphology remain smooth and spherical.

Table 5.2 Particle size distribution of powder samples

Percentile measured in Equivalent diameter (µm)	Matrix alloy (AlSi10Mg)	Composite Mixed [AlSi10Mg + SiCp (1µm)]	Composite Alloyed [(AlSi10Mg + SiCp (1µm)]	Composite Alloyed [(AlSi10Mg + SiCp (10µm)]	Mean	Variance	Standard Deviation
P_{10}	15.90	17.50	9.99	10	13.35	11.56	3.40
P_{50}	36.80	39.80	42.00	42.2	40.2	4.74	2.18
P_{90}	63.60	68.20	76.40	85.3	73.38	68.42	8.27

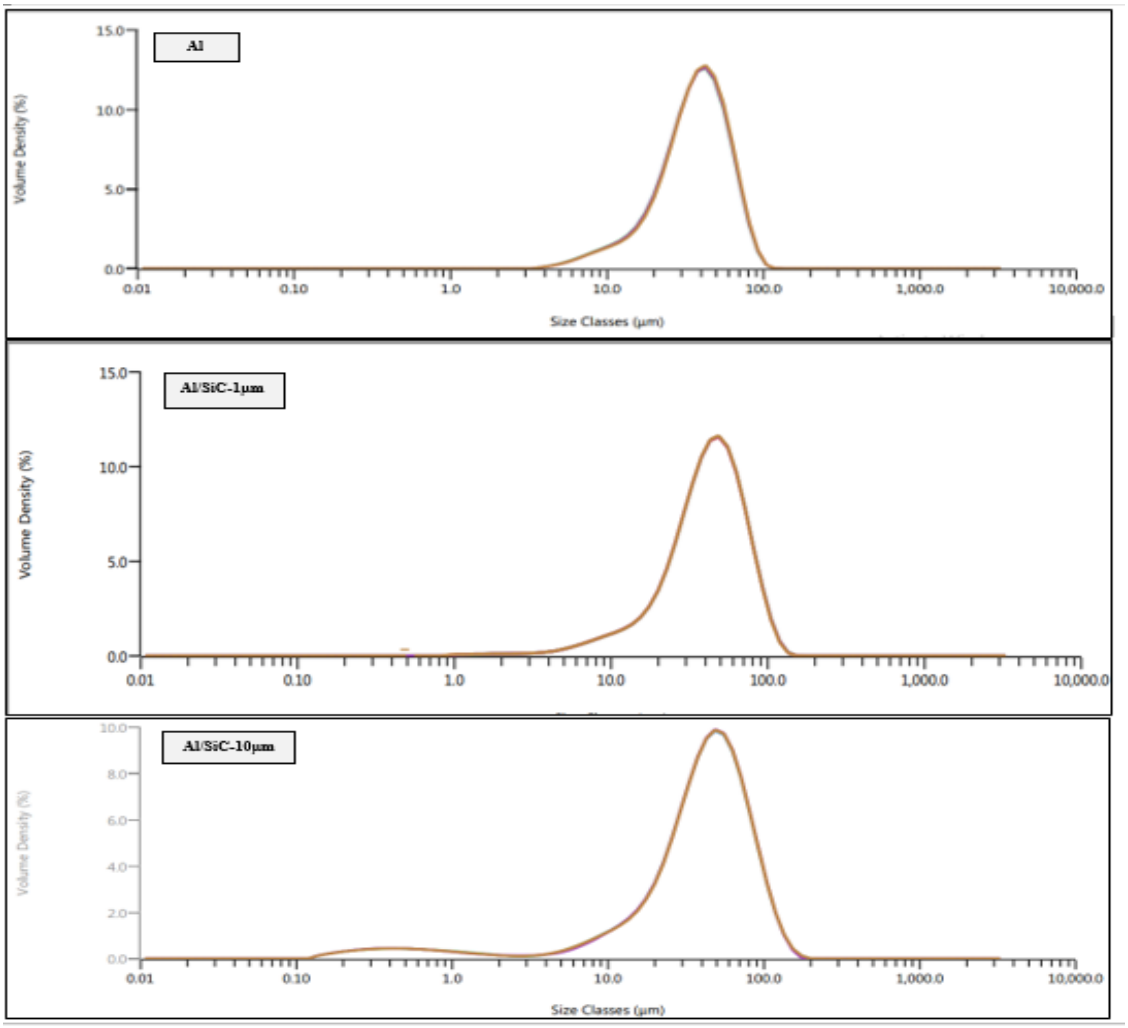

Fig. 5.16 Gaussain Profiles of Particle size distribution

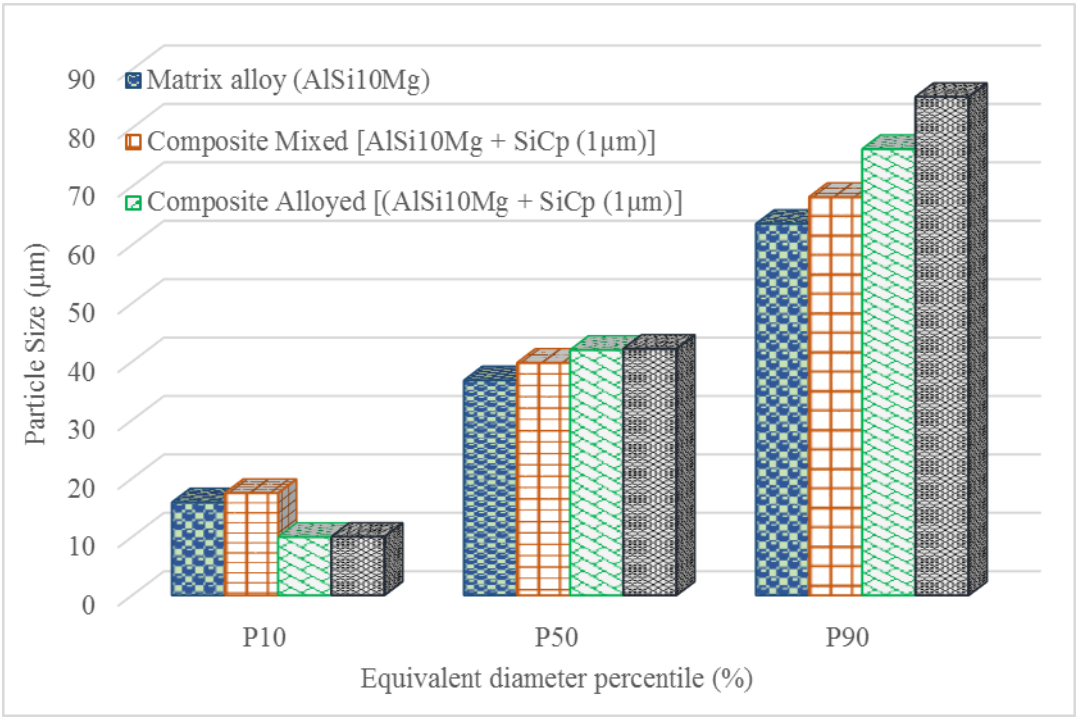

Figure 5.17 Particle size distribution of powders

5.4 X-ray Diffraction Characterisation of Powder Samples.

X-ray Diffraction (XRD) characterisation of the matrix and both alloyed composite was conducted to verify that the structure of the matrix was not compromised during the MA stage. Fig. 5.17, Fig. 5.18 and Fig. 5.19 shows the XRD patterns from the matrix alloy, 5 % reinforced composite and 10 % composite respectively. Four strong diffraction peaks which are characteristic of aluminium (ICDD No. 89-4037) can be observed repeating, while the weaker peaks in Fig. 5.17were identified as Silicon (Manfredi *et al.,* 2013) detected from the elemental X-ray Fluorescence analysis as up to 5.09%.

The 2θ values were used to calculate the lattice spacing for a cubic structure in order to verify the crystalline structure of the materials from Equation 4.2 to Equation 4.4:

$$d_{hkl} = \frac{\lambda}{2Sin\theta} \qquad \text{Equation 5.1}$$

$$d_{hkl} = \frac{a_0}{\sqrt{(h^2+k^2+l^2)}} \qquad \text{Equation 5.2}$$

where λ = X-ray wavelength (nm)
d_{hkl} = Distance between crystal lattice planes (nm)
θ = Diffraction angle (°)
a_o = inter-atomic spacing (nm)

Therefore, combining Equations 5.1 and 5.2

$$d_{hkl} = \frac{\lambda}{2Sin\theta} = \frac{a_0}{\sqrt{h^2+k^2+l^2}} \cong \frac{\lambda^2}{4\,{a_o}^2} = \frac{Sin^2\theta}{h^2+k^2+l^2} \qquad \textit{Equation 5.3}$$

In determining the miller indices of a crystal structure from the XRD peaks and therefore the 2θ values, some parts of Equation 5.3 are regarded as constant; the wavelength of the diffractometer and the atomic spacing for the matrix alloy,

Therefore $\frac{\lambda^2}{4\,{a_o}^2}$ is regarded as negligent.

The 2θ values of the peaks from the XRD data in Fig. 5.17 are given in Table 5.3. Due to destructive interference in the structural planes, a face centred cubic structure like Al will only show intensities when the h, k, l values are either all even or all odd. The basic planes with h, k, l values satisfying the requirement for a FCC structure are (111), (200), (202), (311) and (222) and are listed according to the $h^2 + k^2 + l^2$ values in Table 5.4

Table 5.3 θ values obtained from XRD data analysis

2θ	θ	$Sin^2θ$	Peaks
38.50	19.23	0.11	Peak 1
44.76	22.35	0.14	Peak 2
65.19	32.55	0.29	Peak 3
78.35	39.12	0.40	Peak 4

Table 5.4 hkl values for a FCC structure

(hkl)	$h^2 + k^2 + l^2$	Peaks
(111)	3	Peak 1
(200)	4	Peak 2
(202)	8	Peak 3
(311)	11	Peak 4
(222)	12	Peak 5

In order for the alloy system to meet the FCC crystal for peaks 1 and 2

$$\frac{Sin^2\theta_2}{Sin^2\theta_1} = \frac{h_2{}^2 + k_2{}^2 + l_2{}^2}{h_1{}^2 + k_1{}^2 + l_1{}^2} = \frac{4}{3}$$

Where θ_2 = θ value for second peak

θ_1 = θ value for first peak

Dividing the value of peak 2 by peak 1 in Table 5.3,

$\frac{0.14}{0.11}$ will give a fraction of $\frac{4}{3}$ which satisfies the law for the FCC structure.

Therefore, the peaks in Fig. 5.17 are indexed for the Al alloy based on the FCC structure. In Fig. 5.18 and 5.19, three main peaks were identified for the 5% and 10% reinforced composite powder respectively with the major peaks identified as the Al-alloy, SiC and Si elements.

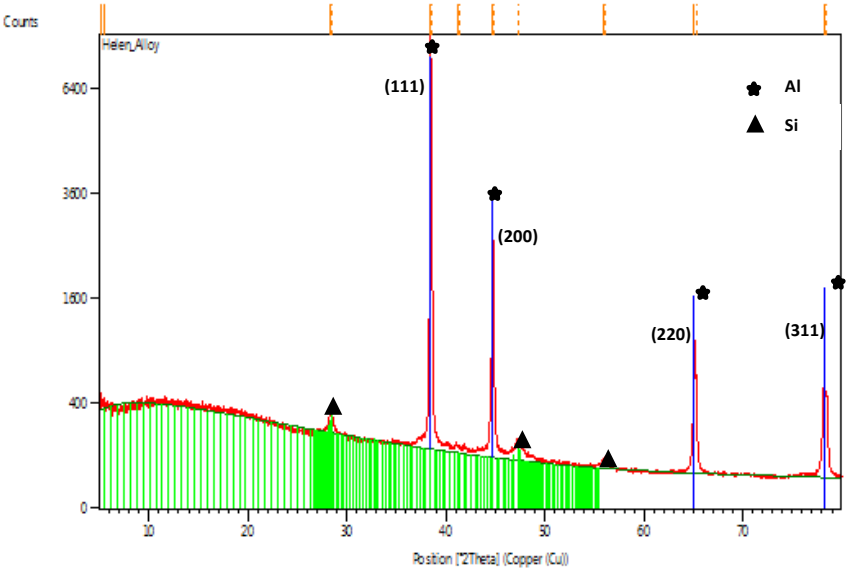

Figure 5.17 XRD pattern for the Matrix alloy

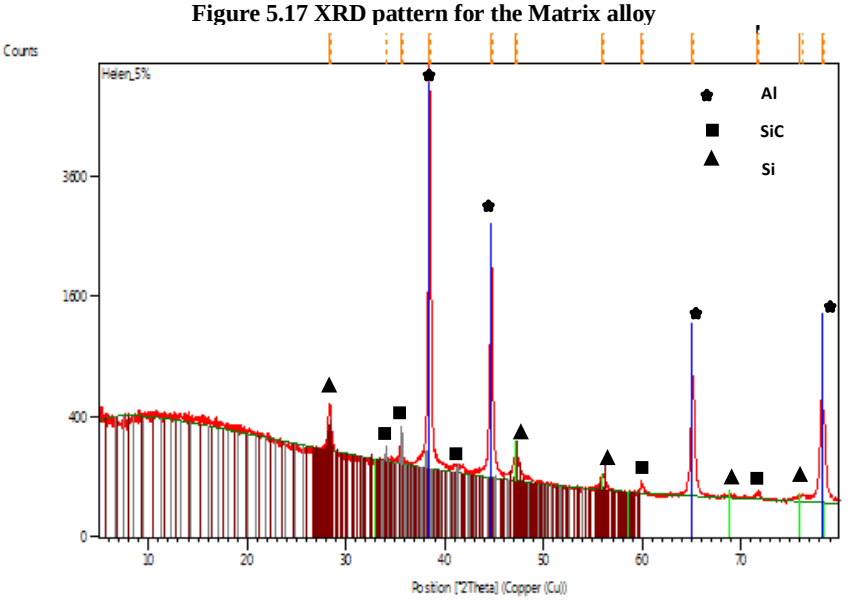

Figure 5.18 XRD for the 5% reinforced MA composite

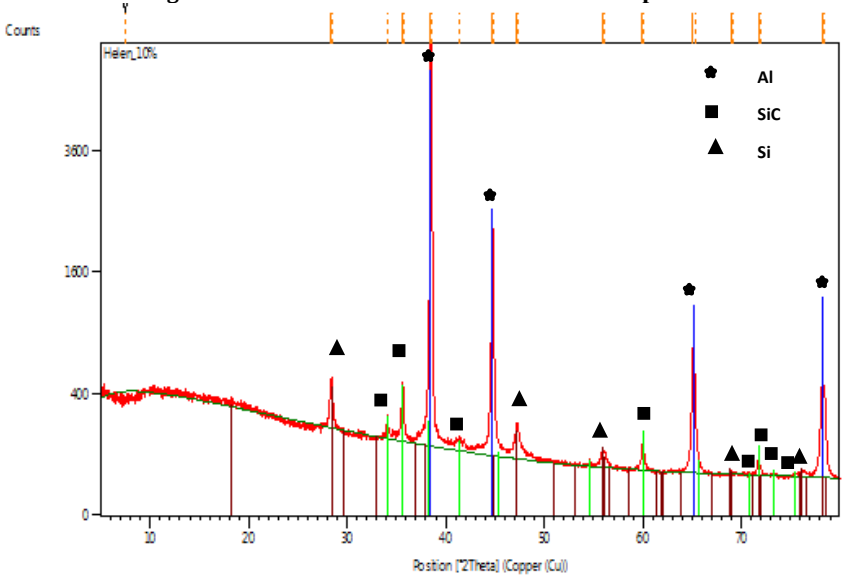

Figure 5.19 XRD for the 10% reinforced MA composite

The intensity of the Si peaks was observed to increase as the percentage reinforcement increases due to the added SiC. As no further chemical compounds were detected by the XRD analysis, it can be assumed that the procedure was used to confirm that no chemical reaction occurred during MA of the composite powder. The peaks for the SiC mapped in the XRD data, were observed to match the 4H polymorph especially in the 10% reinforced composite.

5.5 Chapter Summary

This chapter illustrates the Phase 1 and 2 of the research.

Phase 1 of the research where the individual powders of the Al alloy matrix and SiC reinforcement, were alloyed at 1200 rev/min and 800 rev/min produced composite powder particles which were homogeneously alloyed. However, due to the aggressiveness of the MA process, had resulted into large irregular particles unsuitable for the LM process. This led to investigation at lower rotational speeds for the next phase.

In Phase 2 of the research, speeds between 350 and 550 rev/min with 50 rev/min increments were investigated with samples taken after 15 and 20 mins for observation on homogeneity and morphology of the powder particles in the SEM. The most suitable parameter for producing a fully homogeneous composite and appropriate morphology was obtained at 500 rev/min and 20 mins. XRD confirmed no reactions occurred during the MA process thus strengthening the concept of MA as a reinforcement delivery instrument for the LM process.

Chapter 6

Phase 3 and 4

Laser Melting of the Composite Powder

6.1 Introduction

As previously discussed in Chapter 2, the main concerns for LM of metal matrix composites are density and dimensional accuracy. These factors are influenced predominantly by both the degree of powder homogeneity and behaviour of the composite powder to laser irradiation (Erasenthiran and Beal, 2006). Changes in process parameters has also been established to influence track formation. Previous researches (Song *et al.,* 2012; Zhang *et al.,* 2011; Vilaro *et al.,* 2010) highlighted that modification of the LM process parameters: laser scan speed, step-over and scan strategy, affects the properties of the part either through geometrical irregularity in the sintered track (Niu and Chang, 1999) or the balling effect (Tolochko *et al.*, 2004). Hence, the reproducibility and repeatability of LM of MMCs will be severely impacted, as changes in parameters will occur for each different powder alloy.

Due to the addition of the SiC to the AlSi10Mg matrix, it is therefore paramount to investigate the LM parameters needed for complete melting and solidification of the composite through examining single line tracks and microstructure made by the composite and matrix alloy. The interaction of the composite powder and laser beam in relation to the matrix alloy was studied by initially investigating macrostructures of single line tracks at different scanning speeds and with different reinforcement volumes; Phase 3 of the results with discussions from Section 6.2. The effect of the laser on the scanned tracked was examined by its ability to form continuous tracks with stable and predictable width. The single scan track results are validated in Section 6.3 by building sample blocks and investigating the effect of changing parameters such as scan speed and step-over, on the surface finish (6.3.1) and porosity/ apparent density (6.3.2); Phase 4 of the research. These parameters are particularly known to affect the energy density and the time available for weld pool formation, Kempen *et al.* (2011).

Furthermore, analysis on sample blocks were also carried out using the parameters of the single line tracks. Overall, the characteristics to be investigated during the research are:

1. Single line track characteristics
2. Surface roughness of the top surface transverse and perpendicular to the direction of recoating
3. Porosity and Relative density measured using image analysis and Archimedes principle respectively
4. Microstructural aspects of the composite through change in the scanning speeds
5. Mechanical properties of the composite through transverse rupture testing, heat treatment and microhardness.

6.2 Phase 3 - Single Track Formation

6.2.1 Single Track Formation of the Matrix Alloy – AlSi10Mg

Scan tracks were created on the build plate with the process parameters listed in section 4.6.2 - Table 4.5, while the laser at 800 mm/s as recommended by EOS-GmbH scanned the matrix alloy. This created a weld pool in the powder, which upon solidification gave a fully melted continuous cylindrical shaped track in Fig. 6.1. Simchi and Godlinski (2008), have previously reported this cylindrical shape as being a strong indicator that the internal and external surface energy forces are in equilibrium and the alloy powder was fully melted. In addition, no balling or partial melting was observed along the length of scanned track. The tracks did however, have a heat affected zone (HAZ) where the melt pool interacts with the surrounding areas and the previous layer/ substrate. A clear and defined area of powder depletion was also evident.

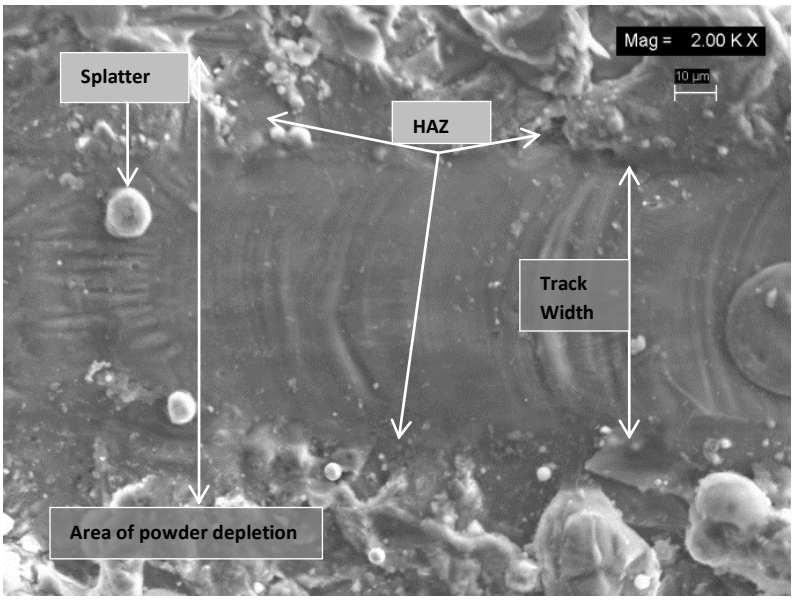

Figure 6.1 AlSi10Mg matrix alloy scanned at 800 mm/s

This speed was consequently used as a baseline for the research into scanning the composite powders and these characteristics were sought to be emulated during the investigation on the melt pool formation of the composite powder. So in this instance, suitability of the composite scanned tracks will be evaluated as reported by Kempen *et al.* (2001); Yadroitsev *et al.* (2007) and Kyogoku *et al.* (2010) for:

1. Continuity – No balling and areas of partial melting
2. Penetration – width of the tracks and HAZ

6.2.2 Single Track Formation of the Composite Powders - AlSi10Mg/SiC_p

Single-track formation as a method of determining the powder reaction to laser irradiation had been investigated. Kyogoku *et al.* (2010) posited that the rate of laser energy absorption by a material would determine the type of melted tracks obtained. Also Simchi and Godlinski (2008) suggested that the addition of SiC particles to the matrix would result in large tracks due to increased absorptivity of the laser energy by the composite powder when compared to the unreinforced matrix in Fig. 6.1. Fig. 6.2 to Fig. 6.7 shows the effect of varying scan speed on track shape and top surface topology for the Al-$MMC_{10\%}$, while Fig. 6.8 to Fig. 6.12 shows the same for the reinforced Al-$MMC_{5\%}$ composite tracks.

The track in Fig. 6.2 scanned at 640 mm/s was observed to be relatively flat rather than cylindrical with the top surface infiltrated with cracks. Delamination from the substrate is also visible along the edges of the track and the area of powder depletion is not discernible, as the molten track has concealed it. The flatness and cracks present are a result of an excess heat absorbed by the matrix due to the decrease in the scanning speed and the addition of the SiC particles. The increase in the absorbed heat leads in this instance to a corresponding increase in the volume of melted powder and melt pool temperature increase, (Yadroitsev *et al.*, 2007) which creates a large thermal mismatch between the AlSi10Mg matrix and the SiC reinforcement. The thermal mismatch then creates a loss of viscosity of the molten metal causing it to spread faster and cool much slower which results in the formation of cracks upon solidification.

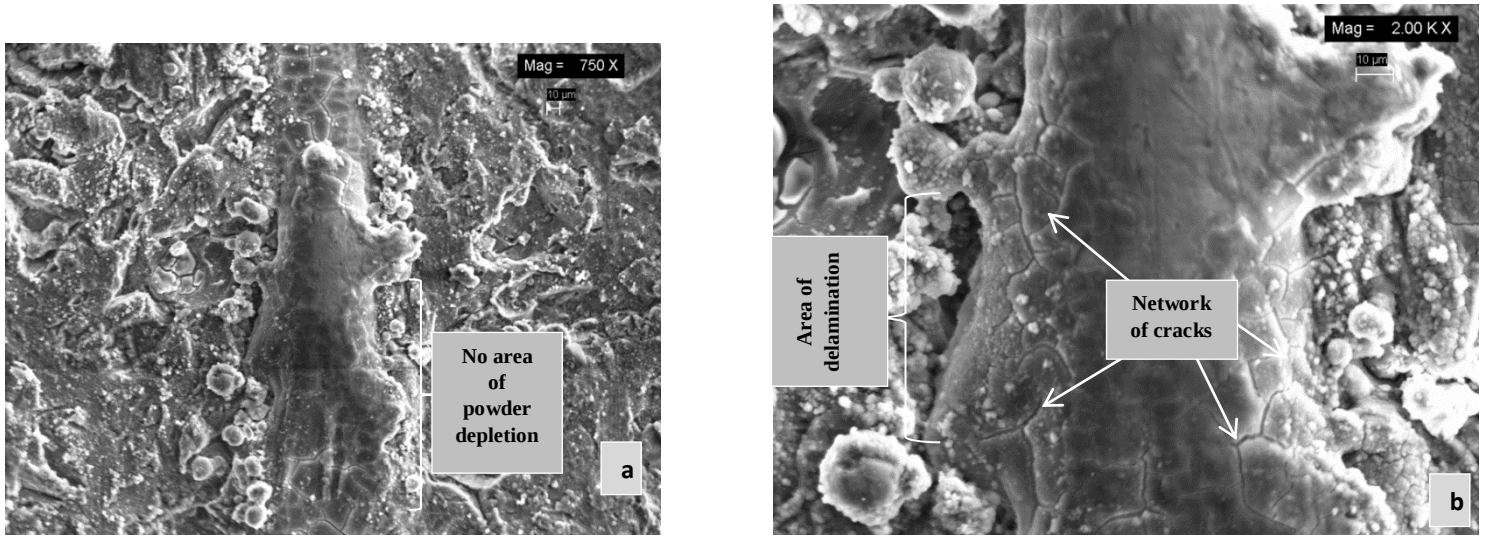

Figure 6.2 Scan line of the 10% reinforced AlSi10Mg/SiC_p Composite Scanned at 640 mm/s (a) Mag 750X (b) Mag 2000X

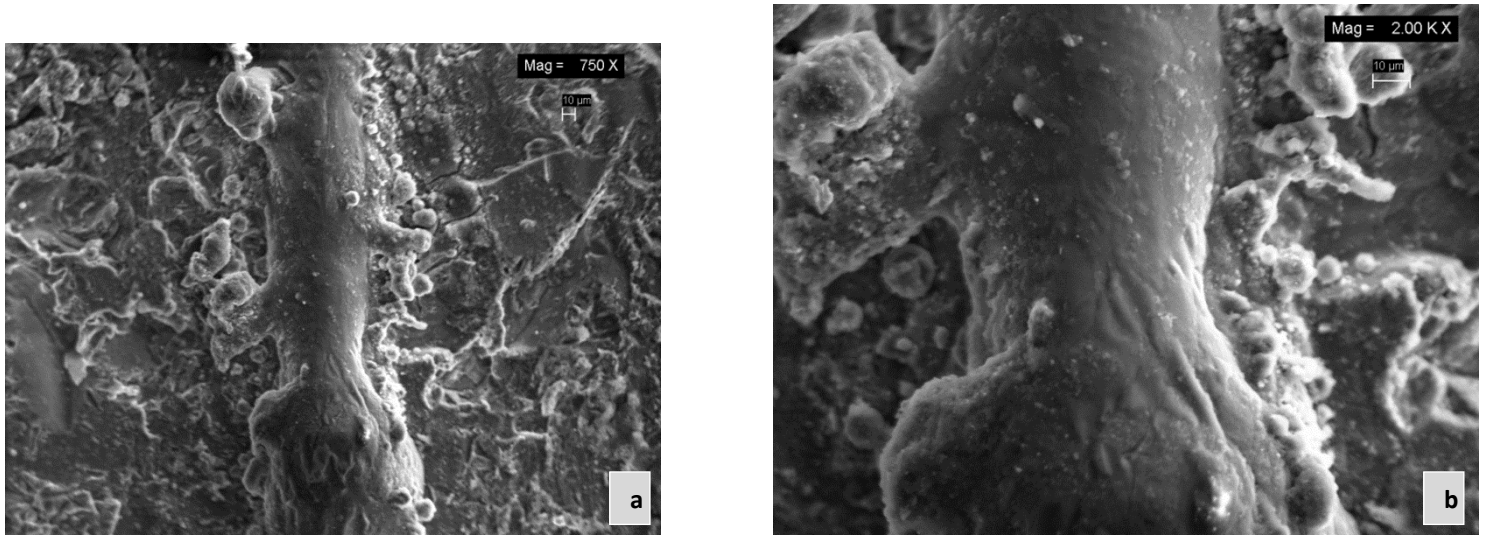

Figure 6.3 Scan line of the 10% reinforced AlSi10Mg/SiC_p Composite Scanned at 720 mm/s (a) Mag 750X (b) Mag 2000X

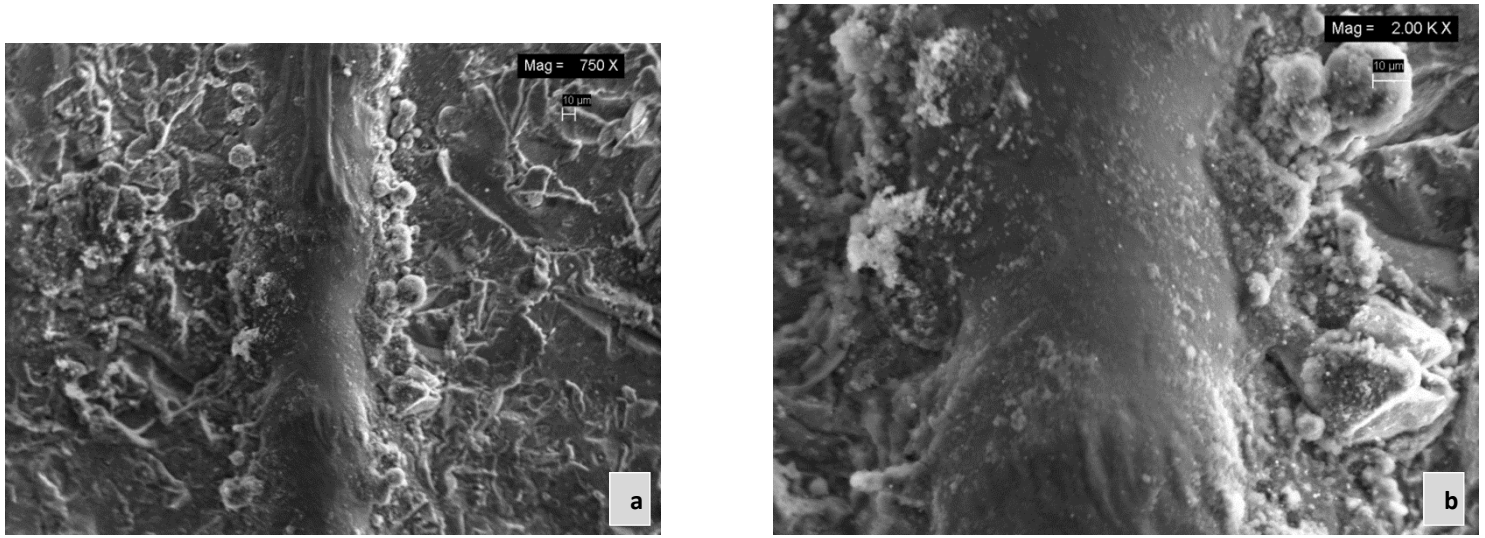

Figure 6.4 Scan line of the 10% reinforced AlSi10Mg/SiC_p Composite Scanned at 800 mm/s (a) Mag 750X (b) Mag 2000X

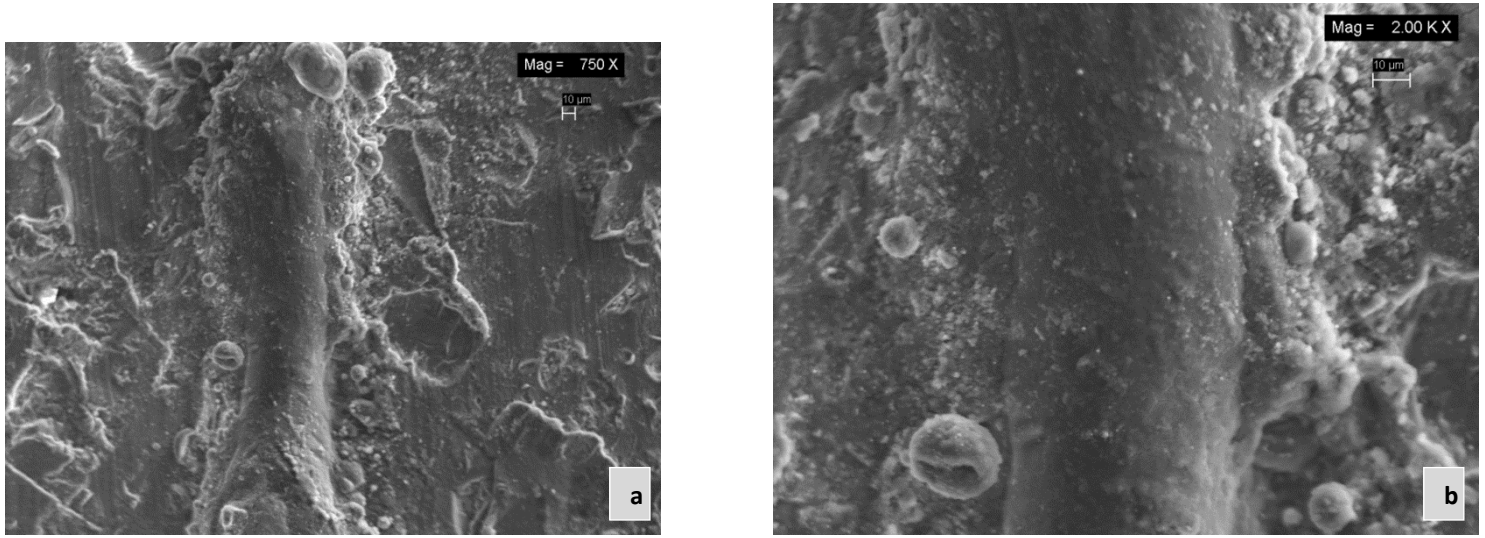

Figure 6.5 Scan line of the 10% reinforced AlSi10Mg/SiC_p Composite Scanned at 880 mm/s (a) Mag 750X (b) Mag 2000X

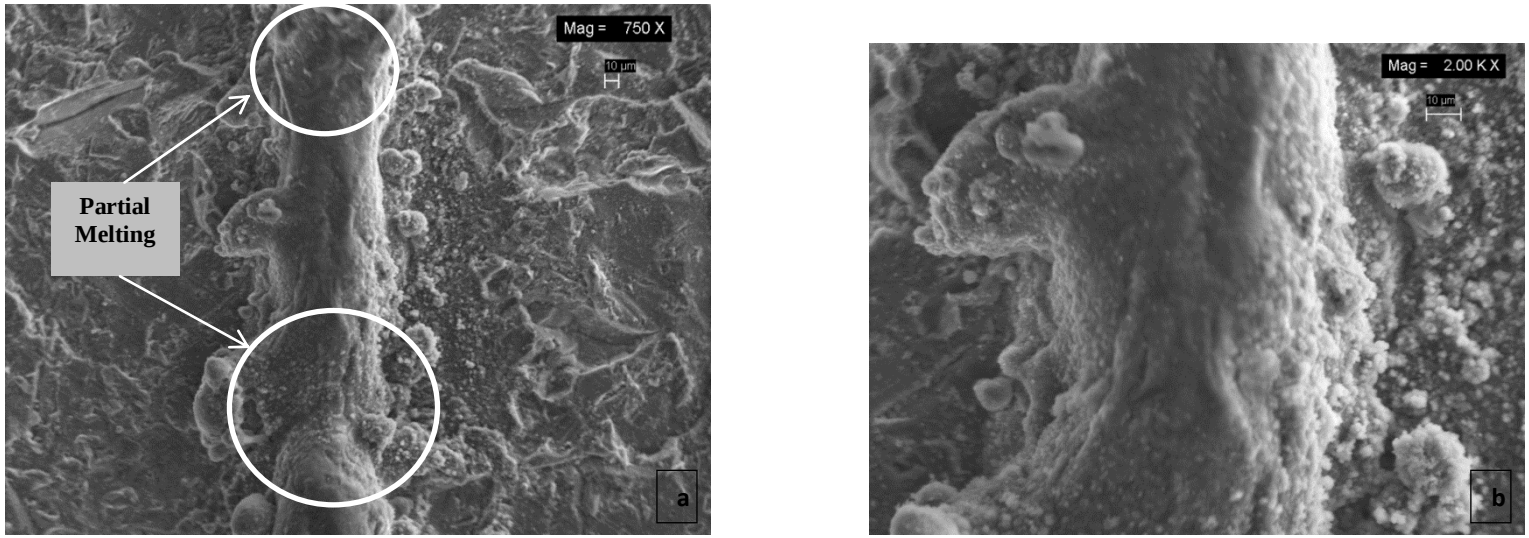

Figure 6.6 Scan line of the 10% reinforced AlSi10Mg/SiC_p Composite Scanned at 960 mm/s (a) Mag 750X (b) Mag 2000X

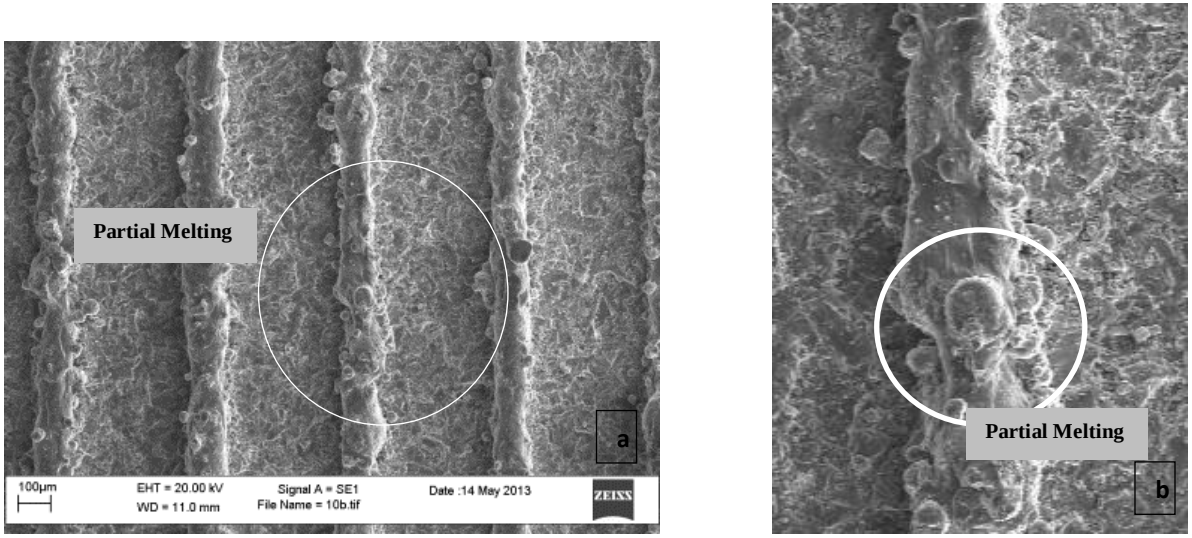

Figure 6.7 Scan line of the 10% reinforced AlSi10Mg/SiC_p Composite Scanned at 1040 mm/s (a) Mag 100X (b) Mag 750X

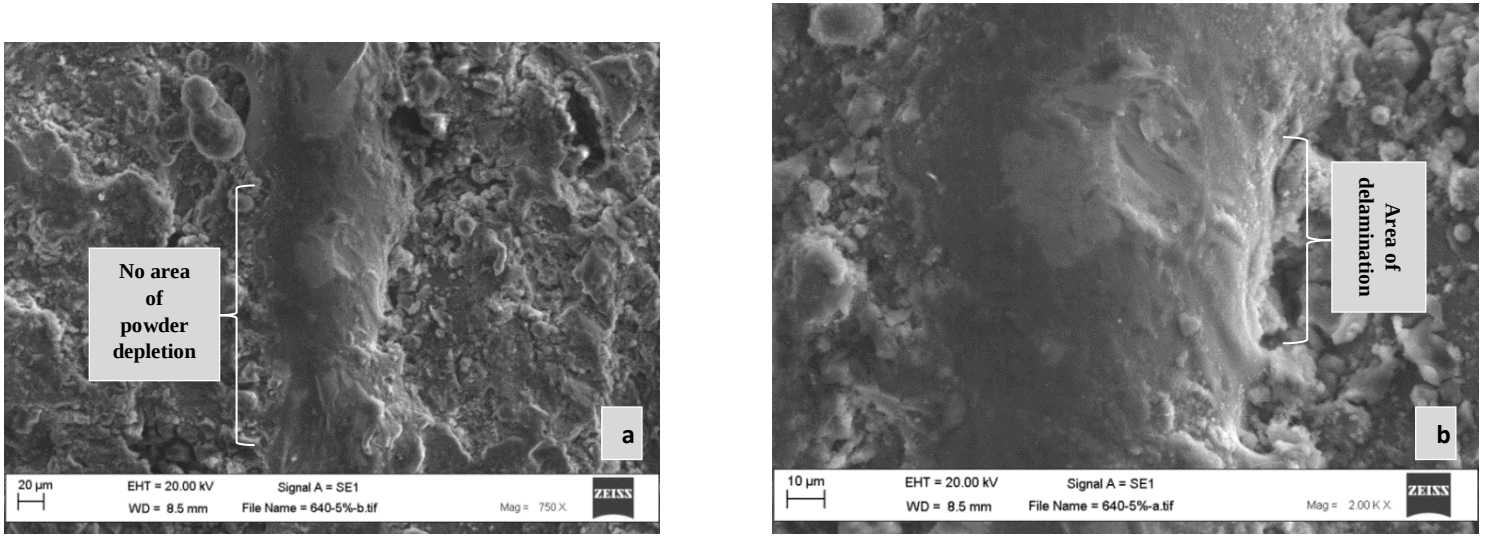

Figure 6.8 Scan line of the 5% reinforced AlSi10Mg/SiC_p Composite Scanned at 640 mm/s (a) Mag 750X (b) Mag 2000X

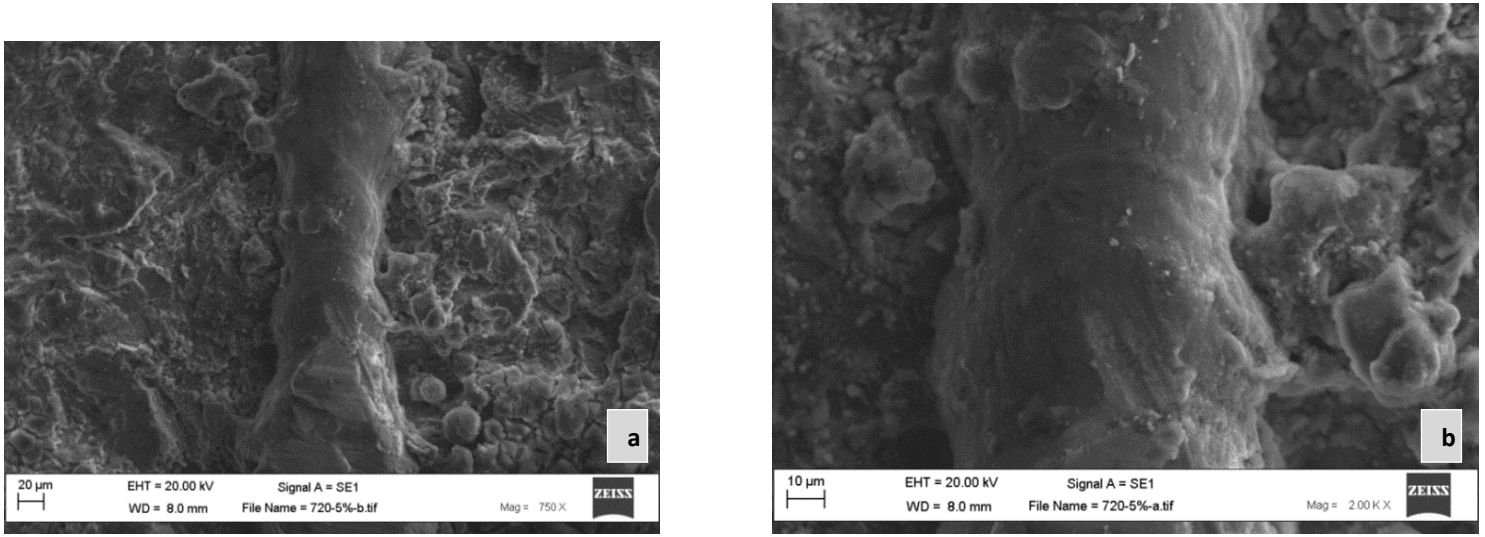

Figure 6.9 Scan line of the 5% reinforced AlSi10Mg/SiC_p Composite Scanned at 720 mm/s (a) Mag 750X (b) Mag 2000X

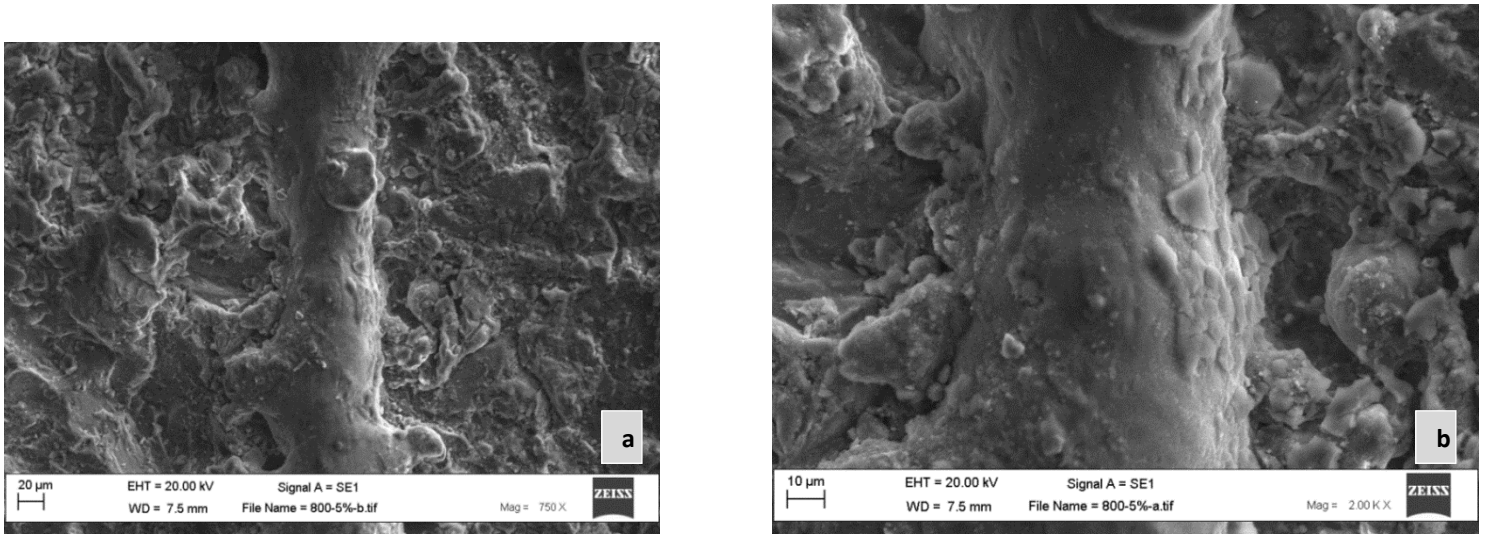

Figure 6.10 Scan line of the 5% reinforced AlSi10Mg/SiC_p Composite Scanned at 800 mm/s (a) Mag 750X (b) Mag 2000X

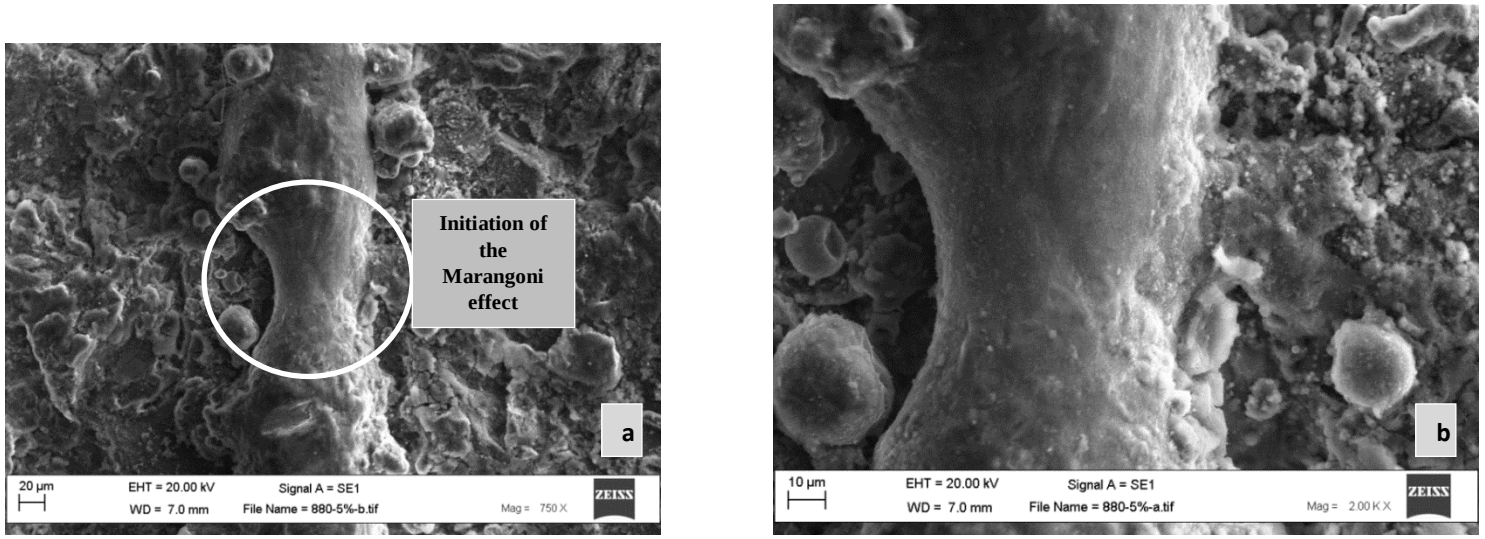

Figure 6.11 Scan line of the 5% reinforced AlSi10Mg/SiC_p Composite Scanned at 880 mm/s (a) Mag 750X (b) Mag 2000X

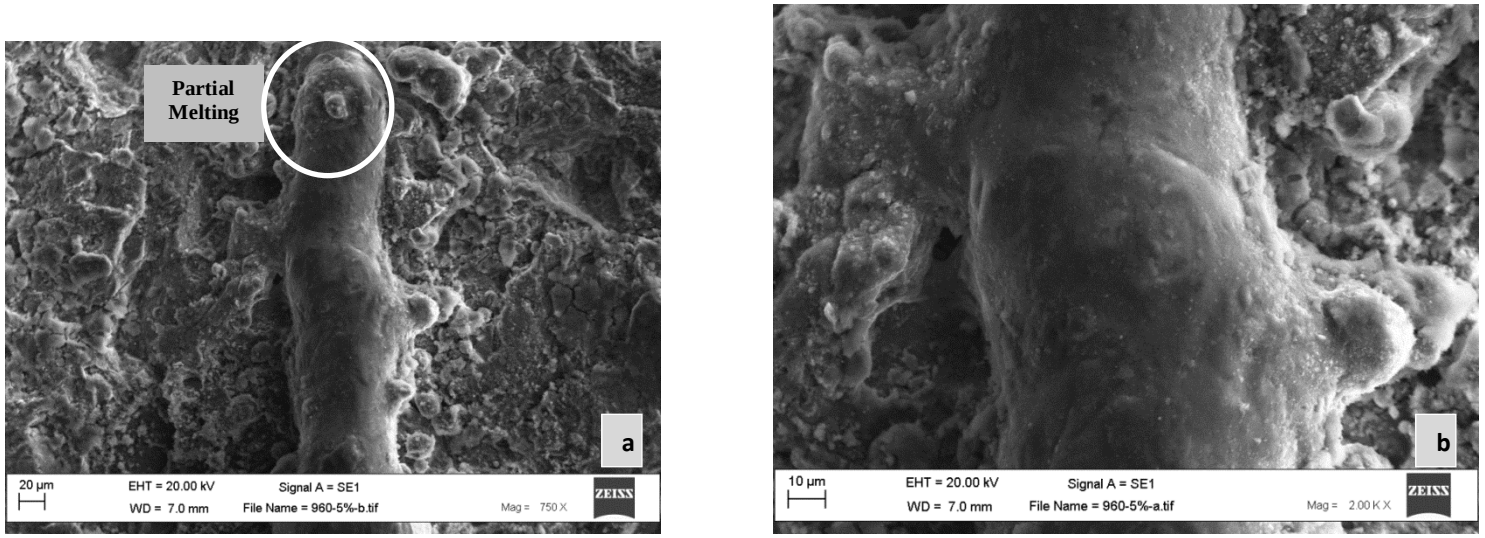

Figure 6.12 scan line of the 5% reinforced AlSi10Mg/SiC_p Composite Scanned at 960 mm/s (a) Mag 750X (b) Mag 2000X

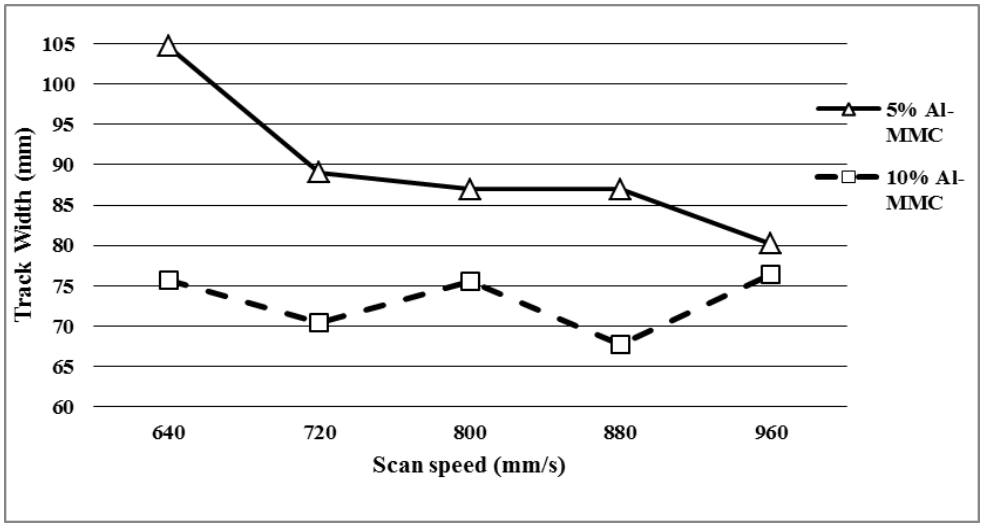

Figure 6.13 Width of Scanned tracks in relation to scanning speed

Tracks in Fig. 6.3 to Fig. 6.5 show an improved shape formation with no apparent cracks with the track beads becoming more convex. However, some balling can be observed in Fig. 6.3 at a scan speed of 720 mm/s whereas the scanned track at 800 mm/s in Fig. 6.4 produces an undulating track, both in the width and height that has been attributed to a possible shrinkage on solidification of the melt pool. The track appears stabilised at 880 mm/s in Fig. 6.5 with a fully continuous length and no apparent balling evident. The onset of the Marangoni effect from insufficient energy input (Yadroitsev *et al.*, 2010) was observed in Fig. 6.6 at a scanning speed of 960 mm/s.

At this scan speed, the fast moving laser creates eddy currents in the melt pool which results in internal shear stresses (Drezet *et al.*, 2004). The shear stresses generate a convective movement of the unmelted powder particles within in the molten pool arising from a thermal mismatch of the solid and liquid phases, thus leading to a reduction of the surface tension of the melt pool and generating partial melting of the tracks at that speed. The area of partial melting is highlighted by the rectangular zone in Fig. 6.6b and extends in Fig. 6.7 at a scanning speed of 1040 mm/s with an increase in the scanning speed as the effect of Marangoni forces increases.

Previous research by Kempen *et al.* (2011) found the process window for AlSi10Mg irradiated by a 200 W fibre laser with a beam diameter of about 150 µm to be between 600 mm/s and 1400 mm/s. However, the addition of SiC, which has a lower reflectivity, has reduced the overall reflectivity of the composite powder and increased its energy absorptivity. This had led to melt pool instability and thus the formation of droplets initiated much earlier at 960 mm/s than in their research at 1400 mm/s. This is apparent at the scan speed of 1040 mm/s (Fig. 6.7b) with the majority of the tracks being unstable and distorted.

The reinforced Al-$MMC_{5\%}$ had a better reaction to the LM of the powder observed in Fig. 6.8 to Fig. 6.12. The single track melted at 640 mm/s in Fig. 6.8 did not display the rapid network of cracks that was observed on the reinforced Al-$MMC_{10\%}$ track in Fig. 6.2. This corroborates the fact that the SiC particles alloyed with the matrix aids in the absorption and retaining of heat by the composite powder. As the amount of reinforced SiC reduces from 10 % to 5 %, the amount of retained heat will also reduce, subsequently reducing the volume of melted powder and the corresponding melt pool temperature. This has resulted in the formation of a more rounded and cylindrical track in Fig. 6.8b, although an area of delamination was still

apparent on one side while the molten metal overran on the other side of the weld bead as in Fig. 6.2.

Like the reinforced Al-$MMC_{10\%}$ in Figs. 6.3, 6.4 and 6.5, the single line tracks LM at 720 mm/s, 800 mm/s and 880 mm/s in Figs. 6.9, 6.10 and 6.11 respectively, progressively becomes more suitable in shape, morphology and adhesion to the substrate to the desired properties of the matrix alloy. There are no apparent signs of balling in Fig. 6.9 unlike the 10 % reinforced Al-MMC in Fig. 6.3, the track appears stabilised over the 720 mm /s, and 800 mm /s scan speeds. The track scanned at 880 mm/s for the 5% reinforced Al-MMC is still a stable single line although the encircled area in Fig. 6.11 shows an obvious thin section that indicates the commencement of Marangoni forces. As observed in Fig. 6.6, there are areas of partial melting also visible in Fig. 6.12 both scanned at 960 mm/s. However, unlike the 10 % reinforced Al-MMC, the single track for the 5 % reinforced Al-MMC is stable over a longer distance. This also indicates that the 5 % reinforced composite powders have absorbed less heat than the 10 % reinforced powders.

The width of the scanned tracks of the matrix alloy - AlSi10Mg and composite powder - AlSi10Mg/SiC_p, at the various speeds between 640 mm/s and 960 mm/s was also measured during the investigation on the shape, morphology and adhesion of the single line tracks. Simchi and Pohl, (2003) had previously reported that the width, including the HAZ, gives an indication of the melt pool width, which also influences the amount of overlap needed for full densification of the part. It was also highlighted that the amount of heat available for the melt pool formation (energy density) has an effect on grain growth and nucleation during re-solidification and will therefore affect the composite microstructure and its density. Fig. 6.13 offers a comparison between the widths of the composite single line tracks to that of the AlSi10Mg matrix. Surprisingly, the widths of the 5% Al-MMC are larger than that obtained for the 10% Al-MMC with the measured widths of the 5% Al-MMC showing a gradual decrease in width as the scan speed increases while the 10% Al-MMC displays a near-stable width with the exception of the 720 mm/s and 880 mm/s scan speeds. The decrease in track widths at increasing scan speeds was also noted by Aboulkhair *et al*. (2016a), thereby suggesting that the addition of 10% SiC has increased the stability of the AlSi10Mg powder to the laser.

Based on the top surface observations of the single tracks, a process window can be defined between 720 mm/s and 960 mm/s. This process range was used for further investigation as continuous tracks as these tracks offered sufficient surface tension to create a bond and penetrate the previous layers. As such, they provided a stabilizing effect for the melting of sample blocks from the composite powders. Sample blocks were therefore fabricated to investigate the porosity, density, surface roughness and microstructural condition at these scan speeds to certify a progression to the mechanical testing of the LM composite parts by selecting a set of parameters for LM fabrication. It should be noted that Buchbinder *et al.* (2011) had previously stated that industrial application of the AM technology was poor due to slow build rates; therefore, the chosen parameter values for the mechanical investigation of the LM AlSi10Mg/SiC_p composite will be a compromise between full density, surface finishing, and high build rates for the composite. Achieving full density is crucial to the mechanical properties of the part and repeatability of the process, while the surface finishing and build rates have an effect on its applicability in the industry.

6.3 Phase 4 - Sample Blocks using Varied Parameters

Samples blocks made from the process window obtained from the single line scans were analysed for surface roughness, porosity and microstructure as outlined in section 4.9.

6.3.1 Visual Inspection of Aluminium Metal Matrix Composite Sample blocks

Visual inspection of the 10% reinforced Al-MMC sample blocks showed a series of crack networks on the EDM wiring plane, which might be attributed to the residual internal stresses. Manfredi *et al.* (2014) reported that the complexity of the melting behaviour between layers during LM could cause the stress fields in the material to overcome the material yield strength thereby causing distortion of the parts. The introduction of SiC particles therefore increases the complexities of the melting behaviour as it introduces extra stress due to the thermal expansivity mismatch between the AlSi10Mg metallic alloy and the ceramic SiC particles. In addition, as the energy density decreases from the higher scan speeds to the lower scan speeds for the 10 % reinforced Al-MMC samples, the cracks reduce successively as observed from Fig. 6.14 to Fig. 6.18. Furthermore, no cracks were observed in any of the 5% Al-MMC sample blocks that suggests that as the volumetric addition of SiC increases, additional internal stresses are created from the increase in the difference of thermal expansion of the matrix and reinforcement.

Figure 6.14 Visual Inspection of LM Sample Blocks scanned at 640 mm/s (i) 0.17 µm Step-over (ii) 0.13 µm Step-over

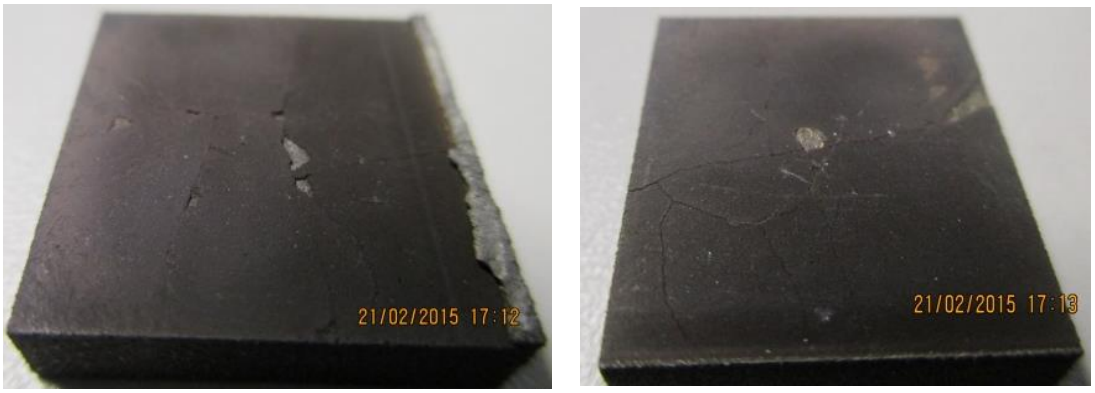

Figure 6.15 Visual Inspection of LM Sample Blocks scanned at 720mm/s (i) 0.17 µm Step-over (ii) 0.15 µm Step-over

Figure 6.16 Visual Inspection of LM Sample Blocks scanned at 800 mm/s, 0.17 µm Step-over - Nominal Parameters

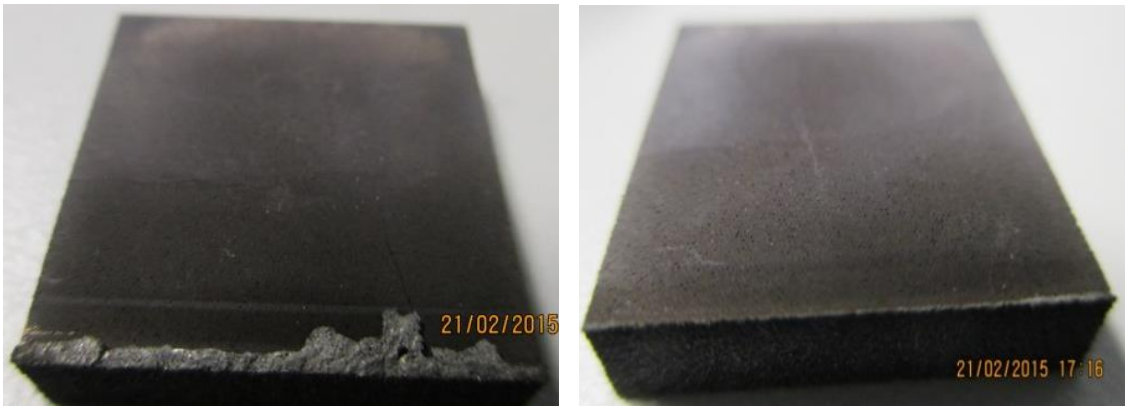

Figure 6.17 Visual Inspection of LM Sample Blocks scanned at 880 (i) 0.17 µm Step-over (ii) 0.19 µm Step-over

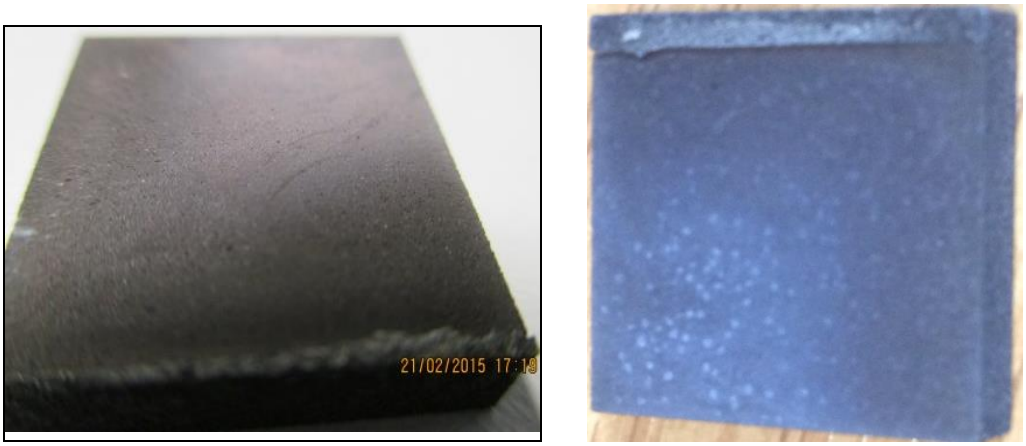

Figure 6.18 Visual Inspection of LM Sample Blocks scanned at 960 (i) 0.17 µm Step-over (ii) 0.21 µm Step-over

6.3.2 Effect of Scanning Speed on the Surface Roughness.

Sateesh *et al.* (2014) state that surface roughness is affected by the shape and size of the powder particles and gives an indication of the powder packing density. Therefore, sample blocks were studied and analysed for their surface roughness. The blocks were scanned with infill parameters and no UpSkin/Downskin or contour parameters were utilised in the experiments. The aim was to achieve full density of the sample blocks.

The Ra value obtained for the AlSi10Mg alloy from the confocal measurements of the top surface was 18.87 µm, which is in the range given by the data sheet, EOS (2011). The surface topology of the matrix in Fig. 6.19 shows a well-distributed surface (green layer) with the little splatter (yellow layer) on the surface and the blue layer representing the next layer beneath. The amount of variation in the colours of the surface topology of the composite powders gives an indication of the porosity of the sample as they represent different layers visible and measured on by the microscope. Increased colours indicate increased visible layers which would suggest that the sample is porous considering the layer-by-layer build of the sample. The highest peak was measured as 320 µm and lowest trough as 160 µm. The scanned lines for the last layer are clearly distinguishable in Fig. 6.19 with sufficient melting of the surrounding areas from the HAZ to ensure full densification. The HAZ thus highlights the importance of the step-over, which creates the distance between each individual scanned track, in achieving densification. If the distance between the each scanned track is too far apart then the heat from the laser will not achieve a HAZ wide enough to intercept initial weld pools from the previous and subsequent tracks. However, if the distance between each track is too close, then the HAZ overlaps without sufficient heat dissipation thereby causing

the agglomeration of powder particles outside of the HAZ, which in turn increases the surface roughness, Badrosamay and Childs (2006).

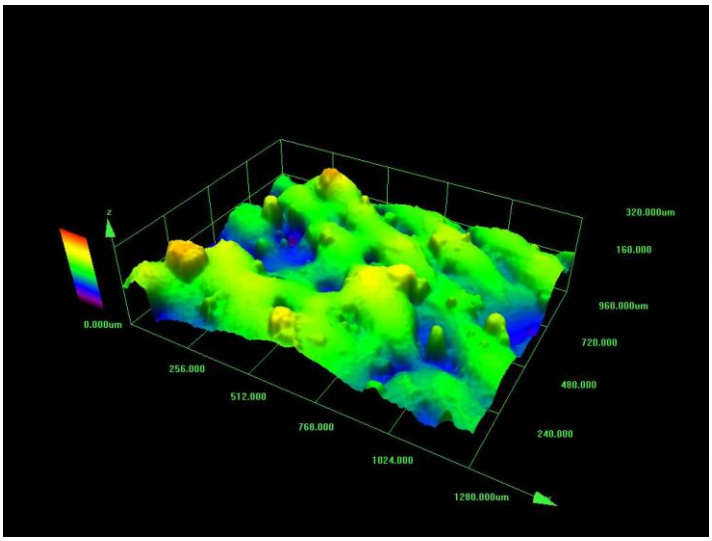

Figure 6.19 Surface Morphology of the Matrix scanned at 800 mm/s; 195 W; 0.17 mm

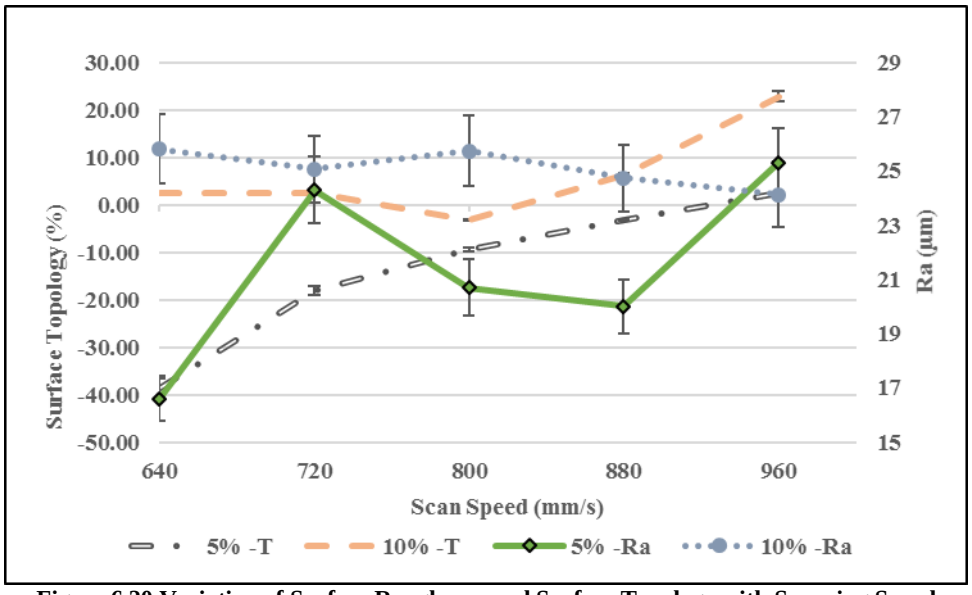

Figure 6.20 Variation of Surface Roughness and Surface Topology with Scanning Speed

Badrosamay *et al.* (2009) presented that the topology of the starting powder influenced the surface roughness of the part and due to addition of the SiC particles, the topology of both composite powders (Al-$MMC_{5\%}$ and Al-$MMC_{10\%}$) has led to a coarser particle size distribution evident in the higher Ra values obtained next to the unreinforced matrix. Satesh *et al.* (2014) had also previously reported that the increase in melt temperature at lower scanning speeds leads to a lower contact angle and higher Marangoni flow, which aids in reducing the surface roughness. This is evident in the Al-$MMC_{5\%}$ which has an apparent

increase in the surface roughness as the scanning speed increases, however, the surface roughness of the 10% Al-MMC seems to decrease with an increase in the SiC particles. Tang *et al.* (2003) have shown that the surface roughness of ceramics decreases with increasing scanning speed, this may explain the difference between the Al-$MMC_{5\%}$ and the Al-$MMC_{10\%}$ as the increase in the SiC particles indicates it supports the ceramic trend rather than the metallic trend.

Spierings *et al.* (2011a) discovered that the surface roughness values obtained for a 316L steel grade laser melted with Nd: YAG laser with a laser power of 105W follows a 2^{nd} order polynomial trend when both the scan speed or energy density were varied. Unlike the steel alloy, the surface roughness of the composite can be observed in Fig. 6.20 to follow different trends as the scanning speed increases. The Ra values for the Al-$MMC_{5\%}$ show a sharp increase and appear to stabilise around 800 mm/s and 880 mm/s after which the surface roughness increases again thereby following a 3^{rd} degree polynomial trend, however the Al-$MMC_{10\%}$ follows a linear trend as the surface roughness decreases with increasing scanning speed. This therefore suggests that the addition and the volume rate of the SiC interferes with the melting characteristics of the powders with a higher volume reinforcement addition weakening the matrix properties thereby justifying the need for modifying the LM parameters to suit the composite. Overall the values of the Al-$MMC_{5\%}$ reinforced sample scanned at 640 mm/s has a lower roughness value than the matrix alloy, while the other scan speeds display higher values resulting from the coarser particles with a narrower particle size distribution as previously explained in chapter 5.

Fig. 6.21 to Fig. 6.30 show the surface topology of the Al-MMC sample blocks for both the 5% and 10% reinforced composite scanned with a constant step over of 0.17 µm. The percentage deviation values of each topology graph from the matrix were converted from Table 6.1 into a graph, Fig. 6.20. As the values for both the troughs and peaks for all scan speeds were observed to be relatively equal when measured surface roughness baseline. from the matrix, an average of both trough and peak values was therefore determined in Table 6.2. The surface topology of the 5% reinforced composite scanned at 640 mm/s in Fig. 6.21 shows a near-uniform layer at the peaks with much lower peaks and troughs at -38% than the matrix, however, the tracks are flat and widespread rather than the cylindrical tracks expected from the LM process Simchi and Godlinski (2008). This supports the previous evidence of cracks previously obtained from the single line scans.

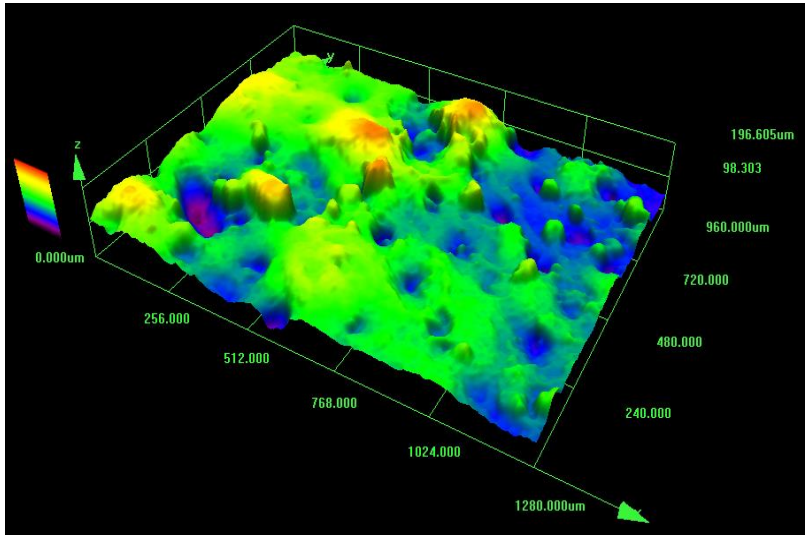

Figure 6.21 Surface topology of Al-MMC$_{5\%}$ scanned at 640 mm/s; 195 W; 0.17 mm

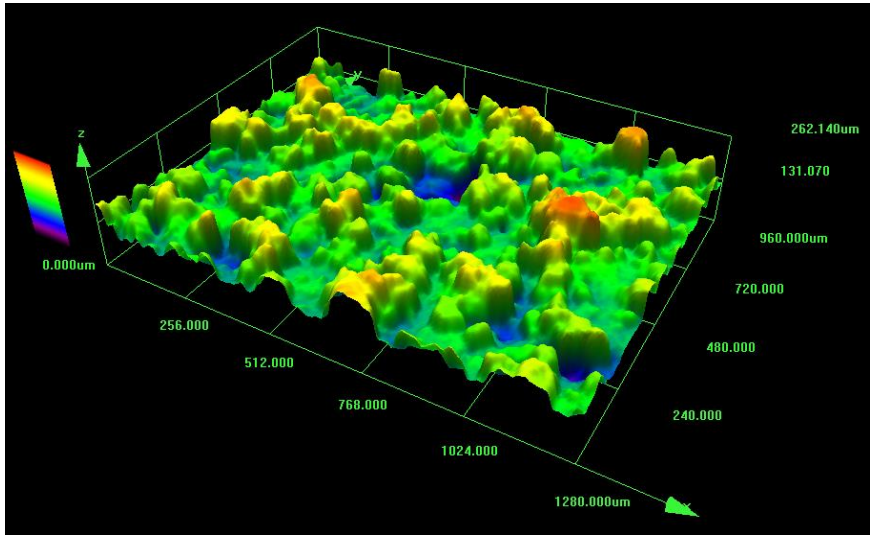

Figure 6.22 Surface topology of Al-MMC$_{5\%}$ scanned at 720 mm/s; 195 W; 0.17 mm

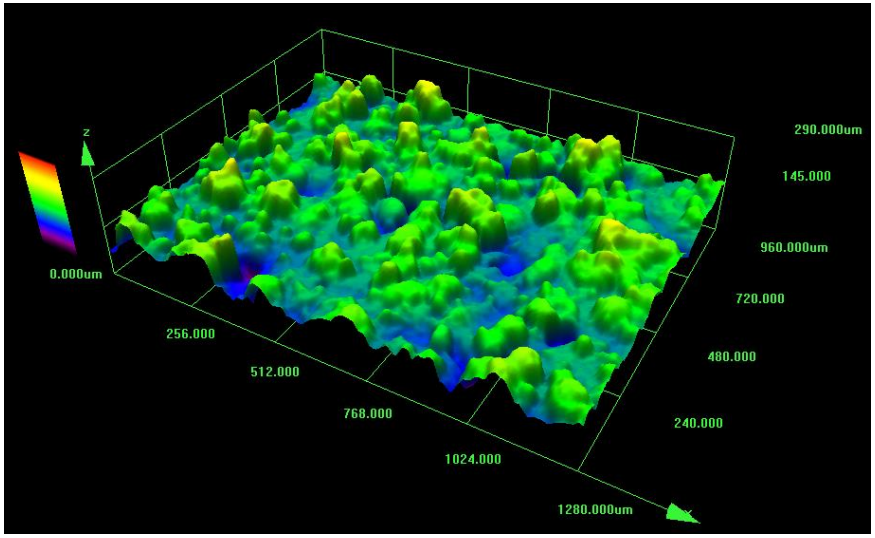

Figure 6.23 Surface topology of Al-MMC$_{5\%}$ scanned at 800 mm/s; 195 W; 0.17 mm

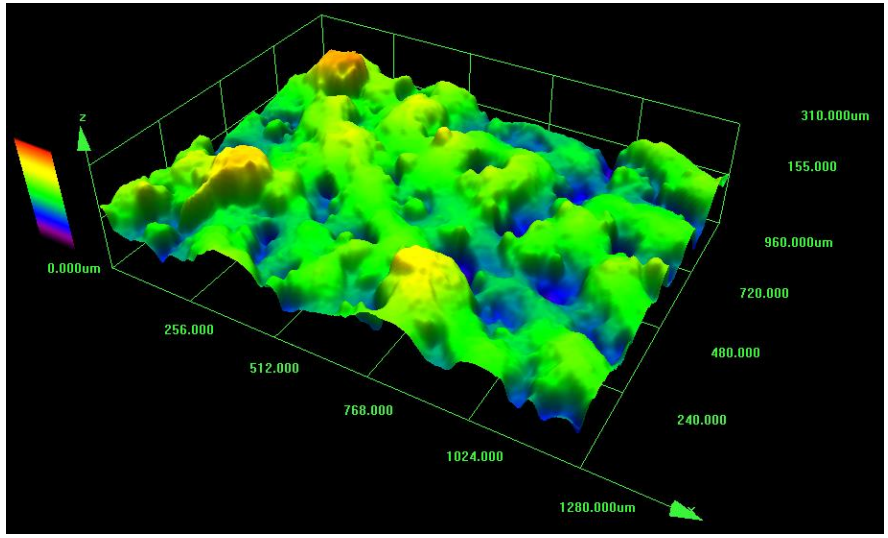

Figure 6.24 Surface topology of Al-MMC$_{5\%}$ scanned at 880 mm/s; 195 W; 0.17 mm

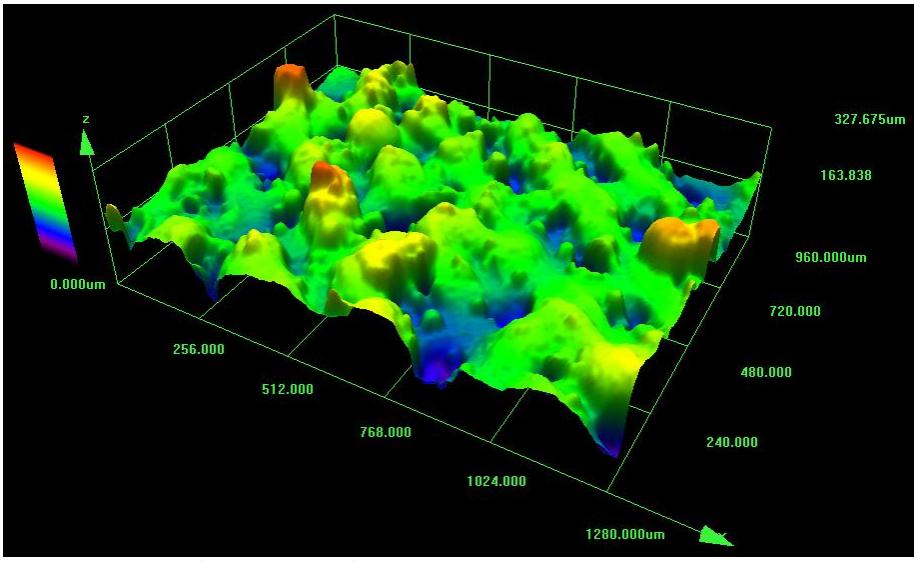

Figure 6.25 Surface topology of Al-MMC$_{5\%}$ scanned at 960 mm/s; 195 W; 0.17 mm

The surface topology of the 10% reinforced composite in Fig. 6.26 shows an increased surface roughness with an average value of 2.40% from the matrix when scanned at 640 mm/s. The surface in Fig. 6.26 also exhibits flat and cylindrical tracks resulting in an uneven melting of the layers. Badrossamay and Childs (2006) reported that low scan speeds results in a higher percentage of porosity from the excessive energy input, which substantiates the fact that 640 mm/s may not be a suitable scan speed for the Al-MMC, however further tests will be conducted to possibly eliminate this speed.

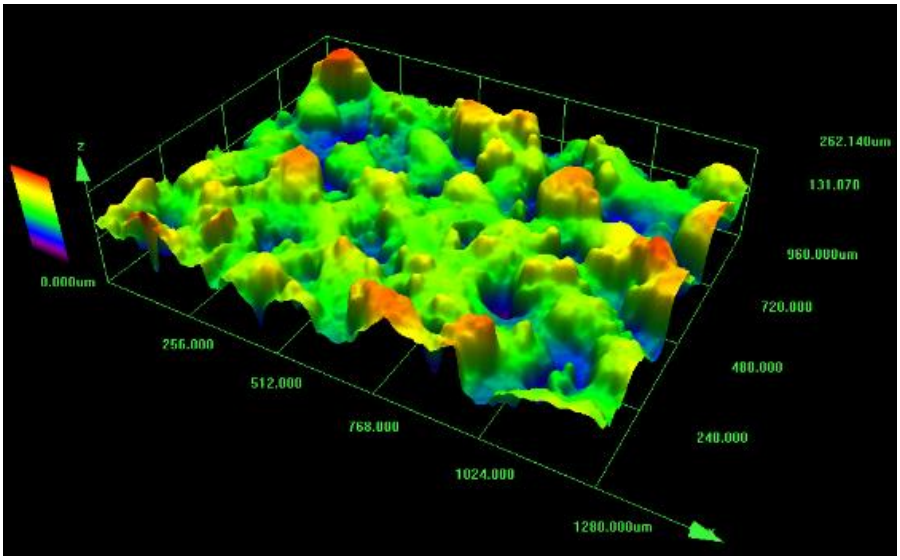

Figure 6.26 Surface topology of Al-MMC$_{10\%}$ scanned at 640 mm/s; 195 W; 0.17 mm

The topology of the 5% reinforced composite showed rough edges with no obvious defined scan track visible when scanned at 720 mm/s and 800 mm/s in Fig. 6.22 and Fig. 6.23 respectively, however the peak and trough values achieved are better than the composite

scanned at 640 mm/s. This may be attributed to the reduction in surface tension of the molten liquid thereby reducing the bonding to the previous layer, which the addition of SiC particles may have caused. As the scanning speed increases, the topology of the 5% reinforced composite gradually reveals cylindrical track topology characteristic of the process. When the laser scans at 880 mm/s and 960 mm/s, clearly defined tracks were established in Fig. 6.24 and 6.25. However, the percentage deviation for the 5 % reinforced composite when scanned at 960 mm/s shows a positive value rather than negative suggesting increased peaks and splatter observed in Fig. 6.25. The improvement in track topology form the increase in scanning speed has also led to an improved surface roughness given by the percentage deviation from the matrix in Table 6.1 and as previously explained, cylindrical tracks would lead to denser parts while flat or balled up tracks will result in porous parts from layers fused improperly.

Unlike the 5 % reinforced composite, the 10 % composite when scanned at 720 mm/s and 800 mm/s displays defined tracks in Fig. 6.27 and 6.28. While increased peaks and splatter were observed at 720 mm/s evidenced by the positive values in Table 6.1, the surface roughness at 800 mm/s has a negative sign suggesting it has a smoother surface than the surfaces scanned at other speeds. The surface roughness increases as the scanning speed increases at 880 mm/s and 960 mm/s with higher positive values and as increased surface roughness had previously been linked with porosity, (Krol *et al.,* 2013), the scan speeds had to be further investigated to determine their suitability in obtaining a fully dense part.

The surface roughness of the composite seems to improve with increasing scanning speed until apparent critical speeds; 800 mm/s for the 10 % Al-MMC and 880 mm/s for the 5 % Al-MMC. This indicates a linear trend for 5% Al-MMC while the dip at 800 mm/s suggests a 2^{nd} order polynomial trend for the 10% Al-MMC with both trends increasing with increase in scanning speed. The increase in surface roughness was attributed to the large disparity in the peaks and valleys of the reinforced composites attributed to the change in melting characteristics from the SiC particles introduced. Due to a wider particle size distribution obtained in phase 2, changing LM parameters and the variation in particle topology between the matrix and reinforcing powder, the surface roughness of the reinforced composite had increased. Sateesh *et al.* (2014) reported that at higher speeds, the matrix would not achieve full melting thereby leading to increased splatter that will in turn increase the surface roughness.

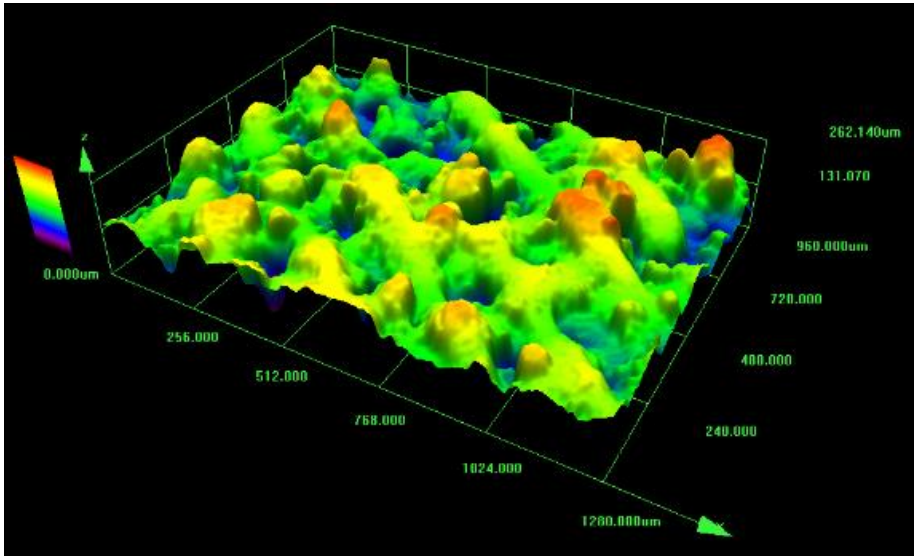

Figure 6.27 Surface topology of Al-MMC$_{10\%}$ scanned at 720 mm/s; 195 W; 0.17 mm

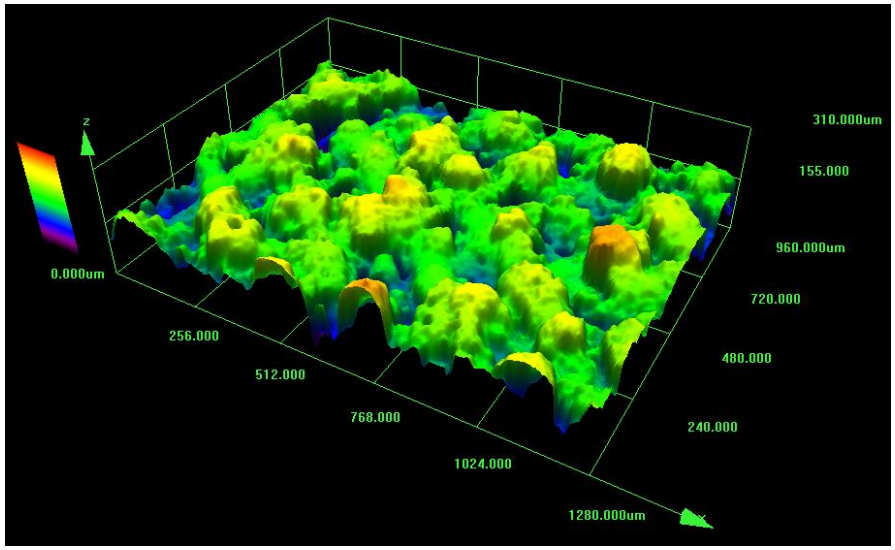

Figure 6.28 Surface topology of Al-MMC$_{10\%}$ scanned at 800 mm/s; 195 W; 0.17 mm

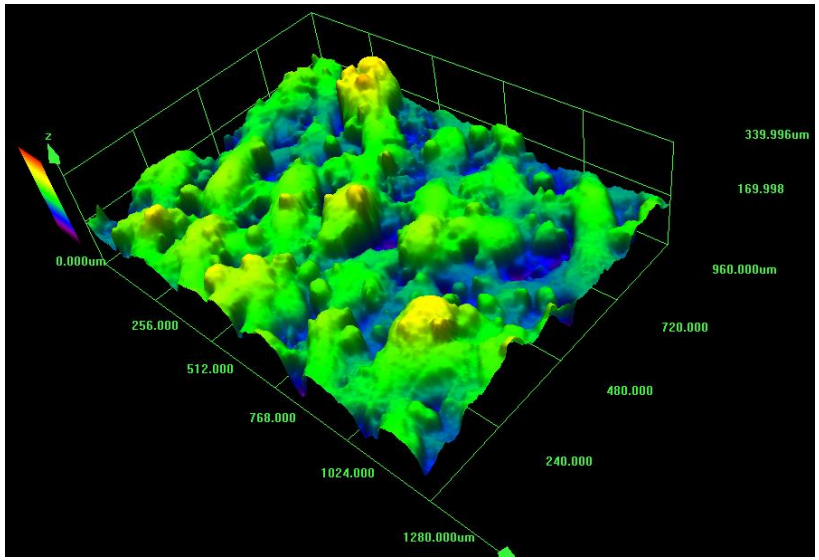

Figure 6.29 Surface topology of Al-MMC$_{10\%}$ scanned at 880 mm/s; 195 W; 0.17 mm

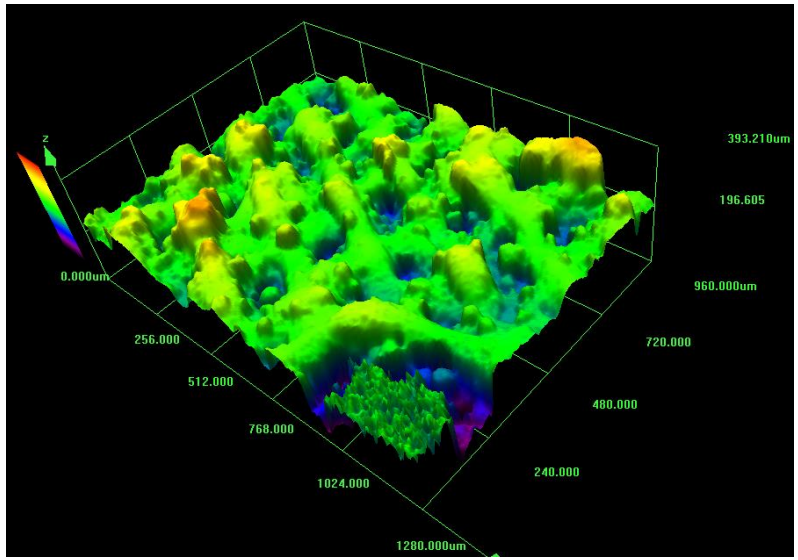

Figure 6.30 Surface topology of Al-MMC$_{10\%}$ scanned at 960 mm/s; 195 W; 0.17 mm

Table 6.1 The average percentage deviation from the surface topology of the matrix

Matrix			
Trough	**Peak**		
160	320		
5%		**10%**	
Trough	**Peak**	**Trough**	**Peak**
98.3	196.61	163.84	327.68
131.07	262.14	163.68	327.68
145	290	155	310
155	310	169.99	339.99
163.83	327.68	196.6	393.21
% difference	**% difference**	**% difference**	**% difference**
-38.56	-38.56	2.40	2.40
-18.08	-18.08	2.30	2.40
-9.38	-9.38	-3.13	-3.13
-3.13	-3.13	6.24	6.25
2.39	2.40	22.88	22.88

Table 6.2 The average percentage deviation from the surface topology of the matrix

Scan Speed (mm/s)	**Al-MMC$_{5\%}$ (%)**	**Al-MMC$_{10\%}$ (%)**
640	-38.56	2.40
720	-18.08	2.35
800	-9.38	-3.13
880	-3.13	6.25
960	2.40	22.88

6.3.3 Effect of Energy Density on the Surface Roughness

The effect of changing energy density is different from the results observed in the previous section as the scanning speed and step-over have been changed simultaneously. The simultaneous modification also highlights the effect of changing the step-over on the surface roughness of the samples as the step–over increases with decreasing energy density. In Fig. 6.31 the 5% Al-MMC displays a linear increase to the surface roughness with the decreasing energy density and the 10% Al-MMC also displays a gradual increase in the surface roughness despite an anomalous decrease at 48 J/cm with a scan speed of 800 mm/s and 0.17 mm step-over.

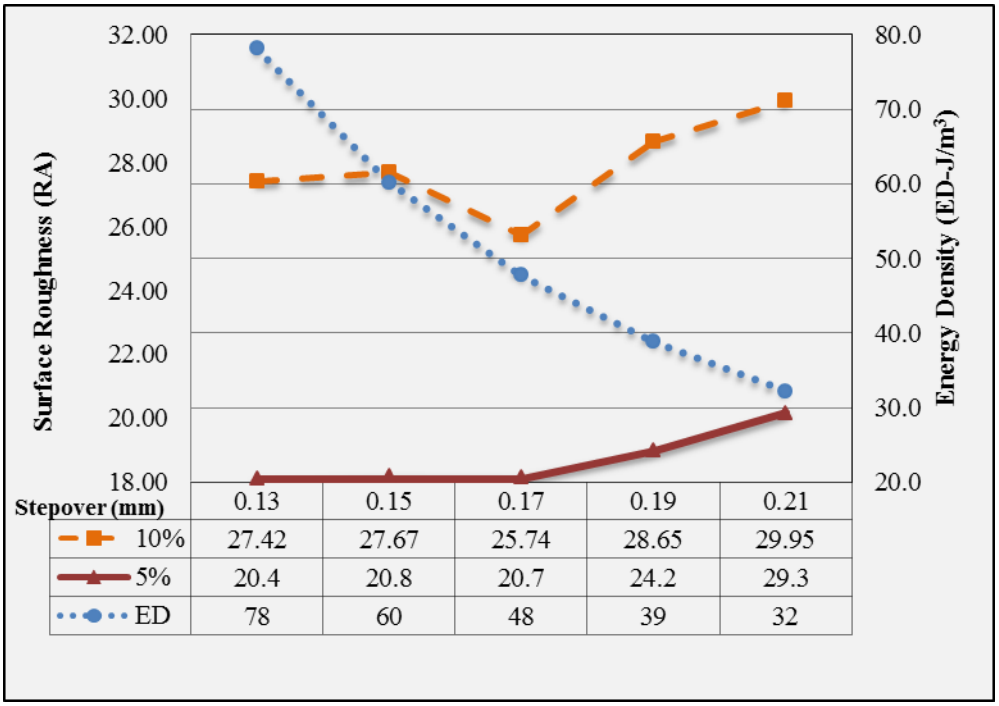

Figure 6.31 Variation of Surface Roughness with Energy Density and Step-over

Overall, the surface roughness values generally show an increase with decreasing energy density. At high energy density the matrix achieves full melting and flows viscously thereby achieving a more uniform dense material, however as the step-over increases and the gap between each track widens, the flow of the molten material has a wider area to cover which leads to insufficient adhesion to the previous substrate and also nearby tracks. In addition, the HAZ around each individual track narrows and the area of powder denudation reduces thereby increasing the surface roughness of the samples as the effective melting diameter has been reduced by the wider step-over. Therefore, when less energy is contributed by the laser which is then absorbed by the powder layers, it reduces the amount of molten pool available, which in turn creates a rougher surface from insufficient bonding.

In addition, the change in topology from the matrix powder has led to the rougher surface finishes obtained. It can also be observed that at 5% volume reinforcement, the Ra values are considerably lower than the 10% Al-MMC, suggesting that a higher volume reinforcement might induce more porosity into the matrix as increased surface roughness could be an indication of incomplete Lm of the part. This is contrary to the work of Simchi and Godlinski (2008) who observed improved surface roughness with increases in the volume reinforcement.

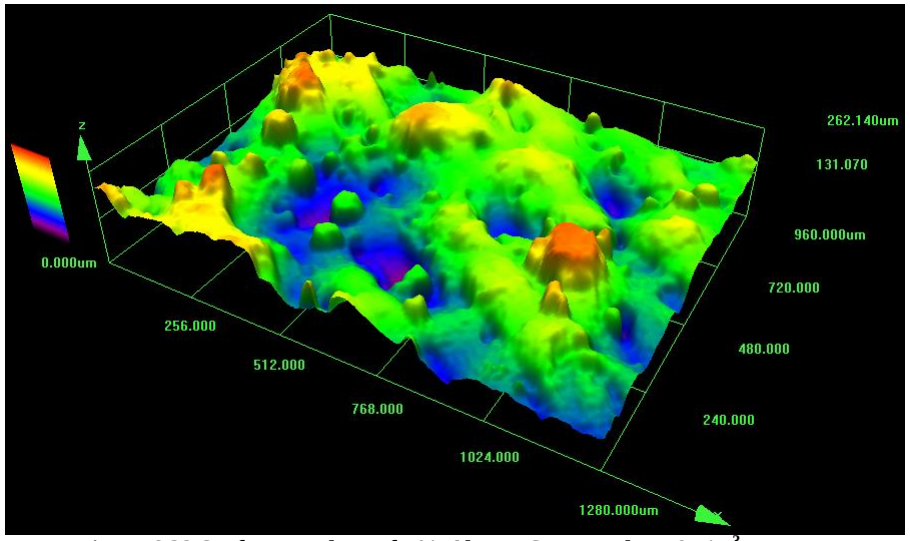

Figure 6.32 Surface topology of 5%-Al-MMC scanned at 78 J/m^3

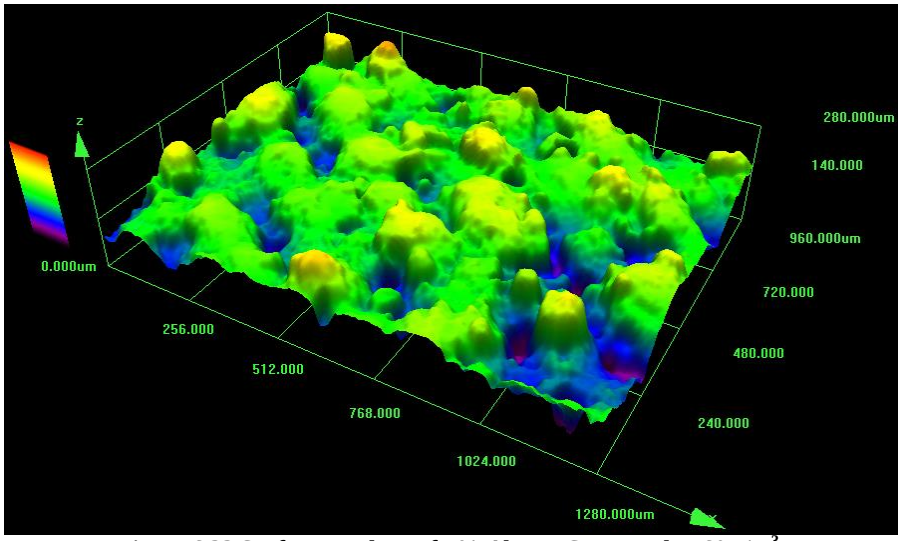

Figure 6.33 Surface topology of 5% Al-MMC scanned at 60 J/m^3

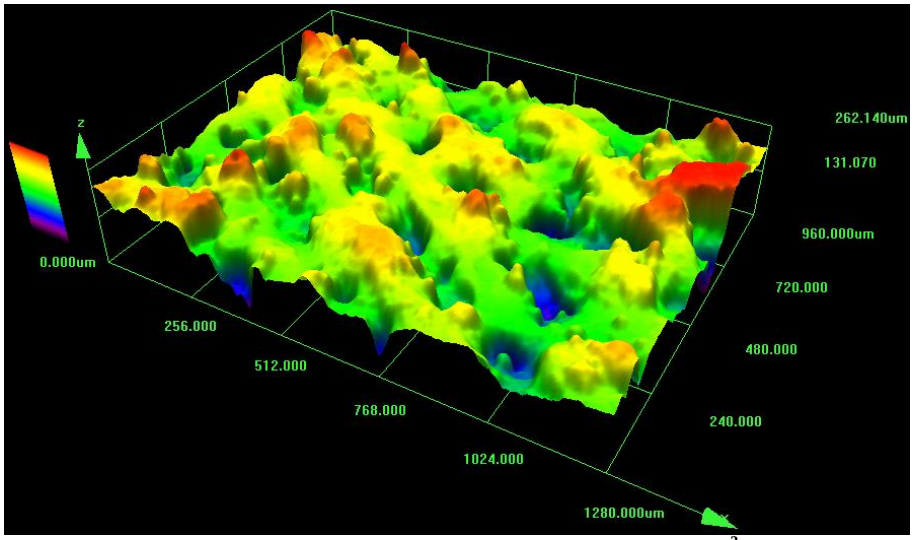

Figure 6.34 Surface topology of 5%-Al-MMC scanned at 48 J/m^3

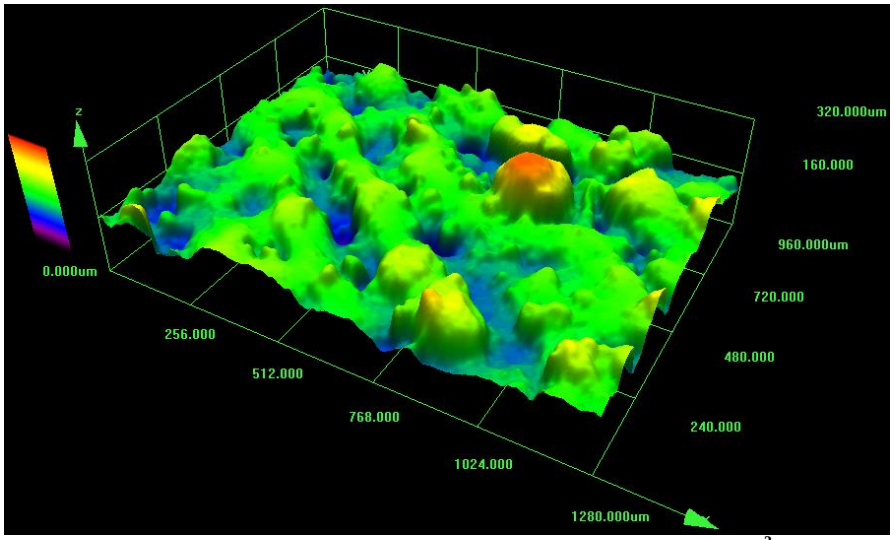

Figure 6.35 Surface topology of 5% Al-MMC scanned at 39 J/m^3

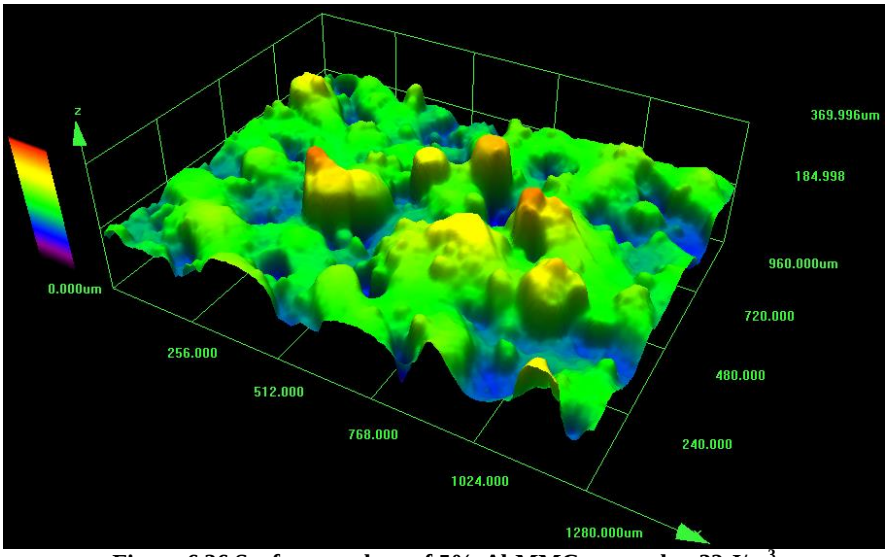

Figure 6.36 Surface topology of 5%-Al-MMC scanned at 32 J/m^3

From the disparity in the values of the surface roughness, it can be inferred that the recoater blade may deposit an inhomogeneous layer of powder arising from the peaks and valleys of the previous layers. This causes an inhomogeneous melting and solidification pattern as regions with thicker powder layer (the valleys) will not melt at the same energy density as thinner layers (the peaks). Also Morgan *et al.* (2004) had previously established that higher surface roughness could cause the entrapment of gases in the melt pool, which upon superheating from the laser scan rapidly expands and creates pores within the part on solidifying. Moreover, as it is almost impossible to eliminate internal pores from the powder particles (Bose, 1995), the specific porosity could be transferred into the finished parts therefore necessitating the importance to investigate the porosity and density of the Al-MMC.

Observing the surface topologies of the samples from Fig. 6.33 to 6.42, the images and values depicts a connection to porosity. Aboulkhair *et al.* (2014) had previously found in their research on AlSi10Mg alloy using a Realizer GmbH SLM-50 that the increase in the hatch spacing corresponds to an increase in the porosity of the material. The sample scanned in Fig. 6.33 at 78 J/m^3 with a scan speed of 640 mm/s and step over of 0.13mm showed indistinct tracks, which were also flat and widespread as in previous experiments. Although more peaks and tracks were observed in Fig. 6.38 for the 10% Al-MMC, however areas of flatness are still clearly visible leading a rougher surface. Table 6.4 gives an overall deviation of the surface roughness of the composites to that of the matrix. It was noted that the 5% Al-MMC consistently showed a rougher surface with the negative values until a noticeable difference

was observed at 39 J/m3 corresponding to the 880 mm/s scan speed and 0.19 mm step-over where the deviation value recorded was zero. The value then increases significantly to 15.62% for the 960 mm/s and 0.21 mm step-over. The results in Table 6.3 for the 5% Al-MMC therefore suggest that as the step-over increases no substantial improvement to the surface roughness and topology was experienced until at 880 mm/s scan speed and 0.19 mm step-over.

At high-energy inputs (78 J/m^3 and 60 J/m^3) and low energy input (32 J/m^3), increased rough topology could be observed for the 10% Al-MMC. The increased roughness obtained from the high-energy input was due to the reduced surface tension that had previously caused the flat tracks observed in the single line scans as a result of enlarged molten pools, indicating that the tracks did not attain the height required for full density, Badrossamay and Childs (2006). However, the increased roughness observed with the low energy input was due to the internal surface tensional forces, Marangoni forces, SiC addition and un-melted powder particles as the scan speed is too fast to achieve full melting of the powder tracks thereby causing increased splatter. In addition, each track was too widespread from the larger step-over for the individual track HAZ to aid in retaining the absorbed heat from the surrounding tracks, which has been known to improve the microstructure and therefore its properties, as surface roughness and properties have been confirmed as a function of laser power and step-over, Song (1997).

The results from the single line scans, surface roughness and topology have given an indication of the set of parameters that will be suitable for scanning the composite powders in order to achieve full density. Therefore, further investigation is required into the LM characteristics of the composites by evaluating the density and pore formation of the samples and the influence of pores on the failure of the parts.

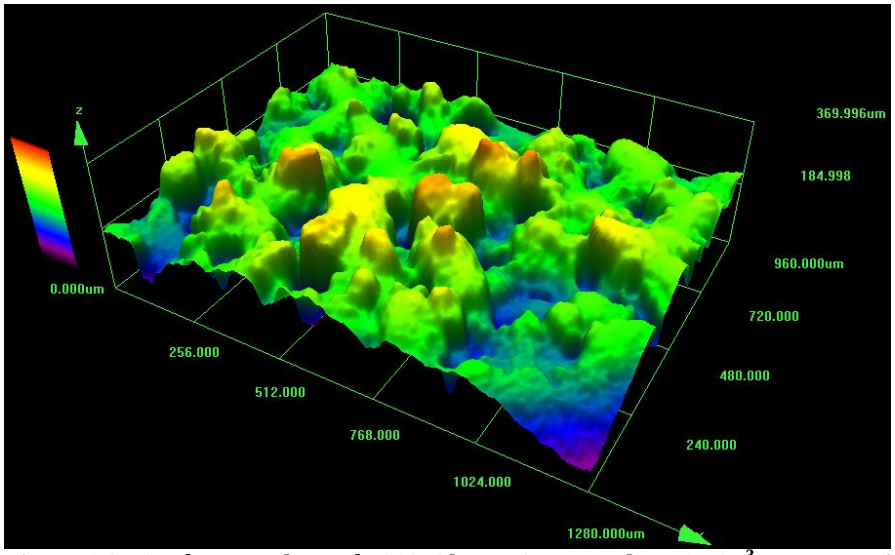

Figure 6.37 Surface topology of 10%-Al-MMC scanned at 78 J/m^3

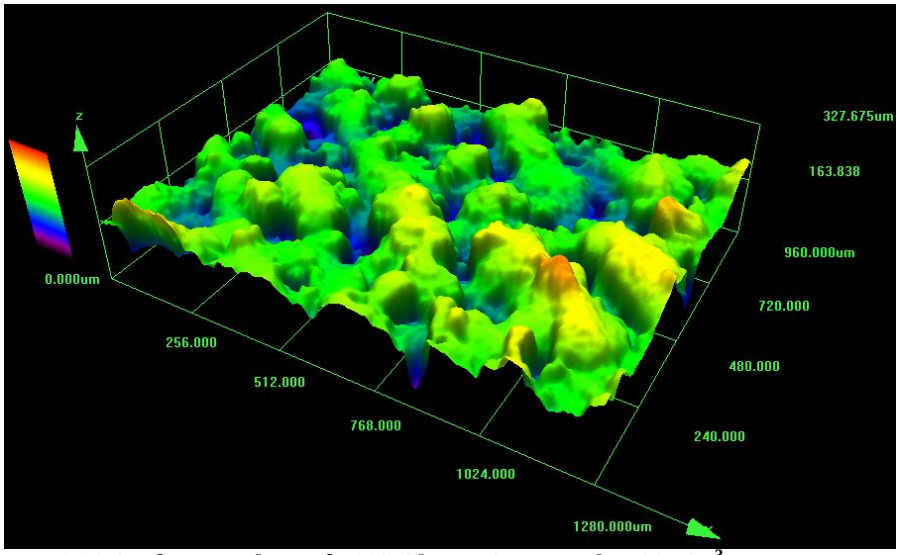

Figure 6.38 Surface topology of 10% Al-MMC scanned at 60 J/m^3

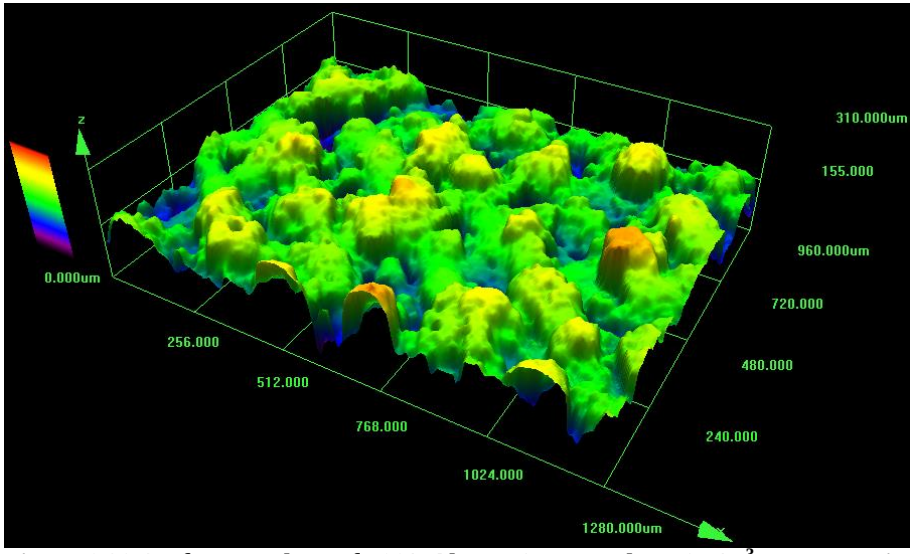

Figure 6.39 Surface topology of 10%-Al-MMC scanned at 48 J/m^3

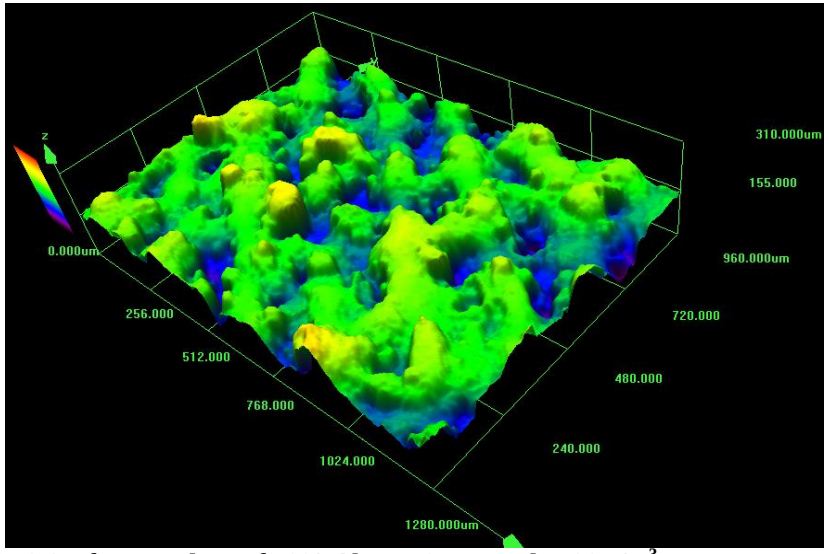

Figure 6.40 Surface topology of 10% Al-MMC scanned at 39 J/m^3

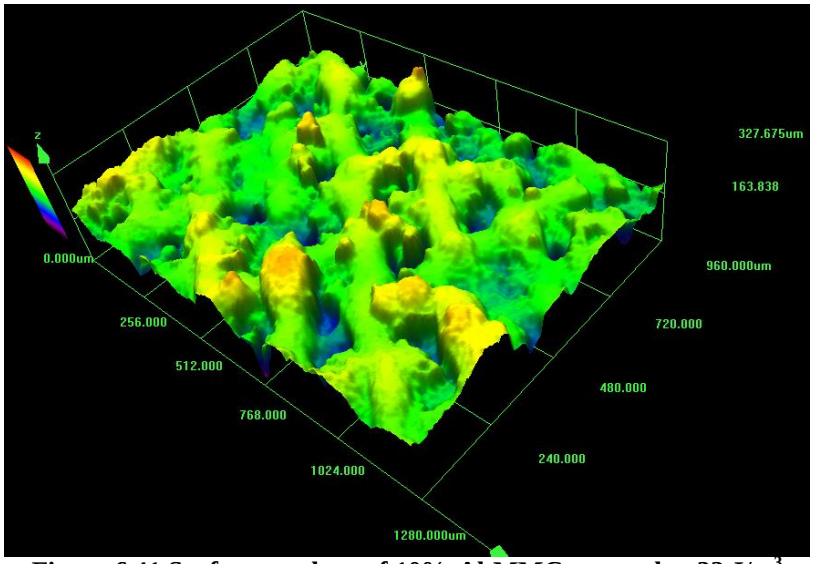

Figure 6.41 Surface topology of 10%-Al-MMC scanned at 32 J/m^3

Table 6.3 The average percentage deviation from the surface topology of the matrix

Matrix			
Scan Speed (mm/s)	**Step-over (µm)**	**Trough**	**Peak**
800	**0.17**	160	320

Composites					
		5%		**10%**	
Scan Speed	**Step-over**	**Trough**	**Peak**	**Trough**	**Peak**
640	**0.13**	131.07	262.14	184.99	369.99
720	**0.15**	140	280	163.84	327.68
800	**0.17**	131	262.14	155	310
880	**0.19**	160	320	155	310
960	**0.21**	184.99	369.99	163.84	327.68
Scan Speed	**Step-over**	**% difference**	**% difference**	**% difference**	**% difference**
640	**0.13**	-18.08%	-18.08%	15.62%	15.62%
720	**0.15**	-12.50%	-12.50%	2.40%	2.40%
800	**0.17**	-18.13%	-18.08%	-3.13%	-3.13%
880	**0.19**	0.00%	0.00%	-3.13%	-3.13%
960	**0.21**	15.62%	15.62%	2.40%	2.40%

Table 6.4 The average percentage deviation from the surface topology of the matrix

Scan Speed (mm/s)	**Step over (mm)**	**Al-MMC$_{5\%}$ (%)**	**Al-MMC$_{10\%}$ (%)**
640	0.13	-18.08%	15.62%
720	0.15	-12.50%	2.40%
800	0.17	-18.10%	-3.13%
880	0.19	0.00%	-3.13%
960	0.21	15.62%	2.40%

6.3.4 Effect of Scanning Speed on Relative Density and Porosity

Previous researches have shown that porosity affects the mechanical strength, fatigue strength and elongation to rupture (Gilbert and Rooy, 2004; Sonsino and Ziese, 1993 and Haynes, 1991). According to Chien, *et al*. (2002), pores are stress concentrators, which are suitable sites for microcrack nucleation and growth and thus lead to the fracture of composites. As all powder-based process have some specific porosity in the part because of internal pores in the actual powder particles (Spierings, *et al.* 2011b), therefore quantifying the density of the composite is essential in determining the mechanical properties.

A reliable density value for each composite mix is required for reference hence the theoretical density of each composite mixture was estimated through the rule of mixtures. 2.68 g/cm^3 was used as the density of the matrix alloy (EOS, 2011) while using 3.2 g/cm^3 as the density value of the SiC. Theoretical density was calculated utilising the rule of mixtures given in Equation 6.1.

$$\frac{1}{\rho_c} = \frac{f_r}{\rho_r} + \frac{f_m}{\rho_m} \quad \text{.....} \textit{Equation 6.1 (Kaw, 2005)}$$

Where ρ_c density of the composite (g/cm^3)

ρ_r density of the reinforcement (g/cm^3)

ρ_m density of the matrix (g/cm^3)

f_r percentage of volume reinforcement

f_m percentage of volume matrix.

$and\ f_r + f_m = 1$

Therefore, from Equation 6.1, the theoretical density of the 5% and 10% Al-MMCs utilising the volume fraction as 0.05 for the 5% and 0.1 for the 10% reinforcement, are given as 2.69 g/cm^3 and 2.71 g/cm^3 respectively. Fig. 6.42 shows that the as percentage reinforcement increases, the theoretical density should increase simultaneously.

Figure 6.42 Theoretical Density versus Percentage Reinforcement

The relative density (RD) measurements of the sample blocks using deionised water show that the relative densities of the 5% Al-MMC are between 95.2 % and 99.3 % exhibiting a complex relation between the scanning speed and the part densities in the Fig. 6.43. The samples achieved near full relative density at the lower scan speed of 640 mm/s however, the presence of cracks in both the single track and the sample block of the Al-MMC composites has led to a high ratio of error, which therefore precludes the usage of this scanning speed.
The sample at 720 mm/s scan speed has a particularly low relative density compared with the other scan speeds although the porosity from the image analysis (IA) shows that it has a low porosity. It can be observed in Fig. 6.43, the RD of the composite increases with scan speed, however the IA depicts that the scan speed at 640 mm/s has the highest internal porosity and the scan speed at 880 mm/s having the lowest internal porosity. At 960 mm/s scan speed, the relative density decreases and the porosity from the image analysis increases. This is congruent with findings from the single line scans and the surface roughness where the critical speeds have been highlighted as 800 mm/s and 880 mm/s. Spierings *et al*. (2011a) had previously found that porosity increased at high scan speeds when utilising a Concept Laser M1 machine for the SLM of a stainless steel and the change in the RD can be attributed to the melt characteristics of the powder as they react to the absorptivity of the laser.

The RD of the 10 % Al-MMC also follows the trend of the 5% Al-MMC in having a high density at 640 mm/s. The RD is lower than the 5 % Al-MMC except at 880 mm/s where it is higher than the 10% Al-MMC. The IA analysis show that for the 10% Al-MMC, the 800 mm/s has the highest internal porosity and its RD is also correspondingly low.

It was observed that samples with a higher surface roughness correspondingly have lower relative densities, which as previously explained in section 6.3.2 is due to the change in packing density and powder topology leading to areas of full and partial melting especially at high scan speeds. Also observed from the surface roughness and the density values of the composites, superior properties should be achieved at higher scan speeds between 800 mm/s and 880 mm/s.

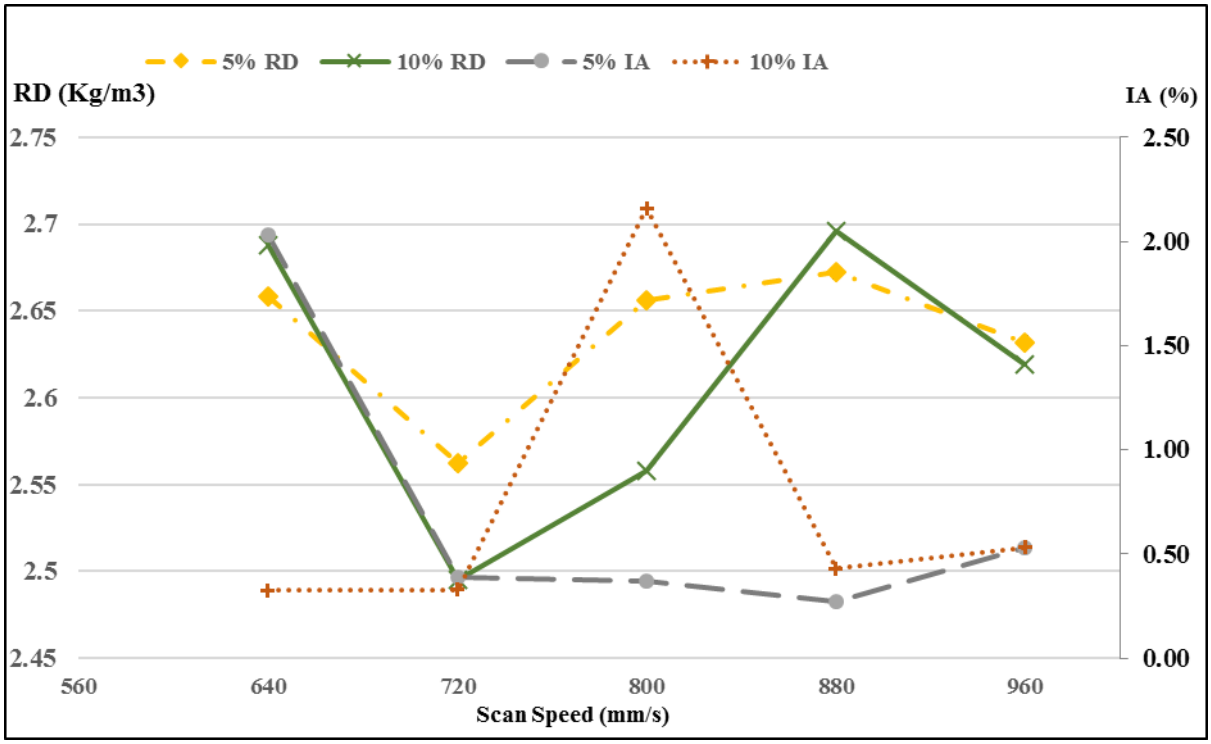

Figure 6.43 Effect of Scanning Speed on Relative Density and Porosity

6.3.5 Effect of Energy Density on Relative Density and Porosity

In Fig. 6.44, the effect of the energy density on the relative density of the Al-MMCs is investigated with the error bars at the top showing the percentage standard error at ± 0.004%. Spiering *et al*. (2011b) had established that for Aluminium alloys, the error in SLM density calculations ($\Delta\rho_{p)}$ utilising the modified Archimedes method is approximately 0.004 g/cm^3 and the error increases when the mass in air tends towards the mass in the fluid. Thus, the error obtained from the experiment is negligible, as the masses-in-air of the Al-MMC sample parts are greater than their respective masses-in-fluid.

It can also be observed that the densities obtained in only changing the scan speeds in Fig. 6.43 are higher than those obtained when both scanning speed and step-over are changed simultaneously in Fig. 6.44. As the step-over increased from 0.13 mm to 0.21 mm, the consolidation achieved from nearby tracks had obviously reduced leading to lower figures.

It is also important to note that the lowest density values were obtained for the scanning speed at the 60 J/m^3 ED in both figures despite the fact that the step-over in Fig. 6.11 was lower than that in Fig. 6.10. Rao *et al*. (2016) established that at ED below and above 50 J/m^3, the porosity increased significantly in the SLM of A357 Al alloy. The 10% is observed to have higher microstructural porosity from the IA values and the porosity decreases as ED decreases. The IA for the 5% however shows little change with respect to the change in the energy density. Read *et al*. (2015) observed that at low scan speeds, the effect of step-over is minimised, however, high scan speeds and step-over resulted into the formation of porosity due to insufficient weld pool overlap and incomplete melting.

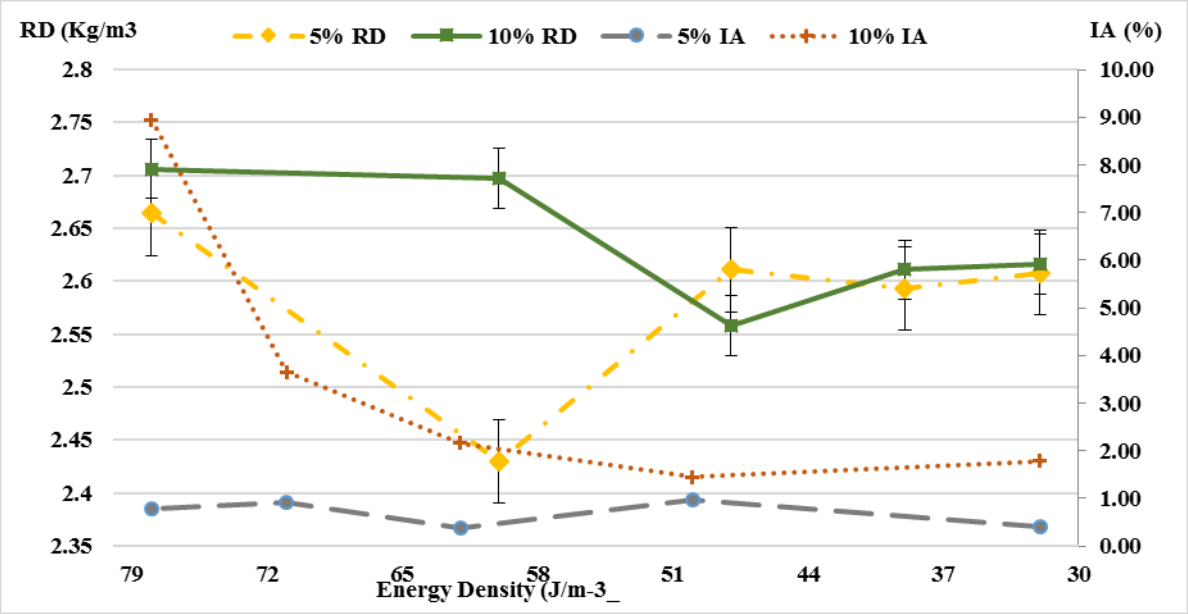

Figure 6.44 Effect of Energy Density on Relative Density

Overall, changing the scan speed and step-over simultaneously has been observed to produce samples with higher surface roughness, microstructural porosity and lower relative density. The 880 mm/s scan speed and 0.17 mm step-over has shown consistent values from the investigations and thus will be utilised in the mechanical characterisation of the composite.

6.3.6 Pore Classification on Variation of Scanning Speed and Energy Density

The unetched samples of the matrix alloy and the composites are given in Fig. 6.45 where both the top surfaces adjacent to the recoater blade and the core surface perpendicular to the recoater direction are viewed. Closed nano-pores, observed to be regular (mostly spherical) were discovered in the core and top surfaces of the matrix alloy and could be attributed to gas emission pores (hydrogen pores) (Weingarten, *et al.* 2015). These pores arise during LM

from discharged gasses that may have been trapped in individual powder particles (Aboulkhair, *et al.* 2014). Although irregular shaped and interconnected pores could also be observed, these were random and widely distributed and could not be termed as keyholes pores, which arise from melt instability.

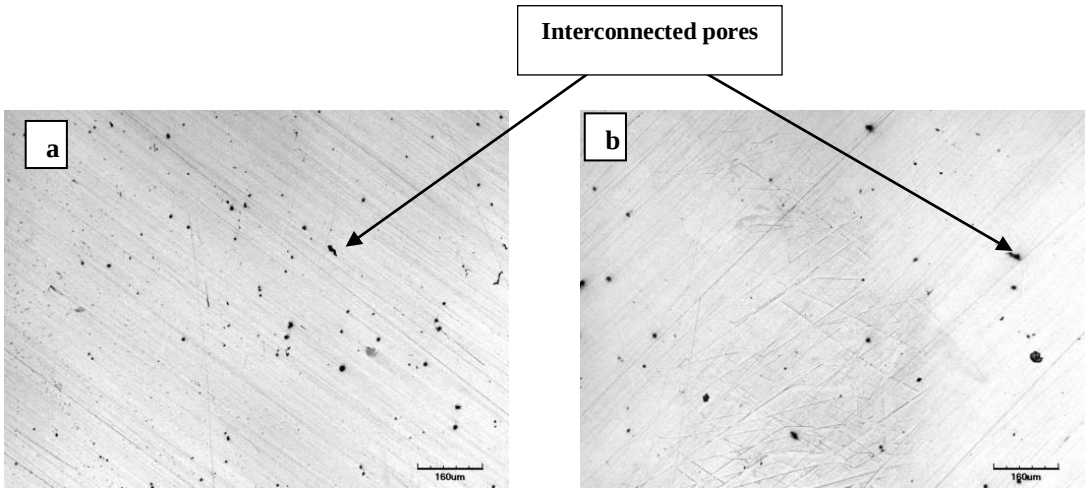

Figure 6.45 Unetched Matrix for Pore classification (a) Vertical Cross-section (b) Parallel Cross-section

The pore formation in the vertical and parallel samples of the 5 % and 10 % Al-MMCs were investigated (Fig. 6.46 and Fig. 6.48), changing only the scan speeds. The porosity in the vertical section gives an indication of the inter-layer closed pores as samples were sectioned through the layers to reveal the microstructure.

At low scan speeds, 640 mm/s and 720 mm/s, large pores were observed in the 5 % Al-MMC vertical samples, which could be attributed to the melt pool instability, previously identified on the single line tracks. The slow scan speed results in the vaporisation of the Al powder particles and the deep V-shaped melt pool created by the absorbed heat. These two phenomena thus lead to the entrapment of gas/vapour in the solidifying melt pool (Louvis, *et al.* 2011; Pang, *et al*. 2015). As the scan speed increases to 800 mm/s and 880 mm/s, the pores and pore size are seen to be reduced with little hydrogen pores observed in them. However, the amount of pores increased at the 960 mm/s scan speed, characterised by a combination of hydrogen pores and possibly condensate pores which have been caused by the entrapment of air/gases. The pores observed at this scan speed were dissimilar to the pores at lower scan speeds and are a result of the balling effect due to earlier identified Marangoni forces.

Scan Speed (mm/s) / Step-over (mm)	5% Al-MMC – Vertical samples	10% Al-MMC - Vertical samples
640/0.17	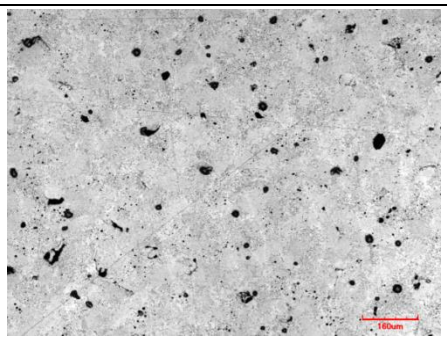	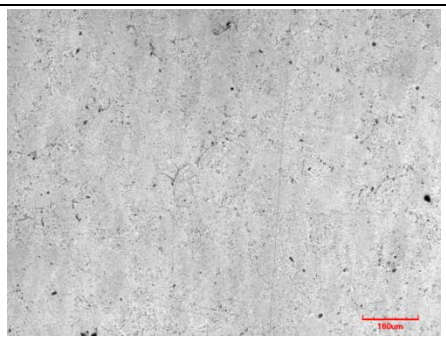
720/0.17	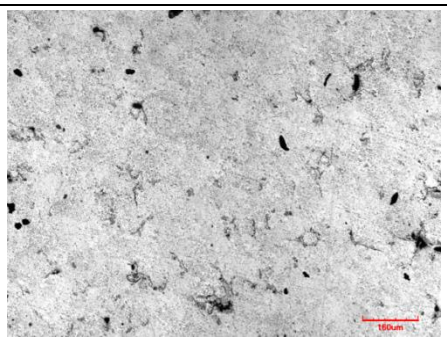	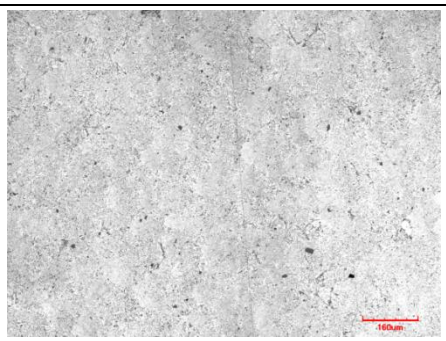
800/0.17	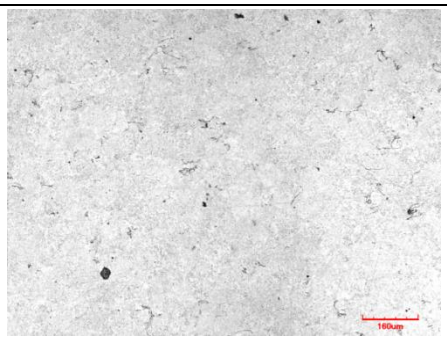	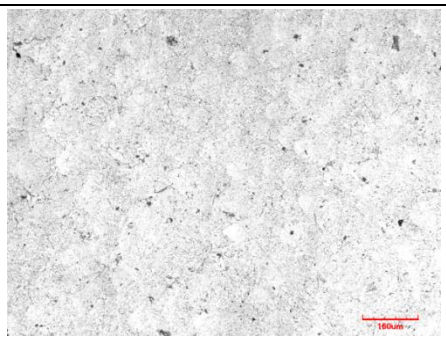
880/0.17	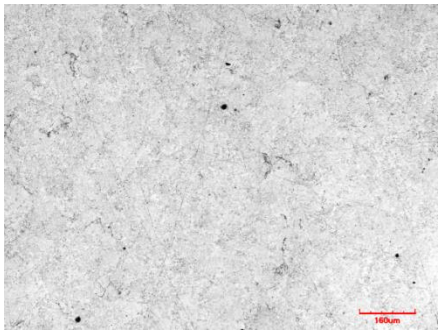	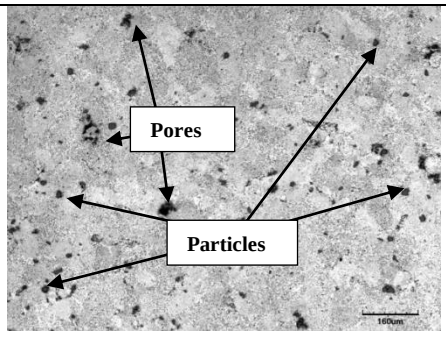
960/0.17	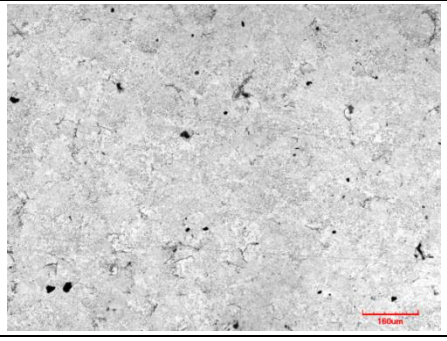	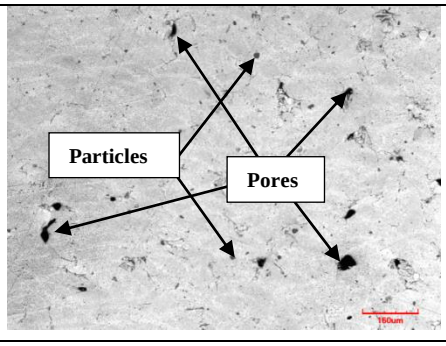

Figure 6.46 Pore classifications on vertical samples with changing scan speed

Scan Speed (mm/s) / Step-over (mm)	5% Al-MMC - Vertical Samples	10% Al-MMC - Vertical Samples
640/0.13		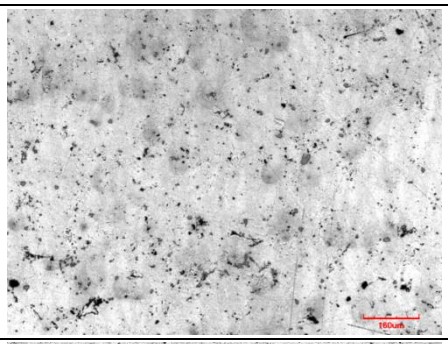
720/0.15	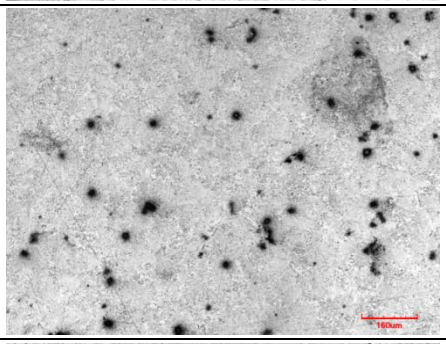	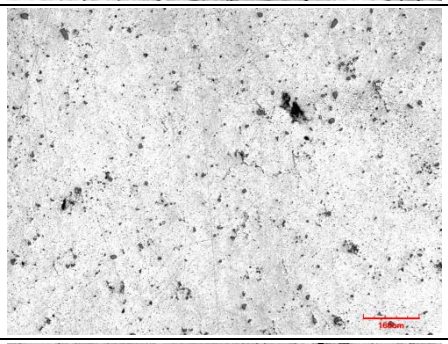
800/0.17	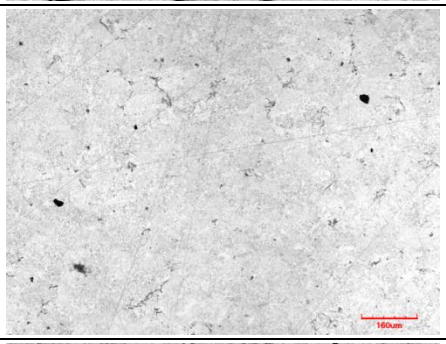	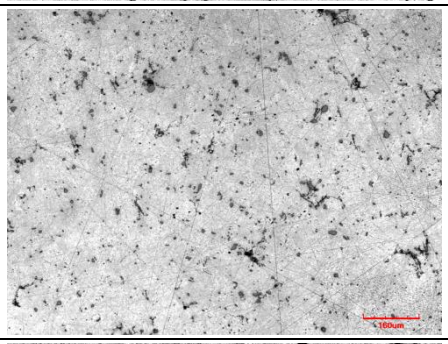
880/0.19	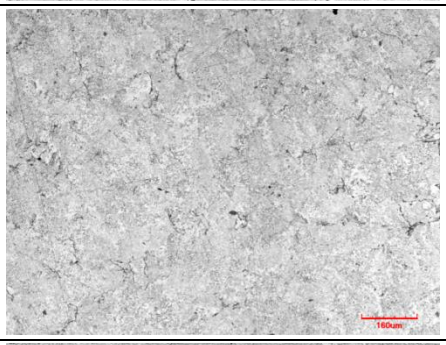	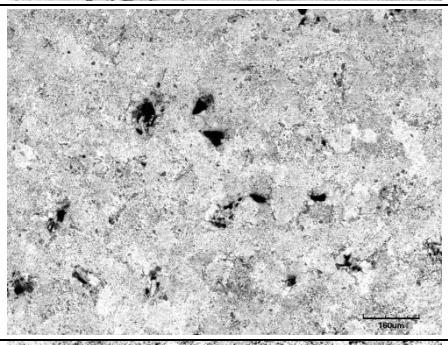
960/0.21	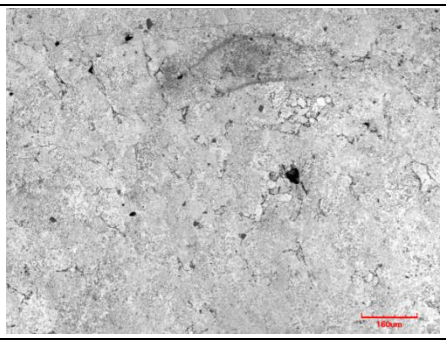	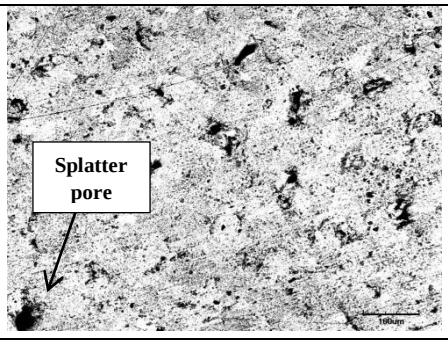

Figure 6.47 Pore classifications on vertical samples with changing energy density

Pore development on the parallel surfaces was aided by the increased splatter from the scan speed triggering the splatter balls into being deposited onto the successive layer thereby causing pores in the new layer, (Osakada and Shiomi, 2006). Interconnected pores therefore characterised the parallel samples especially at the 640 mm/s scan speed, due to the pulling out of the splatter and unmelted powder particles during recoating of a new layer. The parallel samples also displayed reduced pores at increasing scan speed although characterised with more interconnected pores.

Unlike the 5 % Al-MMC, hydrogen pores were more prevalent in the 10 % Al-MMC at the various scan speeds for the vertical samples, with the exception of the 880 mm/s and 960 mm/s scan speeds. The increase in the amount of hydrogen pores could be credited to internal particle porosity that may have increased during the mechanical alloying phase. The presence of embedded particles was also evident at these scan speeds which suggests particle delamination from the matrix. Particle delamination is a significant in the development of MMCs as it is a crack initiation point and as such usually prevented from occurring. The vertical samples for the 10% Al-MMC however displayed less pores in the core than on the surface, although with bigger interconnected pores. The bigger pores will lead to less bonding between the individual layers and therefore the composite is more susceptible to brittleness.

Fig. 6.47 and 6.49 show the unetched samples when both the scanning speed and step-over have been changed simultaneously. The 5% Al-MMC vertical samples with these parameters mostly have reduced pores as compared with the constant step over in the previous Fig. 6.46. The reduction in the step-over ensured that the overlap and HAZ were increased causing a large weld-pool and thereby reducing the pores. The only sample displaying significant pores is at the scan speed 720 mm/s and step-over of 0.15 mm that is characterised predominantly with hydrogen pores like that observed for the 640 mm/s-0.17 mm scan speed step-over combination. The pores on the parallel samples are fewer in number over the total area have bigger feret sizes and thus reduce the overall density of the part.

Scan Speed (mm/s) / Step-over (mm)	5% Al-MMC – Parallel Porosity	10% Al-MMC - Parallel Porosity
640/0.17	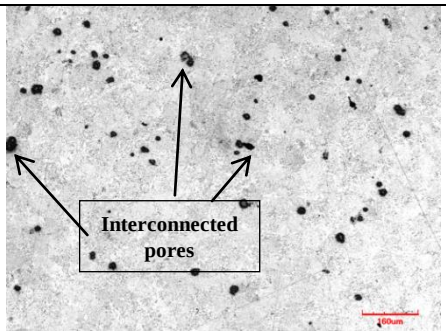	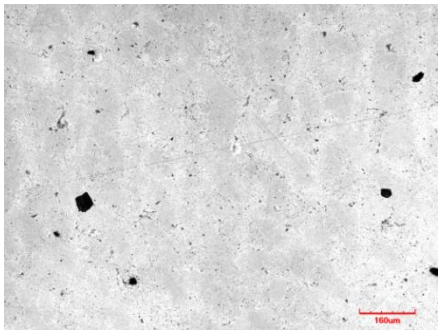
720/0.17	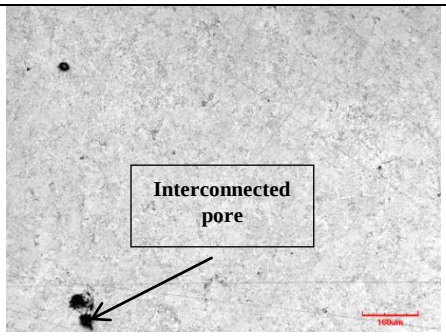	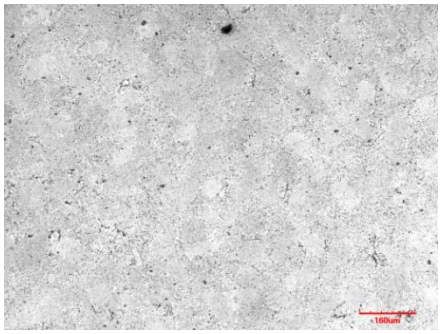
800/0.17	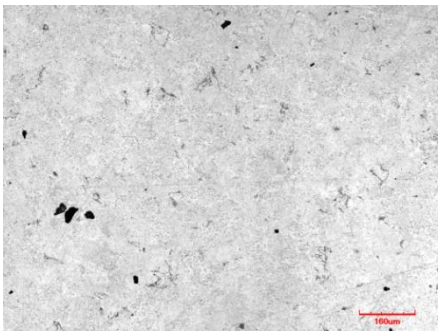	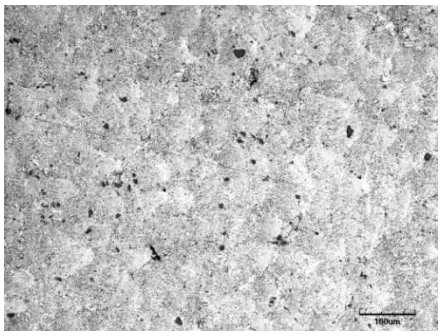
880/0.17	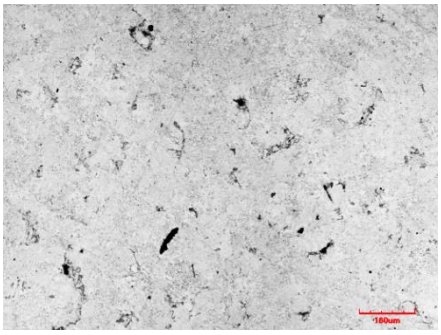	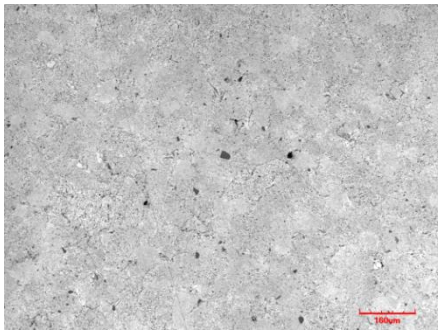
960/0.17	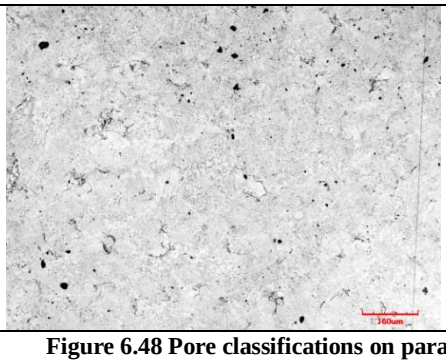	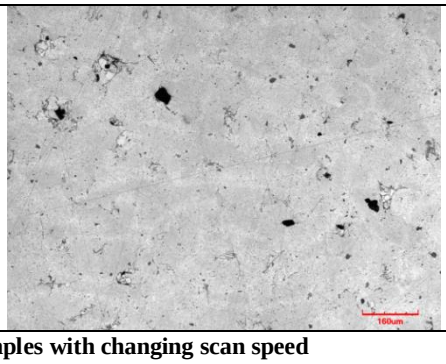

Figure 6.48 Pore classifications on parallel samples with changing scan speed

Scan Speed (mm/s) / Step-over (mm)	5% Al-MMC - Parallel Porosity	10% Al-MMC - Parallel Porosity
640/0.13	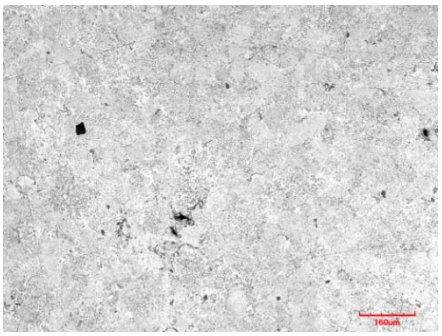	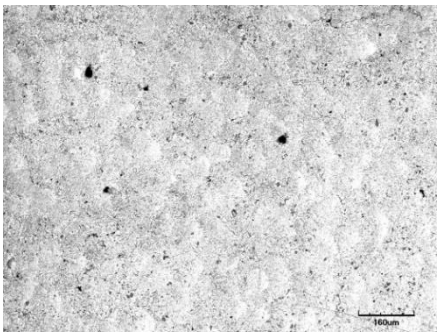
720/0.15	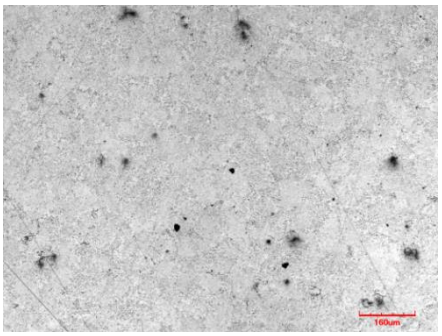	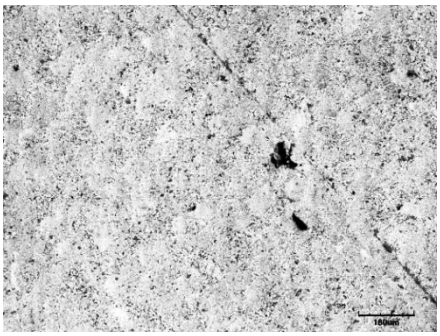
800/0.17	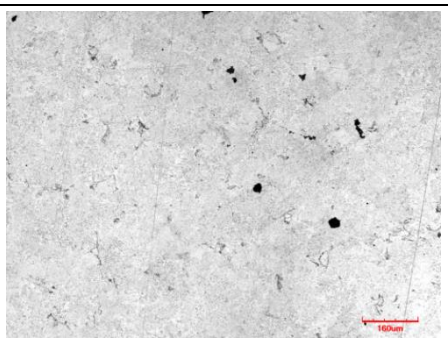	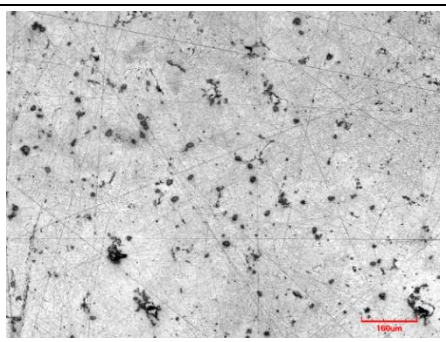
880/0.19	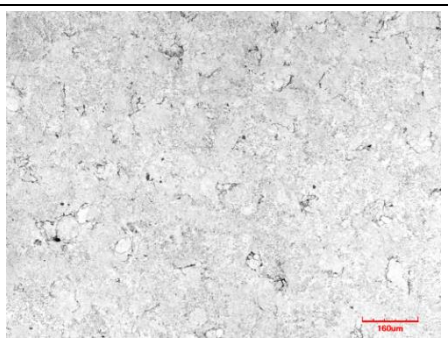	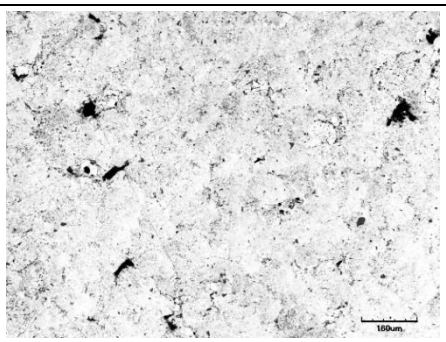
960/0.21	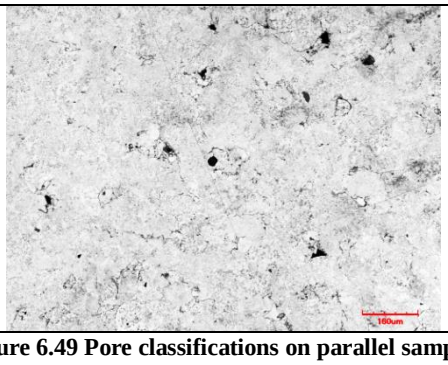	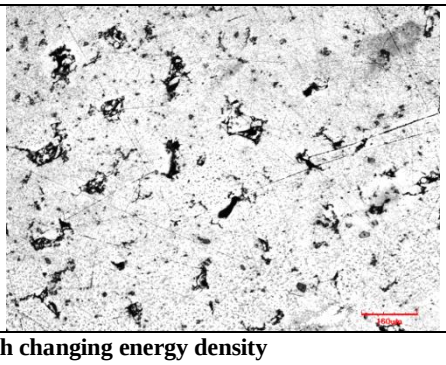

Figure 6.49 Pore classifications on parallel samples with changing energy density

The 10 % Al-MMC samples in Fig. 6.47 and 6.49, had additional pores and more particles were evident when both the scan speed and step-over changed simultaneously. The pores detected at these parameters were also larger than the previous experiment where the step-over had been kept constant. The samples scanned at the high scan speeds and step-overs; 880 mm/s -0.19 mm and 960 mm/s – 0.21 mm, exhibited the pore combination of the splatter and Marangoni forces resulting from incomplete melting of the powder particles. The pores in the parallel samples (Fig. 6.49) are observed to be increasing as the energy density decreases and the amount of molten powder increases. The resultant effect of changing the step-over and thereby varying the energy density for each scan speed therefore indicates that widening the step over will lead to porous samples despite the increased laser absorptivity with the introduction of SiC.

It has been observed generally therefore that the core is mostly characterised by blind gas pores that may not compromise the microstructural integrity of the part in insignificant amounts. In addition, the gas pores tend to increase at higher scan speed and lower energy density thus converting into interconnected pores that are crucial especially in the core (vertical sample) of the material. The 5% Al-MMC has also been established to present lower porosity values than the 10% Al-MMC despite the theoretical density suggesting otherwise.

6.4 Chapter Summary

This chapter focused on modifying the laser melting process parameters as phase 3 and 4 of the research. This included analysis of the single line tracks at different scan speeds, surface roughness of the density blocks, relative density and internal porosity measurement.

Single line tracks were observed in Phase 3, for their adhesion to the substrate and previous layers with the matrix alloy utilised as the control against which the scan tracks of the MMCs were measured against. Previous research had reported a distinct cylindrical shape track during the LM process with no apparent balling or areas of partial melting. The widths of the scan tracks were also investigated for the melt pool formation and width. The cylindrical shape was also confirmed during this research with the single track of the matrix alloy and the composites. The widths of the composite scanned tracks were observed to decrease at increasing scan speeds and percentage reinforcement volume fraction. A window for fabrication between 720 mm/s and 960 mm/s scan speed was observed for the composite powders.

Phase 4 focussed the research on the analysis of the density block starting with a visual inspection of the blocks. Cracks were observed in 10% reinforced Al-MMC blocks which were deemed a result of either increased internal thermal stresses or a reaction with the SiC particles. The surface roughness was next to be analysed for their indication into the packing density and thus the porosity of the blocks. The surface roughness values were higher at larger step-overs and lower energy densities and were also found to increase with increasing scan speed until an apparent critical speed of 800 mm/s. This thus highlighted the importance of both the scan speed and step-over in achieving full densification. The roughness of the 5% Al-MMC were observed to be better than that of the 10% Al-MMC indicative of a better packing density with the lower percentage volume reinforcement.

The relative density and porosity of the blocks were subsequently evaluated and high percentage of porosity was observed at both the low and high scan speeds. It was also observed that samples with higher surface roughness have lower relative densities. Changing the step-over also led to increased porosity, lower relative densities and higher surface roughness of the samples. This allowed the processing window be narrowed even further to 800 mm/s scan speed and 0.17 mm step-over.

The pores from the image analysis were investigated and found to comprise mostly of blond gas or hydrogen pores with some interconnected pores observed within the layers. The pores at the low scan speed were caused by Marangoni forces while at higher scan speed, pores were caused by gas and splatter entrapment. Changing the step-over and thereby varying the energy density led to porous samples despite the increased laser absorptivity with the introduction of SiC.

Chapter 7

Phase 5

Mechanical Testing and Microstructural Characterisation

7.1 Transverse Rupture Stress (TRS) and MicroHardness

Fig. 7.1 shows the plot of the flexural force against the flexural strain (deformation), with the flexural strength and yield strength calculated from Equation 4.7. The flexural strength, yield strength and modulus of elasticity for the AlSiMg/$SiC_{10\%}$ samples were not analysed due to fragmenting during their removal from the base plate, however, the micro-hardness values were examined. The abbreviations on the chart are as noted in Section 4.91 and Table 7.1 for the heat treated samples. Ashby and Jones (2012) stated that the rupture strength is usually higher than the tensile strength due the opposite forces of compression and tension acting on the bar. The compressive stress stops the propagation of cracks resulting from the pores due to contraction and the maximum tensile stress acts only on the point directly below the loads. Therefore, Equation 7.1 is utilised in determining the peak tensile strength that will cause the sample failure.

$$\sigma_{TS} = \frac{\sigma_f}{\{2(m+1)^2\}^{1/m}}$$

Equation 7.1 (*Ashby and Jones, *2012)

Where σ_{TS} is the tensile strength (MPa)

σ_f is the flexural strength (MPa)

m is the Weibull Modulus

The Weibull modulus expresses the rate of failure of a material as it approaches a critical strength (σ_0) given by Equation 7.2.

$$P_s = \exp\left\{-\left(\frac{\sigma}{\sigma_0}\right)^m\right\}$$

Equation 7.2 (Askeland *et al.* 2011)

where P is the probability of survival

V_0 is the volume of the sample (m^3)

σ is the applied stress (N/m^2)

σ_0 is the scaling parameter (dependent on specimen size and shape)

m is the Weibull Modulus

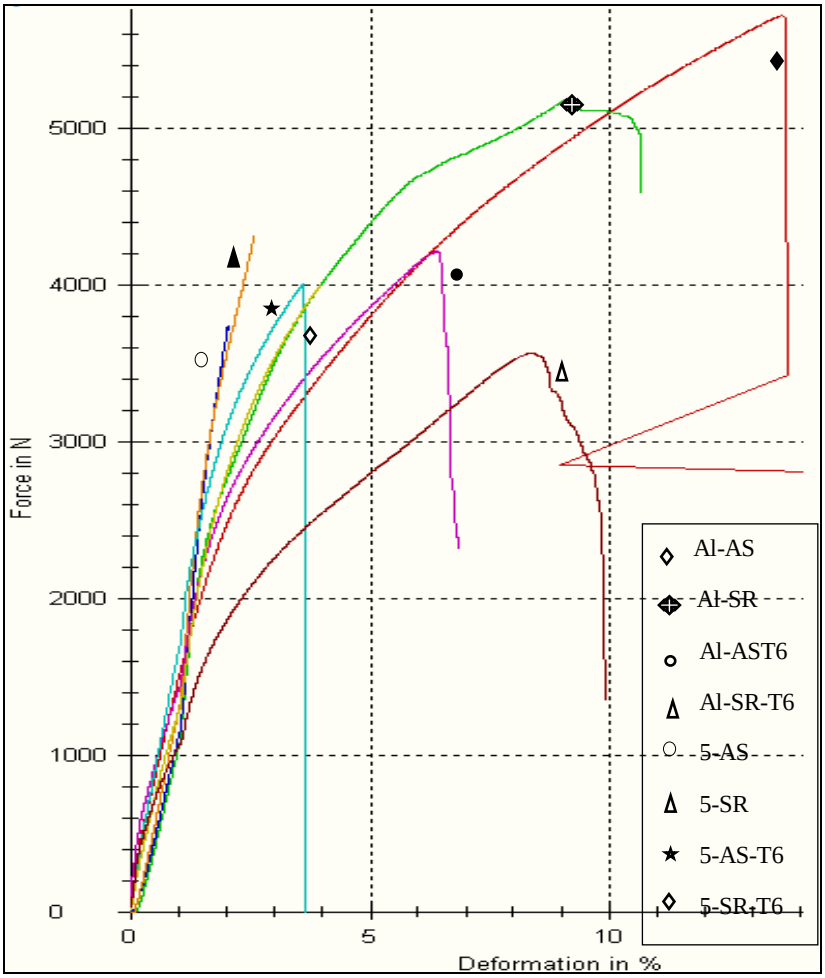

Figure 7.1 4-Point Transverse Rupture Strength Graph

Table 7.1 Specimen Heat Treatment Description

Al-AS	Al-matrix As-built
Al-SR	Al-matrix Stress Relieved
Al-AST6	Al-matrix As-built T6 heat treated
Al-SRT6	Al-matrix Stress Relieved T6 heat treated
5-AS	AlSi10Mg/$SiC_{5\%}$ As-built
5-SR	AlSi10Mg/$SiC_{5\%}$ Stress Relieved
5-AST6	AlSi10Mg/$SiC_{5\%}$ As-built T6 heat treated
5-SRT6	AlSi10Mg/$SiC_{5\%}$ Stress Relieved T6 heat treated

σ_0 and m are constants, where m expresses the reduction in strength as the applied stress approaches σ_0. To determine the tensile strength of the samples, the probability of survival is calculated using Equation 7.2,

$$P_s = 1 - \frac{j-0.375}{n+0.25}$$

Equation 7.3 **(Ashby and Jones, 2012)**

Equation 7.3 is based on Blom's estimation of the dependence of linear and j^{th} order statistics, where j is the rank number of the specimen and n is the total number of specimens. The Weibull distribution was calculated for each specimen by plotting the graph of the natural logs of Equation 7.2.

$$ln\left\{\frac{1}{P_s(V_0)}\right\} = \left(\frac{\sigma}{\sigma_0}\right)^m$$

Taking the natural log again gives…

$$\ln\left\{\ln\left(\frac{1}{P_s(V_0)}\right)\right\} = m\ln\sigma - m\ln\sigma_0$$ *Equation 7.4 (Ashby and Jones, 2012)*

The last term in the equation is a constant and when plotted in a graph, the slope gives the value of the m. Table 7.2 gives the calculated values for the Al-AS sample and Fig. 7.2 shows the graph with the slope given by the value before x in the equation.

Table 7.2 Natural log calculations of Flexural Force versus Probability survival

j	σ_F (MPa)	$\ln\sigma_F$	$\ln(1/P_s)$
1	563.64	6.33	-2.07
2	621.8	6.43	-0.99
3	636.32	6.46	-0.37
4	657.46	6.49	0.16
5	687.6	6.53	0.76

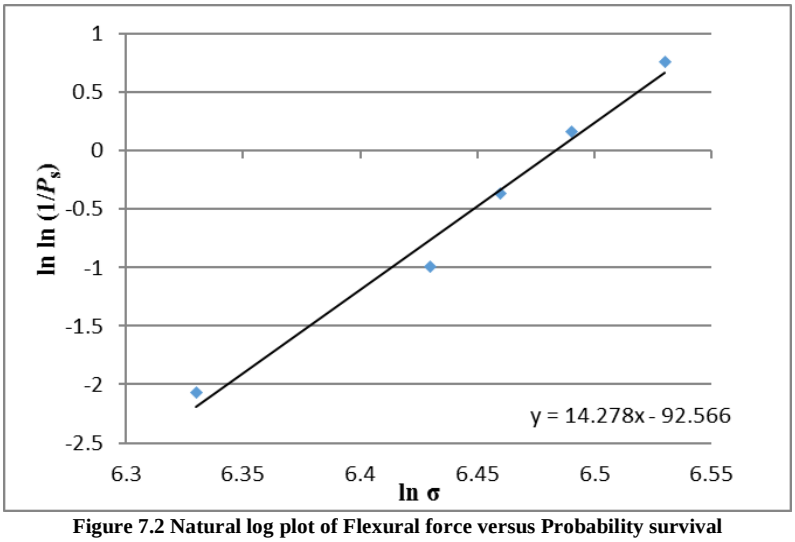

Figure 7.2 Natural log plot of Flexural force versus Probability survival

The Weibull plot and thus the Weibull distribution was calculated for each sample using Equation 7.4 with the results presented in Table 7.3. The average of five experimental flexural values are given in the table with the elastic modulus (Emod) obtained using the extensometer during testing.

The As-built matrix alloy (Al-AS) was observed to have the highest flexural strength and tensile strength. The calculated tensile strength is within the range obtainable in a standard tensile test as given by the EOS datasheet (2011). The tensile strength of the stress relieved matrix sample is also within the range specified on the datasheet. The T6 heat treated samples of the matrix display a remarked drop in strength values which may be attributed to the heat treatment regime. The strength values; both flexural and tensile, for the 5% AlSi10Mg/SiCp consistently had lower values than the matrix alloy with the as-built sample displaying the lowest values. Both the Tensile strength and Weibull modulus of the 5-AS samples have low values indicative of either an inhomogeneous mix during the powder blending stage (Rahman and Rashed, 2014), a reaction between the SiC and matrix alloy or the presence of thermal stress which caused premature failure. The causes of premature failure will be examined further through microstructural and fracture surface evaluation.

The strength of the matrix decreased when stress relieved at 300 °C, the EOS datasheet for the alloy also reported a similar trend after stress annealing. The reduction in strength could be attributed to improved ductility through the reduction of thermal stresses achieved from the stress-relieving regime. The variation in the micro–hardness is however diminutive, suggesting that the stress-relieving regime should not significantly affect the strength. In addition, the fracture mode changes from the ductile fracture observed in the as-built and stress relieved samples to a more brittle fracture when age hardened, Chen *et al*. (2008)

Conversely, the T6 heat treated samples had consistently lower strength values than both the as-built and stress-relieved samples. This could be attributed to over-aging of the material and the microstructure will be examined to confirm this. While the hardness of the as-built Al-AST6 sample decreased as with the tensile/flexural strengths, the hardness of the Al-SRT6 sample increased, with this attributed to the presence of coarse and flaky silicon particles precipitated out from the super saturated solid-solution during the solution treatment and aging process. The silicon particles contribute a higher strength to the matrix, however, due to its inherent brittleness; this strength is not imparted to the matrix, and therefore causing

failure at lower strengths as the applied load is not transferred effectively from the matrix into the reinforcing particles, Min and Cornie (2013).

Table 7.3 Mechanical Properties

Sample	Flexural Strength (FS) [MPa]	Tensile Strength (TS) [MPa]	Yield Strength (YS) [MPa]	Weibull Modulus	Secant Emod (Gpa)	Deformation (%)	Micro-hardness ($HV_{0.10}$)
AL-AS	633.36	412.00	274.34	14.23	68.71	3.72	154
AL-SR	573.38	302.73	299.03	7.93	74.45	2.78	151
AL-AST6	445.53	303.08	244.62	16.72	53.01	1.74	98.5
AL-SRT6	372.17	253.35	179.32	16.79	51.63	1.86	174.9
5-AS	415.52	196.93	398.44	6.24	69.23	0.525	92.6
5-SR	485.47	337.13	481.44	18.03	89.49	0.64	114.4
5-AST6	469.87	334.91	353.78	19.96	81.4	0.96	106.4
5-SRT6	449.22	300.68	274.80	15.78	73.41	0.92	110.5
10-AS	Not Measured	Not Measured	Not Measured	Not Measured	Not Measured	Not Measured	213.6
10-SR	Not Measured	Not Measured	Not Measured	Not Measured	Not Measured	Not Measured	184.9
10-AST6	Not Measured	Not Measured	Not Measured	Not Measured	Not Measured	Not Measured	135.0
10-SRT6	Not Measured	Not Measured	Not Measured	Not Measured	Not Measured	Not Measured	122.2

As observed in Fig. 7.1, the $AlSiC_{5\%}$ samples failed rapidly after the maximum strength, this suggests they experienced a brittle failure unlike the Al-matrix which had more deformation after the maximum stress. This is confirmed by the average maximum deformation values in Table 7.3, the as-built and stress relieved samples of the Al matrix have the highest deformation, while the $AlSiC_{5\%}$ composite had low values below 1% with the age hardened samples having higher values suggesting improved ductility with the aging regime. The

highest elastic modulus was observed with the composite, which is attributed to the addition of the SiC particles. The SiC particles have a higher resistance to deformation than the Al matrix and thus a higher modulus (430-445 GPa; Ashby and Jones (2012)), which explains the higher modulus for the composite.

Fig. 7.3 gives the effect of the heat treatment on the yield strength and flexural strength of the Al matrix and $AlSiC_{5\%}$. The Al matrix shows a decrease in strength with each heat treatment regime. However, the yield strength increased when it was stress relieved but decreased when age hardened. This supports the fact that the stress relieving regime improves the ductility of the sample with a compromise on the strength. It should be noted that although the flexural strength of the matrix reduced when stress relieved, the value at 573 MPa is still higher than those obtained for the composite. The yield strength of the composite samples was much higher than those of Al matrix although the flexural strength is lower. This suggests that the composites would withstand higher strengths in application but as failure occurred almost immediately after yield (brittle failure), the effective strength is reduced further. Min and Cornie (2013) advised that based on the scatter in the data obtained, the maximum allowable stress during design, should be set at 60% (approximately 230 MPa), of the maximum strength as an insignificant amount of parts would fail at this percentage. The age hardened composite samples deforms more elastically than the as-built and stress relieved sample although the strength is lower than that of the matrix. Overall, based on the strength values, the stress relieved samples denotes that this is the best heat treatment regime as it balances both the flexural and yield strength into acceptable properties.

The percentage reinforcement was plotted against the microhardness values in Fig. 7.4. The AST6 samples displayed the lowest hardness range for the heat treatment regimes. The as-built and stress relieved samples of the $AlSiC_{10\%}$ exhibited higher hardness values than both the alloy and $AlSiC_{5\%}$ indicating improved strength. As the samples fractured during the removal from the base plate, the strength values could not be measured. The discrepancy between the high hardness values and fractured sample may have been caused by either inhomogeneity of the phases in the composites, matrix-composite reaction or residual thermal stresses. Kumai *et al.* (1991) revealed internal stresses in the composite as a result of weak interface bonding which also manifests as microcracks within the composite structure.

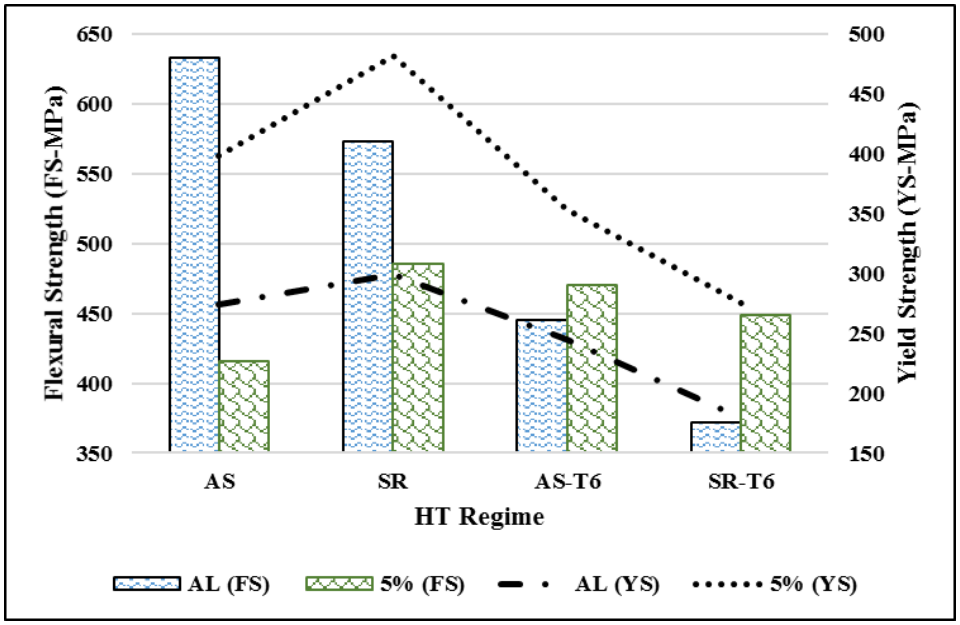

Fig. 7.3 Effect of heat treatment on the flexural and yield strength

Due to the thermal cycle during the LM process and the addition of the SiC reinforcement with a different thermal expansivity to that of the matrix, the risk of residual stresses is increased. The residual stress initiates microcracks into the part which thereby makes the material brittle. Alternatively, the SiC could have reacted with the Al matrix to form aluminium carbide which is hydrophilic. As the wire EDM machine utilises a water-based dielectric in cutting samples from the base plate, the aluminium carbide could have reacted with the water as in Equation 7.5:

$$4Al + 3SiC \rightarrow Al_4C_3 + 3\,Si$$

$$Al_4C_3 + 12\,H_2O \rightarrow 4\,Al(OH)_3 + 3\,CH_4$$

Equation 7.5 (Pech-Cahul, 2011)

The $AlSiC_{5\%}$ had the lowest hardness values overall for the percentage reinforcement which clarifies the low strength values obtained for the composites. Rahman and Rashed (2014) also experienced a drop in the hardness values at 5% reinforcement although an increase in strength was obtained simultaneously.

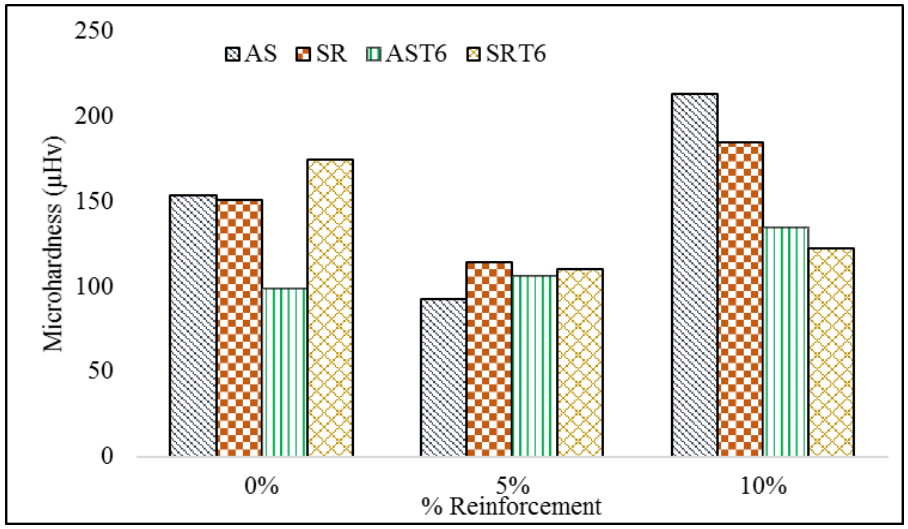

Figure 7.4 Micro-hardness as a function of percentage reinforcement

7.2 Microstructural Characterisation

The microstructure of the matrix and composites examined by the optical and scanning electron microscopes are utilised in determining the melt characteristics and grain size. The microstructure of the Al-AS sample (Fig. 7.5a) is characterised by half-cylindrical melt pools layered over each other. The distinctive shape is obtained from the LM process through the recoating and melting of successive powders layers which penetrate into the previous layers. At higher magnification, 5000 X (Fig. 7.5b) and 20,000 X (Fig. 7.5c) the grains are seen to consist of a network of cellular dendritic α-Al (light grey phase) and the eutectic phase comprising Al + β-Si (dark grey phase) Manfredi *et al.* (2013b) and Kempen *et al.* (2012).

As observed in the Al-Si phase diagram (Fig. 3.2), when Al-Si alloy containing 10% Si solidifies from the liquid phase, α-Al containing a maximum of 1.65% Si is the first to form. When the temperature of liquid reaches equilibrium, the Si-saturated melt simultaneously decreased the melting point of the liquid until at the eutectic (577 °C) a mixture of Al and Si will be obtained, (Sigworth, 2014). Two melt pools are visible in the areas highlighted in the microstructure in Fig. 7.5c with different orientation and contour patterns. There is a visible Heat Affected Zone (HAZ) with a differing orientation and dendrite shape between the two melts. Dendrites are oriented in the direction of heat dissipation which is usually along the (100) plane for cubic structures (Simchi and Godlinski, 2008; Dinda *et al.* 2012) with the HAZ having elongated dendrites due to the slower cooling rate than the melted area (Manfredi *et al.* 2013). EDS spot analysis confirms the presence of α-Al with almost 88 %

atomic weight, Si at 11%, Mg at 0.38 % and trace amounts of Fe and O_2 liberated from the internal pores of the powder particles. This composition is close to the composition given by the EOS specification.

In the review on Al-Si alloy solidification by Makhlouf and Guthy (2001), it concluded that the morphology of the eutectic phase was determined by its nucleation from the liquid phase and the addition of microstructure modifiers such as Tin (Sn) and titanium (Ti). The presence of these two elements in the AlSi10Mg alloy composition enables the aluminium to be nucleated first from the molten liquid by aiding to reduce the surface tension of liquid Al while the Si diffuses at a slower rate. The Sn reduces the attraction between the Si-Si covalent bonds thereby reducing the nucleating point for the eutectic Si. The addition of Mg should also initiate the precipitation of secondary hardening particles Mg_2Si, however this was not detected by the EDS analysis which is in agreement with Manfredi *et al*. (2013a).

The As-built microstructures of the composites, 5% Al-MMC and 10% Al-MMC in Fig. 7.5 (d-f) and Fig. 7.5 (g-i) respectively, possess smaller melt pools especially the 10% Al-MMC, compared with the matrix. The 5% Al-MMC at higher magnification, Fig. 7.5f, shows the α-Al dendritic network having a more fibrous layout due to a gradual coarsening of the dendrites arms. The coarsening can be attributed to dendrite growth and branch thickening (Flemings, 2005), due to the presence of the SiC particles which has increased heat absorptivity and reduced conductivity, thereby increasing the amount of time to achieve solidification as the rate of heat dissipation is reduced. Solidification time has also been known to influence dendrite arm spacing, (Spear and Gardner, 1963), therefore as the solidification time increases, the larger and coarser the dendrites, Sigworth (2014).

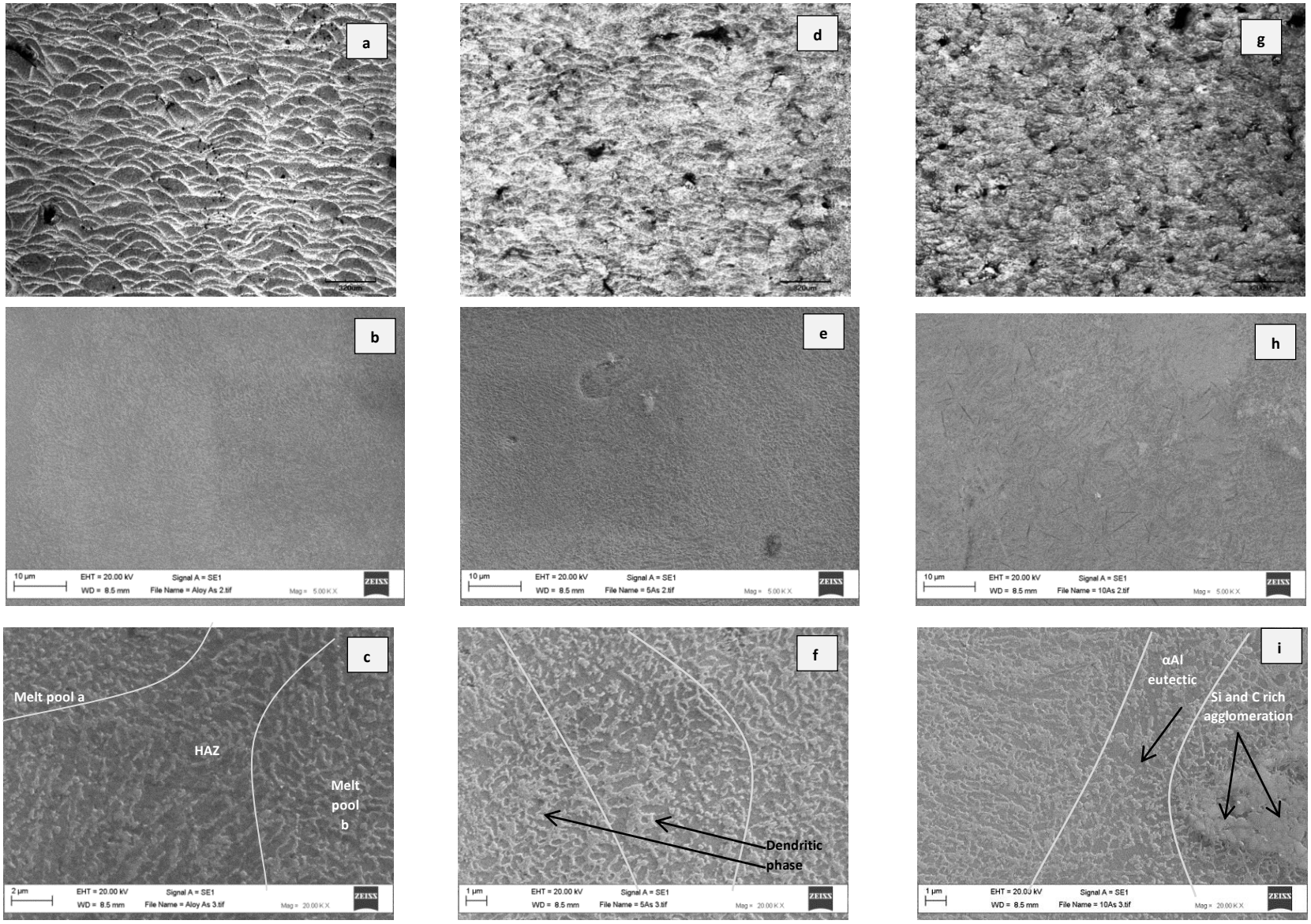

Figure 7.5 Microstructure of As-Built samples taken at magnification - 5X, 5KX and 20KX (a-c) Matrix Alloy (d-f) 5% Al-MMC (g-i) 10% Al-MMC

The Al percentage in the eutectic phase was also depleted by about 15% when measured with the EDS analysis. This suggests that the nucleation mode of the eutectic phase changed due to the addition of the SiC particles, leading the Al to nucleate at a slower rate from the matrix. This allows the Si to have additional time to nucleate at the eutectic phase thereby leading to a lower percentage of Al present in the microstructure. The EDS analysis however showed evidence of C and increased Si in the dendritic phase although the SiC particles were not visible at higher 20000 X magnification and 10000 X backscatter images. There is little difference in the diffraction pattern of both the as-built matrix alloy (Fig. 7.9a) and the as-built 5% Al-MMC (Fig. 7.9b) as the peaks in both figures correspond. However, minute differences in the 2theta angles and the intensities of the phases obtained indicate that when the alloy was reinforced with 5% SiC, the SiC particles reacted with the molten Al alloy. From literature on the Al-SiC MMCs, Aluminium has been known to preferentially react with the carbon in its formation of Aluminium carbide; however, this was not detected in the 5% Al-MMC, Pech-Cahul (2011).

The 10% Al-MMC in Fig 7.5i exhibits three distinct different phases; the base phase is the eutectic mixture of Al and Si, the dendritic α-Al phase and a lamellar agglomeration that is rich in the Si and C but depleted Al, which suggests an agglomeration of the SiC particles. The coarsening of the dendrites is higher, evidenced by a reduction of the dendrite spacing caused by increased particle reinforcement. The eutectic mixture also has about 17% reduced Al while the Al in the agglomeration is depleted about 37.5%. The XRD data for the as-built 10% Al-MMC (Fig. 7.9c) is significantly different from the both the matrix alloys and 5% Al-MMC. The addition of the 10% SiC triggered the formation of aluminium carbide in the reinforced sample thereby leaving residual Si in the molten metal. As a result of the Al depletion from the melt due to the formation of Al_4C_3, the eutectic mixture therefore becomes supersaturated with Si resulting in a hypereutectic solution. The supersaturated mixture also assists the coarsening of the dendrites due to an increase in Si in the melt regarded as an impurity to the pure Al leading to a corresponding change in the melt characteristics. Unlike the matrix and 5% Al-MMC, the supersaturated solution recrystallizes into three different phases; α-Al dendrites, the eutectic mixture and the residual Si combines with the Al to form an intermetallic phase $Al_{3.21}Si_{0.47}$. The higher depletion of Al can therefore be attributed to the formation of both the intermetallic phase $Al_{3.21}Si_{0.47}$ and the deleterious phase Al_4C_3.

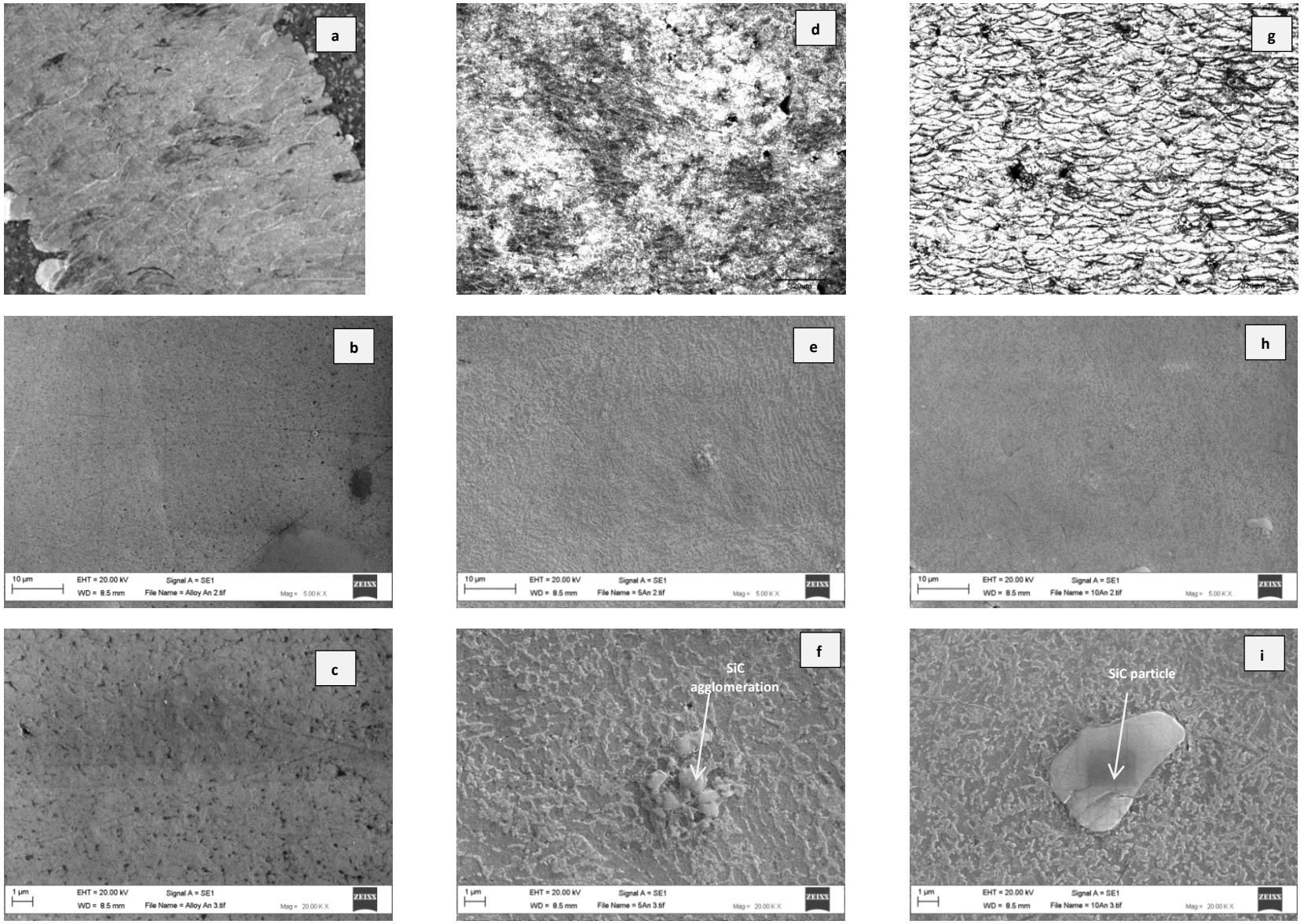

Figure 7.6 Microstructure of Stress Relieved samples taken at magnification - 5X, 5KX and 20KX (a-c) Matrix Alloy (d-f) 5% Al-MMC (g-i) 10% Al-MMC

The annealed sample of the matrix in Fig. 7.6(a-c) exhibits a homogenous microstructure of the eutectic phase with little change in the composition of the eutectic phase from the As-built sample. The annealing process has refined the dendritic phase as its prominence in the microstructure had reduced.

The composites samples also displayed a reduced dendritic network of Al phase, as the dendrite spacing seems larger than the as-built samples. The eutectic has increased Si and C and an agglomeration of SiC particles is evident in the 5% Al-MMC (Fig. 7.6f). A larger SiC particle found in the 10% Al-MMC (Fig. 7.6i) suggests a contamination from earlier experiment utilising the larger particle size of 10 µm. Particle cracking is evident on the particle which leads to the poorer mechanical properties, however, as the large particles are not homogeneous, it was considered negligible to the overall properties of the Al-MMC. The coarsening dendritic phase is however more prominent in the annealed condition than in the as-built condition.

Samples aged with the T6 heat treatment showed remarkably different microstructures to the AS and SR samples as the melt pools are no longer evident in all T6 samples at lower magnifications in Fig 7.7 (a; d; g) and Fig. 7.8 (a; d; g). Brandl *et al*. (2012) also observed this in their T6 heat treatment of AlSi10Mg alloy that had been manufactured through the Trumpf SLM process. At higher magnifications Fig 7.7 (c; f; i) and Fig. 7.8 (c; f; i), the dendritic α-Al has disappeared and the base phase identified as the eutectic mixture of Al and Si while the globular microstructure was identified as secondary Si particles which have precipitated out of the melt due to the heat treatment. Prashanth *et al.* (2014) considered this to have been due the rejection of Si from the supersaturated Al lattice with increasing annealing temperature

The T6 heat treatment dissolves the Al and Si until a homogeneous solid solution is achieved in the solutionising treatment at 560 °C leading to the disappearance of the dendritic phase. When the solid solution was quenched to room temperature, a supersaturated solid solution was achieved containing a fraction of the retained Si, which would have been dissolved in the α-Al at 1.26% from the Al-Si phase diagram. As the diffusion time for the atoms is reduced due to the rapid quenching, the dendrites do not have time to nucleate and thus do not reappear. The artificial aging at 160 °C therefore induces the precipitation of secondary phases meant to impede dislocations.

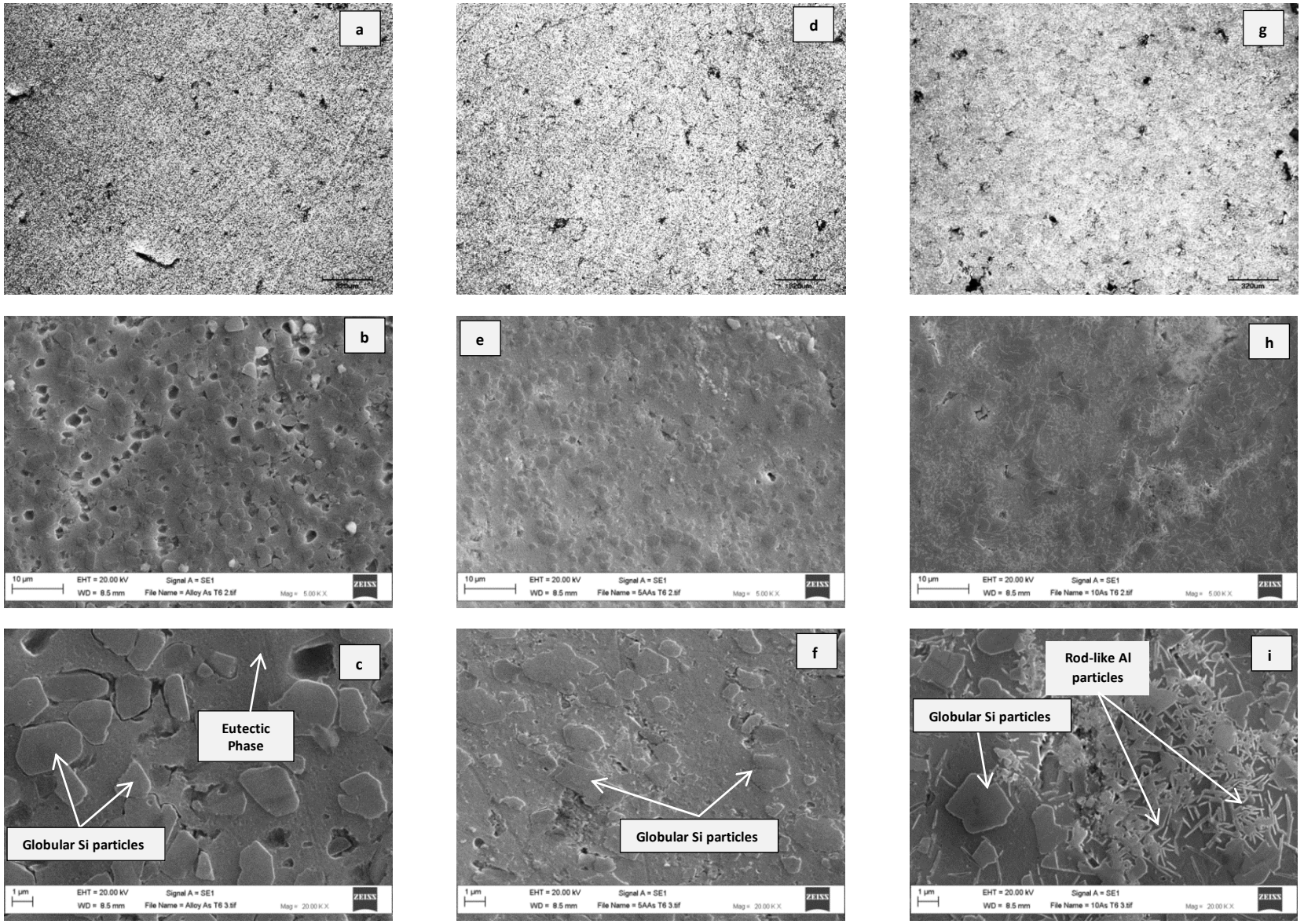

Figure 7.7 Microstructure of As-Built-T6 samples taken at magnification - 5X, 5KX and 20KX (a-c) Matrix Alloy (d-f) 5% Al-MMC (g-i) 10% Al-MMC

The precipitates were identified as globular Si phase using EDS and although the presence of Al-Fe intermetallics was expected, none was visible or detected by either the SEM, EDS or XRD testing. The Si precipitates observed in Figs. 7.7 c, f, i and Figs. 7.8 c, f, i, appear to be coarse and flaky suggesting an over-aging of the matrix resulting from prolonged heat treatment at the aging temperature. The coarse precipitates decrease the interfacial energy between the precipitates and the matrix, with smaller precipitates dissolving into the larger particles while the volume fraction of the precipitates remains constant, otherwise known as Ostwald ripening, (Martin, 1980). The coarse Si particles result in larger inter-particle spacing which reduces the shear stress needed for Orowan strengthening and according to Orowan equation (Equation 7.6), the larger the inter-particle spacing, the lower the strength of the material.

$$\Delta\tau = \frac{2T_i}{\lambda b}$$ ***Equation 7.6 (Martin, 1980)***

Where $\Delta\tau$ = Increase in shear stress (N/m^2)

T_i = Line Tension of bowing dislocations

b = Burgers vector for dislocations

λ = Mean interplanar spacing.

Thus the coarse Si particles accounts for the lower TRS values for the T6 aged samples aided by the brittleness of the coarse Si phase in Al-alloys.

The As-built T6 sample of the 10% Al-MMC Fig. 7.7i also shows that the eutectic composition is saturated with Si precipitates and the presence of rod-like precipitates identified most likely as the metastable phase β' Mg_2Si while the tiny needle-like phase also observed in the 5% Al-MMC Fig. 6.56f) were identified as the β'' phase from earlier literature review (Section 3.4.6). No rod-like or needle-like phase were observed in the matrix composition, however the presence of these phases in the composite suggests that due to lower dissipation of heat, the SiC particles acted as heat sinks, thus did not allow the full transformation of the β' and β'' into the stable Mg_2Si. This explains why no evidence of the precipitates were found and subsequently why no appreciable increase in the strength of the T6 heat treated samples. Ideally, the Si precipitates aid in increasing hardness and strength of the composite due to having superior properties to Al by interlacing with the dendrite network, however, the presence of the microcracks around the Si-precipitation rods, explains

the low strength and hardness values obtained as rather than impede dislocation, the microcracks would absorb any applied stress and propagate the cracks within the material.

The microstructure of the Stress relieved T6 samples are similar to the as-built T6 samples. However, the stress-relieving procedure, which is similar to the annealing procedure, aided in the growth of the as-built grain size due to decreasing the cooling gradient. This has therefore led to the increased globules when the samples were heat treated with the T6 regime.

The detachment of the globules from the matrix seems is more pronounced in the matrix alloy in Fig 7.8c. The 5% Al-MM SR T6 Fig. 7.8e and the 10% Al-MMC SR T6 Fig. 7.8h both exhibits higher ratio of globular phase than the AST6 samples. Higher magnification for the 5% Al-MM SR T6 in Fig. 7.8f displays small precipitates which explains the higher hardness values to the 10% Al-MMC SRT6. Like in the 10% Al-MMC AST6 sample, the presence of microcracks can be observed near the nucleating sites of the Si-rod precipitates in the 10% Al-MMC SR T6 Fig. 7.8i.

The formation of the intermetallic Mg_2Si normally present in Al-alloys with similar composition when casted and heat treated with the T6 regime has been noticeably absent throughout the whole heat treatment regime described in the research. This does not however, discount its formation entirely as it may be present in minute size and volume fractions not identifiable with either the SEM or XRD.

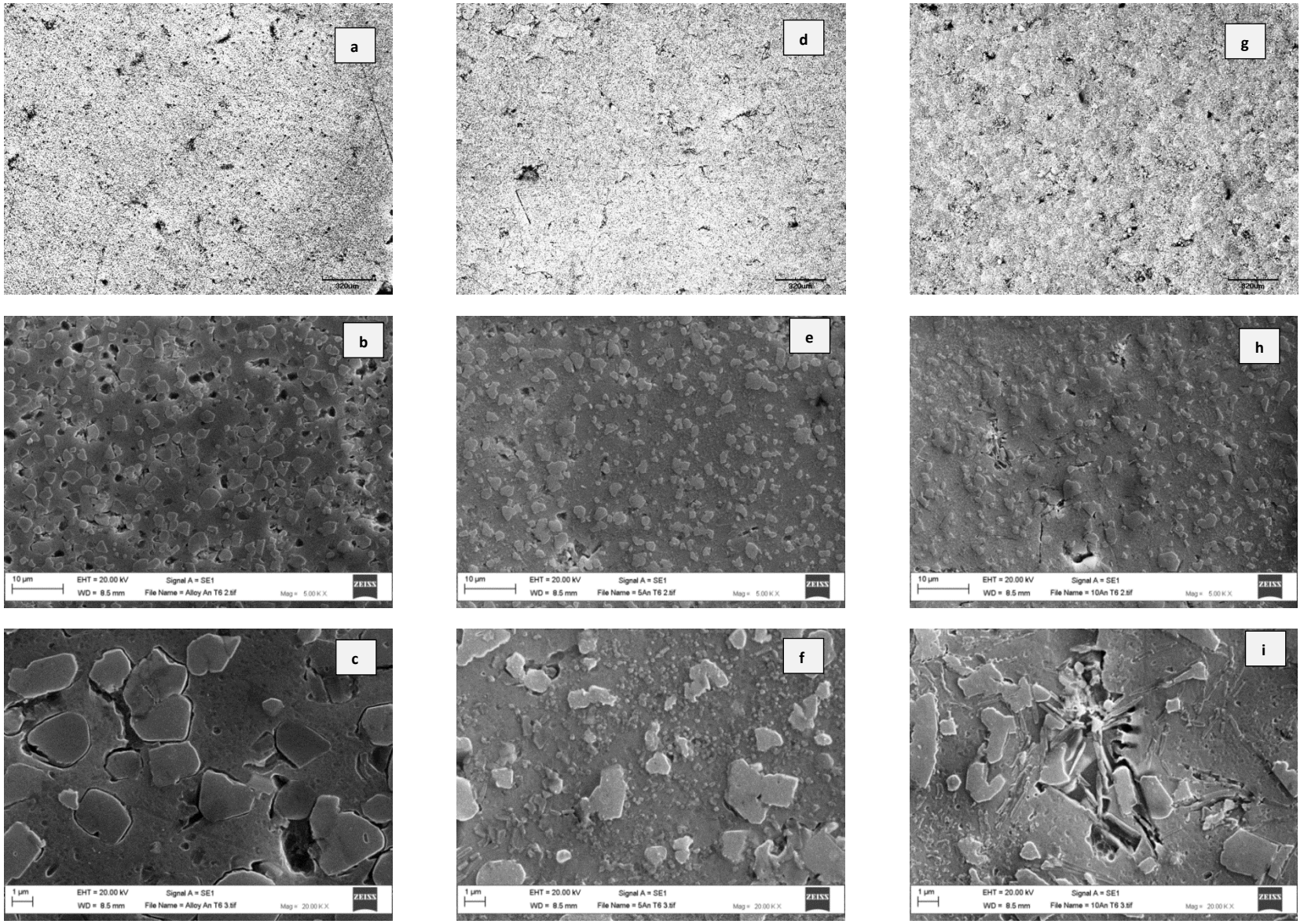

Figure 7.8 Microstructure of Stress Relieved-T6 samples taken at magnification - 5X, 5KX and 20KX (a-c) Matrix Alloy (d-f) 5% Al-MMC (g-i) 10% Al-MMC

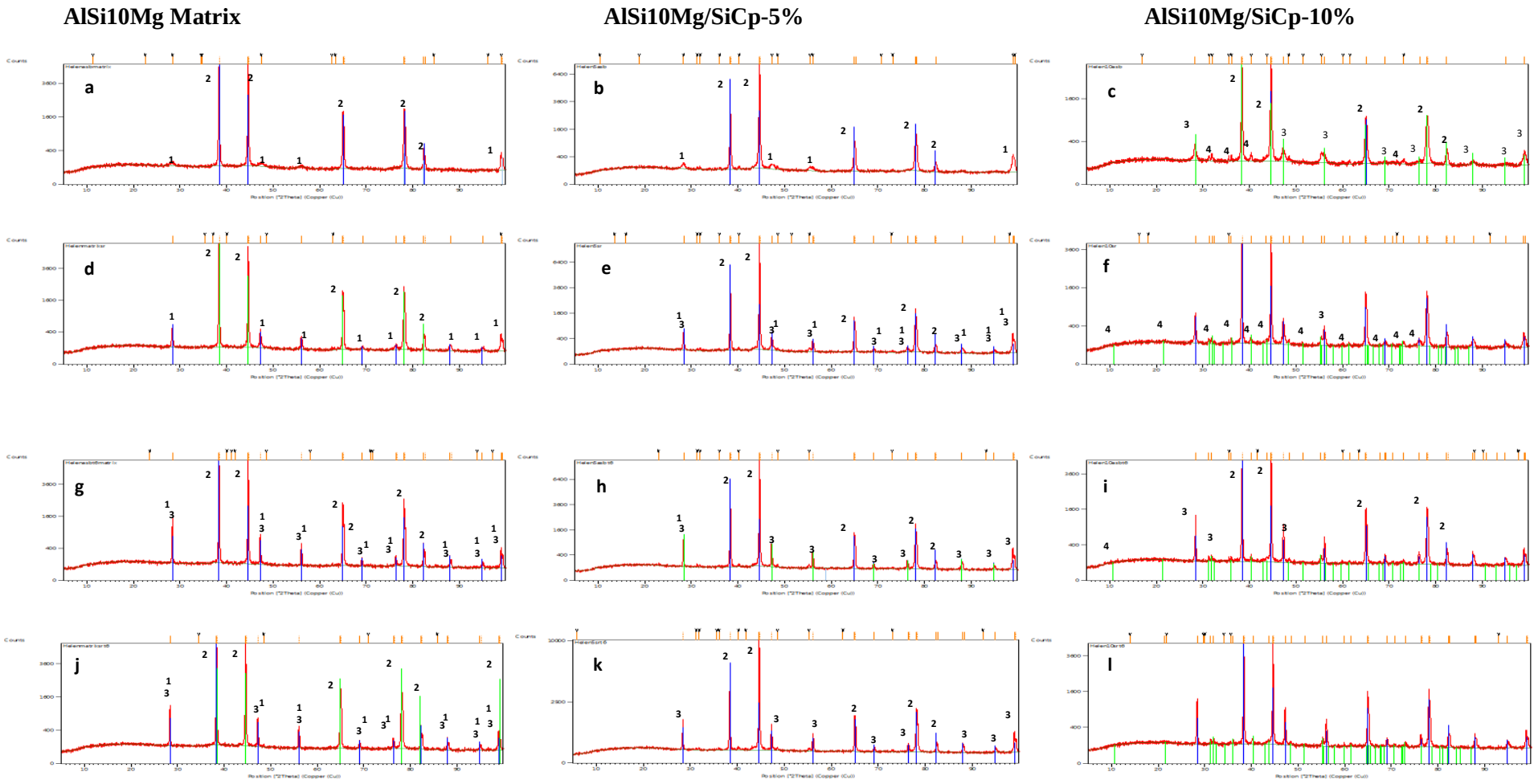

Figure 7.9 XRD Pattern of the matrix alloy, 5% Al-MMC, 10% Al-MMC (a, b, c) As-Built (d, e, f) Stress Relieved (g, h, i) As-Built T6 (j, k, l) Stress Relieved T6. Phases (Peaks) identified (1) β-Si (2) α-Al (3) $Al_{3.21}Si_{0.47}$ (4) Al_4C_3

7.3 Fracture Surfaces

The surfaces of the fractured samples were examined in order to understand the mode of fracture prevalent in the samples. It should be noted that the As-Built and As-Built-T6 samples of the matrix alloy did not fracture however, the tests were stopped when the samples buckled before reaching maximum loading of 20 KN. Other samples fractured along the tensile loading direction where samples experienced the maximum shear moment.

The Al-SR sample was characterised by dimples with an average of about 809 nm diameter indicating the ductile fracture experienced by the sample. Manfredi *et al*. (2013b) observed that the tensile fracture of AlSi10Mg-SR was characterised by the growth and coalescence of microvoids prevalent in the microstructure. The microvoids can be observed in Fig. 7.10b while the larger pores can be observed near the tensile border of the sample (Fig. 7.10a). It can be concluded that these 'borderline pores' initiated the crack which then propagated throughout the sample.

The fracture surface of the 5% Al-MMC was also characterised by a combination of ductile fracture and shear failure for both the as-built sample and the stress-relieved sample. The as-built sample (Fig. 7.11) were observed to have microvoids (4 µm) and a particle of un-melted powder was also observed in the fracture surface. The crack was observed to have started from a microvoid close to the surface and can be seen propagating in the arrow direction. Fig. 7.11b shows the microvoids and dimpled structure of the fracture surface. The dimples in the sample were larger (2.8 µm) than the those of the Al-SR sample. Larger dimples sizes are usually indicative of a loss in ductility and strength of the sample, which confirms the result of the TRS testing.

The stress relieved sample (Fig. 7.12) is also characterised with microvoids and microscopic cracks can be observed on the fracture surface. Two types of cracks were observed in Fig. 7.12, the propagating crack from the edge seen between the double lines and the intra-granular cracking within the circle. The microvoids and dimples however are about the same average size (4 µm) with the as built 5% Al-MMC.

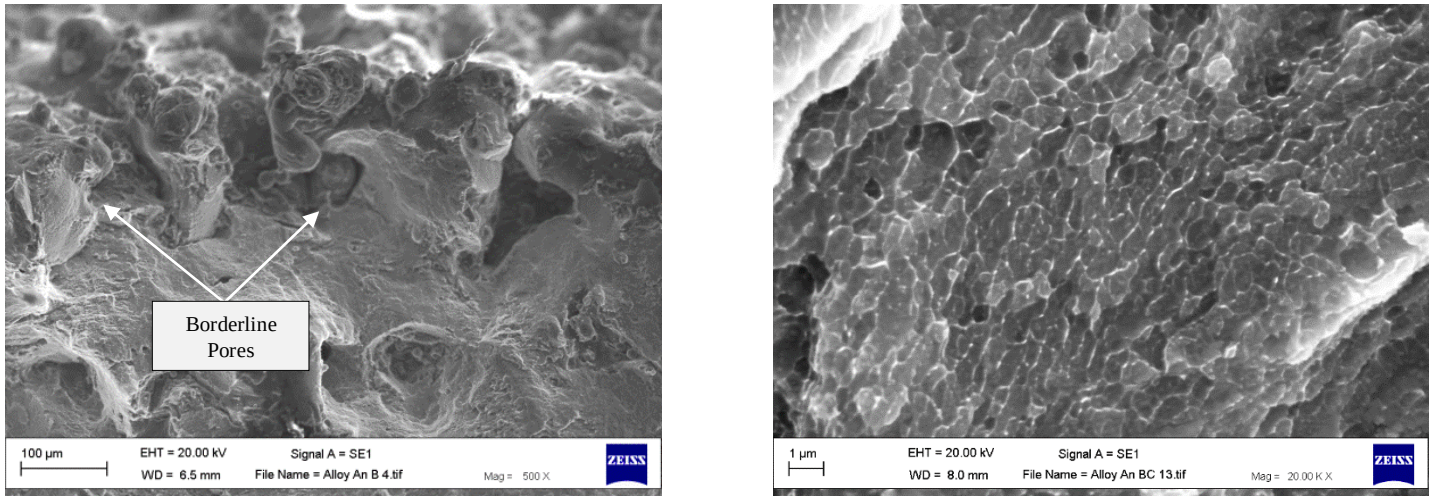

Figure 7.10 Fracture surface of Alloy SR

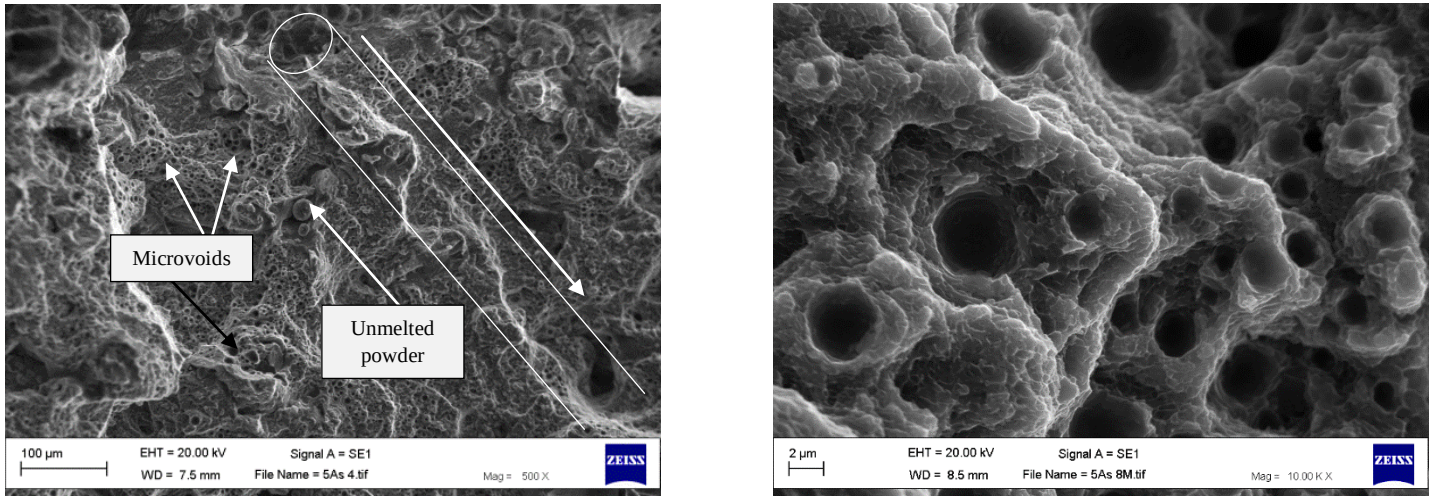

Figure 7.11 Fracture surface of 5-AS Al-MMC

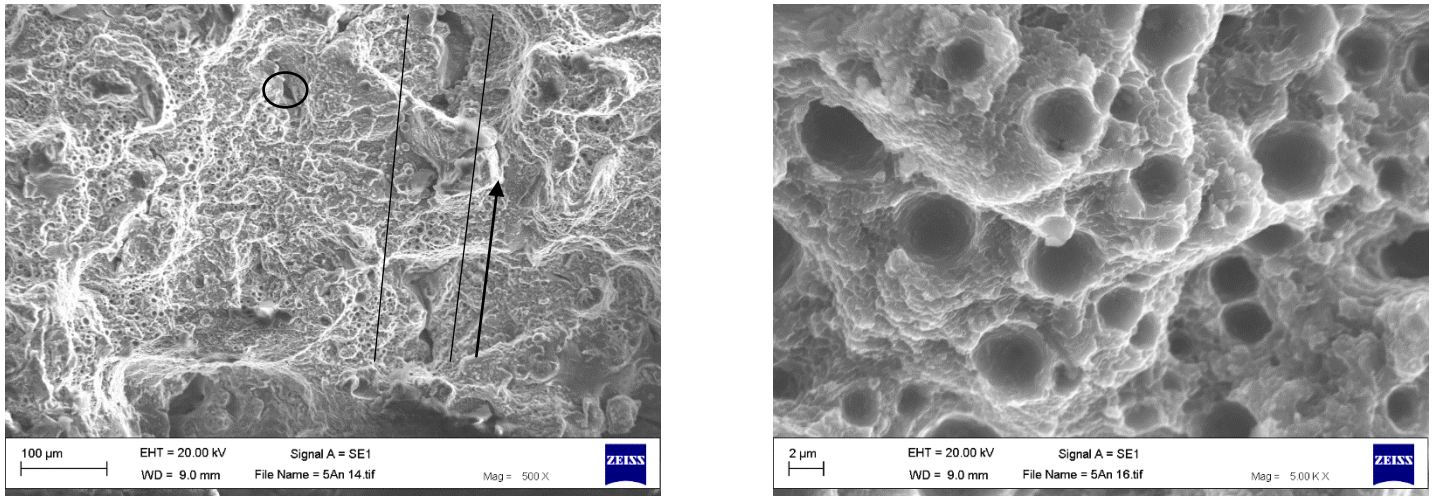

Figure 7.12 Fracture surface of 5%-SR Al-MMC

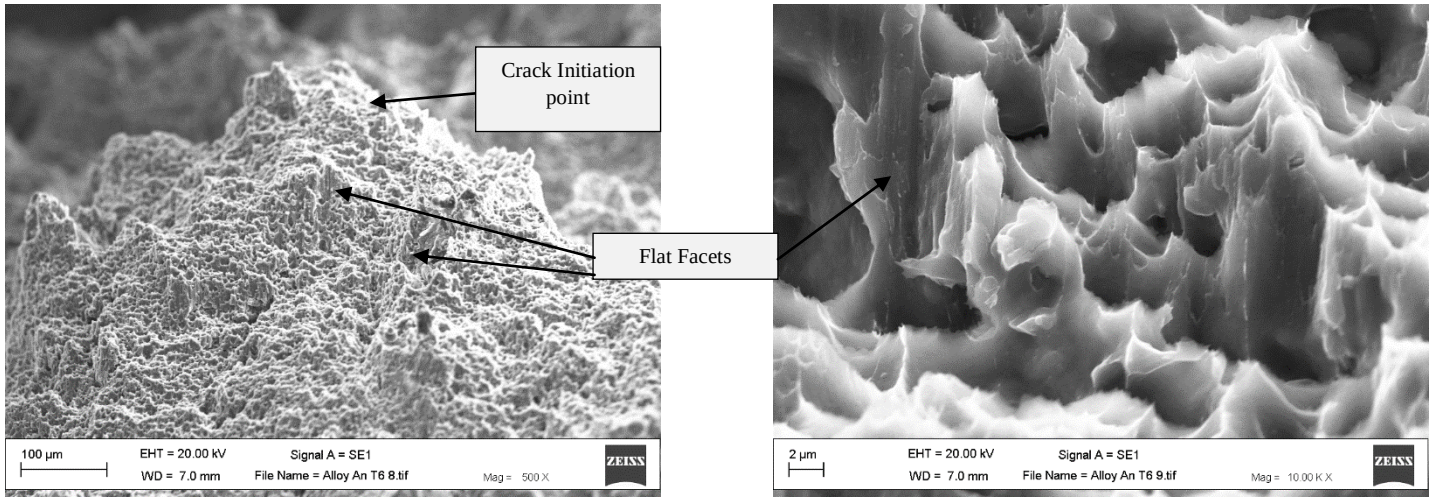

Figure 7.13 Fracture surface of Al-SR T6 specimen

The T6 heat treated samples were all characterised by cleavage fracture unlike the previous specimens. The cleavage of the Al-SR-T6 sample (Fig. 7.13a) was particularly elongated representative of a transgranular fracture whereby the fracture passes through the grain resulting in flat facets. Although a few dimples 3.6 μm diameter were observed at higher magnification (Fig. 7.13b), these were elongated and the faceted microstructure is readily evident. The 5% AS-T6 Al-MMC was characterised by the presence and coalescence of microvoids (Fig. 7.14a) pervading the fractured surface. Higher magnifications (Fig. 7.14b) however, exhibit the features of both transgranular and intergranular fracture along with the presence of microcracks. The surface of the voids was also filled with fractured silicon particles which contribute to the fracture propagation by due to the inherent brittleness of the coarse Si phase. The 5% SR-T6-Al-MMC has a similar fractography as that of the as-built-5% Al-MMC, however the cleavage failure is more evident in Fig. 7.15a and the microvoids and microcracks are seen to be larger (approximately 4 μm) (Fig. 7.15b).

Although none of the 10% reinforced Al-MMC samples could be tested and fractured, the edges of the damaged samples of the as-built and stress relieved samples were examined. Both samples (Fig. 7.16 and Fig. 7.17) exhibited macro-cracks and matrix delamination which in combination with each other is indicative of a thermal expansion crack. In Fig.7.16a, an agglomerated cluster highlighted was identified as aluminium carbide. However, the small needle like dendrites visible on the damaged surface of the 10% SR Al sample were identified as the primary Al phase in the eutectic composition.

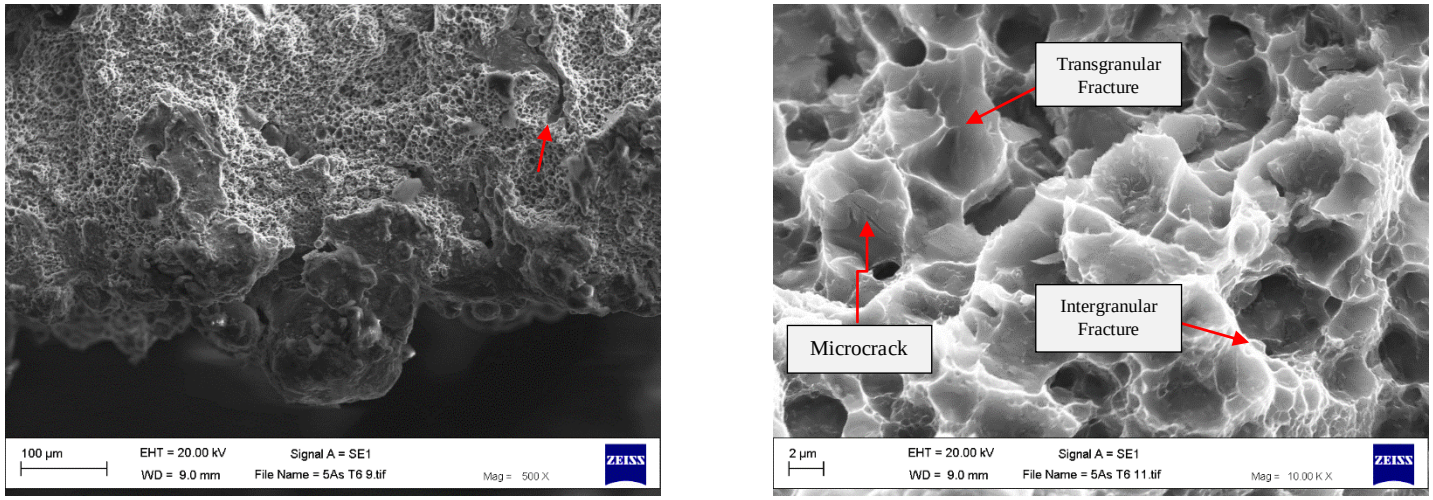

Figure 7.14 Fracture surface of 5-AS T6 Al-MMC

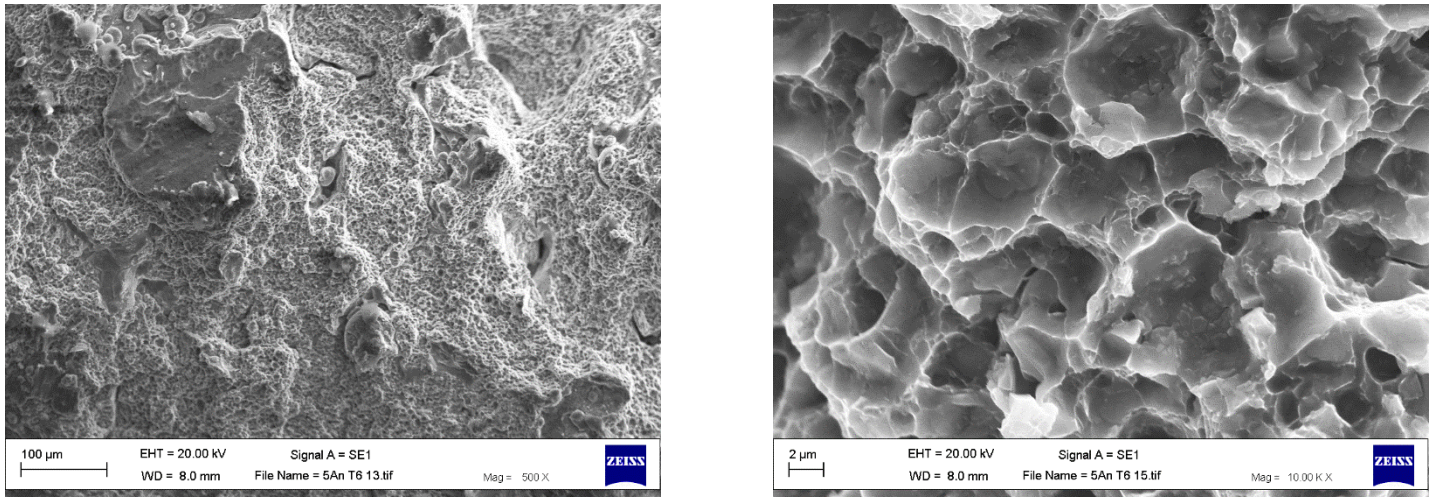

Figure 7.15 Fracture surface of 5-SR T6 Al-MMC

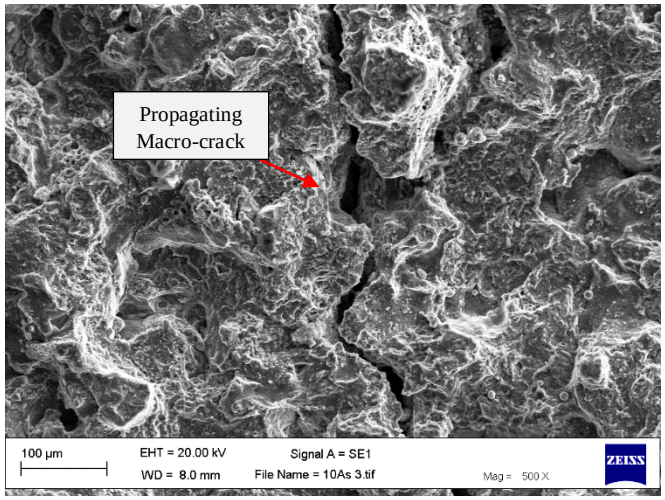

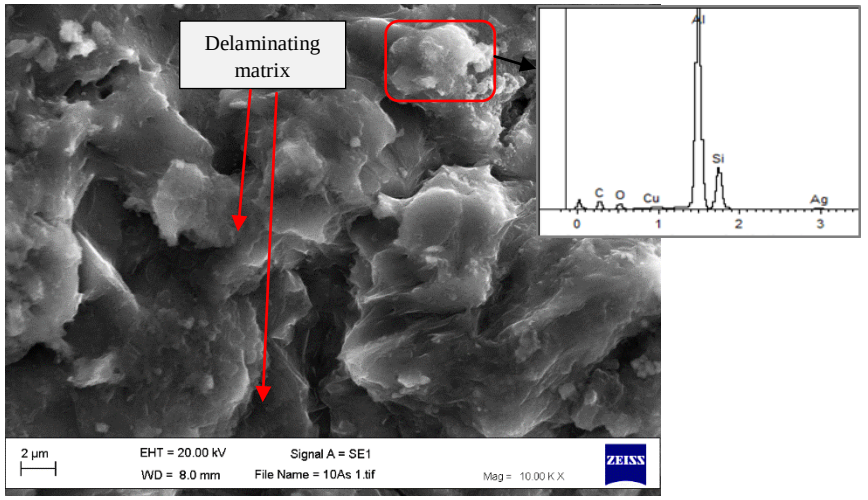

Figure 7.16 Fracture surface of 10% AS Al-MMC

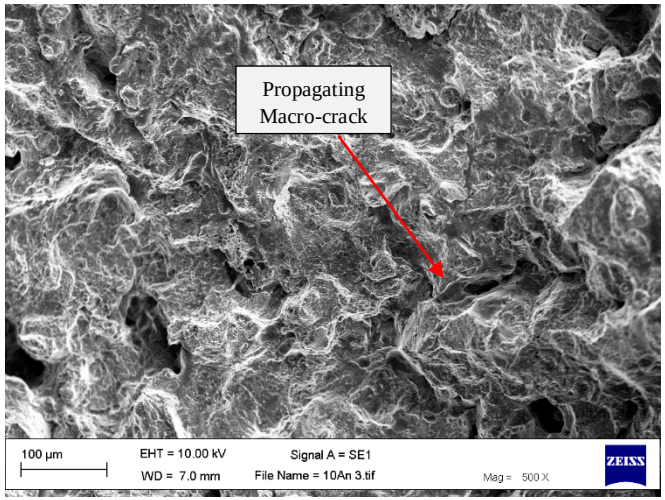

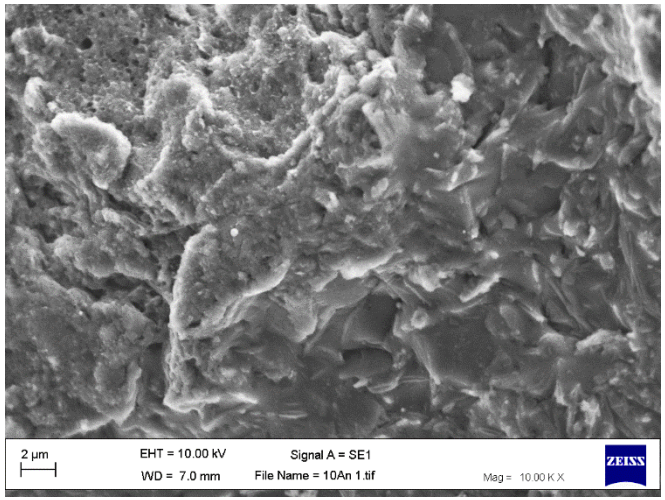

Figure 7.17 Fracture surface of 10% SR Al-MMC

7.4 Evaluation of the Mechanical Properties

Assuming the relative density of the matrix is 100%, the AlSi10Mg/$SiC_{5\%}$ and AlSi10Mg/$SiC_{10\%}$ scanned at 880 mm/s and 0.17 mm step over were 99.33% and 99.48% dense respectively. The Al matrix had the highest tensile values even though the composite samples had achieved near full densities, the effect on the reinforcement on the strength was not apparent in the composites. It had previously been established that the Al-matrix has comparable properties to the T6 heat treated Al-alloys and Table 7.4 gives a comparison of the mechanical properties obtained in this research with previous literature on Al matrixes and Al-Si MMCs.

As observed in Table 7.4, the as-built sample of the matrix has the highest strength values, which supports previous research on the topic (Aboulkhair *et al.*, 2016) while the sintering manufacturing route displayed surprising low values for the tensile strength and hardness. The higher strength values for the LM alloy have been linked to the high rate of solidification, which is prevalent in the LM process unlike the sintering and casting routes. This resulted into a fine microstructure thereby improving its ability to withstand applied loads before the initiation of plastic deformation thereby associating the strengthening mechanism to increase in grain boundaries governed by the Hall-Petch mechanism (Aboulkhair *et al.*, 2015) and dislocation strengthening of the primary Si particles. Mertens *et al*. (2015) observed a decrease in the hardness, yield strength and tensile strength values when the AlSi10Mg alloy was annealed at 250 C for two hrs, attributed to a relief of the internal stresses, which correlates to the results obtained in this research. The T6 heat treatment for both the as-cast and as-LM-built AlSi10Mg alloys resulted in surprisingly similar hardness values signifying that while it improved the properties of the cast alloy, the properties of LM alloy was degraded.

The properties of the composites were slightly different on the introduction of the 5% reinforcement, the sintering route still had the lowest values, however, while the as-cast had the highest hardness values, the LM composite had the highest strength after the T6 heat treatment. Therefore, when the LM composite was aged, it resulted in properties which are comparable with the as-cast composite, unlike the matrix alloy where the aging decreased the properties. Unlike the 5% reinforced composite, the SLM/DMLS/LM route was observed to be unsuitable for the AlSi10Mg/$SiC_{10\%}$ composite although, Canali (2015) observed an

improved strength in his research. The high strength and hardness values were however negated by the formation of Al_4C_3.

Table 7.4 comparison of results with previous research

Material (Condition)	Manufacturing Method	Strength (N/mm^2)	Hardness	References
AlSi10Mg (As cast)	Chill Cast	180 (Tensile)	55 (HB)	Jura-Guss (2016)
AlSi10Mg (T6)	Chill Cast	260 (Tensile)	90 (HB)	Jura-Guss (2016)
Al	Sintered	232 (Flexural)	27.7 (HB)	Leszczynska-Madej (2013)
AlSi10Mg (As built)	LM	412 (Tensile)	154 (HV)	This thesis
AlSi10Mg (T6) (As-Built)	LM	303 (Tensile)	98.5 (HV)	This thesis
Al-$SiC_{5\%}$	Sintered	209 (Flexural)	30.5 (HB)	Leszczynska-Madej (2013)
Al-$SiC_{5\%}$	Cast	305 (Tensile)	68 (HRB)	Meena *et al.* (2013)
AlSi10Mg -$SiC_{5\%}$ (As-Built)	LM	196.93 (Tensile)	92.6 (HV)	This thesis
AlSi10Mg -$SiC_{5\%}$ (AST6)	LM	334.91 (Tensile)	106.4 (HV)	This thesis
Al-$SiC_{10\%}$	Sintered	189 (Flexural)	31.7 (HB)	Leszczynska-Madej (2013)
AlSi10Mg-$TiC_{10\%}$ (As built)	SLM	486	181.2 (HV)	Gu *et al.* (2014)
Al-$SiC_{10\%\text{-}220mesh}$	Cast	330 (Tensile)	72 (HRB)	Meena *et al.* (2013)
AlSi10Mg-$SiC_{10\%}$ (As built)	DMLS	515.7 (Flexural)	~220 (HV)	Canali (2015)
AlSi10Mg-$Fe_2O_{15wt\%}$	SLM	130 (Compressive)	165 (HV)	Dadbakhsh (2012)

The AlSi10Mg/$SiC_{10\%}$ had the highest hardness values although the strength could not be determined due to its premature fracture and failure however, the hardness values suggest that the strength would be higher than the matrix if tested as observed by previous research (Table 4). The AlSi10Mg/$SiC_{5\%}$ which had the lowest relative density, was also observed to consistently have the lowest mechanical properties. However, unlike the cast samples which show an improvement in their properties when subjected to a T6 heat treatment, the strength of the alloy degenerates when also subjected to the same heat treatment regime (Aboulkhair *et al.*, 2016) due to the increase in precipitates which makes the dislocation circumvent the precipitate rather than bowing around them, thus suppressing the effect of the Orowan bowing (Aboulkhair *et al.*, 2015). This research observed that that the values achieved from the T6 regime was due to over-aging of the samples.

7.5 Evaluation of the Microstructural Development

The formation of precipitation hardening particles such as Mg_2Si, Al_4SiC_4, AlFeSi particles and other intermetallics have been observed in different researches (Gu *et al.*, 2015) investigating the Al/SiC composites. In-situ formation of the precipitates has also been investigated with a view to strengthening the matrix. However, during the course of this research, Si precipitates formed because of over-aging during the T6 heat treatment regime were observed. Other precipitation hardening compounds were not observed in the microstructure, despite this, an intermetallic phase $Al_{3.21}Si_{0.47}$ was found by XRD after the T6 heat treatment of the matrix and this could be attributed to the presence of the excess Si in the melt. Vaucher *et al.* (2003) support the interfacial retardation premise as the formation of in-situ phases and other interfacial reactions was limited when AlSi20-$SiC_{45\%}$ composite was laser sintered. They concluded that the amount of Si in the alloy suppressed the influence of the reinforcement size and shape thereby restricting the interfacial reaction, which might have otherwise resulted in forming reinforcing precipitates. Another principle to be considered is that due to the rate of undercooling and solidification customary in the LM process, the precipitates; Mg_2Si and AlFeSi, would not have enough time to grow into visible particles.

The XRD analysis of the samples revealed that the matrix alloy reacted with the 10% SiC reinforcement to form aluminium carbide (Al_4C_3). This reaction occurs around 650 °C which would explain why no SiC particles were also observed in the AlSi10Mg/$SiC_{5\%}$ as the SiC would have reacted completely with the matrix. This would also explain the low strength values obtained for the AlSi10Mg/$SiC5_{\%}$ as the Al_4C_3 makes the composite samples brittle.

This confirms the work done by Manfredi *et al.* (2014), here an increase in hardness in the AlSi10Mg/$SiC_{10\%}$, was be explained by the addition of the SiC particles, the presence of the intermetallic phase $Al_{3.21}Si_{0.47}$ and the Al_4C_3 precipitates.

Due to the higher volume of reinforcement present in the AlSi10Mg/$SiC_{10\%}$, and the hydrophilic nature of Al_4C_3, the composite sample reacted with the water from the EDM machine as per Equation 7.5 during its removal from the substrate. The methane gas is liberated (Equation 7.5) in the form of a gas bubble resulting in a gas pore through which water enters the sample. This would therefore result in the weak samples which are easily broken evidenced by the fractured samples.

Chapter 8

Conclusion and Future Work

8.1 Contribution to knowledge

The aim of this research was to fabricate a particulate reinforced aluminium alloy matrix composite utilising the LM through the development a homogeneous feed material. The suitability of the mechanical alloying process as a novel method for the production of a homogeneous feedstock material for the LM process was confirmed through experimental results. This feedstock production route can be tailored for each matrix/reinforcement combination until homogeneity is achieved. The laser melting parameters were explored and modified to achieve near-full densities for the composite powders. Furthermore, after the LM fabrication, the mechanical properties, fractography, and microstructural evolution during heat treatment was examined as an added contribution to knowledge.

8.2 Conclusions

The research undertaken and the outcomes in this chapter are summarised below:

1. Mechanical alloying was deemed a viable route for the production of metal matrix composite powder for LM feedstock. An ideal shape, size and morphology for the composite powder was obtained at 500 rev/min when milled for 20 mins.
2. Single track formation: Single track formation AlSi10Mg alloy was observed to be a cylindrical line track, with an apparent HAZ devoid of balling and partial melting.
3. The formation of single line tracks was investigated for their shape (cylindrical), morphology and their adhesion to the substrate. Samples were found to deteriorate by cracking at lower scan speeds while track instability and distortion were observed at high scan speeds. A possible process window for full densification was identified between 720 mm/s and 960 mm/s for the matrix alloy and composite.
4. Visual inspection of the Al matrix and Al-$MMC_{5\%}$ sample blocks revealed a uniform part with no cracks, however, cracks were found in the Al-$MMC_{10\%}$. The cracks were attributed to a possible volumetric addition of SiC causing residual stress from the thermal expansivity mismatch.
5. The effect of scan speed on the surface roughness: - The surface roughness of the part seems to improve for the composites until apparent critical speeds between 800 – 880

mm/s with the surface roughness increasing as the scan speed increases due to the changing melt characteristics and machine parameters from the introduction of SiC.

6. Effect of energy density on surface roughness: - Increase in the step over will result in increasing surface roughness, thus allowing more porosity into the part. Overall, as the step over increases and the Energy Density decreases, the surface roughness increases for all samples.
7. Effect of scan speed on the relative density and porosity: - when the Al-$MMC_{5\%}$ was scanned at lower scan speeds, a near full density was obtained however, the presence of cracks precluded it as a viable parameter.
8. Changing the scan speed simultaneously with the step over resulted into higher micro-porosity, surface roughness and eventually lower relative density.
9. Large pores were observed at lower scan speeds while at higher scan speeds between 800 and 880 mm/s, hydrogen pores were observed. Hydrogen pores were found to be prevalent in the Al-$MMC_{10\%}$ while larger pores were observed in for the Al-$MMC_{5\%}$ composite. Overall, widening of the step-over and thus decreasing the energy density led to more pore formation. Also the Al-$MMC_{5\%}$ presents lower porosity values than the Al-$MMC_{10\%}$ composite.
10. The results of the Transverse Rupture Stress testing were utilized in calculating the Weibull distribution and tensile strength of the sample. The tensile strength obtained for the Al matrix is within the scope of EOS parameters for the alloy. Low values were obtained for the Al-$MMC_{5\%}$ and the Al-$MMC10_{\%}$ could not be tested due to its fracture from the substrate. The Al matrix shows a decrease in strength with each heat treatment regime with the SR sample having the highest yield strength. The Al-$MMC_{5\%}$ had higher yield strength values although they also experienced brittle failure.
11. The AST6 heat treatment regime for all samples had the lowest hardness values, therefore considered the weakest regime, while the Al$MMC_{5\%}$ composite consistently also had the lowest values after testing. The Al$MMC_{10\%}$ composite had the highest hardness values which suggests the highest strength, however, the strength could not be measured as a result of fracturing during the removal from the substrate.
12. Microstructural investigations revealed that the AS and SR samples consists of dendritic α-Al and the eutectic composition for the Al alloy. The Al-$MMC_{5\%}$ exhibited relatively the same microstructure as the Al-matrix in both heat treatment regimens except for a reduction in the eutectic composition. The Al-$MMC_{10\%}$ triggered the formation of an aluminium carbide which was identified by XRD measurements. The

reduction of Al from the solid solution led to the formation of an intermetallic $Al_{3.21}Si_{0.47}$.

13. The age hardened samples exhibited signs of over-aging by the appearance of globular Si particles which had precipitated out of the solid solution due to super-saturation. No evidence of Mg_2Si or AlFe intermetallics were found in the microstructure.
14. Fractography of the Al matrix revealed a ductile fracture characterised by a dimpled surface. The Al-$MMC_{5\%}$ was characterised by a combination of both the brittle and ductile fracture while the broken surface of the Al-$MMC_{10\%}$ was characterised by cracks which resulted in matrix delamination. T6 age hardened samples were all characterised by the brittle cleavage fracture.

8.3 Outlook and Future Work

The above results demonstrate the importance of powder characterisation and LM process modification in obtaining suitable mechanical properties for the MMC produced via the LM route. The present research due to the complex nature of the LM process has not explored all quality and optimisation issues in the fabrication of MMCs via LM however, the knowledge gained from the present work can be utilised in processing other MMCs including Ti-MMCs and other Al-MMCs.

Powder characterisation is an important aspect for the research as it aids in determining a suitable feed stock for the LM process. Further research on MMCs should not only focus on the homogeneity of the reinforcement particles and the particle size/particle size distribution but also on the packing density and powder flowability procedures with a view to adapting them for applications.

Process optimisation is an important aspect of the research into MMC fabrication utilising LM. New powders have to be characterised for their laser absorptivity, thermal conductivity and reaction to changing parameters. The mechanical and microstructural evolutions also have to be mapped to gain insight to the effect of the changing parameters.

Thermal gradients and weld pools during the LM fabrication could be monitored through the use of infrared sensors. This would aid in monitoring the effect of lasers on the composite powders and in understanding more effectively, the melting and solidification phenomena during LM. Utilising a controlled heated platform in the EOS M290 LM equipment with the

aim of monitoring and reducing the internal thermal stresses is also an area that needs to be explored.

From the research, the T6 heat treatment resulted in the over-aging of the Al-matrix and MMCs resulting in lower mechanical properties. The heat treatment regime could be mapped from the solutionising stage to the aging stage to aid in further understanding of the microstructural changes and the variation with the cast microstructure.

Numerical models or computer simulations such as the finite element method (FEM) would aid in the material interactions and mechanical test simulations for new powder systems. It would also aid in predicting the effect of various parameters such as thermal conductivity and crystal plasticity on the properties of the new powder systems.

Other reinforcement particles with no adverse reactions with Al alloys unlike SiC, are required for further research. This includes reinforcements, which can form in-situ reinforcements during processing, such as Fe_2O_3 and Si_3N_4. The in-situ reinforcements will therefore form other precipitates, which can be used to harden the composite. Intermetallic compounds also have the potential as reinforcements; however, careful selection based on the desired property for improvement is necessary.

References

Aboulkhair, N. T., Everitt, N. M., Ashcroft, I. and Tuck, C. (2014) Reducing porosity in AlSi10Mg parts processed by selective laser melting. *Additive Manufacturing*, 1–4, pp. 77–86

Aboulkhair, N. T., Tuck, C., Ashcroft, I., Maskery, I. and Everitt, N. M. (2015) On the precipitation hardening of selective laser melted AlSi10Mg. *Metallurgical and Materials Transactions A*, 46 (8), pp. 3337-3341.

Aboulkhair, N.T., Maskery, I., Tuck, C., Ashcroft, I. and Everitt, N.M., (2016a) On the formation of AlSi10Mg single tracks and layers in selective laser melting: Microstructure and nano-mechanical properties. *Journal of Materials Processing Technology, 230*, pp. 88-98.

Aboulkhair, N.T., Maskery, I., Tuck, C., Ashcroft, I. and Everitt, N.M., (2016b) The microstructure and mechanical properties of selectively laser melted AlSi10Mg: The effect of a conventional T6-like heat treatment. *Materials Science and Engineering: A, 667*, pp.139-146.

Aluminium Association (2001) *Aluminium: The Corrosion Resistant Automobile Material* [Online] [Accessed 11th August, 2016] < http://bibvir1.uqac.ca/archivage/18237626.pdf>

Ashby, M. F. (1966) Work Hardening of Dispersion – Hardened Crystals. *Philosophical Magazine*, 14 (132), pp. 1157 – 1178.

Ashby, M., Shercliff, H. and Cebon, D. (2007) *Materials: Engineering, Science, Processing and Design*. 2nd ed. Oxford: Butterworth-Heinemann.

ASM International (1990) *ASM Handbook, Volume 4 – Heat treating*. The Materials Information Company, United States of America, ISBN 0-87170-379-3.

ASM Handbook (2004) *Aluminum-Silicon casting alloys*, the Materials Information Company, United States of America

ASTM B962 (2015) Standard Test Methods for Density of Compacted or Sintered Powder Metallurgy (PM) Products Using Archimedes' Principle

ASTM D7481 – (2009) Standard Test Methods for Determining Loose and Tapped Bulk Densities of Powders using a Graduated Cylinder

ASTM E11 – (2015) Standard Specification for Woven Wire Test Sieve Cloth and Test Sieves

ASTM F2792 (2012) Standard terminology for Additive Manufacturing Technologies

Aziz, I. A. (2010) *Microstructure and Mechanical properties of Ti-6Al-4V produced by selective laser sintering of pre-alloyed powders*. Master thesis submitted to the University of Waikato, New Zealand, Unpublished.

Balaz, P. (2008) High-Energy Milling. *Mechanochemistry in Nanoscience and Materials Engineering*, 8, pp. 413.

Badrossamay, M. and Childs, T.H.C. (2006), Layer formation studies in selective laser melting of steel powders, *Proceedings of Solid Freeform Fabrication symposium*, University of Texas, Austin, Texas, pp.268-279.

Badrosamay, M., Yasa, E., van-Vaerenbergh, J., and Kruth, J. P. (2009) Improving Productivity Rate in SLM of commercial steel powders. *In Rapid*, Schaumburg, IL, USA, pp. 1-13.

Bao, G., Hutchinson, J. W. and McMeeking, R. M. (1991) Particle reinforcement of ductile matrixes against plastic flow and creep. *Acta Metallurgica et Materialia*, 39 (8), pp. 1871 – 1882.

Bartkowiaka, K., Ullrich, S., Frick, T. and Schmidt, M. (2011) New Developments of Laser Processing Aluminium Alloys via Additive Manufacturing Technique. *Physics Procedia*, 12, pp. 393–401.

Bayraktar, E. and Katundi, D. (2010) Development of a new aluminium matrix composite reinforced with iron oxide (Fe_3O_4). *Journal of Achievements in Materials and Manufacturing Engineering*, 38 (1) pp. 7 – 14.

Benjamin, J., (1976) Mechanical Alloying. *Scientific American*, pp. 234-255.

Benjamin, J. and Volin, T. (1974) The mechanism of mechanical alloying. *Metallurgical and Materials Transactions B*, 5 (8), pp. 1929-1934

Berretta, S., Ghita, O., Evans, K. E., Anderson, A., and Newman, C. (2013) *Size, shape and flow of powders for use in Selective Laser Sintering (SLS)*. In *High Value Manufacturing: Advanced Research in Virtual and Rapid Prototyping*: Proceedings of the 6th International Conference on Advanced Research in Virtual and Rapid Prototyping, Leiria, Portugal, 1-5 October, 2013 (p. 49).

Beuth, J. and Klingbeil, N. (2001) The role of process variables in laser-based direct metal solid freeform fabrication. JOM, 53 (9), pp 36-39

Bineli, A. R. R., Peres, A. P. G., Jardini, A. L. and Filho, R. M. (2011) *Direct Metal Laser Sintering (Dmls): Technology for Design and Construction of Microreactors*. 6th Brazilian Conference On Manufacturing Engineering, Caxias do Sul: 11th to 15th April, Brazil.

Birkholz, M. (2006) *Thin Film Analysis by X-Ray Scattering*. Weinheim: Wiley-VCH

Boey, F. Y. C., Yuan, Z. and Khor, K. A. (1998) Mechanical alloying for the effective dispersion of sub-micron SiCp reinforcements in Al–Li alloy composite. *Materials Science and Engineering*: A, 252(2), pp. 276-287.

Bolton, W. (1989) *Newness – Engineering Materials Pocket book*. Oxford: Elsevier

Bose, A. (1995) *Advances in Particulate Materials*. Newton, USA: Butterworth-Heinemann

Bourell, D.L., Marcus, H.L., Barlow, J.W. and Beaman, J.J. (1992) Selective laser sintering of metals and ceramics. *International Journal of Powder Metallurgy*, 28 (4) pp. 369-381.

Bozic, D., Vilotijevic, M., Rajkovic, V. and Gnjidic, Z., (2005) *Mechanical and Fracture Behaviour of a SiC-Particle-Reinforced Aluminum Alloy at High Temperature*. In Uskokovic, D.P., Milonjic, S.K. and Rakovic, D. I. (eds.) *Material Science Forum*. Current Research in Advanced Materials and Processes, 494, pp. 487-492.

Brodarac, Z., Mrvar, P., Medved, J. and Fajfar, P. (2007) Local Squeezing Casting Influence on the Compactness of AlSi10Mg Alloy Castings. *Metalurgija*, 46, pp. 29-35

BS EN ISO 6507-1 (2005) Metallic materials - Vickers hardness test - Test method

BS EN ISO 3252 (2000) Powder metallurgy. Vocabulary

BS ISO 14610 (2012) Fine ceramics (advanced ceramics, advanced technical ceramics). Test method for flexural strength of porous ceramics at room temperature.

Buchbinder, D., Schleifenbaum, H., Heidrich, S., Meiners, W. and Bültmann, J. (2011) High Power Selective Laser Melting (HP SLM) of Aluminum Parts. *Physics Procedia* (12) pp. 271-278

Bunnell, D.E., Das, S., Bourell, D.L., Beaman, J.B. and Marcus, H.L. (1995) *Fundamentals of liquid phase sintering during selective laser sintering*, In: Proceedings of Solid Freeform Fabrication Symposium, The University of Texas, Austin, TX, 1995, pp. 440-447.

Burakowski, T. and Wierzchon, T. (1998) *Surface Engineering of Metals: Principles, Equipment, Technologies; Cleveland*: CRC Press.

Campanelli, S. L., Contuzzi, N., Angelastro, A. and Ludovico A. D. (2010) *Capabilities and Performances of the Selective Laser Melting Process*. In Meng Joo Er (Ed.) *New Trends in Technologies: Devices, Computer, Communication and Industrial Systems*, InTech, [Available from: http://www.intechopen.com/books/new-trends-in-technologies--devices--computer--communication-and-industrial-systems/capabilities-and-performances-of-the-selective-laser-melting-process]

Canali, R. (2015) Study, development and characterization of aluminum based materials by additive manufacturing. PhD thesis, Unpublished.

Center for Additive Layer Manufacturing (CALM) (2013) What is additive layer manufacturing? University of Exeter, [Online] [Accessed 12th August, 2016] <Available through http://emps.exeter.ac.uk/engineering/research/calm/whatis/>

Chawla, K. K. (2012) *Composite Materials: Science and Engineering* (3rd ed.). New York: Springer Science & Business Media.

Chen, J. K., Tang, T. P., Chan, S. F. and Chang, S. H. (2008) Effects of Particle Size on Mechanical Properties of a TiC Containing Tool Steel by Hot Isostatic Press. *Materials Transactions*, 49 (3) pp. 624 – 628.

Chien, C. W., Lee, S. L., Lin, J. C. and Jahn, M. T. (2002) Effects of Sip size and volume fraction on properties of Al/Sip composites. *Materials Letters*, 52, pp. 334–341.

Chikwanda, H. K. and Maweja, K. (2008) *Effects of high energy ball milling on synthesis and characteristics of Ti-Mg alloys*. Advanced Processing for Novel Functional Materials, APNFM 2008: International Congress Centre, Dresden, Germany, 23-25 January, pp 10.

Custom Part (2013) Additive Fabrication [Online] [Accessed 11th August, 2016] <Available through http://www.custompartnet.com/wu/additive-fabrication>

Dadbakhsh, S. (2012) The Selective Laser Melting of Metals and In-situ Aluminium Matrix Composites. PhD thesis. Unpublished.

Dadbakhsh, S. and Hao, L. (2012) In situ formation of particle reinforced Al matrix composite by selective laser melting of Al/Fe2O3 powder mixture. *Advanced Engineering Materials*, 14 (1-2), pp. 45-48

Daneshmand, S. and Aghanajafi, C. (2012) Description and modelling of the additive manufacturing technology for aerodynamic coefficients measurement. *Journal of Mechanical Engineering*, (58) 2, pp. 125-133

Das, D. K., Mishra, P. C., Singh, S. and Pattanaik, S. (2014a) Fabrication and heat treatment of ceramic-reinforced aluminium matrix composites – a review. *Journal of Mechanical and Materials Engineering*, 9 (1).

Das, R. M., Ali, E. and Hamid, S.B.A., (2014b) Current Applications of X-Ray Powder. *Rev. Adv. Mater. Sci*, 38, pp.95-109.

Davis, J. R. (ed.) (1993) *Aluminium and Aluminium alloys*. U.S.A.: ASM International

Davis, J. R. (1999) *Corrosion of Aluminum and Aluminum alloys*. Ohio: ASM International.

De Castro, C. L. and Mitchell, B. S., (2002) *Nanoparticles from Mechanical Attrition*. In: M. Baraton, Ed. *Synthesis, Functionalization and Surface Treatment of Nanoparticles*. California: America Scientific Publishers, pp. 1-14.

Despeisse, M. and Ford, S. (2015) The Role of Additive Manufacturing in Improving Resource Efficiency and Sustainability. Centre for Technology Management working paper series (3) [Available through http://www.ifm.eng.cam.ac.uk/uploads/Research/CTM/working_paper/2015-03-Despeisse-Ford.pdf]

Dinda, G.P., Dasgupta, A. K. and Mazumder, J. (2012) Evolution of microstructure in laser deposited Al-11.28%Si alloy. *Surface Coating Technology*, 206, pp. 2152 – 2160.

Drezet, J-M., Pellerin, S., Bezencon, C. and Mokadem, S. (2004) Modelling the Marangoni convection in laser heat treatment. *Journal de Physique IV*, 120. Pp 299- 306, Proceedings of the 2nd International Conference on Thermal Process Modelling and Computer Simulation, Nancy, France, 31st Mar - 2nd Apr, 2003

Dutta, I., Bourell, D. L. and Latimer, D. (1988) A Theoretical Investigation of Accelerated Aging in Metal-Matrix Composites. *Journal of Composite Materials*, 22 (9), pp. 829-849.

El-Eskandarany, M. S. (1998) Mechanical solid state mixing for synthesizing of SiC /Al nanocomposites. *Journal of Alloys and Compounds*, 279, pp. 263–271.

EOS GmbH (2009) *EOSINT M270*. [Online] [Accessed on 12th August, 2016] < http://www.rmsiberia.com/Producto/eosint_m270_en.pdf>

EOS Gmbh (2011) *EOS Aluminium AlSi10Mg for EOSINT M 270*. [Online] [Accessed on 12th August, 2016] <Available through http://www.detekt.com.tw/download/eos/4%E6%9D%90%E6%96%99%E7%A8%AE%E9%A1%9E/Metal/AlSi10Mg_Material_data_sheet_05-11_en.pdf>

Erasenthiran, P. and Beal, V. E. (2006) *Functionally Graded Materials*, In Hopkinson, N., Hague, R. J. M. and Dickens, P. M.(Eds.) *Rapid Manufacturing - An Industrial Revolution for the digital age*. Chichester – UK: John Wiley and Sons.

ESAB Knowledge Center (2014) *How and why alloying elements are added to aluminium*. [Online] [Accessed on 12th August, 2016] <Available through http://www.esabna.com/us/en/education/blog/how-and-why-alloying-elements-are-added-to-aluminum.cfm>

Excell, J. and Nathan, S., (2010). *The rise of additive manufacturing*. The Engineer. [Online] [Accessed on 12th August, 2016] <http://www.theengineer.co.uk/in-depth/the-big-story/the-rise-of-additive-manufacturing/1002560.article>

Fischer, T. (2009) *Materials Science for Engineering Students*. Canada: Elsevier

Fink, W. L., Smith, D. W. and Willey, L. A. (1940) *Precipitation hardening of high purity binary and ternary aluminium-cooper alloys*. In Proceedings from the Symposium on Precipitation Hardening (age hardening) at the 21st Annual Convention of the American Society for Metal, Chicago, Oct. 23 -27, 1939.

Flemings, M. C. (2005) Coarsening in Solidification Processing. *Materials Transactions*, 46 (5), pp. 895 to 900

Fogagnolo, J. B., Robert, M. H., Ruiz-Navaz, E. M. and Torralba, J. M. (2004) 6061 Al reinforced with zirconium diboride particles processed by conventional powder metallurgy and mechanical alloying. *Journal of Materials Science*, 39, pp. 127-132.

Foltz, J. V. and Blackmon, C. M., (1990) *Metal-Matrix Composites*. In ASM International, Metals Handbook, Properties and Selection: Nonferrous Alloys and Special-Purpose Materials, 10 (2), pp. 903-912.

Garg, A. and Gurao, N. (2013) *X-ray Diffraction: Principles and Practice*. *Unpublished*, [Online] [Accessed on 12th August, 2016] <Available through https://www.google.co.uk/url?sa=t&rct=j&q=&esrc=s&source=web&cd=7&cad=rja&uact=8&ved=0ahUKEwi48pGn84fNAhUkKMAKHfNyAtUQFghFMAY&url=http%3A%2F%2Fwww.iitk.ac.in%2Facms%2Fdoc%2FXRD_AG%2520NPG.ppt&usg=AFQjCNEYdV6xgRXwHluQFSrIav16HX9YNA>

Garg, H. K., Verma, K., Manna, A. and Kumar, R. (2012) Hybrid metal matrix composites and further improvement in their machinability – A Review. *International Journal of Latest Research in Science and Technology*, 1 (1), pp. 36 – 44.

Ghosh, S. K., Saha, P. and Kishore, S. (2010) Influence of size and volume fraction of SiC particulates on properties of ex situ reinforced Al–4.5Cu–3Mg metal matrix composite prepared by direct metal laser sintering process. *Materials Science and Engineering A*, 527, pp. 4694–4701

Ghosh, S. and Saha, P., (2011) Crack and wear behaviour of SiC particulate reinforced aluminium based metal matrix composite fabricated by direct metal laser sintering process. *Materials and Design*, 32, pp. 139-145.

Graat, P. (2004) *Technical Note 13 - X-ray Diffraction (XRD) In Materials Analysis by Philips Research*. [Online] [Accessed on 9th July, 2015] <http://www.research.philips.com/technologies/projects/matanalysis/downloads/xrd.pdf>

Groover, M. P. (1996). *Fundamentals of modern manufacturing: materials, processes, and systems*. Upper Saddle River, New Jersey: Prentice Hall

Gu, D. (2015) *Laser Additive Manufacturing of High-Performance Materials*. Berlin: Springer

Gu, D., Chang, F. and Dai, D. (2015) Selective Laser Melting Additive Manufacturing of Novel Aluminum Based Composites with Multiple Reinforcing Phases. *Journal of Manufacturing Science and Engineering*, 137 (2)

Gu, D., Meiners, W., Hagedorn, Y-C., Wissenbach, K. and Poprawe, R. (2010) Structural evolution and formation mechanisms of TiC/Ti nanocomposites prepared by high-energy mechanical alloying. *Journal of Physics D: Applied Physics*, 43 (13)

Gu, D., Wang, H., Chang, F., Dai, D., Yuan, P., Hagedorn, Y. C. and Meiners, W. (2014) Selective Laser Melting Additive Manufacturing of TiC/AlSi10Mg Bulk-form Nanocomposites with Tailored Microstructures and Properties. *Physics Procedia*, 56, pp. 108–116

Guan, K., Wang, Z., Gao, M., Li, X. and Zeng, X. (2013) Effects of processing parameters on tensile properties of selective laser melted 304 stainless steel, *Materials and Design*, 50, pp. 581-586

Gur, C. H. (2002) *Ultrasonic investigation of SiC-particle reinforced aluminium matrix composites*. Annual Meeting of the German Society for Non-destructive Testing: NDT in application development and research, Weimar, 6 - 8 Mai 2002 May, Germany, 80.

Hanzl, P., Zetek, M., Baksa, T. and Kroupa, T. (2015) The Influence of Processing Parameters on the Mechanical Properties of SLM Parts. *Procedia Engineering*, 100, pp. 1405 - 1413.

Hao, L. and Dadbakhsh, S. (2009) Materials and process aspects of selective laser melting of metals and metal matrix composites: a review. *Chinese Journal of Lasers*, 36 (12), pp. 3192–3203

Hauser, C., Childs, T.H.C. and Badrossamay, M. (2004) Further Developments in Process Mapping and Modelling in Direct Metal Selective Laser Melting. [Online] [Accessed Sept, 2014] <http://sffsymposium.engr.utexas.edu/Manuscripts/2004/2004-45-Hauser.pdf. >

Herderick, E. (2011) *Additive Manufacturing of Metals: A Review*. Proceedings of Material Science and Technology Conference and Exhibition, Columbus, Ohio, October 16 – 20, 2011.

Hernández-Méndez, F., Altamirano-Torres, A., Miranda-Hernández, J. G., Térres-Rojas, E. and Rocha-Rangel, E. (2011) Effect of Nickel Addition on Microstructure and Mechanical Properties of Aluminum-Based Alloys, *Materials Science Forum*, 691, pp.10-14.

Herzog, D., Seyda, V., Wycisk, E. and Emmelmann, C. (2016) Additive manufacturing of metals, *Acta Materialia*, pp. 1-22, [Corrected Proof, available through - http://dx.doi.org/10.1016/j.actamat.2016.07.019]

Hiemenz, J. (2007) Electron Beam Melting. *Advanced Materials & Processes*, pp. 45.46

Ibrahim, I. A., Mohamed, F. A. and Lavernia, E. J. (1991) Particulate reinforced metal matrix composites — a review. *Journal of Materials Science*, 26 (5), pp. 1137-1156.

Inno-shape GmbH (2012) Laser Melting of Aluminum Alloys. [Online] [Accessed on 18 November, 2012] < http://www.inno-shape.de/pdf/Produktblatt_AlSi10Mg_eng.pdf, >

International Centre for Diffraction Data (2016) Diffraction Data for Elements and Compounds. [Online] [Website Accessed on 12th August, 2016)

Izhevskyi, V. A., Genova, L. A., Bressiani, J. C. and Bressiani, A. H. A. (2000) Review Article: Silicon Carbide. Structure, Properties and Processing. *Ceramica*, 46 (297), pp. 4-13.

Jaradeh, M. and Carlberg, T. (2005) Effect of titanium additions on the microstructure of DC-cast aluminium alloys. *Materials Science and Engineering A*, 413 –414, pp. 277–282.

Jenkins, I. and Wood, J., (1991) *Powder Metallurgy: An Overview*. London: The Institute of Metals.

Jones, H. (2004) Gas-atomised aluminium alloy powders and their products: An update 1996–2001. *Materials Science and Engineering A*, 375–377, pp. 104–111

Jura-Guss GmbH (2016) Mechanical properties of sand/chill casting alloys - AlSi10Mg(a) in ingot form. [Online – Accessed on 7th Sept, 2016; Available through - http://aluminium-giesserei.com/hp628/AlSi10Mg-a.htm]

Kainer, K. U. (2006) *Metal Matrix Composites – Custom-made parts for Automotive and Aerospace Engineering*. Germany: Wiley-VCH.

Kalpakjian, S. and Schmid, S. R. (2006) *Manufacturing Engineering and Technology*. New Jersey: Pearson Prentice Hall.

Kamwaya, M. E. (2002) A Simple Method for Indexing Powder diffraction patterns of cubic materials: (I) Using the θ-Values of Reference. *Tanzania Journal of Science*, 28 (1), pp. 1-5

Kaufman, J. G. and Rooy, E. L. (2004) *Aluminum Alloy Castings: Properties, Processes, and Applications*. USA: ASM International.

Kaupp, G. (2009) Mechanochemistry: the varied applications of mechanical bond-breaking. *Cryst Eng Comm*, 11 (3), pp. 388-403.

Kaw, A. K. (2005) *Mechanics of composite materials*, (2nd Ed.) Boca Raton: CRC Press

Kearney, A. (1990) *Properties of Cast Aluminium Alloys: Nonferrous Alloys and Special Purpose Materials*. In Davis, J. R. (1990) *ASM handbook. Volume 2*. Materials Park, OH, ASM International.

Kempen, K., Thijs, L., Van Humbeeck, J. and Kruth, J. P. (2012) Mechanical properties of AlSi10Mg produced by Selective Laser Melting. *Physics Procedia*, 39, pp. 439 -446

Keppler, A. (2011) EOS – *A Strategic Outlook. Presented at the International User Management*, IUM 2011, Bad Wörishofen, April, 2011.

Khaing, H. Y. and Kywe, T. T. (2011) Production of Fine Aluminium Powder from Metallic Aluminium. The 1st International Conference on Interdisciplinary Research and Development, 31st May – 1 June, Thailand in *The International Journal of the Computer, the Internet and Management*, 19 (1), pp. 651 – 656.

Kirk-Othmer (2001) *Encyclopaedia of Chemical Technology*, 16, (4th ed.). USA: John Wiley & Sons Inc.

Kopeliovich, D. (2012) *Effects of alloying elements on properties of aluminium alloys*. [Online] [Accessed on 12th August, 2016] <Available through

http://www.substech.com/dokuwiki/doku.php?id=effects_of_alloying_elements_on_properties_of_aluminum_alloys>

Krol, M., Dobrzanski, L. A., Reimann, L. and Czaja, I. (2013) Surface quality in selective laser melting of metal powders. *Archives of Materials Science and Engineering*, 60 (2), pp. 87-92

Kruth, J. P., Wang, X., Laoui, T. and Froyen, L. (2003) Lasers and materials in selective laser sintering. *Assembly Automation*, 23 (4), pp. 357 – 371

Kumai, S., King, J. E. and Knott, J. F. (1991). Fatigue in SiC-particulate-reinforced aluminium alloy composites. *Material Science and Engineering A*, Vol. 146, pp. 317-326.

Kumar, S. (2003) Selective Laser Sintering: A Qualitative and Objective Approach. *The Journal of the Minerals, Metals and Materials Society*, 55 (10), pp. 43 – 47

Kumar, S. and Kruth J.-P (2010) Composites by rapid prototyping technology. *Materials and Design*, 31, pp 850–856

Kumar, S. and Pityana, S. (2011) Laser-based additive manufacturing of metals. *Adv. Mater. Res.* 227, pp. 92–95.

Kumar, G. B. V., Rao, C. S. P. and Selvaraj, N. (2011) Mechanical and Tribological Behaviour of Particulate Reinforced Aluminum Metal Matrix Composites – a review. *Journal of Minerals & Materials Characterization & Engineering*, 10 (1), pp. 59-91.

Kurz, W. and Fisher, D. J. (1998) Fundamentals of Solidification, 4th Ed. *Trans Tech Publications*: Uetikon-Zuerich

Kyogoku, H., Hagiwara, M. and Shinno, T. (2010) Freeform Fabrication of Aluminum Alloy Prototypes Using Laser Melting. *Laser*, 10 (50)

Lambrakos, S. G. and Cooper, K. P. (2011) A Physically Consistent Path-Weighted Diffusivity Function for Modeling of Drop-by-Drop Liquid Metal Deposition. *Journal of Materials Engineering and Performance*, 20 (9), pp. 1512-1519

Lee, H. M., Huang, C. Y. and Wang, C. J. (2009) Forming and sintering behaviours of commercial α-Al2O3 powders with different particle size distribution and agglomeration. *Journal of Materials Processing Technology*, 209, pp.714-722.

Leong, K. F., Phua, K. K. S., Chua, C. K., Du, Z. H., and Teo, K. O. M. (2001) Fabrication of porous polymeric matrix drug delivery devices using the selective laser sintering technique. Proceedings of the Institution of Mechanical Engineers, Part H: *Journal of Engineering in Medicine*, 215 (2) 191–201.

Leszczynska-Madej, B. (2013) The Effect of Sintering Temperature on Microstructure and Properties of Al - SiC Composites. *Archives of Metallurgy and Materials*, 58 (1), pp. 43-48

Leu, M. C., Pattnaik, S. and Hilmas, G. E. (2010) *Optimization of selective laser sintering process for fabrication of zirconium diboride parts*. Proceedings of the 21st International Solid Freeform Fabrication Symposium, Austin: The University of Texas, Austin, USA, Aug 9-11, 2010. pp. 493–503

Li, B., Li, G., Zhang, W. and Ding, A. (2005) Influence of particle size on the sintering behaviour and high-power piezoelectric properties of PMnN-PZT ceramics. *Materials Science and Engineering: B*, 121, pp. 92-97.

Libo, L., Maozhong, A., and Gaohui, W. (2004). A new electroless nickel deposition technique to metallise SiCp/Al composites. *Surface and Coatings Technology*, 200, pp. 5102-5112.

Liu, B., Wildman, R., Tuck, C., Ashcroft, I. and Hague, R. (2011), *Investigation the effect of particle size distribution on processing parameters optimization in selective laser melting process*, Proceedings of Solid Freeform Fabrication Symposium, University of Texas at Austin, TX, pp. 227-238.

Liu, Y. B., Lim, S. C., Lu, L. and Lai, M. O. (1994) Recent development in the fabrication of metal matrix-particulate composites using powder metallurgy techniques. *Journal of Materials Science*, 29 (8), pp. 1999 – 2007.

Looney, L. A., Monaghan, J. M., O'Reilly, P. and Taplin, D. M. R., (1992) The turning of an Al/SiC metal-matrix composite. *Journal of Materials Processing Technology*, 33, pp. 453-468.

Louvis, E., Fox, P. and Sutcliffe, C. J. (2011) Selective laser melting of aluminium components. *Journal of Materials Processing Technology*, 211, pp. 275–284.

Lu, L., Fuh, J. Y. H. and Wong, Y. S. (2001) *Laser-induced materials and processes for rapid prototyping*, 1st Ed. Norwell: Kluwer Academic Publishers:

Lu, L., Lai, M. O. and Ng, C. W. (1998) Enhanced mechanical properties of an Al based metal matrix composite prepared using mechanical alloying. *Materials Science and Engineering*, A252, pp. 203-211.

Lu, L. and Lai, M. O. (2013) *Mechanical Alloying*. New York: Springer Science and Business Media

Lundqvist, D. (1949) On the Crystal Structure of Silicon Carbide and its content of impurities. *Acta Chemica Scandinavica*, 2, pp. 177 -191.

Makhlouf, M. M. and Guthy, H. V. (2001) The Aluminium-Silicon eutectic reaction: mechanism and crystallography. *Journal of Light Metals*, 1 (4), pp. 199 – 218.

Malvern Instruments, (2015) Mastersizer 3000 User manual. [Online] [Accessed 6th May, 2016] <http://www.malvern.com/Assets/Mastersizer-3000-User-Manual-English-MAN0474-07-EN-00.pdf>

Maňas, K., Svoboda, E., Sukáč, J. and Kusmič, D. (2008) *Possibilities of Measuring Surface Roughness with Confocal Laser Scanning Microscope OLS 3000*. Presented at the 12th International Research/Expert Conference. *Trends in the Development of Machinery and Associated Technology TMT*, Istanbul, Turkey, 26-30 August, 2008

Manfredi, D., Calignano, F., Ambrosio, E. P., Krishnan, M., Canali, R., Biamino, S., Pavese, M., Atzeni, E., Iuliano, L., Fino, P. and Badini, C. (2013a) Direct Metal Laser Sintering: an additive manufacturing technology ready to produce lightweight structural parts for robotic applications. *La Metallurgia Italiana*. 105 (10): 15-24.

Manfredi, D., Calignano, F., Krishnan, M., Canali, R., Ambrosio, E. P., Atzeni, E., (2013b) From Powders to Dense Metal Parts: Characterization of a Commercial AlSiMg Alloy Processes through Direct Metal Laser Sintering. *Materials*, 6, pp. 856-869

Manfredi, D., Calignano, F., Krishnan, M., Canali, R., Ambrosio, E. P., Biamino, S., Ugues, D., Pavese, M. and Fino, P. (2014) Additive Manufacturing of Al Alloys and Aluminium

Matrix Composites (AMCs) In Monteiro, W. A. (ed.) Light Metal Alloys Applications, InTech [Online], [Accessed 12th August, 2016] <Available through http://www.intechopen.com/books/light-metal-alloys-applications/additive-manufacturing-of-al-alloys-and-aluminium-matrix-composites-amcs>

Martin, J. W. (1980) *Micromechanisms in particle-hardened alloys*. Cambridge: Cambridge University Press.

Matsumoto, M., Shiomi, M., Osakada, K. and Abe, F. (2002) Finite element analysis of single layer forming on metallic powder bed in rapid prototyping by selective laser processing. *International Journal of Machine Tools and Manufacture*, 42, pp. 61-67

McGeough, J.A. (2014) *Introduction to Casting, Semi-Solid Forming and Hot Metal Forming*, In Hashmi, S., Batalha, G. F., Van Tyne, C. J. and Yilbas, B. (2014) *Comprehensive Materials Processing*, Elsevier: Oxford, UK.

Meena, K., Manna, D. A., Banwait, D. S., and Jaswanti, D. (2013). An Analysis of Mechanical Properties of the Developed Al/SiC-MMC's. *American Journal of Mechanical Engineering*, 1(1), 14-19.

Mertens, A., Dedry, O., Reuter, D., Rigo, O. and Lecomte-Beckers, J., (2015) Thermal Treatments of AlSi10Mg Processed by Laser Beam Melting. In *Proceedings of the 26th International Solid Freeform Fabrication Symposium* (pp. 1007-1016). Austin.

Miani, F. (2012) *Recent Developments of Direct Metal Selective Laser Sintering*", [Online] [Accessed 13 September 2012] < http://www.ics.trieste.it/media/133856/df143.pdf>

Min, J. B. and Cornie, J. A. (2013) Fracture Analysis of Particulate Reinforced Metal Matrix Composites. NASA/TM, [Online] [Accessed 24th March, 2016] <http://www.sti.nasa.gov>

Miracle, D. B. and Donaldson, S. L. (2001) *Introduction to Composites*. In *ASM Handbook - Composites*, 21, - USA: ASM International.

Mondolfo, L. F. (1976) *Aluminum alloys: Structure and Properties*. London: Butterworths

Montanari, R. (2009) Metal matrix composites. [Online] [Accessed on 11th February, 2013] < http://dspace.uniroma2.it/dspace/bitstream/2108/868/3/Chapter+1.pdf>

Morgan, R.H, Papworth, A.J., Sutcliffe, C., Fox, F. and O'Neill, W. (2002) High density net shape components by direct laser re-melting of single phase powders, *Journal of Materials Science*, 37, pp. 3093 – 3100.

Murray, J. L. and McAlister, A. J. (1984) The AI-Si (Aluminum-Silicon) System. *Bulletin of Alloy Phase Diagrams*, 5 (1), pp. 74 – 84.

Murray, G., White, C. V. and Weise, W. (2008) *Introduction to Engineering Materials*, 2nd Ed. Boca Raton: CRC Press

Murty, B. S. and Ranganathan, S. (1998) Novel materials synthesis by mechanical alloying/milling. *International Materials Reviews*, 43 (3). pp. 101-141.

Nayeb-Hashemi, H. and Shan, D., (1999) Evaluation of heat damage on B4C particulate reinforced aluminium alloy matrix composite using acoustic emission techniques. *Materials Science and Engineering A*, 266, pp. 8-17.

Newey, C. and Weaver, G. (eds.) (1990) *Materials Principles and Practice. Materials in Action Series*. London: Butterworth Scientific

Nikanorov, S. P., Volkov, M. P., Gurin, V. N., Burenkov, Y. A., Derkachenko, L. I., Kardashev, B. K., Regel, L. L. and Wilcox, W. R. (2005) Structural and mechanical properties of Al–Si alloys obtained by fast cooling of a levitated melt. *Materials Science and Engineering A*, 390, pp. 63–69.

Niu, H. J. and Chang, I. T. H. (1999) Instability of scan tracks of selective laser sintering of high speed steel powder. *Scripta Materialia*, 41, pp. 1229–1234.

Noble, B., Trowsdale, A. J. and Harris, S. J. (1997) Low-temperature interface reaction in Aluminium-Silicon Carbide particulate composites produced by Mechanical Alloying. *Journal of Material Science*, 32 (22), pp. 5969-5978.

Ohring, M. (1995) *Engineering Materials Science*, California: Academic Press Inc.

Ohsaki, S., Kato, S., Tsuji, N., Ohkubo, T. and Hono, K. (2007) Bulk mechanical alloying of Cu-Ag and Cu/Zr two-phase microstructures by accumulative roll-bonding process. *Acta Materialia*, 55 (8), pp. 2885-2895.

Olakanmi, E. O., Cochrane, R. F. and Dalgarno, K. W. (2015) A review on selective laser sintering/melting (SLS/SLM) of aluminium alloy powders: Processing, microstructure, and properties. *Progress in Materials Science*, 74, pp.401–477

Olympus (2010) 3D Measuring Laser Microscope – OLS4000 LEXT Specification manual. [Online] [Accessed on 20th August, 2016; Available through http://news.stust.edu.tw/user/news_file%5C%5C20100709092800_2.pdf]

Onoro, J., Salvador, M. D. and Cambronero, L. E. G. (2009) High-temperature mechanical properties of aluminium alloys reinforced with boron carbide particles. *Materials Science and Engineering* A, 499, pp. 421-426.

Osakada, K. and Shiomi, M. (2006) Flexible manufacturing of metallic products by selective laser melting of powder. *International Journal of Machine Tools and Manufacture*, 46, pp. 1183 – 1193.

Othman, R. and Zakaria, A. (2011). Optimization of Milling Parameters during mechanical activation for Direct Synthesis of Hydroxyapatite, *ASEAN Engineering Journal*, 1 (4), pp. 5-11

Ozben, T., Kilickap, E. and Cakir, O. (2008) Investigation of mechanical and machinability properties of SiC particle reinforced Al-MMC. *Journal of Materials Processing Technology*, 198, pp. 220 - 225.

Pang, S., Chen, X., Zhou, J., Shao, X. and Wang, C. (2015) 3D transient multiphase model for keyhole, vapour plume, and weldpool dynamics in laser welding including the ambient pressure effect. *Optics and Lasers in Engineering*, 74, pp. 47 - 58

Pech-Canul, M. I. (2011) *Aluminum Alloys for Al/SiC Composite*s. In Ahmad, Z. (ed.) *Recent Trends in Processing and Degradation of Aluminium Alloys*. InTech [Online] [Accessed on 12th August, 2016] <Available through http://www.intechopen.com/books/recent-trends-in-processing-and-degradation-of-aluminium-alloys/aluminum-alloys-for-al-sic-composites>

Petrovic, V., Gonzalez, J.V.H., Ferrando, O.J., Gordillo, J.D., Puchades, J.R.B. and Grinan, L.P. (2011) Additive layered manufacturing: sectors of industrial application shown through case studies. *International Journal of Production Research*, 49 (4) pp 1061-1079

Pickens, J. R. (1981) Aluminium powder metallurgy technology for high-strength applications. *Journal of Materials Science*, 16, pp. 1437 – 1457

Pinkerton, A. J. (2016) Lasers in additive manufacturing. *Optics & Laser Technology*, 78 (A), pp. 25–32

Pohl, H., Simchi, A., Issa, M., and Dias, H. C., (2001) *Thermal Stresses in Direct Metal Laser Sintering*. Proceedings of twelfth solid freeform fabrication (SFF) symposium, Austin, pp. 366-372.

Polmear, I. J. (1995*) Light alloys: metallurgy of the light metals*, 3rd Ed. London: Wiley

Poprawe, R., Hinke, C., Meiners, W., Schrage, J., Bremen, S. and Merkt, S. (2015) *SLM Production Systems: Recent Developments in Process Development, Machine Concepts and Component Design*. In Brecher, C. (Ed.) *Advances in Production Technology*, Switzerland: Springer Open

Prabhu, B., Suryanarayana, C., An, L. and Vaidyanathan, R. (2006) Synthesis and characterization of high volume fraction Al–Al2O3 nanocomposite powders by high-energy milling. *Materials Science and Engineering A*, 425, pp. 192-200.

Prado, R. A., Murr, L. E., Soto, K. F. and McClure, J. C. (2003) Self-optimization in tool wear for friction-stir welding of Al 6061 + 20% Al2O3 MMC. *Materials Science and Engineering* A, 349, pp. 156-165.

Prashanth, K. G., Scudino, S., Klauss, H. J., Surreddi, K. B., Löber, L., Wang, Z., Chaubey, A. K., Kühn, U. and Eckert, J. (2014) Microstructure and mechanical properties of Al–12Si produced by selective laser melting: Effect of heat treatment, *Materials Science and Engineering: A*, 590, pp. 153-160,

Rahman, Md. H. and Rashed, H. M. M-Al. (2014) Characterization of Silicon Carbide Reinforced Aluminum Matrix Composites. *Procedia Engineering*, 90, pp. 103-109

Rajasekaran, S., Udayashankar, N. K. and Nayak, J. (2012) T4 and T6 Treatment of 6061 Al-15 Vol. % SiCp Composite. *ISRN Materials Science*, 2012.

Rana, R. S., Purohit, R. and Das, S. (2012a) Reviews on the Influences of Alloying elements on the Microstructure and Mechanical Properties of Aluminum Alloys and Aluminum Alloy Composites. *International Journal of Scientific and Research Publications*, 2 (6).

Rana, R. S., Purohit, R. and Das, S (2012b) Review of recent studies in Al matrix composites. *International Journal of Scientific and Engineering Research*, 3 (6).

Rao, H., Giet, S., Yang, K., Wu, X. and Davies C. H. J. (2016) The influence of processing parameters on aluminium alloy A357 manufactured by Selective Laser Melting. *Materials & Design*, 109, pp. 334-346

Read, N., Wang, W., Essa, K. and Attallah, M. M. (2015) Selective laser melting of AlSi10Mg alloy: Process optimisation and mechanical properties development. *Materials and Design*, 65, pp. 417–424

Reeves, P. (2008) *How the Socioeconomic Benefits of Rapid Manufacturing Can Offset Technological Limitations in S.M.E.* Technical Paper, Society of Manufacturing Engineers, Dearborn, U.S.A.

Romero, J.C., Wang, L. and Arsenault, R.J., 1996. Interfacial structure of a SiC/Al composite. *Materials Science and Engineering A*, 212(1), pp.1-5.

Rosso, M. (2006) Ceramic and Metal Matrix Composites: Routes and properties. *Journal of Materials Processing Technology*, 175, pp. 364-375.

Ruiz-Navas, E. M., Fogagnolo, J.B., Velasco, F., Ruiz-Prieto, J.M. and Froyen L. (2006) One step production of aluminium matrix composite powders by mechanical alloying. *Composites Part A*, 37 (11), pp. 2114-2120.

Saheb, N., Laoui, T., Daud, A. R., Harun, M., Radiman, S. and Yahaya, R. (2001) Influence of Ti addition on wear properties of Al–Si eutectic alloys. *Wear*, 249 (8), pp. 656–662

Sames, W. J., List, F. A., Pannala, S., Dehoff, R. R. and Babu, S. S. (2016) The metallurgy and processing science of metal additive manufacturing. *International Materials Reviews*

Sarkar, J. (1995) Aspects of Strengthening and Work Hardening in Particulate Metal Matrix Composites. *Scripta Metallurgica et Materialia*, 32 (1), pp. 37 – 42.

Sateesh, N. H., Mohankumar, G. C. and Krishna, P. (2014) Effect of Process Parameters on Surface Roughness of Laser Processed Inconel Superalloy. *International Journal of Scientific & Engineering Research*, 5 (8)

Savalani, M. M., Chung, C. C., Poon, C. and Yeung, W. (2011) *Selective laser melting of Aluminium and its alloys*. New Zealand Rapid Product Development Conference. Auckland University of Technology, Auckland 7 -8 February.

Schaffer, G. B. (2004) *Powder Processed Aluminium Alloys*. In Nie, J. F., Morton, A. J. and Muddle, B. C. (Eds) *Materials Forum*, 28, pp. 65 -74

Scudino, S., Liu, G., Prashanth, K. G., Bartusch, B., Surreddi, K. B., Murty, B. S. and Eckert, J. (2009) Mechanical Properties of Al-based Metal Matrix Composites reinforced with Zr-based Glassy Particles produced by Powder Metallurgy. *Acta Materialia*, 57, pp. 2029-2039.

Shankar, S., Riddle, Y. W. and Makhlouf, M. M. (2004) Eutectic Solidification of Aluminum- Silicon Alloys. *Metallurgical and Materials Transactions A, Physical Metallurgy and Materials Science*, 35A (9), pp. 3038-3043

Shellabear, M. and Nyrhila, O. (2004) DMLS – *Development History and State of the art*. Presented at LANE 2004 conference, Erlangen, Germany, Sept. 21-24, 2004

Simchi, A. and Godlinski, D. (2008) Effect of SiC particles on the laser sintering of Al–7Si–0.3Mg alloy. *Scripta Materialia*, 59, pp. 199–202

Simchi, A. and Pohl, H. (2003) Effects of laser sintering processing parameters on the microstructure and densification of iron powder. *Materials and Engineering A*, 359 119-128

Simchi A., Petzoldt F. and Pohl H. (2003) On the development of direct metal laser sintering for rapid tooling. *Journal of Materials Processing Technology*, 141 (3) pp. 319-328(10)

Slezenev, L., Slezenev, I.L., Cornie, J.A., Argon, A.S., and Mason, P.R. (1998) *Effect of composite particle size and heat treatment on the mechanical properties of Al–4.5 wt.% Cu based alumina particulate reinforced composites*. In: Proceeding of the International Congress and Exposition, 1998 Detroit, pp. 23–26.

Slipenyuk, A., Kuprin, V., Milman, Y., Spowart, J.E. and Miracle, D.B (2004) The effect of matrix to reinforcement particle size ratio (PSR) on the microstructure and mechanical

properties of a P/M processed AlCuMn/SiCp MMC. *Materials Science and Engineering A*, 381 (1-2), pp. 165-170.

Smith, W. F. (1986) *Principles of Materials Science and Engineering*. 3rd Ed. New York: McGraw Hill.

Song, Y. (1997) Experimental study of the basic process mechanism for direct selective laser sintering of low-melting powder, *Ann CIRP*, 46(1), 127–130

Song, B., Dong, S., Zhang, B., Liao, H. and Coddet, C. (2012) Effects of processing parameters on microstructure and mechanical property of selective laser melted Ti6Al4V. *Materials and Design*, 35, pp. 120-125.

Spear, R. E. and Gardner, G. R. (1963) Dendrite Cell Size. *AFS Transactions*, 71, pp. 209-215.

Spears, T. G. and Gold, S. A (2016) In-process sensing in selective laser melting (SLM) additive manufacturing. *Integrating Materials and Manufacturing Innovation*, 5 (1)

Spierings, A. B. and Levy, G. (2009) Comparison of density of stainless steel 316L parts produced with selective laser melting using different powder grades. Proceedings of the 20th Annual International Solid Freeform Fabrication (SFF) Symposium, The University of Texas, Austin, August 3-5, 2009

Spierings, A. B., Herres, N. and Levy, G. (2011a) Influence of the particle size distribution on surface quality and mechanical properties in additive manufactured stainless steel parts. *Rapid Prototyping Journal*, 17 (3), pp. 195-202(8)

Spierings, A. B., Schneider, M. and Eggenberger, R. (2011b) Comparison of Density Measurement Techniques for Additive Manufactured Metallic Parts. *Rapid Prototyping Journal*, 17 (5), pp. 380-386

Srivastava, V., Parida, S. K. and Pandey, P. M. (2010) *Surface roughness studies in selective laser sintering of glass filled polyamide*. Proceedings of the 36th International MATADOR conference. Springer Science & Business Media, 5th Aug

Stwora, A. and Skrabalak, G. (2013) Influence of selected parameters of Selective Laser Sintering process on properties of sintered materials. *Journal of Achievements in Materials and Manufacturing Engineering*, 61 (2), pp. 375-380

Surappa, M. K. (2003) Aluminium matrix composites: Challenges and opportunities. *Sadhana*, 28, (1-2) pp. 319–334.

Suryanarayana, C. (2001) Mechanical alloying and milling. *Progress in Materials Science*, 46 (1-2), pp. 1-184.

Suryanarayana, C. (2004) *Mechanical Alloying and Milling*. Florida: CRC Press

Sustarsic, B., Paulin, I., Godec, M., Glodez, S., Sori, M., Flasker, J., Korosec, A., Kores, S. and Abramovic, G. (2014) Morphological and Microstructural Features of Al-Based Alloyed Powders for Powder-Metallurgy Applications. *Materials and technology*, 48 (3), pp. 439–450

Takacs. L (2009). Self-sustaining reactions induced by ball milling (overview). *International journal of self-propagating high temperature synthesis*, 18, pp 276-282.

Tang, Y., Fuh, J. Y. H., Loh, H. T., Wong, Y. S., and Lu, L. (2003) Direct laser sintering of a silica sand, *Materials and Design*, 24, pp. 623–629

Taylor, J. A. (2012) Iron-containing intermetallic phases in Al-Si based casting alloys. *Procedia Materials Science*, 1, pp. 19 – 33.

Thijs, L., Kempen, K., Kruth, J-P. and Humbeeck, J. V. (2013) Fine structured aluminium products with controllable texture by Selective Laser Melting of pre-alloyed AlSi10Mg powder. *Acta Materialia*, 61 (5), pp. 1809 – 1819.

Thijs, L., Verhaeghe, F., Craeghs, T., Humbeeck, J. V. and Kruth J. P. (2010) A study of the microstructural evolution during selective laser melting of Ti-6Al-4V. *Acta Materialia*, 58 (9), pp. 3303–3312.

Thummler, F. and Oberacker, R. (1993) *Introduction to Powder Metallurgy*. In Jenkins, I. and Wood, J. V (eds.) *The Institute of Materials Series on Powder Metallurgy*. The Institute of Materials: London

Tjong, S. C. and Ma, Z. Y. (1997) The high-temperature creep behaviour of aluminium-matrix composites reinforced with SiC, A12O3 and TiB2 particles. *Composites Science and Technology* (51) 697-702

Tolochko, N. K., Mozzharov, S. E., Yadroitsev, I. A., Laoui, T., Froyen, L., Titov, V. I. and Ignatiev M. B. (2004) Balling processes during selective laser treatment of powders. *Rapid Prototyping Journal*, 10, pp. 78–87

Torralba, J., Da-Costa, C. and Velasco, F. (2003) P/M Aluminium Matrix Composites: An Overview. *Journal of Materials Processing Technology*, 133, pp. 203-206.

Torres, C. d-S. and Schaeffer, L. (2010) Effect of High Energy Milling on the Microstructure and Properties of Wc-Ni Composite. *Materials Research*, 13 (3), pp. 293-298

Total Materia, (2002) *Aluminium Alloys – Effects of Alloying Elements*. [Online] [Accessed on 12th August, 2016] < Available through http://www.totalmateria.com/Article55.htm>

Tzamtzis, S., Barekar, N. S., Hari Babu, N., Patel, J., Dhindaw, B. K. and Fan, Z. (2009) Processing of advanced Al/SiC particulate Metal Matrix Composites under intensive shearing – a Novel Rheo Process. *Composites*, A40, pp. 144–151

Vaucher, S., Carreno-Morelli, E., Andre, C. and Beffort, O. (2003) Selective laser sintering of aluminium and titanium-based composites: processing and characterisation. *Physica Status Solidi A*, 119 (3), R11-R13

Verlinden, B., and Froyen, L. (1994) *Aluminum Powder Metallurgy. TALAT Lecture 1401*, EAA European Aluminum Association, University of Leuven, Belgium,

Vilaro, T., Kottman-Rexerodt, V., Thomas, M., Colin, C., Bertrand, P., Thivillon, L., Abed, S., Ji, V., Aubry, P., Peyre, P. and Malot, T. (2010) Direct Fabrication of a Ti-47Al-2Cr-2Nb Alloy by Selective Laser Melting and Direct Metal Deposition Processes. *Advanced Materials Research*, 89-91, pp. 586-591.

Voncina, M., Mrvar, R. and Medved, J. (2006) Thermodynamic Analysis of AlSi10Mg Alloy. RMZ – *Materials and Geoenvironment*, 52 (3), pp. 621 – 633.

Wagener, H. W. and Wolf, J. (1993) Cold forging of MMCs of aluminium alloy matrix. *Journal of Materials Processing Technology*. 37 (1-4), pp. 253 – 265.

Wang, Y., Bergström, J. and Burman, C. (2006) Characterization of an iron-based laser sintered material. *Journal of Materials Processing Technology*, 172 (1) pp77-87

Warmuzek, M. (2004) *Aluminum-Silicon Casting Alloys: Atlas of Microfractographs*. USA: ASM International.

Weingarten, C., Buchbinder, D., Pirch, N., Meiners, W., Wissenbach, K. and Poprawe, R. (2015) Formation and reduction of hydrogen porosity during selective laser melting of AlSi10Mg. *Journal of Materials Processing Technology*, 221, pp. 112-120

Wenzelburger, M., Silber, M. and Gadow, B, R. (2010) *Manufacturing of Light Metal Matrix Composites by Combined Thermal Spray and Semisolid Forming Processes — Summary of The Current State of Technology*. In Taha, M. A. El-Sabbagh, A. M. and Taha, I. M. (2010). *Trends in Composite Materials and their Design*. Trans Tech Publications Ltd. [Online] [Accessed on 12th August, 2016] <Available through http://app.knovel.com/hotlink/toc/id:kpTCMD0001/trends-in-composite-materials/trends-in-composite-materials>

Williams, J. D. and Deckard, C. R. (1998) Advances in modelling the effects of selected parameters on the SLS process. *Rapid Prototyping Journal*, 4 (2), pp 90-100.

Wilson, S. and Ball, A. (1993) *Performance of Metal Matrix Composites in various Tribological Conditions*, In Friedrich, K. (ed.) (1993) *Advances in Composite Tribology, Composite Materials Series 8*, Amsterdam: Elsevier Science Publishers.

Wollenberger, J. (2002) *The challenges of laser cutting: Overcoming some common obstacles*. [Online] [Accessed 12th August, 2016] <Available through http://www.thefabricator.com/article/lasercutting/the-challenges-of-laser-cutting-overcoming-some-common-obstacles>

Wu, L. and Ferguson, W. G. (2011) *Modelling of Precipitation Hardening in Casting Aluminium Alloys, Aluminium Alloys in Theory and Applications*. In Prof. Tibor Kvackaj (Ed.), Intech [Online] [[Accessed 12th August, 2016] <Available through http://www.intechopen.com/books/aluminium-alloys-theory-and-applications/modelling-of-precipitation-hardening-in-casting-aluminium-alloys>

Yadroitsev, I., Bertrand, Ph. and Smurov, I. (2007) Parametric analysis of the selective laser melting process. *Applied Surface Science*, 253, pp. 8064–8069

Yadroitsev, I., Gusarov, A., Yadroitsava, I. and Smurov, I. (2010) Single track formation in selective laser melting of metal powders. *Journal of Materials Processing Technology*, 210 (12), pp. 1624–1631

Yadroitsev, I., Krakhmalev, P., Yadroitsava, I., Johanssonc, S. and Smurova I. (2013) Energy input effect on morphology and microstructure of selective laser melting single track from metallic powder. *Journal of Materials Processing Technology*, 213 (4), pp. 606 –613.

Yuan, W. and An, B. (2012) Effect of heat treatment on microstructure and mechanical property of extruded 7090/SiCp composite. *Transactions of Nonferrous Metals Society of China*, 22, pp.2080 - 2086

Zhang, H., Ramesh, K. T. and Chin, E. S. C. (2004) High strain rate response of aluminium 6092/B4C composites. *Materials Science and Engineering A*, 384, pp. 26-34.

Zhang, H., Chen, M. W., Ramesh, K. T., Ye, J., Schoenung, J. M. and Chin, E. S. C., (2006) Tensile Behaviour and Dynamic Failure of Aluminium 6092/B4C Composites. *Materials Science and Engineering A*, 433, pp. 70-82.

Zhang, L., Klemm, D., Eckert, J., Hao, Y. and Sercombe, T. (2011) Manufacture by selective laser melting and mechanical behaviour of a biomedical Ti-24Zr-4Nb-7.9 Sn alloy. *Scripta Materialia*, 65 (1) pp. 21-24.

Zoz, H., Ren, H., Reichardt, R. and Benz, H. U. (1999) *High energy milling/ Mechanical alloying/ Reactive Milling*. [Online], 3rd International Symposium of the School of Chemical Engineering, University of Mexico, Mexico City, May 1998. [Accessed 12th August, 2016] <Available through http://www.zoz-group.de/zoz.main/pdf_content/publications/v14.pdf>

Zoz, H. and Ren, H. (2000) Processing of ceramic powder using high energy milling. *Journal of Metastable and Nanocrystalline Materials*, 8, pp. 955-963.

Zoz, H. (2002) *Simoloyer: major characteristics and features*. Zoz GmbH: Wenden, Germany